Towards Ab Initio Simulations of High-Temperature Superconductivity

Thesis by
Zhi-Hao Cui

In Partial Fulfillment of the Requirements for the
Degree of
Doctor of Philosophy

CALIFORNIA INSTITUTE OF TECHNOLOGY
Pasadena, California

2023
Defended October 12, 2022

© 2023

Zhi-Hao Cui
ORCID: 0000-0002-7389-4063

All rights reserved except where otherwise noted

ACKNOWLEDGEMENTS

First and foremost, I would like to thank my advisor, Prof. Garnet Chan, for his outstanding advising and continuous support during my whole Ph.D. period. Garnet taught me how to creatively and critically think about scientific problems, how to efficiently and calmly manage complicated projects, and how to be passionate and optimistic on research progresses. He has been always encouraging me to think about important scientific questions and to face major challenges bravely. Besides the research, he has always been supportive on every aspect of my life, especially on my mental health during the pandemic.

I would like to thank my graduation committee, Prof. Mitchio Okumura, Prof. Nai-Chang Yeh, Prof. Marco Bernardi and Prof. Tom Miller, for their time and advice on my research, proposals, and suggestions on my academic career.

During several projects in my Ph.D., I feel so lucky to meet so many talented collaborators. I am grateful to Lin Lin, Tianyu Zhu, Tim Berkelbach, Huanchen Zhai, Xing Zhang, Chong Sun, Ushnish Ray, Bo-Xiao Zheng, Qiming Sun, Mario Motta, Xiaojie Wu, Yu Tong, Michael Lindsey, Fabian Faulstich, Raehyun Kim, Reza Haghshenas, Hong-Zhou Ye, Linqing Peng, Junjie Yang, Liao Ke, Seunghoon Lee and Chenghan Li. Without their efforts, I can not finish the research projects smoothly and comprehensively.

I am grateful to be a member of the Chan group and meet so many friendly people. Besides the collaborators mentioned above, I would thank the general help in my office time and organizing the excellent group events from Matt O'Rourke, Johnnie Gray, Ruojing Peng, Zuxin Jin, Johannes Tölle, Rohit Dilip, Wenyuan Liu, Kasra Hejazi, Gunhee Park, Rui Li and other Chan group members. I also thank the previous members Zhendong Li, Yang Gao, Jason Yu, Alec White, Henrik Larrson, Sheng Guo, Narbe Mardirossian, Joshua Kretchmer, Elvira Sayfutyarova, Min Liu, Peng Bao and our group coordinator Sadie Rubalcava. I appreciate Brian Stoltz and Alison Ross for their help in my graduation process.

I would like to thank the whole Caltech community to provide a friendly and free environment for me and my colleagues. Since the age of Linus Pauling, the Division of Chemistry and Chemical Engineering has always been one of the centers of theoretical chemistry all over the world. I feel so proud to be a member of it and inspired by many pioneers in chemistry.

Special thanks are given to the Resnick High Performance Computing Center at Caltech and National Energy Research Scientific Computing Center (NERSC) for providing powerful computational resources and support during my research. I would like to thank Eddleman Graduate Research Fellowship, Caltech C Fellowship, Weldon Brown Fellowship, Department of Energy (DOE) and the Simons Foundation for the financial support of the research. I have learned a lot from the Simons meetings and summer schools and had very insightful discussions with many distinguished scientists in the computational quantum physics, including Steve White, Andy Millis, Shiwei Zhang, Kristjan Haule, Lucas Wagner, Sandeep Sharma, Dominika Zgid and many others.

I would like to thank my roommates, Quan Gan, Jiajun Du and Shuoyan Xiong for their support and help in my daily life. It is my great luck to have them in my last student days. There are so many friends I would like to thank: Kun Miao, Chenxi Qian, Tian Zeng, Zhen Liu, Lixue Cheng, Xuecheng Tao, Yao Luo, Xinhong Chen, Yalu Chen, Yu Chen, Xiaoran Hu, Hanwei Liu, Shumao Zhang, Guanya Shi, Jianchun Wang, Juner Zhang, Zhiao Yu, Yu Zheng, Shujia Liang, Peiyun Zhu, Yanruide Li, Shuaijing Du ... Please forgive me if I missed someone's name here.

Finally, I would like to thank my parents, who raised me up and consistently support me for every single decision I made during my scientific journey. This thesis is dedicated to them.

To my beloved parents

ABSTRACT

The high-temperature superconductors have been known for more than three decades. Nonetheless, the theoretical understanding of their microscopic properties remains unclear, and there are substantial difficulties in linking the observed phenomena to the material composition and structures. This thesis aims to establish a theoretical hierarchy (from lattice models to realistic materials) for faithful simulations of high-temperature superconductivity.

We start with the lattice models of superconductors by using quantum embedding theory, whose self-consistency allows magnetic and superconducting phases to emerge. We extended the density matrix embedding theory (DMET) with improved self-consistency algorithms and determined the ground-state phase diagrams for both one-band [Chap. 3] and three-band Hubbard models [Chap. 4]. In particular, in the three-band model, we explored the atomic-scale nature of the antiferromagnetic and superconducting orders for different model parametrizations, and highlighted the role of the oxygen degrees of freedom beyond the one-band picture.

To go beyond models, we extended the original theory [DMET and dynamical mean-field theory (DMFT)] to realistic *ab initio* descriptions of solids [Chap. 5]. The methods, named full-cell quantum embeddings, are distinct from other embedding schemes in the literature in three aspects: (i) all local orbitals in a unit cell are included in the embedding problem whereas the bath orbitals are truncated according to their atomic valence character; (ii) The embedding Hamiltonian is of the full quartic fermionic form rather than a simplified Hubbard-like Hamiltonian; (iii) Many-body quantum chemistry solvers such as coupled cluster (CC) are used to generate the embedding density matrix and Green's functions. As demonstrated across a variety of semiconducting and insulating materials, full-cell quantum embedding provides accurate energies, equations of state, spin-spin correlation functions, and excited-state band structures.

We then applied our *ab initio* quantum embedding methods to the parent state of a series of cuprate superconductors [Chap. 6]. We uncovered microscopic trends in the electron correlations and revealed the link between the material composition and magnetic energy scales via a many-body picture of excitation processes involving the buffer layers. We found a direct process involving competition between the in-plane superexchange and the CuO_2-buffer layer excitations, which explained the

magnetic coupling difference among a series of superconducting materials.

Finally, we investigated the doped cuprates, where the superconducting orders appear in the phase diagram [Chap. 7]. We generalized our *ab initio* framework to allow for particle-number symmetry breaking states such that the superconducting orders can spontaneously emerge during the self-consistency. We showed that the d-wave superconducting magnitude increases with the pressure applied to the crystals and the trend mimics that of the superexchange coupling J. Furthermore, we also studied the layer effect on superconductivity. Unlike the pressure effect, the layer effect between different compounds is affected by more factors - both magnetic coupling J and charge distribution matter. The work provides a starting point to study the material-specific physics in the superconducting phases of high-temperature superconductors.

The aforementioned applications relied on (i) the development and adaptation of many-body solvers, including the CC singles and doubles (CCSD) method with a Newton-Krylov solver for better numerical convergence, and active-space quantum chemistry techniques using large-scale density matrix renormalization group calculations. (ii) projection-based orbital localization techniques for metallic systems, frozen core techniques, and symmetry adaptations. These contents are discussed in Chap. 2 and Appendices, including their efficient implementation and parallelization.

In the concluding remarks [Chap. 8], we summarize the current status and limitations of the high-temperature superconductivity studies. In addition, we propose several possible directions to address the challenges in electronic correlation and atomic modeling of other exotic phases from an *ab initio* perspective.

PUBLISHED CONTENT AND CONTRIBUTIONS

[1] Z.-H. Cui, H. Zhai, X. Zhang, and G. K.-L. Chan, Systematic electronic structure in the cuprate parent state from quantum many-body simulations, Science **377**, 1192 (2022),
Z.-H. C. participated in designing the study, performing the calculations, and writing of the manuscript.

[2] F. M. Faulstich, R. Kim, Z.-H. Cui, Z. Wen, G. Kin-Lic Chan, and L. Lin, Pure state v-representability of density matrix embedding theory, J. Chem. Theory Comput. **18**, 851 (2022),
Z.-H. C. participated in the preparing and validating the data, and the writing of the manuscript.

[3] S. Lee, J. Lee, H. Zhai, Y. Tong, A. M. Dalzell, A. Kumar, P. Helms, J. Gray, Z.-H. Cui, W. Liu, et al., Is there evidence for exponential quantum advantage in quantum chemistry?, arXiv preprint arXiv:2208.02199 (2022),
Z.-H. C. participated in preparing benchmark data.

[4] R. Haghshenas, Z.-H. Cui, and G. K.-L. Chan, Numerical continuum tensor networks in two dimensions, Phys. Rev. Research **3**, 023057 (2021),
Z.-H. C. participated in preparing the benchmark data.

[5] Z.-H. Cui, C. Sun, U. Ray, B.-X. Zheng, Q. Sun, and G. K.-L. Chan, Ground-state phase diagram of the three-band Hubbard model from density matrix embedding theory, Phys. Rev. Research **2**, 043259 (2020),
Z.-H. C. participated in designing the study, performing the calculations, and writing of the manuscript.

[6] Z.-H. Cui, T. Zhu, and G. K.-L. Chan, Efficient implementation of ab initio quantum embedding in periodic systems: density matrix embedding theory, J. Chem. Theory Comput. **16**, 119 (2020),
Z.-H. C. participated in designing the study, performing the calculations, and writing of the manuscript.

[7] M. Motta, C. Genovese, F. Ma, Z.-H. Cui, R. Sawaya, G. K.-L. Chan, N. Chepiga, P. Helms, C. Jiménez-Hoyos, A. J. Millis, et al., Ground-state properties of the hydrogen chain: dimerization, insulator-to-metal transition, and magnetic phases, Phys. Rev. X **10**, 031058 (2020),
M. M., C. G., F. M., Z.-H. C., and R. S. contributed equally. Z.-H. C. participated in performing the DMRG, CAS calculations, basis set cross-checking and writing of the manuscript.

[8] C. Sun, U. Ray, Z.-H. Cui, M. Stoudenmire, M. Ferrero, and G. K.-L. Chan, Finite-temperature density matrix embedding theory, Phys. Rev. B **101**, 075131 (2020),

Z.-H. C. participated in writing and optimizing computer codes and data validation.

[9] Q. Sun, X. Zhang, S. Banerjee, P. Bao, M. Barbry, N. S. Blunt, N. A. Bogdanov, G. H. Booth, J. Chen, Z.-H. Cui, J. J. Eriksen, Y. Gao, S. Guo, J. Hermann, M. R. Hermes, K. Koh, P. Koval, S. Lehtola, Z. Li, J. Liu, N. Mardirossian, J. D. McClain, M. Motta, B. Mussard, H. Q. Pham, A. Pulkin, W. Purwanto, P. J. Robinson, E. Ronca, E. Sayfutyarova, M. Scheurer, H. F. Schurkus, J. E. T. Smith, C. Sun, S.-N. Sun, S. Upadhyay, L. K. Wagner, X. Wang, A. White, J. D. Whitfield, M. J. Williamson, S. Wouters, J. Yang, J. M. Yu, T. Zhu, T. C. Berkelbach, S. Sharma, A. Sokolov, and G. K.-L. Chan, Recent developments in the PySCF program package, J. Chem. Phys. **153**, 024109 (2020),
Z.-H. C. participated in writing computer codes and providing examples.

[10] T. Zhu, Z.-H. Cui, and G. K.-L. Chan, Efficient formulation of ab initio quantum embedding in periodic systems: dynamical mean-field theory, J. Chem. Theory Comput. **16**, 141 (2020),
Z.-H. C. participated in designing the study, performing the calculations, and writing of the manuscript.

[11] X. Wu, Z.-H. Cui, Y. Tong, M. Lindsey, G. K.-L. Chan, and L. Lin, Projected density matrix embedding theory with applications to the two-dimensional Hubbard model, J. Chem. Phys. **151**, 064108 (2019),
X. W. and Z.-H. C contributed equally. Z.-H. C. participated in designing the study, performing the calculations, and writing of the manuscript.

TABLE OF CONTENTS

Chapter 1

INTRODUCTION

1.1 Challenge of high-temperature superconductivity

A high-temperature superconductor (HTSC), as the name suggests, is distinguished from a conventional superconductor by its unusually high superconducting critical temperature T_c. The discovery of HTSC [1] is undoubtedly one of the most important breakthroughs in physics in the second half of the twentieth century, which opens up a new field for condensed matter physics and illuminates the path to underlying applications of superconducting materials in real life [2, 3]. Currently, an HTSC primarily falls within one of the two families of compounds, i.e. copper-based and iron-based superconductors. The former, also known as *cuprates*, is the most typical HTSC and holds the highest record of T_c up to date (133 K at ambient pressure in mercury-based tri-layer compound $HgBa_2Ca_2Cu_3O_{8+\delta}$ [4]).

The crystal structure of cuprates typically contains alternating (multiple) CuO_2 plane(s) with other kinds of metal atoms serving as interstitial ions, called *buffer layer*. For instance, Fig. 1.1 (a) and (b) provide the basic structure of Nd_2CuO_4 and La_2CuO_4, where Cu and O atoms form the pure CuO_2 plane and distorted CuO_6 octahedrons (CuO_2 plane with additional apical oxygens) respectively. The apical oxygen, Nd and La play the role of an interlayer charge reservoir. These compounds without doping are known as *parent compounds*. When dopant ions (e.g. Ce, Sr) are introduced, such cuprates become real superconducting materials at low temperature. Concretely, substituting Sr^{II} for La^{III} would effectively introduce a hole in the CuO_2 layer and the resulting material is thus called a hole-doped HTSC. Similarly, by replacing Nd^{III} with Ce^{IV}, an excess electron transfers to the CuO_2 plane, leading to an electron-doped HTSC. In literature, the doping concentration x is usually defined as the number of additional change carriers per CuO_2 unit.

More interesting physics emerges at the electronic structure level, particularly in the phase diagram of cuprates [5], see Fig. 1.1 (c). Despite the existence of many variants of cuprates, there are actually several common features in the phase diagram: (i) The parent state is an antiferromagnetic (AFM) insulator. (ii) The long-range AFM order quickly drops and eventually disappears after doping. (iii) The superconducting (SC) order emerges with some doping at low temperature, showing an SC dome in the

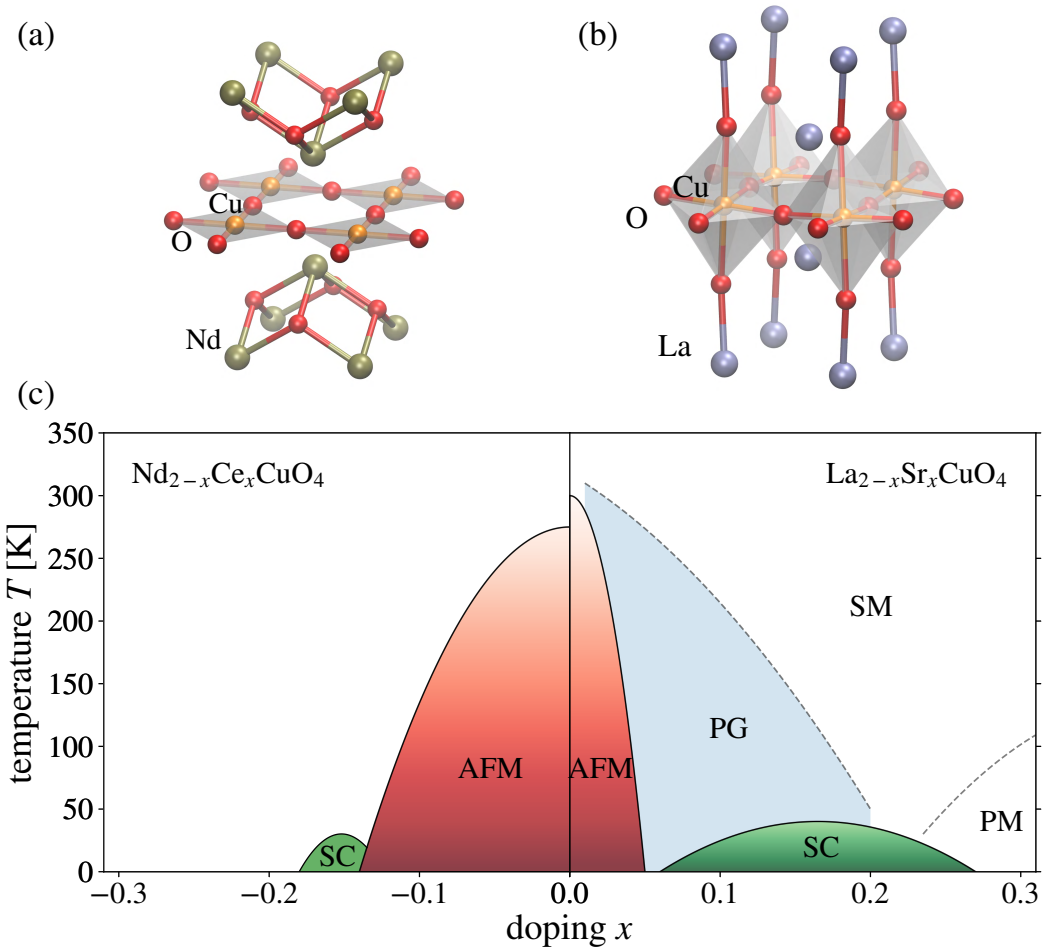

Figure 1.1: Crystal structure of cuprates (parent compounds) and a typical electronic phase diagram. (a) electron-doped Nd_2CuO_4 and (b) hole-doped La_2CuO_4; (c) doping-temperature phase diagram, different phases are shown: antiferromagnetic (AFM), superconducting (SC), pseudogap (PG) .

phase diagram. The doping concentration corresponding to the apex of the dome is called the optimal doping and the region before (after) it is referred to as underdoped (overdoped) region. (iv) There is significant particle-hole asymmetry along doping, e.g., the AFM phase is more robust against electron doping, whereas the SC order is usually more evident in the hole-doped case. (v) In the underdoped region of the hole doped side of phase diagram, there is the so-called pseudogap (PG) phase, where the system is partially gapped on the Fermi surface [6]. Usually, competing orders [AFM, SC, stripe, density waves (DW) etc.] coexist in the PG region [7, 8]. The PG phase is typically not very evident in the electron-doped side. (vi) By overdoping or increasing the temperature, the AFM and SC correlations finally decay and the system becomes a paramagnetic (PM) metal and can be satisfactorily

described by the Fermi liquid theory [9] (although there are regions, called strange metal (SM) phase, showing significantly more correlated behaviors than the PM metal phase [10]).

Although such a sophisticated phase diagram has been established by extensive experimental efforts (see Ref. [5, 11] and references therein), a universal theory that explains all components of the phase diagram, has yet to emerge. Historically, the microscopic superconducting mechanism of conventional superconductors was successfully established by the Bardeen–Cooper–Schrieffer (BCS) theory [12], whose key idea is the formation of electron pairs (Cooper pairs) due to the interactions of the electrons with the vibrations of the atoms in the lattice (phonon). It was proven that an arbitrarily small attraction between electrons can stabilize the electron pair as a bound state against a non-interacting Fermi gas. Many experiments (especially the isotope effect) have verified the electron-phonon interaction as the "glue" of the electron pairing state. As a consequence, the T_c of a conventional superconductor can be qualitatively predicted by estimating the averaged phonon-frequency ω_0, electron-phonon coupling parameter g and the electronic density of states around the Fermi level N_F,

$$T_c \sim \omega_0 \exp\left(-\frac{1}{gN_F}\right). \tag{1.1}$$

However, the phonon-mediated mechanism can not explain the high-T_c superconductivity because the phonon frequency as well as its coupling with electrons can not be sufficiently large (the current highest T_c of conventional superconductors at ambient pressure is about 40 K [13]). Unlike the conventional superconductors, the role of isotope effect by replacing ^{16}O by ^{18}O, is not clear and in many cases it does not change T_c significantly [14]. Therefore, a new type of glue needs to be determined and its energy scale ω_0 should be larger than the typical lattice vibration.

Besides the mysterious superconducting mechanism, there are substantial differences in the electronic structure compared to the conventional superconductors. The conventional superconductors are mostly simple sp metals, alloys or compounds (e.g., Hg, Nb_3Ge, MgB_2). These materials are usually weakly correlated (i.e., a single Slater determinant dominates the electron's behavior) and are thus well described by the density functional theory (DFT) with standard approximate functionals [15, 16]. The HTSCs, on the other hand, are a typical class of strongly correlated materials. From their chemical compositions, there exists fractionally occupied d orbitals; or from a band structure perspective, there are narrow bands (localized states) entangled with the itinerant electrons in the normal bands [17].

As a result, the DFT with local or semi-local functionals fails to describe the magnetic properties of HTSC. Similarly, the low-order perturbation theory based on a mean-field reference is not applicable, especially for the doped states. One should note that the formation of the Cooper pair is intrinsically a many-body process and makes the electron correlation even stronger and more long-range. A correct theory, therefore, should be able to treat the strongly correlated electrons and in the meanwhile, scales to large enough systems to mimic the emergence of distinct phases - this is often a dilemma for quantum chemistry or computational physics methods, and some trade-off must be taken to balance the accuracy and efficiency.

Moreover, due to the mysterious superconducting mechanism and strong electron correlation, most of the studies of HTSCs heavily rely on simplified model Hamiltonians, especially for the studies of exotic phases like superconducting and density-wave orders. Since all details of materials are encoded in a few model parameters (the effects of buffer layers are largely ignored), people have little understanding of the relation between material compositions and corresponding properties, let alone effectively predicting new materials with higher T_c. Overall, the high-temperature superconductivity problem remains a great challenge for condensed matter physics and quantum chemistry.

1.2 Roadmap to ab initio modelling of superconductivity

Given such a sufficiently complicated system and increasingly powerful computing capabilities, one may naturally ask: Can we resort to numerical approaches and provide a quantitative solution to the high T_c problem? From the perspective of theoretical chemists, the ultimate goal of high T_c study is thus to

> *Ab initially* determine the electronic structure of cuprates at both *zero* and *finite* temperature, and understand the *factors* that influence the strength of superconductivity.

There is unfortunately no one-stop solution to achieve such a goal due to the enormous complexity of the problem. There is, however, a hierarchical roadmap to gradually take the relevant degrees of freedom into account, see Fig. 1.2.

Hamiltonian. On the first dimension of the roadmap, one expects an effective lattice model that captures the most essential static correlation effects. The procedure of mapping a realistic material to an effective Hamiltonian is known as *downfolding* [18–20]. As we have mentioned in Sec. 1.1, a common structural feature of

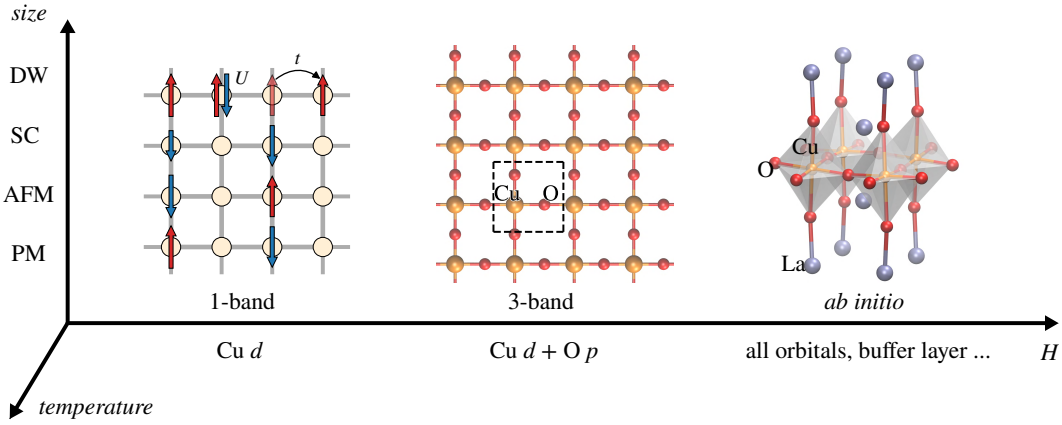

Figure 1.2: A roadmap to the *ab initio* simulation of high-T_c superconductivity. Three dimensions of complexity are shown: (i) Degrees of freedom in the Hamiltonian H increase from the simplest 1-band model to the 3-band model to the *ab initio* Hamiltonian. More orbitals are incremented to represent the dynamical correlation and buffer layers. (ii) Increasing system size allows for different types of symmetry breaking and more complicated phases to emerge. (iii) The finite-temperature effect can be in principle considered to study the phase transition in the real world.

cuprates is the existence of CuO_2 plane. In addition, transport experiments show a strong anisotropic conductance, where the superconducting current along the plane direction is significantly more evident. One can therefore extract the CuO_2 layer as an effective model and regard the other parts of the material as a charge reservoir that mediates the doping concentration. If we further consider only the minimal relevant orbitals, namely Cu $d_{x^2-y^2}$ and O $p_{x(y)}$ orbitals, the model becomes a *three-band model* (per CuO_2 unit cell) [21] as shown in the middle of Fig. 1.2. The three-band model is, however, still very complicated and the degrees of freedom on oxygen can be approximately integrated out, leading to a *one-band model* without explicit atomic structures. This Hamiltonian is known as the two-dimensional (2D) one-band Hubbard model [22, 23],

$$\hat{H} = \sum_{\sigma ij} t_{ij} \left(a^{\dagger}_{i\sigma} a_{j\sigma} + \text{H.c.} \right) + U \sum_{i} n_{i\alpha} n_{i\beta}, \tag{1.2}$$

where t is the hopping matrix and the *ab initio* Coulomb four-index integral is replaced by an on-site Coulomb repulsion U, which is comparable to the bandwidth in cuprates. In the large-U limit, the model is a typical strongly correlated system, for which the mean-field like method, e.g. Hartree-Fock (HF) approach, breaks down. To solve the model, an expensive non-perturbative treatment is usually necessary. Regardless of the simplicity, the one-band and three-band models already show some general features in HTSCs, e.g., AFM, SC, DW and various inhomogeneous

charge, spin and pairing orders (see Refs. [24, 25] and references therein). The primary difficulties are two-fold: (i) the energy scale of different competing orders generally falls in a very small energy window, meaning that a tiny change of the parameter can drastically change the inherent physics. The realistic physical process of materials are governed by the fine structure of the lattice. As an instance, there are obvious discrepancies between the 1-band model prediction and experiments in the wavelength of the stripe order [24]. (ii) More importantly, it is still largely unknown how the buffer layer and geometry distortion influence the properties of the HTSCs, e.g. through static electricity or one-body potential or many-body electron correlation? The answers to these questions are unlikely to be lurking in these simplified models and demand more *ab initio* insights. Hence, the last rung of the first dimension is the *ab initio* Hamiltonian involving all orbitals in the lattice.

System size. The second dimension in the roadmap is the size of the system. Since we are interested in the phase diagram of HTSCs, the system size, in principle, should be at the thermodynamic limit (TDL), so that different orders spontaneously appear. Noether's theorem states that the symmetry of a quantum state corresponds to a conserved physical quantity. For a finite-system Hamiltonian with conserved spin SU(2) symmetry, the exact diagonalization can not generate an AFM ground state that breaks the spin symmetry, whereas the symmetry break can happen if the system is infinite (the energy gap between the ground and AFM state is infinitely small). To simulate the symmetry-breaking phenomena, there are typically three ways: (i) Estimating the order parameter through correlation functions of a non-symmetry-breaking state. By definition, the correlation function measures the response of an external perturbation. It is particularly useful when studying the long-range order, corresponding to large eigenvalues (comparable to the system size) of many-body density matrices. (ii) Adding a pinning field to the boundary of a finite system to artificially break the symmetry. The order parameter should be read from the center of the system where the direct influence of the boundary condition has vanished. (iii) Simulating the symmetry breaking through a self-consistent field (SCF). It is well-known that the mean-field like methods, e.g., DFT and HF are able to stabilize different phases by allowing symmetry-breaking fields during the SCF. A carefully chosen density functional (e.g., certain hybrid functional) could provide a reasonable description of magnetic properties, but not for more complicated phases such as superconductivity, where the electron correlation is crucial. One needs a *quantum embedding* procedure to incorporate electron correlation and during its SCF the symmetry breaking automatically happens. In other words, the quantum

embedding is directly treating the system as TDL, and the final order parameters are determined from some extrapolation procedure with respect to fragment sizes. The size of fragments constrains the allowed types of orders and the increasing of the supercell size will allow more and more inhomogeneous order (from the simplest PM phase to DW phase etc in Fig. 1.2).We will mainly discuss how quantum embedding can be used to study the high-T_c problem in the thesis.

The idea of embedding is rooted in the *local* nature of entanglement in the low-lying states [26]. A large (infinite) system can thus be divided into small fragments and for each fragment, the enormous number of environment states are effectively replaced by a small amount of *bath* degrees of freedom. One can then perform a high-level calculation on each small embedding problem and collect them together to improve the overall description of the whole system until the procedure reaches a fixed point. A famous realization of embedding is the dynamical mean-field theory (DMFT) [27, 28], which uses the Green's function as its basic variable and utilizes the locality of the impurity (fragment) self-energy $\Sigma^{\text{imp}}(\omega)$ to construct the new lattice Green's function $G^{\text{latt}}(\mathbf{k}, \omega)$. The coupling between impurity and bath is described by the so-called hybridization $\Delta(\omega)$. DMFT is probably the first embedding theory that works for strongly correlated electrons and has been successfully applied to various lattice models [27]. However, DMFT suffers severely from the bath discretization error[1] and its large computational complexity due to the frequency dependence. Because of its large computational cost, the impurity model is usually chosen as Anderson impurity model [29] or a very small cluster.

Over the past few years, density matrix embedding theory (DMET) [30] has emerged as a powerful cluster embedding method. The basic idea of DMET is similar to that of (cellular) DMFT in the sense that they both map the infinite lattice to an impurity model with the environment described by the bath degrees of freedom, and attempt to self-consistently match the physical quantities between the mean-field lattice solution and the correlated cluster (impurity) calculations. Compared to the Green's function based embedding methods, DMET is featured by its limited number of bath orbitals (up to the number of impurity orbitals) and the frequency independence, which enables DMET to utilize efficient wavefunction-based solvers and to treat potentially larger clusters. With such appealing features, DMET has been applied to lattice models [24, 30–33], *ab initio* chemical Hamiltonians [34–36]

[1] In principle, one can circumvent the bath discretization error by integrating out the bath degree of freedom in continuous time quantum Monte Carlo (CT-QMC) solver. However, the CT-QMC solver is costly and has severe sign problems at low temperature.

and non-fermionic systems [37, 38], as well as excited states [39] and real-time extensions [40]. For a detailed review of DMET, we refer the interested readers to Ref [35]. It is noteworthy that DMET has successfully provided an accurate ground state phase diagram of the one-band Hubbard model [32], even in the most difficult underdoped region [24], which can be viewed as an elegant integration over the two dimensions on the above roadmap (i.e., the simplest Hamiltonian but with a large supercell size allowing DW-type stripe orders). It is therefore highly interesting to move one step forward to examine its performance on the more complicated three-band model and realistic *ab initio* Hamiltonians.

Temperature. In principle, all realistic physics is not at 0 K. And in Fig. 1.1(c), many phases are measured at the finite temperature and undergo a phase transition to the normal state after heating. In particular, the formation and transition of PG and SM phases are still substantially controversial. Despite its importance, in this thesis we will not focus on the third dimension, the finite temperature effect, but will mention related concepts (such as finite-temperature smearing for gapless systems) and estimate the influence of temperature from zero-temperature observables.

1.3 Structure of the thesis

In the remaining parts of the thesis, we present the theoretical developments of the quantum embedding and how it can be applied to both lattice models and realistic materials, including the high-T_c cuprates.

In Chap. 2, we present the theoretical formulation of quantum embedding, including the basic idea of DMET and DMFT, their *ab initio* formulations, self-consistency for symmetry breaking, generalized spin-orbital formulation for superconductivity, various impurity solvers adapted for the HTSCs problems and their efficient implementation.

In Chap. 3, we discuss the DMET self-consistency algorithm and developed a projection-based algorithm (p-DMET) to improve the numerical stability of the self-consistency. The concept "global density matrix" introduced in this work has been used in many recent literatures to improve the self-consistency or energy accuracy of DMET. We studied the magnetic phase diagram of the one-band Hubbard model using DMET and p-DMET.

In Chap. 4, we go beyond the one-band picture and studied the three-band Hubbard model, which, although still simplified, contains the atomic information of the 2D CuO_2 plane. Using the symmetry-broken DMET formalism, we explored

the atomic-scale nature of the antiferromagnetic and superconducting orders, and highlighted the role of the oxygen degrees of freedom beyond the one-band picture. The influence of model parameters in the phase diagram is also discussed.

In Chap. 5, we extended the quantum embedding theory [DMET and DMFT] to *ab initio* realistic solids. The methods, namely the full-cell quantum embedding, are distinct from other embedding schemes in three aspects: (i) all local orbitals in a unit cell are included in the embedding problem whereas the bath orbitals are truncated according to the atomic valence characters; (ii) The embedding Hamiltonian is of full quartic fermionic form rather simplified Hubbard like Hamiltonian; (iii) Many-body quantum chemistry solvers such as coupled cluster (CC) are used to generate embedding density matrix and Green's functions. As demonstrated across a variety of semiconducting and insulating materials, the full-cell quantum embedding provides accurate energy, equation of state, spin-spin correlation functions, and excited-state band structures.

In Chap. 6, we then applied our *ab initio* quantum embedding methods to the parent state of a series of cuprate superconductors. We uncovered microscopic trends in the electron correlations and revealed the link between the material composition and magnetic energy scales via a many-body picture of excitation processes involving the buffer layers. We found the competition between the in-plane superexchange and the CuO_2-buffer layer excitations, which explains the magnetic coupling difference among a series of superconducting materials.

In Chap. 7, we applied our approach to the doped cuprates, where the superconducting orders enter into the phase diagram. We showed that the d-wave superconducting magnitude increases with the pressure applied to crystals and the trend connects to the exchange coupling J. Furthermore, we also studied the buffer layer effect on superconductivity. Unlike the pressure effect, the layer effect between different compounds is affected by more factors - both magnetic coupling J and charge distribution matter. This work provides a promising route to study the material-specific physics of HTSCs.

In Chap. 8, we summarize the current status and limitations of the high-temperature superconductivity study. We also propose several possible directions to address the challenges in electronic correlation and atomic modeling of other exotic phases from an *ab initio* perspective.

Chapter 2

QUANTUM EMBEDDING THEORY

2.1 Introduction

The *ab initio* description of strongly correlated electrons in solids is a major challenge, limiting the quantitative understanding of interacting electronic phases, such as the Mott [41] and high-temperature superconducting phases [17, 42, 43]. The heart of the difficulty lies in the need to use computational methods that can treat correlated electrons, which usually means a steep computational scaling with system size, as well as treat the thermodynamic limit (TDL), in order to observe distinct phases.

A formal route to extend high-level correlated electron methods to infinite systems is provided by *quantum embedding* [44, 45]. While there are today a wide variety of techniques termed embedding [45–48], we will be concerned with the type of quantum embeddings in condensed phases that historically started with the treatment of defects in solids via the Anderson impurity model, where the interacting impurity site is surrounded by a set of bath orbitals that approximately represent the environment [29]. This impurity idea can be generalized to translationally invariant systems, where the lattice is subdivided into multiple clusters (also termed impurities or fragments) where each is embedded in a self-consistent environment generated by the other impurities. In the embedding treatment, only the solution of the embedded cluster (i.e. the cluster along with its quantum bath) is treated by the high-level correlated method (the impurity solver), while interactions between clusters are treated at a lower level of theory, typically within a single-particle framework such as mean-field.

Dynamical mean-field theory (DMFT) was the first quantum embedding algorithm for periodic systems based on the above self-consistent quantum impurity idea [27, 49], and has since been extended in many different directions and settings [27, 28, 50–56]. DMFT is formulated in terms of the one-particle Green's function, and solving the embedded impurity problem yields a local self-energy that is then used in the single-particle Green's function description of the periodic lattice. More recently, density matrix embedding theory (DMET) [30] has been proposed as a computationally simpler quantum embedding algorithm, also for a self-consistent

quantum impurity, but adopting the one-particle reduced density matrix as the fundamental variable, in conjunction with a static mean-field description of the periodic lattice [30–33, 57]. Because DMET only requires to compute frequency-independent observables, it is less expensive than DMFT, and in practice, a wider variety of correlated electron methods can be applied to the impurity problem. A further kind of quantum embedding, density functional (or wavefunction-in-density functional) embedding [58–66] is also of much current interest. However, this is not usually applied to strongly correlated phases, and thus we do not consider it further here.

In this chapter, we will focus our attention on the formulation of DMET and DMFT in periodic solids, especially for their extension to *ab initio* system and the symmetry-breaking generalization for superconductivity. In Sec. 2.2 and 2.3 we review the basic formulation of DMET and DMFT. Sec. 2.4 extends the framework to *ab initio* solid-state materials and the details of efficient implementation are discussed. Sec. 2.5 introduces the formulation to superconducting states by using a generalized spin orbitals formalism. Sec. 2.6 discusses the impurity solvers used in the following works and how they can be seamlessly combined with the quantum embedding framework.

2.2 Density matrix embedding theory

Exact embedding

DMET can be viewed as a wavefunction-in-wavefunction embedding scheme, where a low-level treatment for the whole lattice is combined with multiple high-level calculations on the embedded fragments, and a self-consistency condition naturally connects the two levels of description. The base of its bath construction lies on the *Schmidt decomposition* of quantum states [26, 67], which defines a set of rotated basis that has entanglement with a pre-selected fragment.

Suppose we partition the whole lattice (with n_{latt} sites) into two parts, i.e. impurity A and environment B, which contains n_A and n_B orbitals respectively and we assume $n_A < n_B$, e.g. a 6-site lattice with periodic boundary condition (PBC) is partitioned in Fig. 2.1(a). The wavefunction of whole system can be expanded on the tensor-product basis of subsystem A and B,

$$|\Psi\rangle = \sum_{ij} \Psi_{ij} |i\rangle_A |j\rangle_B , \tag{2.1}$$

where $\{|i\rangle_A\}$ and $\{|j\rangle_B\}$ are orthonormal basis of A and B with dimension 2^{n_A}

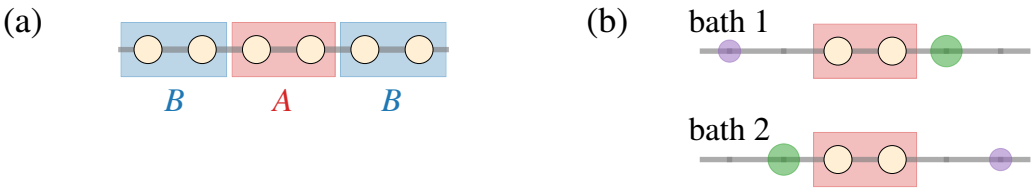

Figure 2.1: Lattice partition and DMET bath orbitals. (a) Illustration of lattice partition, where A defines the impurity and B denotes the remaining environment. (b) Two bath orbitals that coupled to the two-site impurity. Different colors denote different phases of orbitals.

and 2^{n_B} respectively. By factorizing the coefficient tensor Ψ_{ij} with singular value decomposition (SVD), we have

$$\begin{aligned} |\Psi\rangle &= \sum_{ij} \sum_{p}^{\min(2^{n_A}, 2^{n_B})} U_{ip} \Sigma_{pp} V^{\dagger}_{pj} |i\rangle_A |j\rangle_B , \\ &= \sum_{p}^{2^{n_A}} \left(\sum_{i} U_{ip} |i\rangle_A \right) \Sigma_{pp} \left(\sum_{j} V^{\dagger}_{pj} |j\rangle_B \right), \\ &= \sum_{p}^{2^{n_A}} \Sigma_{pp} |\alpha\rangle_p |\beta\rangle_p , \end{aligned} \tag{2.2}$$

which is referred to as *Schmidt decomposition* of a general quantum state [67] and the Schmidt bases $\{|\beta\rangle_p\}$ span a small subspace (with same size as the impurity) in the environment and thus naturally define a set of bath states. Note that the size of the Hilbert space has been reduced to 2^{n_A} regardless of the total lattice size. We are then able to project the original lattice Hamiltonian to the embedding space,

$$\hat{H}^{\text{emb}} = \hat{P} \hat{H}^{\text{latt}} \hat{P} \tag{2.3}$$

with projector $\hat{P}$ defined as,

$$\hat{P} = \sum_{pq} |\alpha\rangle_p |\beta\rangle_q \langle\alpha|_p \langle\beta|_q . \tag{2.4}$$

It is easy to verify that the embedding Hamiltonian shares the same ground state as the original one ($\langle\Psi|\hat{P}\hat{H}\hat{P}|\Psi\rangle = \langle\Psi|\hat{H}|\Psi\rangle = E_0$), and is therefore called *exact embedding*.

Mean-field embedding

In practice, however, the exact wavefunction is unknown and the some approximation is necessary. The idea is to iteratively build up the wavefunction in a self-improved

manner. Specifically, when the low-level solution is chosen as a mean-field Slater determinant, the bath states turn out to be a set of single-particle orbitals whose overlap with the fragment is non-zero [35, 68]. The bath orbitals can be constructed from either the molecular orbital (MO) coefficients or the corresponding one-body reduced density matrix. The occupied block of the MO coefficients can be then written in a bipartite form,

$$C^{\mathrm{occ}} = \begin{bmatrix} M \\ N \end{bmatrix}, \tag{2.5}$$

where M and N are of shape $n_A \times n_{\mathrm{occ}}$ and shape $n_B \times n_{\mathrm{occ}}$ respectively. In the following, we assume $n_{\mathrm{occ}} > n_A$ and the row rank of M is n_A. This is a weak requirement if the number of basis per fragment is not extremely large (we will discuss the special treatment if the condition is not fully satisfied in Sec. 2.4). One can perform an SVD on M,

$$M = U \Sigma V^{\dagger}, \tag{2.6}$$

to find the orbitals which have non-zero overlap with A, where the singular value Σ is exactly the overlap matrix (with shape $n_A \times n_{\mathrm{occ}}$), and V (with shape $n_{\mathrm{occ}} \times n_{\mathrm{occ}}$) defines the rotation matrix that transforms the MOs to embedding orbitals (EOs) (rotation on the occupied space does not change the mean-field [69]),

$$\bar{C}^{\mathrm{occ}} = C^{\mathrm{occ}} V = \begin{bmatrix} U \cdot \Sigma \\ N \cdot V \end{bmatrix} = \begin{bmatrix} P & \mathbf{0} \\ Q & E \end{bmatrix}, \tag{2.7}$$

where the first n_A columns $\begin{bmatrix} P \\ Q \end{bmatrix}$ are embedding orbitals whose overlap with A is non-zero, whereas the remaining orbitals are pure environment orbitals. By orthonormalizing Q, we get the bath orbitals B, which together with the unit matrix of the impurity part, define the transformation matrix $C^{\mathrm{AO,EO}}$ from atomic orbitals (AOs, or site basis in a lattice) to the embedding space,

$$\bar{a}^{\dagger} = a^{\dagger} C^{\mathrm{AO,EO}} = a^{\dagger} \begin{bmatrix} I & \mathbf{0} \\ \mathbf{0} & B \end{bmatrix}, \tag{2.8}$$

where $\bar{a}$ is the new fermion operator in the embedding space. We notice that the columns of matrix P are orthogonal to each other, because U is unitary and the first n_A columns of Σ form a diagonal square matrix $\bar{\Sigma}$. And therefore the columns of Q are also orthogonal and the following orthonormalization procedure is actually a normalization, $Q = BR$, where R is a diagonal matrix (with shape $n_A \times n_A$) that scales the columns of Q.

On the other hand, one can find the bath orbitals from the reduced one-body density matrix,

$$\gamma = \bar{C}^{\mathrm{occ}} \bar{C}^{\mathrm{occ}\dagger} = \begin{bmatrix} PP^\dagger & PQ^\dagger \\ QP^\dagger & QQ^\dagger + EE^\dagger \end{bmatrix}. \tag{2.9}$$

The off-diagonal block reads,

$$QP^\dagger = Q\bar{\Sigma}U^\dagger = BR\bar{\Sigma}U^\dagger \tag{2.10}$$

and therefore the bath orbital coefficients B can be directly generated by the SVD of the off-diagonal block of density matrix. Fig. 2.1 (b) shows an example of DMET bath orbitals. We can easily find that the number of bath orbitals is the same as that of impurity; and the bath orbitals have more weights on the sites near the fragment, which reflects the local property of the correlation.

Once we have the transformation in Eq. (2.8), we can project the lattice Hamiltonian

$$\hat{H} = \sum_{ij} h_{ij} a_i^\dagger a_j^\dagger + \sum_{ijkl} V_{ijkl} a_i^\dagger a_k^\dagger a_l a_j \tag{2.11}$$

to the embedding space (similar to the AO to MO transformation, except that the space is truncated via $C \equiv C^{\mathrm{AO,EO}}$). We obtain the expression for the one-body embedding Hamiltonian,

$$h_{pq}^{\mathrm{emb}} = \sum_{ij} C_{pi}^\dagger h_{ij} C_{jq} \tag{2.12}$$

and the two-body electron repulsion integral (ERI) in chemists' notation,

$$V_{pqrs}^{\mathrm{emb}} = \sum_{ijkl} C_{pi}^\dagger C_{rk}^\dagger V_{ijkl} C_{jq} C_{ls}. \tag{2.13}$$

Note that in this expression, all terms in lattice Hamiltonian are transformed and in general the two-electron interactions between bath orbitals are non-zero. These transformations are therefore called *interacting bath* formalism [34, 35]. On the other hand, there is a simpler formalism where the bath orbitals remain non-interacting and the two-body integral with bath index is effectively simulated by a one-body *correlation potential* u. Within this *non-interacting bath* formalism [30], the embedding Hamiltonian is very similar to that in DMFT (see Sec. 2.3).

It is worth to mention several properties of such embedding process: The number of electrons in the embedding Hamiltonian is exactly the number of impurity orbitals (i.e., the problem is half-filled). This can be seen from the shape of E in Eq.

(2.7): the number of core orbitals is $\left(n_{\mathrm{occ}} - n_{\mathrm{imp}}\right)$, and the number of electrons in the embedding space is thus n_{imp}. This is a unique feature of DMET compared to other embedding schemes, such as some variants of DFT embedding or DMFT, where the number of electrons in the embedding problem may not be an integer and some adjustment of chemical potential is required. The embedding is exact in several limits, (i) isolated atom limit (no off-diagonal terms between different impurities), where no bath is needed; (ii) non-interacting limit ($V = 0$); (iii) HF-in-HF embedding (i.e., both lattice and impurity are solved by HF). In this case, the Hamiltonian is very similar to that in a complete active space calculation, where an HF-form core potential should be include in h^{emb} (This is usually used in the *ab initio* formulation, see Sec. 2.4).

The embedding Hamiltonian can then be solved by any correlated method (called *impurity solver*) as long as it is able to provide the density matrix. After solving the embedding problem, we can measure the expectation values of the system. For local properties (i.e., within the impurities), we can directly evaluate them by the density matrices from the solver. For non-local properties (i.e., across different impurities), one can use the so-called democratic partitioning [35], e.g.

$$\left\langle a_i^\dagger a_j \right\rangle = \frac{1}{2}\Big(\left\langle \Psi^I \middle| a_i^\dagger a_j \middle| \Psi^I \right\rangle + \left\langle \Psi^J \middle| a_i^\dagger a_j \middle| \Psi^J \right\rangle \Big), \tag{2.14}$$

where index i belongs to I^{th} cluster, j belongs to J^{th} cluster, and the result is therefore an average between I^{th} and J^{th} embedding problems.

Self-consistency and symmetry breaking

Once we have the high-level solution from the impurity solver, we can improve the low-level theory through self-consistency. This is usually achieved by using a correlation potential u that minimize the density matrix difference between the two levels of the theories. Mathematically, this can be done from a least-square (LS) minimization,

$$\min_u \sum_{ij} ||\gamma_{ij}(u) - \gamma_{ij}^{\mathrm{target}}||^2, \tag{2.15}$$

where γ^{target} is from the impurity solver and keeps fixed during the minimization and the fitted density matrix γ is generated from the diagonalization of the modified lattice mean-field Hamiltonian F,

$$\begin{aligned} (F + u)C &= CE, \\ \gamma(u) &= C^{\mathrm{occ}} C^{\mathrm{occ}\dagger}. \end{aligned} \tag{2.16}$$

Note that ij can run over a subset of the impurity indices (e.g., Cu $3d$ orbitals) to reduce the cost and improve numerical stability. The specific form of u also determines the possible way of breaking symmetry. A generic form of u reads as,

$$u = \sum_{ij\sigma} v_{ij}^{\sigma} a_{i\sigma}^{\dagger} a_{j\sigma} + \sum_{ij} \Delta_{ij}^{\alpha\beta} a_{i\alpha}^{\dagger} a_{j\beta}^{\dagger} + \text{H.c.}, \tag{2.17}$$

where the first term v is spin unrestricted ($\sigma = \alpha$ or β) and can generate SU(2) symmetry breaking magnetic orders, while the second and third terms Δ break the particle number symmetry and allow for the SC pairing orders. We will discuss the SC order in more details in Sec. 2.5. This DMET self-consistency procedure is repeated until the γ (or u) is unchanged.

2.3 Dynamical mean-field theory

Green's function embedding

DMFT is a quantum embedding scheme using Green's function (GF) as the basic variable, which connects the large lattice and the impurity problem. Specifically, DMFT self-consistency requires the match between local GF (of the lattice) and impurity GF,

$$G(\mathbf{R} = \mathbf{0}, \omega) = G^{\text{imp}}(\omega), \tag{2.18}$$

where $\mathbf{R} = \mathbf{0}$ denotes the reference cell. Such condition is achieved by adding a self-energy, called *hybridization* $\Delta(\omega)$, to the impurity problem. The $\Delta(\omega)$ therefore measures the missing information from the environment,

$$\Delta(\omega) = \left[\omega - h^{\text{imp}} - \Sigma^{\text{imp}}(\omega)\right] - \left[G(\mathbf{R} = \mathbf{0}, \omega)\right]^{-1}. \tag{2.19}$$

Once the hybridization is given, the impurity problem is determined by some non-interacting bath orbitals that mimic the behavior of Δ. We can then solve the impurity problem by a more accurate impurity solver, which generates impurity GF G^{imp} and impurity self-energy Σ^{imp}. To get the self-energy of the total system, the DMFT approximation [70] is introduced, i.e. the self-energy of the whole system is by diagonally tiling the impurity self-energy and ignoring the inter-cluster self-energy,

$$\Sigma(\omega) = \begin{bmatrix} \Sigma^{\text{imp}} & & \\ & \ddots & \\ & & \Sigma^{\text{imp}} \end{bmatrix}. \tag{2.20}$$

From such self-energy, one can obtain the new local GF,

$$G(\mathbf{R} = \mathbf{0}, \omega) = \frac{1}{N_{\mathbf{k}}} \sum_{\mathbf{k}} \left[\omega - h(\mathbf{k}) - \Sigma^{\text{imp}}(\omega)\right]^{-1}, \tag{2.21}$$

which, combined with G^{imp} defines the new hybridization from Eq. (2.19) and starts a new iteration. The whole DMFT loop can be summarized as,

$$\Delta(\omega) \xrightarrow{\text{solver}} G^{\text{imp}}(\omega) \xrightarrow{\text{Dyson eq.}} \Sigma^{\text{imp}}(\omega) \xrightarrow{\text{Eq.(2.21)}} G(\mathbf{R}=\mathbf{0},\omega) \xrightarrow{\text{Eq.(2.19)}} \Delta(\omega). \tag{2.22}$$

Bath discretization

In bath-based DMFT, the hybridization $\Delta(\omega)$ is represented by a finite set of discrete bath sites and couplings. Here, we choose to approximate $\Delta(\omega)$ along the real frequency axis [71–74] so that dynamical quantities (e.g. spectral functions) can be computed more accurately than when fitting along the imaginary frequency axis [75–77]. We consider $\Delta(\omega)$ as the Hilbert transform [78]

$$\Delta(\omega) = \int \mathrm{d}\epsilon \frac{J(\epsilon)}{\omega - \epsilon} \tag{2.23}$$

with the spectral density

$$J(\epsilon) = -\frac{1}{\pi} \operatorname{Im} \Delta(\epsilon + \mathrm{i}\eta), \tag{2.24}$$

where η is a broadening parameter. The Hilbert transform integral can be approximated by a numerical quadrature (e.g., Gauss-Legendre quadrature) along the real axis

$$\Delta(\omega) = \sum_{n=1}^{N_\omega} w_n \frac{J(\epsilon_n)}{\omega - \epsilon_n}, \tag{2.25}$$

where w_n and ϵ_n are the weights and positions of the N_ω quadrature grid points. To derive the couplings between the impurity and bath sites, we diagonalize the spectral density

$$J(\epsilon_n) = U^{(n)} \lambda^{(n)} U^{(n)\dagger}. \tag{2.26}$$

Eq. (2.25) then becomes:

$$\Delta_{ij}(\omega) = \sum_{n=1}^{N_\omega} \sum_{k=1}^{N_C} \frac{V_{ik}^{(n)} V_{jk}^{(n)}}{\omega - \epsilon_n}, \tag{2.27}$$

with

$$V_{ik}^{(n)} = w_n^{\frac{1}{2}} U_{ik}^{(n)} (\lambda_{kk}^{(n)})^{\frac{1}{2}}. \tag{2.28}$$

Thus, $V_{ik}^{(n)}$ and ϵ_n can be interpreted as the impurity-bath couplings and energy levels of bath orbitals. With this bath discretization, we can define the DMFT

embedding Hamiltonian

$$\begin{aligned}\hat{H}^{\text{emb}} &= h_{ij}^{\text{imp}} a_i^\dagger a_j + V^{\text{imp}} a_i^\dagger a_k^\dagger a_l a_j \\ &+ \sum_{n=1}^{N_\omega} \sum_{k=1}^{N_C} \left(\sum_i V_{ik}^{(n)} (a_i^\dagger a_{nk} + a_{nk}^\dagger a_i) + \epsilon_n a_{nk}^\dagger a_{nk} \right),\end{aligned} \tag{2.29}$$

where h^{imp} and V^{imp} are similar to Eq. (2.12) and (2.13), but with only the impurity part of the Hamiltonian.

Comparison between DMET and DMFT

DMET shares many common features as DMET, e.g., using bath to represent the environment, self-consistently generating phases, and having similar exact limits (except that DMFT is also exact in the infinite dimension limit [27]). The physical quantities have some correspondence,

$$\begin{aligned}\gamma &\leftrightarrow G(\omega), \\ u &\leftrightarrow \Delta(\omega).\end{aligned} \tag{2.30}$$

The main difference roots in the frequency-dependent nature of G and Δ, which makes DMFT intrinsically an excited state theory. One of the basic quantity extracted from the GF is the local spectral function,

$$A(\mathbf{R} = \mathbf{0}, \omega) = -\frac{1}{\pi} \operatorname{Im} G(\mathbf{R} = \mathbf{0}, \omega + \mathrm{i}0^+), \tag{2.31}$$

which can be directly compared to experiments, e.g., x-ray photoemission spectroscopy and bremsstrahlung-isochromat spectroscopy. DMET, on the other hand, is a static theory using density matrices as the basic variable (density matrix can be viewed as a equal-time GF or a frequency integrated GF). Therefore, DMET is more appropriate for ground-state problems.

Another difference between DMET and DMFT is the number of bath orbitals. The n_{bath} in DMET is at most n_{imp}, whereas the n_{bath} in DMFT is in principle infinite and there is correspondingly the bath discretization error. This feature makes DMET has a significantly lower cost compared to DMFT.

2.4 Ab initio quantum embedding

Periodic quantum chemistry formalism

Periodic Gaussian bases. In simulations of realistic materials, we use a quantum chemistry formalism based on crystalline Gaussian bases, i.e., translational-

symmetry-adapted linear combinations of Gaussian atomic orbitals (AO) [79],

$$\chi_p^{\mathbf{k}}(\mathbf{r}) = \sum_{\mathbf{T}} \mathrm{e}^{\mathrm{i}\mathbf{k}\cdot\mathbf{T}} \chi_p(\mathbf{r}-\mathbf{T}), \tag{2.32}$$

where $\mathbf{T}$ denotes a lattice vector and $\mathbf{k}$ is a crystal momentum vector in the first Brillouin zone (FBZ). We will frequently use the Fourier transform between the $\mathbf{R}$ space and $\mathbf{k}$ space. The relevant formulas are summarized in Appendix A. To formulate the *ab initio* calculation, it is necessary to express the Hamiltonian matrix elements (integrals) in this basis. The one-electron integrals, namely the overlap S, kinetic T and electron-nuclear interaction integrals $V^{\text{N-el}}$ are [80, 81],

$$S_{pq}^{\mathbf{k}} = \frac{1}{N} \langle \chi_p | \chi_q \rangle = \sum_{\mathbf{T}} \mathrm{e}^{\mathrm{i}\mathbf{k}\cdot\mathbf{T}} \int \mathrm{d}\mathbf{r}\, \chi_p^*(\mathbf{r}) \chi_q(\mathbf{r}-\mathbf{T}), \tag{2.33}$$

$$T_{pq}^{\mathbf{k}} = -\frac{1}{2N} \langle \chi_p^{\mathbf{k}} | \nabla_{\mathbf{r}}^2 | \chi_q^{\mathbf{k}} \rangle = -\frac{1}{2} \sum_{\mathbf{T}} \mathrm{e}^{\mathrm{i}\mathbf{k}\cdot\mathbf{T}} \int \mathrm{d}\mathbf{r}\, \chi_p^*(\mathbf{r}) \nabla_{\mathbf{r}}^2 \chi_q(\mathbf{r}-\mathbf{T}), \tag{2.34}$$

$$V_{pq}^{\text{N-el},\mathbf{k}} = \frac{1}{N} \langle \chi_p^{\mathbf{k}} | v^{\text{N-el}} | \chi_q^{\mathbf{k}} \rangle = \sum_{\mathbf{T}} \mathrm{e}^{\mathrm{i}\mathbf{k}\cdot\mathbf{T}} \int \mathrm{d}\mathbf{r}\, \chi_p^*(\mathbf{r}) v^{\text{N-el}}(\mathbf{r}) \chi_q(\mathbf{r}-\mathbf{T}), \tag{2.35}$$

where N is the number of $\mathbf{k}$-points and the divergent part ($\mathbf{G} = \mathbf{0}$) in the electron-nuclear interaction $v^{\text{N-el}}(\mathbf{r})$ is removed. This guarantees that the integral is not divergent for charge-doped systems, see Chap. 7. The total one-electron Hamiltonian integral (core Hamiltonian matrix element) is then,

$$h_{pq}^{\text{core},\mathbf{k}} = T_{pq}^{\mathbf{k}} + V_{pq}^{\text{N-el},\mathbf{k}}. \tag{2.36}$$

We also define the matrix elements of the 2-electron Coulomb interaction. This leads to electron repulsion integrals (ERI) involving 4 crystalline Gaussian AOs (4 "centers"),

$$V_{pqrs}^{\mathbf{k}_p\mathbf{k}_q\mathbf{k}_r\mathbf{k}_s} = \int \mathrm{d}\mathbf{r}_1\, \mathrm{d}\mathbf{r}_2\, \chi_p^{\mathbf{k}_p *}(\mathbf{r}_1) \chi_q^{\mathbf{k}_q}(\mathbf{r}_1) \frac{1}{r_{12}} \chi_r^{\mathbf{k}_r *}(\mathbf{r}_2) \chi_s^{\mathbf{k}_s}(\mathbf{r}_2). \tag{2.37}$$

Note that crystal momentum conservation means that the ERI vanishes unless $\mathbf{k}_p + \mathbf{k}_r - \mathbf{k}_q - \mathbf{k}_s = n\mathbf{b}$, where $n\mathbf{b}$ is an integer multiple of the reciprocal lattice vectors.

With all the matrix elements evaluated, standard molecular quantum chemistry techniques can be applied in the periodic setting. This lays the foundation for the efficient *ab initio* implementation of quantum embedding theories below.

Density fitting. There are a large number of ERIs in the above formulation. To reduce the cost of evaluating them, we employ density fitting (DF) which factorizes

the 4-center ERI into a product of 3-center ERIs and a metric matrix. Using the Coulomb metric [81, 82] and for auxiliary basis functions labelled $\{P, Q, \cdots\}$, we obtain

$$V_{pqrs}^{\mathbf{k}_p\mathbf{k}_q\mathbf{k}_r\mathbf{k}_s} = \sum_{PQ} \big(p\mathbf{k}_p q\mathbf{k}_q \big| P\big) \mathcal{J}^{-1}_{PQ} (Q|r\mathbf{k}_r s\mathbf{k}_s), \tag{2.38}$$

with the 3-center ERI,

$$\big(P\big|p\mathbf{k}_p q\mathbf{k}_q\big) = \sum_{\mathbf{T}_p\mathbf{T}_q} \int \mathrm{d}\mathbf{r}_1 \mathrm{d}\mathbf{r}_2 \, \mathrm{e}^{\mathrm{i}\mathbf{k}_q\cdot\mathbf{T}_q - \mathrm{i}\mathbf{k}_p\cdot\mathbf{T}_p} \chi_P(\mathbf{r}_1) \frac{1}{r_{12}} \chi_p^*(\mathbf{r}_2 - \mathbf{T}_p) \chi_q(\mathbf{r}_2 - \mathbf{T}_q), \tag{2.39}$$

and the Coulomb metric,

$$\mathcal{J}_{PQ} = \int \mathrm{d}\mathbf{r}_1 \mathrm{d}\mathbf{r}_2 \, \chi_P^*(\mathbf{r}_1) \frac{1}{r_{12}} \chi_Q(\mathbf{r}_2). \tag{2.40}$$

It is computationally convenient to absorb the Coulomb metric symmetrically into the definition of the 3-center integrals,

$$\begin{aligned} V_{pqrs}^{\mathbf{k}_p\mathbf{k}_q\mathbf{k}_r\mathbf{k}_s} &= \sum_{L}\sum_{PQ} \Big[\big(p\mathbf{k}_p q\mathbf{k}_q\big|P\big)\mathcal{J}^{-\frac{1}{2}}_{PL}\Big]\Big[\mathcal{J}^{-\frac{1}{2}}_{LQ}(Q|r\mathbf{k}_r s\mathbf{k}_s)\Big] \\ &= \sum_{L} W_{Lpq}^{\mathbf{k}_p\mathbf{k}_q} W_{Lrs}^{\mathbf{k}_r\mathbf{k}_s}. \end{aligned} \tag{2.41}$$

where the symmetrical decomposition can be carried out using the eigenvalue decomposition of $\mathcal{J}$ and linear dependence is handled by discarding small eigenvalues. In the following, we use the symmetric DF form and use L to label auxiliary basis functions. We choose the auxiliary basis to be also a crystalline Gaussian basis, thus the above formulae correspond to (crystalline) Gaussian density fitting (GDF).

The 3-center integral W obeys several useful relations, which we use later to derive some of formulae. Similar to the 4-center integral, there is momentum conservation,

$$\mathbf{k}_L = \mathbf{k}_p - \mathbf{k}_q + n\mathbf{b}. \tag{2.42}$$

From Eq. (2.39) and Eq. (2.40), one can also verify the following complex conjugation relation,

$$W_{Lqp}^{\mathbf{k}_q\mathbf{k}_p *} = W_{Lpq}^{\mathbf{k}_p\mathbf{k}_q}. \tag{2.43}$$

Local orbitals

The infrastructure of *ab initio* mean-field theory uses crystal (Bloch) orbitals and $\mathbf{k}$-point quantities, while quantum embedding is naturally formulated in terms of

local orbitals and real-space quantities. Thus, we first define a translation from the mean-field computational basis to one appropriate for embedding.

To do so, we construct atom-centered orthogonal local orbitals (LO) $\{w_i(\mathbf{r})\}$ that define the lattice Hilbert space, which can be cleanly partitioned into a product of impurity Hilbert spaces. Here, we will assume that the mean-field computational basis is a set of crystal atomic orbitals (AOs) $\left\{\phi_\mu^{\mathbf{k}}(\mathbf{r})\right\}$ (which constitutes a non-orthogonal basis, with an AO index μ and a $\mathbf{k}$-point index in the first Brillouin zone). It is convenient to first define an intermediate set of local crystal orbitals,

$$w_i^{\mathbf{k}}(\mathbf{r}) = \sum_\mu \phi_\mu^{\mathbf{k}}(\mathbf{r}) C_{\mu i}^{\mathbf{k},\mathrm{AO,LO}}, \tag{2.44}$$

where the notation $C^{\mathrm{X,Y}}$ denotes the transformation from basis X to basis Y. The real-space LOs in any cell can then be obtained by a Wannier summation over the local crystal orbitals, for example, the LOs at the lattice origin ($\mathbf{R} = \mathbf{0}$) are given by

$$w_i^{\mathbf{R}=\mathbf{0}}(\mathbf{r}) = \frac{1}{\sqrt{N_{\mathbf{k}}}} \sum_{\mathbf{k}} w_i^{\mathbf{k}}(\mathbf{r}). \tag{2.45}$$

Expressed in the LOs, the *ab initio* periodic system is isomorphic to a periodic lattice problem, with reciprocal lattice vectors $\mathbf{k}$. We choose a subset of $\{w_i(\mathbf{r})\}$ to define the impurity. It is natural to choose the impurity to be spanned by LOs in a single unit cell or a supercell, and for definiteness, we choose the cell or supercell at the lattice origin as the impurity.

The next computational task is to specify the coefficients in Eq. (2.44) that define the LOs in terms of the crystal AOs. There are two strategies to construct orthogonal local orbitals: a *top-down* strategy [transforming from canonical mean-field molecular orbitals (MOs) to LOs] and a *bottom-up* strategy (transforming from the AO computational basis to LOs). The first strategy finds a unitary transformation of the MOs to optimize a metric (such as $\left\langle r^2 \right\rangle - \langle \mathbf{r} \rangle^2$) that measures the spatial locality of the LOs. Examples of such approaches are the Boys[83], Pipek-Mezey (PM)[84] and Edmiston-Ruedenberg (ER)[85] methods in molecules, and the maximally localized Wannier function (MLWF)[86, 87] and Pipek-Mezey Wannier function (PMWF)[88] methods in solids. The top-down scheme can yield more localized orbitals than bottom-up schemes. We have an implementation of MLWF by interfacing WANNIER90 program with PySCF and the relevant matrix elements are summarized in Appendix C.1 (see also the DMET work by Pham et al. [89]). However, due to the need to carry out an optimization, the disadvantages are also

apparent: (i) the procedure can be numerically expensive and one can easily get stuck in a local minimum of the cost function, particularly when constructing a large number of local virtual orbitals; (ii) with periodic boundary conditions, entangled bands [90, 91] often exist among the high-energy virtual MOs, and special techniques are required; (iii) a false minimum or discontinuity in **k**-space can lead to non-real orbitals after the Wannier summation in Eq. (2.45), giving a Hamiltonian with complex coefficients in the LO basis, which is incompatible with many impurity solver implementations.

In the bottom-up strategy, one avoids optimization and relies only on linear algebra to construct the LOs. Examples of LOs of this type are the Löwdin and meta-Löwdin orbitals [92, 93], natural atomic orbitals (NAO) [94] and intrinsic atomic orbitals (IAO) [95]. Bottom-up methods avoid the difficulties of the top-down strategy: (i) the construction is usually cheap (i.e. suited to producing large numbers of local orbitals); (ii) there is no initial guess dependence or local minimum problem; (iii) the LOs are guaranteed to be real as long as the phases of crystal AOs and other **k**-space orbitals in the formalism (e.g. the reference crystal AOs used to construct the IAOs) are smooth in **k**-space. Since we aim to carry out calculations beyond a minimal basis, and thus with many virtual orbitals, we have chosen the bottom-up strategy to avoid difficulties in optimization and non-real Hamiltonian coefficients. In particular, we have adapted the molecular IAO routine to crystal MOs with **k**-point sampling (see Appendix C.2) to generate the set of crystal IAOs. The crystal IAOs are *valence* orbitals that exactly span the occupied space of the mean-field calculation. Note that the number of IAOs is the same as the size of the minimal basis only. To obtain a complete set of LOs that span the same space as the original AO basis (thus making a square rotation matrix $C^{\mathbf{k},\mathrm{AO,LO}}$ in Eq. (2.44)) we need to further augment the IAOs with LOs that live purely in the virtual space. Here we choose these additional orbitals to be the projected atomic orbitals (PAO) for non-valence orbitals [96], orthogonalized with Löwdin orthogonalization, as originally proposed for local correlation calculations[96]. The IAOs + PAOs then together span the complete space of AOs and constitute a complete LO basis. A related scheme has previously been used in the molecular DMET calculations[35, 97]. We summarize the formulations of IAO and PAO in Appendix C.

In the following, we transform the Gaussian AOs into periodic IAOs and PAOs, and use these as our local orbitals. These orbitals can be viewed as a series of atom-centered projected Wannier functions, and therefore, no numerical optimization

is required during their construction. In particular, the periodic IAOs are based on the projection to a set of predefined valence AO orbitals (the so-called IAO reference functions), whose number is smaller than the computational AO basis and do not include polarization or diffuse components. See Refs. [95, 98] for their construction. In this work, we use atomic spherically averaged Hartree-Fock orbitals as the IAO reference functions, because the segmented Gaussian basis functions that we use (such as def2-SVP or cc-pVDZ) do not individually possess meaningful AO character. The IAOs represent the valence space (occupied + virtuals of valence character) of the materials, while the PAOs represent the remaining virtual space,

$$\left|\phi_p^{\mathrm{PAO},\mathbf{k}}\right\rangle = \sum_i \left(1 - \left|\phi_i^{\mathrm{IAO},\mathbf{k}}\right\rangle\left\langle\phi_i^{\mathrm{IAO},\mathbf{k}}\right|\right)\left|\chi_p^{\mathrm{AO},\mathbf{k}}\right\rangle. \tag{2.46}$$

The union of the two sets spans the full orbital space. The coefficient matrix C^{LO} defines the transformation from the computational AO basis to the LO basis. For practical calculations, especially with all-electron basis, it is necessary to use the frozen-core approximation to freeze the low-energy bands (like $1s$ orbitals). Depending on the mean-field methods (HF or hybrid DFT), the effective potential from the core bands can be evaluated from Coulomb J and (scaled) exchange K matrices (see Appendix B.1), as well as the DFT Kohn-Sham potential v_{xc}. After the freezing the core bands, the LOs need to be defined accordingly. In Appendix C.2, we show how IAOs can be defined with non-core bands (with core bands being projected out). We also show how the IAOs can be extend for metallic systems whose orbital occupations are not integers. These advances lay the foundation for large-scale quantum embedding simulation of doped materials.

Bath truncation

DMET bath truncation.

The DMET embedded Hilbert space consists of the impurity LOs and a set of bath orbitals; these together are the embedding orbitals (EOs). We define the bath orbitals in DMET by using the SVD of the valence (IAO, not PAO) part of the one-particle density matrix. We assume below that the impurity corresponds to a reference cell $\mathbf{R} = 0$, thus the bath orbitals live in the cells $\mathbf{R} \neq 0$. The off-diagonal block of the density matrix of the whole crystal ("lattice") is computed directly from the Fourier transform of the $\mathbf{k}$-space density matrix obtained in the mean-field calculation [98, 99],

$$\gamma_{ij}^{\mathbf{R}\neq\mathbf{0}} = \frac{1}{N_{\mathbf{k}}}\sum_{\mathbf{k}} \mathrm{e}^{\mathrm{i}\mathbf{k}\cdot\mathbf{R}}\gamma_{ij}^{\mathbf{k}}. \tag{2.47}$$

Constraining i, j to be IAO (i.e., valence) indices, the valence bath is obtained from an SVD of the off-diagonal block,

$$\gamma_{ij}^{\mathbf{R}\neq\mathbf{0}} = \sum_{ik} B_{ik}^{\mathbf{R}\neq\mathbf{0}} \Lambda_k V_{kj}^{\dagger}, \tag{2.48}$$

where Λ measures the entanglement between the bath and impurity orbitals and B is the coefficient matrix of the (orthogonalized) bath orbitals,

$$\left|\phi_j^{\text{bath}}\right\rangle = \sum_{\mathbf{R}\neq\mathbf{0},i} \left|\phi_i^{\text{LO},\mathbf{R}}\right\rangle B_{ij}^{\mathbf{R}}. \tag{2.49}$$

The overall embedding orbital (EO) space is spanned by impurity orbitals (in the reference cell $\mathbf{R} = \mathbf{0}$) and the above bath orbitals,

$$C_{ij}^{\text{EO},\mathbf{R}} = \begin{bmatrix} \mathbf{1} & \mathbf{0} \\ \mathbf{0} & \mathbf{B}^{\mathbf{R}\neq\mathbf{0}} \end{bmatrix}. \tag{2.50}$$

For subsequent integral transformations (see below), it is more convenient to Fourier transform the embedding orbitals to the $\mathbf{k}$-space,

$$C_{ij}^{\text{EO},\mathbf{k}} = \sum_{\mathbf{R}} \mathrm{e}^{-\mathrm{i}\mathbf{k}\cdot\mathbf{R}} C_{ij}^{\text{EO},\mathbf{R}}. \tag{2.51}$$

Although the DMET bath is formally of the same size as the number of impurity orbitals, the mean-field wavefunction only contains appreciable entanglement between partially occupied LOs on the impurity and corresponding bath orbitals. Very low-lying core and high-energy virtual impurity orbitals thus are not entangled with any bath orbitals. In practice, this manifests as very small singular values $\Lambda_{\tilde{i}\tilde{i}}$ and the corresponding singular vectors (bath orbitals) can vary between different DMET iterations [35] leading to difficulties in converging the DMET self-consistency procedure. To eliminate this instability, we use the procedure previously recommended in molecular DMET calculations [35]. We first partition the impurity orbitals into core, valence and virtual orbitals, and only carry out the SVD for the impurity valence columns of the off-diagonal density matrix to construct corresponding valence bath orbitals [35], i.e. the index j in Eq. (2.48) can be constrained to the valence orbitals only. Note that when frozen-core approximation or pseudopotentials are used in the calculation, there is no core subspace, and thus no core bath orbitals appear. With this construction, the number of embedding orbitals is reduced from $2n_{\text{imp}}$ to $n_{\text{imp}} + n_{\text{val}}$, where n_{val} is the number of valence orbitals, which is smaller than the number of impurity orbitals n_{imp}, and we recover smooth DMET convergence.

DMFT bath truncation. It is known that bath discretization introduces discretization errors into DMFT, thus many bath orbitals per impurity site are required to minimize this error. In our case, the number of bath orbitals is formally $N_b = N_\omega N_C$, which can easily be as many as a few hundred, as N_C includes all orbitals in the unit cell. To reduce the bath size and thus computational cost, we employ several strategies to truncate the bath degrees of freedom, while minimizing the error introduced. First, we only couple bath orbitals to the IAOs (valence orbitals). Note that PAOs (non-valence virtuals) are still included in the embedding problem and interact with the IAOs. With this choice, the number of bath orbitals is reduced to $N_b = N_\omega N_{\mathrm{IAO}}$. Second, we remove the bath orbitals which are very weakly coupled to the impurity. As seen in Eq. (2.28), the scale of the bath coupling is set by the eigenvalues $\lambda^{(n)}_{kk}$. By dropping the bath orbitals with eigenvalues below a threshold, we can further decrease the bath dimension as necessary.

Integral transformation

The construction of the embedding Hamiltonian is equivalent to a set of integral transformations using the coefficient matrix C of the embedding basis [98, 100].

The one-body part of the embedding Hamiltonian can be directly evaluated using the projection,

$$H^{\mathrm{emb}}_{ij} = \frac{1}{N_{\mathbf{k}}} \sum_{\mathbf{k}} C^{\mathbf{k}\dagger}_{ip} \left[h^{\mathrm{core},\mathbf{k}}_{pq} + v^{\mathrm{eff},\mathbf{k}}_{pq} \right] C^{\mathbf{k}}_{qj} - v^{\mathrm{eff,loc}}_{ij} - \mu \delta_{ij} \delta_{i \in \mathrm{imp}}, \tag{2.52}$$

where we have included in the definition μ, a chemical potential that adjusts the electron density on the fragment such that each cell has the correct number of electrons. $v^{\mathrm{eff,loc}}_{ij}$ is the effective potential in the embedding space originating from the density matrix of the embedded space,

$$v^{\mathrm{eff,loc},\sigma}_{ij} = J - K = \left(\sum_{\sigma'} V^{\mathrm{emb},\sigma\sigma'}_{ijkl} \gamma^{\mathrm{emb},\sigma'}_{lk} \right) - V^{\mathrm{emb},\sigma\sigma}_{iklj} \gamma^{\mathrm{emb},\sigma}_{kl}, \tag{2.53}$$

where V^{emb} is the embedding two-body hamiltonian (see below for its construction) and σ is a spin label. Note that in our current scheme, the v^{eff} always contain Coulomb J and full exchange K regardless of the types of mean-field theory (HF or DFT).

The two-body part of the embedding hamiltonian must be constructed appropriately to minimize computational cost. With density fitting, ERIs in the embedding space

can be evaluated from 3-center integrals in the reference cell,

$$W_{Lij}^{\mathbf{k}_L\mathbf{00}} = \frac{1}{N_\mathbf{k}} \sum_{\mathbf{k}_p\mathbf{k}_q}{}' C_{ip}^{\mathbf{k}_p\dagger} W_{Lpq}^{\mathbf{k}_p\mathbf{k}_q} C_{qj}^{\mathbf{k}_q}, \tag{2.54}$$

where $'$ indicates the summation is over momentum conserving crystal momenta $\mathbf{k}_L = \mathbf{k}_p - \mathbf{k}_q + n\mathbf{b}$. The cost of this step scales as $\mathcal{O}(n_\mathbf{k}^2 n_\text{bas}^4)$. The final embedding ERI is a contraction which scales as $\mathcal{O}(n_\mathbf{k} n_\text{bas}^5)$,

$$V_{ijkl}^\text{emb} = \frac{1}{N_\mathbf{k}} \sum_{\mathbf{k}_L L} W_{Lij}^{\mathbf{k}_L\mathbf{00}*} W_{Lkl}^{\mathbf{k}_L\mathbf{00}}. \tag{2.55}$$

Note that time reversal symmetry of the integrals and coefficients can be used to reduce the computational cost. For example, time reversal symmetry over $\mathbf{k}_L$ effectively reduces costs by about a factor of 2, as we only need consider the non-negative $\mathbf{k}_L$.

For each pair $(\mathbf{k}_p, \mathbf{k}_q)$, there will be another pair $\bar{\mathbf{k}}_q = -\mathbf{k}_q$ and $\bar{\mathbf{k}}_p = -\mathbf{k}_p$ that are related,

$$\begin{aligned} W_{Lji}^{\bar{\mathbf{k}}_q\bar{\mathbf{k}}_p} &= C_{jq}^{\bar{\mathbf{k}}_q\dagger} W_{Lqp}^{\bar{\mathbf{k}}_q\bar{\mathbf{k}}_p} C_{pi}^{\bar{\mathbf{k}}_p} \\ &= C_{jq}^{\mathbf{k}_q T} W_{Lpq}^{\mathbf{k}_p\mathbf{k}_q} C_{pi}^{\mathbf{k}_p *} \\ &= W_{Lij}^{\mathbf{k}_p\mathbf{k}_q T}, \end{aligned} \tag{2.56}$$

where we have used the relation $C^\mathbf{k} = C^{\bar{\mathbf{k}}*}$. This relation further gives a factor of 2 cost reduction in the transformation.

Finally, we note that after the summation over $\mathbf{k}$, the resulting embedding 3-center integrals and the final embedding 4-center integrals have permutation symmetry over the orbital indices. In fact, the embedding ERI is real and has 8-fold symmetry: $V_{ijkl}^\text{emb} = V_{jikl}^\text{emb} = V_{ijlk}^\text{emb} = V_{klij}^\text{emb} = \cdots$. This relation gives another factor of 4 during the contraction step.

There are many choices of auxiliary basis and here we will mainly use Gaussian density fitting (GDF), where L is a set of chargeless Gaussian crystal orbitals, with the divergent part of the Coulomb term treated in Fourier space [81]. (We discuss plane-wave density fitting (FFTDF) in Appendix of Ref. [98]).

An alternative choice of embedding Hamiltonian is the DMET (and DMFT) *non-interacting bath* formalism [35]. In this case, the two-particle interactions are restricted to the impurity orbitals, and interactions on the bath are mimicked by

adding the correlation potential to the bath. For further details, we refer to Ref. [35]. We primarily use the interacting bath formalism for *ab initio* DMET, and only consider the non-interacting bath formalism for DMFT and in the model calculations of DMET.

DMET and charge self-consistency

A key component in the DMET description of phases and order parameters is the imposition of self-consistency between the "high-level" (HL) embedded wavefunction and the "low-level" (LL) mean-field description. We matched the correlated one-particle density matrix γ from the impurity solver and the mean-field one-particle density matrix by minimizing their Frobenius norm difference with respect to the correlation potential u,

$$\min_{u} \sum_{ij}^{\text{selected indices}} \left[\gamma_{ij}^{\text{LL}}(u) - \gamma_{ij}^{\text{HL}}\right]^2, \tag{2.57}$$

where the indices i, j loop over selected orbitals and the high-level density matrix γ_{ij}^{HL} is kept fixed during the correlation potential fitting. Other choices of cost function are also possible, e.g. only matching the impurity [34, 35] or diagonal part [31] of the density matrix. The correlation potential u is a local quantity (i.e. independent of the impurity cell $\mathbf{k}$). With large basis sets, the number of parameters in u can be very large. To reduce the degrees of freedom in the numerical optimization, we can add u only to a subset of orbitals, e.g. the valence orbitals. With a small set of parameters, the optimization problem can be easily solved, e.g. by a conjugate gradient algorithm. It should be noted that the minimization of the cost function is not a convex problem, thus in principle there can be multiple local minima; for example in an AFM system, there may be multiple solutions corresponding to different spin polarization patterns. We typically use conjugate gradient (CG) or Broyden-Fletcher-Goldfarb-Shanno (BFGS) algorithm to solve LS fitting problem (see Appendix D for the analytic gradient of the cost function at both zero and finite temperatures).

γ^{LL} can be solved in the global lattice space, called *global fitting*, which is more stable in the metallic case and we will use it in the doped HTSCs. Alternatively, γ^{LL} can be solved in the embedding space and only small Fock matrix F^{emb} needs to be diagonalized. This fitting scheme is called *local fitting* [101] and is computationally cheaper than the global fitting. One can prove that the self-consistent solutions of DMET using the local fitting procedure are equivalent to those of the DMET with

global fitting [102].

In an *ab initio* DMET calculation, an additional layer of self-consistency appears associated with the non-linear *ab initio* lattice mean-field calculation [this is sometimes referred to as *charge self-consistency* (CSC) in DMFT calculations [103–106]]. In our implementation, the AO-based Fock matrix $F^{\mathbf{k},\mathrm{AO}}$ is updated at the beginning of each DMET cycle, using the improved DMET mean-field density matrix from the previous iteration, which reflects the response of the mean-field density (matrix) to the DMET local correction.

We finally note that the LOs, in principle, can be redefined based on the new mean-field MOs at each DMET iteration. However, we do not consider such an update in the current work. Instead, we only determine the LOs at the beginning of the calculation and keep the LOs fixed in the following DMET self-consistency loops. This choice introduces a small dependence on the initial orbitals (e.g. using HF- or DFT-MOs to define the LOs). However, it is usually reasonable to assume that the LOs do not change significantly during the embedding self-consistency.

We illustrate the periodic *ab initio* DMET algorithm, with both DMET correlation potential and charge self-consistency, in Fig. 2.2.

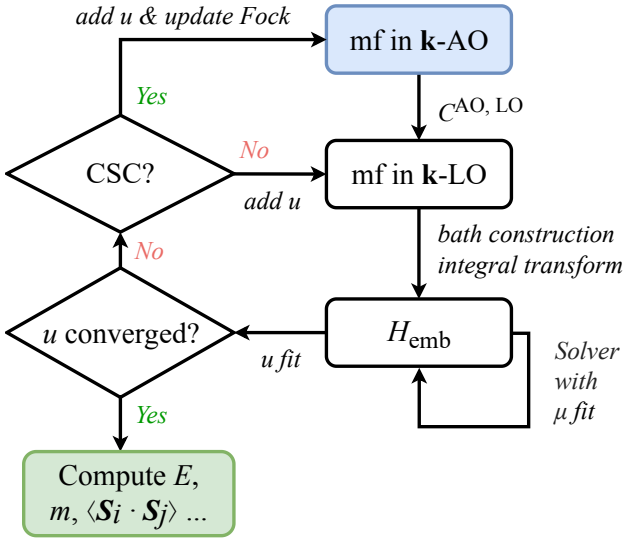

Figure 2.2: The *ab initio* DMET self-consistency procedure, where "mf" is used to denote the relevant mean-field physical quantities, e.g. the Fock matrix F, density matrix γ; μ and u are used to denote the chemical potential and correlation potential respectively. "CSC" denotes charge self-consistency and is an optional step in the algorithm. The flowchart starts at the blue block and ends at the green block when self-consistency is reached.

Multi-fragment extension

The above *ab initio* DMET formulation assumes we are embedding a full crystal cell (which may be a supercell of primitive cells) in the environment of other cells. However, for complicated crystal structures, e.g., in the multi-layer compounds, or for inhomogeneous systems and defect calculations, the full cell calculation is prohibitively expensive. New techniques are thus required to further reduce the impurity size. Here we have developed and implemented a multi-fragment extension of the *ab initio* DMET. This allows a further decomposition of the full cell impurity into fragments while retaining the periodicity among different cells.

In this scheme, the reference impurity cell is divided into fragments which are each embedded in the bath of the other fragments and other cells. For example, for the double-layer compound Hg-1212, the cell is sliced into 3 fragments, the first one involving the bottom layer of the CuO_2 plane and the corresponding apical oxygen; the second, the upper layer of copper and oxygen; and the third fragment, the other buffer-layer atoms, i.e., Hg, Ba and Ca [see Fig. 2.3 (a)].

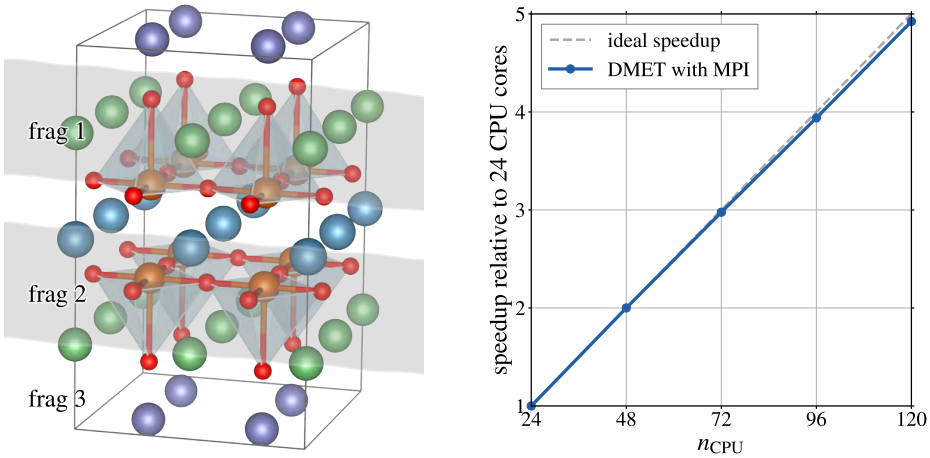

(a) (b)

Figure 2.3: (a) Illustration of the multi-fragmentation scheme in the multi-layer cuprate Hg-1212. The system is divided into 3 pieces: the fragments 1 and 2 involve the two Cu-O layers and fragment 3 contains all other ions in the cell. (b) MPI efficiency of the multi-fragment implementation of a h-BN crystal.

The total energy is defined as the sum of all fragment energies, $E = \sum_x E^x$. Implementing the DMET democratic partitioning formula (which defines how to reassemble expectation values from each fragment) , each fragment energy is the

expectation value of a scaled Hamiltonian,

$$E^x = \sum_{ij} \left\langle \tilde{H}^x_{ij} a^\dagger_i a_j \right\rangle + \frac{1}{2} \sum_{ijkl} \left\langle \tilde{V}^x_{ijkl} a^\dagger_i a^\dagger_k a_l a_j \right\rangle = \sum_{ij} \tilde{H}^x_{ij} \gamma^x_{ji} + \frac{1}{2} \sum_{ijkl} \tilde{V}^x_{ijkl} \Gamma^x_{ijkl}, \tag{2.58}$$

where $\tilde{H}$ and $\tilde{V}$ are scaled Hamiltonians, and γ and Γ are 1-body and 2-body density matrices respectively. $\tilde{H}$ is defined as,

$$\tilde{H}_{ij} = w_{ij} \left(h^{\text{core}}_{ij} + \frac{1}{2} v^{\text{eff}}_{ij} - \frac{1}{2} v^{\text{eff,dc}}_{ij} \right). \tag{2.59}$$

Note the $\frac{1}{2}$ factor in the Coulomb energy. The scaling weight is defined by the fraction of indices in the local orbitals of fragment x,

$$w_{ij} = \begin{cases} 1, \text{ if } ij \in x, \\ \dfrac{1}{2}, \text{ if } i \in x \text{ or } j \in x, \\ 0, \text{ if } i \notin x \text{ and } j \notin x. \end{cases} \tag{2.60}$$

Similarly, the 2-body part of the Hamiltonian,

$$\tilde{V}_{ijkl} = w_{ijkl} V^{\text{emb}}_{ijkl}, \tag{2.61}$$

includes a weight factor w_{ijkl} to correctly account for the number of fragment indices.

v^{eff} in Eq. (2.59) is re-evaluated using the DMET global density matrix γ^{glob} [107],

$$\gamma^{\text{glob},\mathbf{R}} = \frac{1}{2} \left(C^{\mathbf{R}} \gamma^{\text{emb}} C^{\mathbf{0}\dagger} + C^{\mathbf{0}} \gamma^{\text{emb}} C^{\mathbf{R}\dagger} \right), \tag{2.62}$$

where $C^{\mathbf{R}}$ is the coefficient of the embedding basis of the $\mathbf{R}^{\text{th}}$ unit cell. This ensures a consistent Fock potential is used in all fragments.

The multi-fragment calculations in DMET are easily parallelized e.g., using MPI. The evaluation of the bath orbitals, construction of the embedding Hamiltonian, high-level solver calculations, energy computation and correlation potential fitting are all independent of each other. The communication only happens when (1) determining the chemical potential [communication cost $\mathcal{O}(1)$]; (2) constructing the global density matrix [cost $\mathcal{O}(N)$], where N is the number of embedding orbitals; (3) combining subblocks of the correlation potential [cost $\mathcal{O}(N)$]. We illustrate the MPI efficiency in Fig. 2.3 (b), in which the fragments are pairs of atoms (i.e., of equal size) in a 2D boron nitride crystal. The speedup is very close to ideal.

2.5 Generalized spin orbital formalism for superconductivity

Mean-field theory for superconductivity

The central idea of BCS theory is the formation of the Cooper pair, a quasiparticle of two binding electrons. There are significant fluctuations of creation and annihilation of electron pairs in the system, corresponding to non-zero expectation values of $\langle a^\dagger a^\dagger \rangle$ and $\langle aa \rangle$. In other words, the particle-number is not conserved in a superconducting system [1].

The BCS theory is based on a one-band picture and simplified two-electron Hamiltonian,

$$\hat{H}^{\text{simplified}} = \sum_{\mathbf{k}\sigma} (\varepsilon_{\mathbf{k}} - \mu) a^\dagger_{\mathbf{k}\sigma} a_{\mathbf{k}\sigma} - \sum_{\mathbf{k}\mathbf{k}'} V_{\mathbf{k}\mathbf{k}'} a^\dagger_{\mathbf{k}\alpha} a^\dagger_{-\mathbf{k}\beta} a_{-\mathbf{k}'\beta} a_{\mathbf{k}'\alpha}. \tag{2.63}$$

Comparing to the generic quantum chemistry Hamiltonian, there are three noticeable differences: (i) There is no orbital indices since the BCS theory starts with the free-fermion sea (and $\mathbf{k}$ is enough to label the quantum states). (ii) There only two $\mathbf{k}$ labels (not three in the full Hamiltonian). This is an approximation with only pair interactions. (iii) There is a negative sign before the two-electron terms, meaning the electron-electron interaction is effectively attractive.

Now we discuss the mean-field treatment of such Hamiltonian. The two-electron part of the Hamiltonian can be factorized as

$$\begin{aligned} \left\langle a^\dagger_{\mathbf{k}\alpha} a^\dagger_{-\mathbf{k}\beta} a_{-\mathbf{k}'\beta} a_{\mathbf{k}'\alpha} \right\rangle \approx & \left\langle a^\dagger_{\mathbf{k}\alpha} a_{\mathbf{k}'\alpha} \right\rangle \left\langle a^\dagger_{-\mathbf{k}\beta} a_{-\mathbf{k}'\beta} \right\rangle - \left\langle a^\dagger_{\mathbf{k}\alpha} a_{-\mathbf{k}'\beta} \right\rangle \left\langle a^\dagger_{-\mathbf{k}\beta} a_{\mathbf{k}'\alpha} \right\rangle \\ & + \left\langle a^\dagger_{\mathbf{k}\alpha} a^\dagger_{-\mathbf{k}\beta} \right\rangle \left\langle a_{-\mathbf{k}'\beta} a_{\mathbf{k}'\alpha} \right\rangle, \end{aligned} \tag{2.64}$$

where the first two terms are normal Coulomb and exchange expectation values and their effect can be absorbed into the $\varepsilon_{\mathbf{k}}$, whereas the last term is the key ingredient of the BCS theory, i.e., the pair-pair interaction (this channel is forbidden for particle-number conserved calculations). We can then formulate a mean-field description by approximating the two-body interactions as

$$\begin{aligned} a^\dagger_{\mathbf{k}\alpha} a^\dagger_{-\mathbf{k}\beta} a_{-\mathbf{k}'\beta} a_{\mathbf{k}'\alpha} \approx & \left\langle a^\dagger_{\mathbf{k}\alpha} a^\dagger_{-\mathbf{k}\beta} \right\rangle a_{-\mathbf{k}'\beta} a_{\mathbf{k}'\alpha} + a^\dagger_{\mathbf{k}\alpha} a^\dagger_{-\mathbf{k}\beta} \left\langle a_{-\mathbf{k}'\beta} a_{\mathbf{k}'\alpha} \right\rangle \\ & + \left\langle a^\dagger_{\mathbf{k}\alpha} a^\dagger_{-\mathbf{k}\beta} \right\rangle \left\langle a_{-\mathbf{k}'\beta} a_{\mathbf{k}'\alpha} \right\rangle. \end{aligned} \tag{2.65}$$

[1] One can understand the breaking of particle-number symmetry by considering the Cooper pair condensation at the TDL. There are macroscopic number of condensed Cooper pairs serving as the reservoir that compensates the deviation of the particle number. In this sense, the particle-number symmetry breaking is only a mathematical trick that ignores the contribution of the charge background.

By defining the superconducting order parameter

$$\Delta_{\mathbf{k}} = \sum_{\mathbf{k}'} -V_{\mathbf{k}\mathbf{k}'} \left\langle a_{-\mathbf{k}'\beta} a_{\mathbf{k}'\alpha} \right\rangle . \tag{2.66}$$

we can write the mean-field Hamiltonian for superconductivity,

$$\hat{H}^{\mathrm{BCS}} = \sum_{\mathbf{k}} \left[\sum_{\sigma} (\varepsilon_{\mathbf{k}} - \mu) a^{\dagger}_{\mathbf{k}\sigma} a_{\mathbf{k}\sigma} + \left(\Delta_{\mathbf{k}} a^{\dagger}_{\mathbf{k}\alpha} a^{\dagger}_{-\mathbf{k}\beta} + \mathrm{H.c.} \right) \right] + \text{const.}. \tag{2.67}$$

This Hamiltonian can be diagonalized by the *Bogoliubov transformation* [108, 109],

$$\begin{bmatrix} a_{\mathbf{k}\alpha} \\ a^{\dagger}_{-\mathbf{k}\beta} \end{bmatrix} = \begin{bmatrix} u_{\mathbf{k}} & v_{\mathbf{k}} \\ -v_{\mathbf{k}} & u_{\mathbf{k}} \end{bmatrix} \begin{bmatrix} p_{\mathbf{k}} \\ q^{\dagger}_{\mathbf{k}} \end{bmatrix} . \tag{2.68}$$

The new quasiparticles (p and q) are the mixing of particles and holes, and u and v are coefficients determined by the diagonalization and normalization conditions. In the new quasiparticle basis, the Hamiltonian is diagonalized,

$$\hat{H}^{\mathrm{BCS}} = \sum_{\mathbf{k}} E_{\mathbf{k}} (p^{\dagger}_{\mathbf{k}} p_{\mathbf{k}} + q^{\dagger}_{\mathbf{k}} q_{\mathbf{k}}) + \sum_{\mathbf{k}} (\varepsilon_{\mathbf{k}} - \mu - E_{\mathbf{k}}) + \text{const.}, \tag{2.69}$$

where

$$E_{\mathbf{k}} = \sqrt{(\varepsilon_{\mathbf{k}} - \mu)^2 + \Delta^2_{\mathbf{k}}}. \tag{2.70}$$

The form is reminiscent of quantum harmonic oscillators. The order parameter $\Delta_{\mathbf{k}}$ is the also gap function of elementary excitations since $E_{\mathbf{k}} = |\Delta_{\mathbf{k}}|$ at the Fermi level ($\varepsilon = \mu$). The non-zero pairing also makes the ground-state energy lower than the free fermion sea, and this proves the statement of Cooper that an arbitrarily small attraction between electrons (e.g., through electron-phonon coupling) can cause a binding state of electron pairs.

An alternative way to diagonalize the superconducting Hamiltonian in Eq. (2.67) is to redefine the vacuum such that the particle-number breaking terms become normal ones. We define the partial particle-hole (p-h) transformation T,

$$\begin{aligned} \hat{H}^{\mathrm{BCS}} &= \sum_{\mathbf{k}} \begin{bmatrix} a^{\dagger}_{\mathbf{k}\alpha} & a_{-\mathbf{k}\beta} \end{bmatrix} \begin{bmatrix} \varepsilon_{\mathbf{k}} - \mu & \Delta_{\mathbf{k}} \\ \Delta^{\dagger}_{\mathbf{k}} & -\varepsilon_{\mathbf{k}} + \mu \end{bmatrix} \begin{bmatrix} a_{\mathbf{k}\alpha} \\ a^{\dagger}_{-\mathbf{k}\beta} \end{bmatrix} \\ &= \sum_{\mathbf{k}} \begin{bmatrix} c^{\dagger}_{\mathbf{k}\alpha} & c^{\dagger}_{-\mathbf{k}\beta} \end{bmatrix} \begin{bmatrix} \varepsilon_{\mathbf{k}} - \mu & \Delta_{\mathbf{k}} \\ \Delta^{\dagger}_{\mathbf{k}} & -\varepsilon_{\mathbf{k}} + \mu \end{bmatrix} \begin{bmatrix} c_{\mathbf{k}\alpha} \\ c_{-\mathbf{k}\beta} \end{bmatrix} . \end{aligned} \tag{2.71}$$

This form is called *Nambu representation*[110, 111], which effectively defines the following partial p-h transformation T,

$$\begin{aligned} c^{\dagger}_{\mathbf{k}\alpha} &= T a^{\dagger}_{\mathbf{k}\alpha} T^{-1}, \\ c_{-\mathbf{k}\beta} &= T a^{\dagger}_{-\mathbf{k}\beta} T^{-1}, \end{aligned} \tag{2.72}$$

and the transformation makes the Hamiltonian in the normal ordering form. The new vacuum of β particles is a ferromagnetic state where all the $\mathbf{k}$ states are occupied by spin-down electrons, such that any further creation of β electrons will destroy the state. In the Nambu representation, the particle-number symmetry ($c^\dagger c$) comes conserved at the expense of spin symmetry S_z breaking. Diagonalizing the quadratic Hamiltonian gives exactly the Bogoliubov coefficients in Eq. (2.68). In a more quantum chemistry view, the Hamiltonian has a spin-coupling block Δ which mixes two flavors of spin. Therefore, we call this formulation a *generalized spin orbital* (GSO) formalism, which connects the superconducting problem to the generalized quantum chemistry approaches. We will derive the formulation for *ab initio* quantum embedding using the GSO formalism in the next section.

We note that we have assumed the *singlet pairing*, i.e. the electron pair is composed of different spins $\langle a_\alpha a_\beta \rangle$. It is also possible to have triplet pairing, where $\langle a_\alpha a_\alpha \rangle$ is not zero. In that case, the Nambu representation is still applicable, but the resulting Hamiltonian does not have simple interpretation of generalized spin mixing (e.g., see the discussion in the literature of Hartree-Fock-Bogoliubov (HFB) theory [112, 113]). We will only consider the singlet pairing in this thesis.

Finally, we discuss the pairing symmetry. If no spin-orbital coupling exists, a two-electron wavefunction can be decomposed as spatial and spin components,

$$\Psi(\mathbf{r}_1, \sigma_1, \mathbf{r}_2, \sigma_2) = \Delta(\mathbf{R}, \mathbf{r})\chi(\sigma_1, \sigma_2), \tag{2.73}$$

where $\mathbf{R} = \mathbf{r}_1 + \mathbf{r}_2$ is the center of mass and $\mathbf{r} = \mathbf{r}_1 - \mathbf{r}_2$ is the relative coordination. When the singlet pairing is assumed, the spin component $\chi(\sigma_1, \sigma_2) = -\chi(\sigma_2, \sigma_1)$ is anti-symmetric. Since the overall wavefunction is anti-symmetric, the spatial part Δ must be symmetric. If we assume the Hamiltonian is spatially rotation invariant, we can classify the Δ by the angular momentum l. The symmetric Δ then has even integer numbers of l, such as s ($l = 0$), d ($l = 2$). The corresponding superconductors are called s-wave and d-wave respectively. For realistic materials, there is no continuous rotation invariance, but only point group rotation invariance. One can, however, still classify the pairing symmetry using l by considering the small region around an atom, e.g., the Cu atom in cuprates. It has been measured that the conventional superconductors belong to the s-wave superconductors, while most of the evidence supports the d-wave character in the HTSCs. We will compute the order parameters in the three-band model and *ab initio* cuprates later.

Ab initio superconducting Hamiltonian

In this section, we discuss how to construct the *ab initio* lattice and embedding Hamiltonian using the partial p-h transformation T,

$$\begin{aligned} c_{i\alpha}^{\dagger} &= T a_{i\alpha}^{\dagger} T^{-1}, \\ c_{j\beta} &= T a_{j\beta}^{\dagger} T^{-1}. \end{aligned} \tag{2.74}$$

One can verify the transformed quasiparticle operators obey the fermionic anti-commutation relations,

$$\begin{aligned} \left\{c_{i\sigma}^{\dagger}, c_{j\tau}^{\dagger}\right\} &= 0, \\ \left\{c_{i\sigma}, c_{j\tau}\right\} &= 0, \\ \left\{c_{i\sigma}, c_{j\tau}^{\dagger}\right\} &= \delta_{ij}\delta_{\sigma\tau} = \delta_{(i\sigma),(j\tau)}. \end{aligned} \tag{2.75}$$

We then focus on how to construct the integrals in the new quasiparticle representation, where we use calligraphic letters ($\mathcal{H}$, $\mathcal{D}$ etc) to denote the quantities.

- One-particle Hamiltonian

  The partial p-h transform of a one-particle Hamiltonian, $H_1^{\mathbf{k}}$,

  $$H_1^{\mathbf{k}} = \left[h^{\alpha\mathbf{k}}, h^{\beta\mathbf{k}}, \Delta^{\alpha\beta\mathbf{k}}\right] \to \mathcal{H}_1^{\mathbf{k}} \equiv \begin{bmatrix} h^{\alpha\mathbf{k}} & \Delta^{\alpha\beta\mathbf{k}} \\ \Delta^{\alpha\beta\mathbf{k}\dagger} & -h^{\beta\mathbf{k}} \end{bmatrix} + \mathcal{H}_0, \tag{2.76}$$

  where the energy constant $\mathcal{H}_0 = \sum_{\mathbf{k}} \mathrm{Tr}\left(h^{\beta\mathbf{k}} S^{\mathbf{k},-1}\right)$.

- Overlap matrix and orbital coefficients

  The partial p-h transform of the overlap matrix S or orbital coefficients C,

  $$S^{\mathbf{k}} \to \mathcal{S}^{\mathbf{k}} \equiv \begin{bmatrix} S^{\mathbf{k}} & 0 \\ 0 & S^{\mathbf{k}} \end{bmatrix}, \tag{2.77}$$

  $$C^{\mathbf{k}} = \left[C^{\alpha\mathbf{k}}, C^{\beta\mathbf{k}}\right] \to \mathcal{C}^{\mathbf{k}} \equiv \begin{bmatrix} C^{\alpha\mathbf{k}} & 0 \\ 0 & C^{\beta\mathbf{k}} \end{bmatrix}. \tag{2.78}$$

- One-particle density matrix

  The partial p-h transformation of a one-particle reduced density matrix $\gamma_1^{\mathbf{k}}$,

  $$\gamma_1^{\mathbf{k}} = \left[\gamma^{\alpha\mathbf{k}}, \gamma^{\beta\mathbf{k}}, \kappa^{\alpha\beta\mathbf{k}}\right] \to \mathcal{D}_1^{\mathbf{k}} \equiv \begin{bmatrix} \gamma^{\alpha\mathbf{k}} & \kappa^{\alpha\beta\mathbf{k}} \\ \kappa^{\alpha\beta\mathbf{k}\dagger} & S^{\mathbf{k},-1} - \gamma^{\beta\mathbf{k}} \end{bmatrix}. \tag{2.79}$$

  $\mathcal{D}_1$ will serve as the *generalized density matrix* for constructing the bath orbitals C of DMET.

- Local two-particle Hamiltonian

  The partial p-h transform of a local electron repulsion integral (ERI), V_2^{loc},

$$V_2^{\text{loc}} \to \mathcal{V}_2 \equiv \begin{bmatrix} V & -V \\ -V^\dagger & V \end{bmatrix} + \mathcal{V}_1 + \mathcal{V}_0, \tag{2.80}$$

  where

$$\mathcal{V}_1 = \begin{bmatrix} v^J & 0 \\ 0 & v^K - v^J \end{bmatrix} \tag{2.81}$$

  with

$$v^J_{rs} = \sum_{pq} S^{-1}_{qp} V_{pqrs}, \tag{2.82}$$

$$v^K_{ps} = \sum_{qr} S^{-1}_{qr} V_{pqrs}, \tag{2.83}$$

  and

$$\mathcal{V}_0 = \frac{1}{2} \text{Tr}\big[(v_J - v_K) S^{-1}\big]. \tag{2.84}$$

- Vacuum terms from density fitting

  The construction of $\mathcal{V}_1$ using density fitting (using $W^{\mathbf{k}_p\mathbf{k}_q}_{Lpq}$ to represent the 3-centered AO integral),

$$\mathcal{V}_1^{\mathbf{k}} = \begin{bmatrix} v^{J\mathbf{k}} & 0 \\ 0 & v^{K\mathbf{k}} - v^{J\mathbf{k}} \end{bmatrix} \tag{2.85}$$

  with $v^{J\mathbf{k}}$ is computed as

$$\rho_L = \frac{1}{N_{\mathbf{k}}} \sum_{\mathbf{k}pq} S^{\mathbf{k},-1}_{qp} W^{\mathbf{kk}}_{Lpq}, \tag{2.86}$$

$$v^{J\mathbf{k}}_{rs} = \sum_L \rho_L W^{\mathbf{kk}}_{Lrs}. \tag{2.87}$$

  Similarly, $v^{K\mathbf{k}}$ is evaluated through

$$X^{\mathbf{k}_q\mathbf{k}_p}_{Lqs} = \sum_r S^{\mathbf{k}_q,-1}_{qr} W^{\mathbf{k}_q\mathbf{k}_p}_{Lrs}, \tag{2.88}$$

$$v^{K\mathbf{k}_p}_{ps} = \frac{1}{N_{\mathbf{k}}} \sum_{\mathbf{k}_q Lq} W^{\mathbf{k}_q\mathbf{k}_p *}_{Lqp} X^{\mathbf{k}_q\mathbf{k}_p}_{Lqs}. \tag{2.89}$$

  Constant term reads,

$$\mathcal{V}_0 = \frac{1}{2N_{\mathbf{k}}} \sum_{\mathbf{k}} \text{Tr}\big[(v^{J\mathbf{k}} - v^{K\mathbf{k}}) S^{\mathbf{k},-1}\big]. \tag{2.90}$$

- Embedding ERI

  The construction of the embedding ERI using density fitting and the partial p-h transform,

$$\begin{aligned}\mathcal{V}^{\text{emb}}_{ijkl} = \frac{1}{N_{\mathbf{k}}}\sum_{\mathbf{k}_L L}\Big(&W^{\alpha\alpha\mathbf{k}_L 00*}_{Lij} W^{\alpha\alpha\mathbf{k}_L 00}_{Lkl} + W^{\beta\beta\mathbf{k}_L 00*}_{Lij} W^{\beta\beta\mathbf{k}_L 00}_{Lkl} \\ &- W^{\alpha\alpha\mathbf{k}_L 00*}_{Lij} W^{\beta\beta\mathbf{k}_L 00}_{Lkl} - W^{\beta\beta\mathbf{k}_L 00*}_{Lij} W^{\alpha\alpha\mathbf{k}_L 00}_{Lkl}\Big),\end{aligned} \tag{2.91}$$

  where the reference cell 3-centered embedding integral W is calculated as,

$$W^{\sigma\tau\mathbf{k}_L 00}_{Lij} = \frac{1}{N_{\mathbf{k}}}\sum_{\mathbf{k}_p\mathbf{k}_q}{}' C^{\sigma\mathbf{k}_p\dagger}_{ip} W^{\mathbf{k}_p\mathbf{k}_q}_{Lpq} C^{\tau\mathbf{k}_q}_{qj}, \tag{2.92}$$

  where C^{σ} is the coefficients of embedding orbitals with spin $\sigma = \{\alpha, \beta\}$ and the $'$ limits the summation through the momentum conservation $\mathbf{k}_L = \mathbf{k}_p - \mathbf{k}_q + n\mathbf{b}$.

- Coulomb and exchange potential

  This Coulomb $\mathcal{J}$ and exchange $\mathcal{K}$ potential in the quasiparticle representation formally should be evaluated via the contractions between $\mathcal{V}_2$ and $\mathcal{D}_1$,

$$\mathcal{J}_{rs} = \sum_{pq}\mathcal{D}_{qp}\mathcal{V}_{pqrs}, \tag{2.93}$$

$$\mathcal{K}_{ps} = \sum_{qr}\mathcal{D}_{qr}\mathcal{V}_{pqrs}. \tag{2.94}$$

  By substituting Eq. (2.79) and (2.80), we have

$$\begin{aligned}\mathcal{J}^{\alpha}_{rs} &= \sum_{pq}\mathcal{D}^{\alpha}_{qp}\mathcal{V}^{\alpha\alpha}_{pqrs} + \mathcal{D}^{\beta}_{qp}\mathcal{V}^{\beta\alpha}_{pqrs} \\ &= \sum_{pq}\mathcal{D}^{\alpha}_{qp}V_{pqrs} - \mathcal{D}^{\beta}_{qp}V_{pqrs} \\ &= \sum_{pq}\gamma^{\alpha}_{pq}V_{pqrs} + \gamma^{\beta}_{pq}V_{pqrs} - S^{-1}_{pq}V_{pqrs} \\ &= \left(TJ^{\alpha}T^{-1}\right)_{rs} - v^{J}_{rs}.\end{aligned} \tag{2.95}$$

$$\begin{aligned}\mathcal{J}^{\beta}_{rs} &= \sum_{pq}\mathcal{D}^{\beta}_{qp}\mathcal{V}^{\beta\beta}_{pqrs} + \mathcal{D}^{\alpha}_{qp}\mathcal{V}^{\alpha\beta}_{pqrs} \\ &= \sum_{pq}\mathcal{D}^{\beta}_{qp}V_{pqrs} - \mathcal{D}^{\alpha}_{qp}V_{pqrs} \\ &= \sum_{pq} -(\gamma^{\beta}_{pq}V_{pqrs} + \gamma^{\alpha}_{pq}V_{pqrs}) + S^{-1}_{pq}V_{pqrs} \\ &= \left(TJ^{\beta}T^{-1}\right)_{rs} + v^{J}_{rs}.\end{aligned} \tag{2.96}$$

Note the difference between the direct transform of J, the additional term will be cancelled out in the generalized Fock matrix $\mathcal{F}$ when adding with $\mathcal{V}_1$.

$$\begin{aligned} \mathcal{K}^{\alpha}_{ps} &= \sum_{qr} \mathcal{D}^{\alpha}_{qr} \mathcal{V}^{\alpha\alpha}_{pqrs} \\ &= \sum_{qr} \mathcal{D}^{\alpha}_{qr} V_{pqrs} \\ &= \sum_{qr} \gamma^{\alpha}_{qr} V_{pqrs} \\ &= \left(T K^{\alpha} T^{-1}\right)_{ps}. \end{aligned} \tag{2.97}$$

$$\begin{aligned} \mathcal{K}^{\beta}_{ps} &= \sum_{qr} \mathcal{D}^{\beta}_{qr} \mathcal{V}^{\beta\beta}_{pqrs} \\ &= \sum_{qr} \mathcal{D}^{\beta}_{qr} V_{pqrs} \\ &= \sum_{qr} -\gamma^{\beta}_{qr} V_{pqrs} + S^{-1}_{qr} V_{pqrs} \\ &= \left(T K^{\beta} T^{-1}\right)_{ps} + v^{K}_{ps}. \end{aligned} \tag{2.98}$$

Note the difference between the direct transform of K, the additional term will be cancelled out in the generalized Fock matrix $\mathcal{F}$ when adding with $\mathcal{V}_1$.

$$\begin{aligned} \mathcal{K}^{\alpha\beta}_{ps} &= \sum_{qr} \mathcal{D}^{\alpha\beta}_{qr} \mathcal{V}^{\alpha\beta}_{pqrs} \\ &= \sum_{qr} -\mathcal{D}^{\alpha\beta}_{qr} V_{pqrs} \\ &= \sum_{qr} -\kappa^{\alpha\beta}_{qr} V_{pqrs} \end{aligned} \tag{2.99}$$

Note this term does not appear in the normal state unrestricted Hartree-Fock (UHF) potential.

- frozen-core approximation and DFT as low-level theory The frozen-core potential can be calculated using $\mathcal{D}^{\text{core}}$ and the above functions. In a density functional theory (DFT) Kohn-Sham Hamiltonian, the $\mathcal{K}$ matrix should be ignored for pure functionals, or be scaled with the hybrid parameter of hybrid functionals (e.g., $x^{\text{hyb}} = 0.25$ in the PBE0 functional). So far, we do not include DFT v_{xc} in the embedding Hamiltonian because it requires some proper treatment of double-counting.

DMET algorithms for superconducting states

In this section, we discuss how to perform a DMET calculation of a doped cuprate. The following algorithm is implemented in libDMET [98, 114].

1. Set up the cell and the lattice. The doping need to modify the total number of electrons of the cell.

2. Mean-field calculation of the doped system (e.g., from unrestricted PBE0).

3. Local (core, valence and virtual) orbitals are constructed, $C^{\text{AO,core}}$, $C^{\text{AO,non-core}}$.

4. Partial p-h transform: Construct $\mathcal{C}^{\text{AO,core}}$, $\mathcal{C}^{\text{AO,non-core}}$, $\mathcal{S}$, $\mathcal{H}_1$, $\mathcal{H}_0$, $\mathcal{V}_1$, $\mathcal{V}_0$, $\mathcal{D}^{\text{core}}$, $\mathcal{J}^{\text{core}}$, $\mathcal{K}^{\text{core}}$, $\mathcal{E}^{\text{core}}$.

   The resulting lattice Hamiltonian (all in the LO basis without core, **k**-point labels are omitted for clarity) is

$$\mathcal{E} = E^{\text{nuc}} + \mathcal{E}^{\text{core}} + \mathcal{H}_0 + \mathcal{V}_0. \tag{2.100}$$

$$\mathcal{H} = \mathcal{H}_1 + \mathcal{V}_1 + \mathcal{J}^{\text{core}} - x^{\text{hyb}}\mathcal{K}^{\text{core}}. \tag{2.101}$$

   Note that here $\mathcal{V}_1$ and $\mathcal{V}_0$ will also include a factor x^{hyb} if DFT is used.

   The generalized Fock matrix comes from a direct transform of the mean-field unrestricted Fock matrices,

$$\mathcal{F} = \begin{bmatrix} F^{\alpha} & 0 \\ 0 & -F^{\beta} \end{bmatrix}. \tag{2.102}$$

   To make the expectation value of physical particle number correct, an additional chemical potential should be included in $\mathcal{H}$ and $\mathcal{F}$,

$$\begin{bmatrix} \mu S & 0 \\ 0 & -\mu S \end{bmatrix}. \tag{2.103}$$

5. Set up the correlation potential.

$$u^{\text{corr}} = \begin{bmatrix} 0 & \Delta^{\alpha\beta} \\ \Delta^{\alpha\beta\dagger} & 0 \end{bmatrix}. \tag{2.104}$$

   The particle-number non-conserving part is from the correlation potential and will be determined self-consistently through DMET. We also constrain the

form of Δ to be a subset of local orbitals (e.g., 3-band orbitals and Cu-4s) and the point group symmetry is applied. The initial guess is a d-wave potential among the Cu-3$d_{x^2-y^2}$ orbitals. In principle, we can include the diagonal part in u^{corr} such that the magnetic order is also determined self-consistently. We do not consider such degrees of freedom here.

6. DMET @ DFT main loop.

   a) Diagonalize the generalized lattice Fock matrix $\mathcal{F} + u^{\text{corr}}$ to get the generalized density matrix $\mathcal{D}$ and determine the lattice chemical potential μ that ensures the correct particle number. Note that the smearing should be used to treat the doped states.

   b) Construct the bath orbitals C from $\mathcal{D}$ using SVD.

   c) Construct the embedding Hamiltonian from C and integrals. Specifically, the embedding $\mathcal{V}_2$ is calculated using Eq. (2.91). Note that the DFT v^{xc} does not enter into the embedding Hamiltonian, only the HF-form embedding-core interaction is considered.

   d) Solve the embedding problem with generalized solvers (e.g., GCCSD). We need to solve a chemical potential of the embedding problem μ^{emb} such that the physical particle number is the same as the projection from the lattice,

   $$N^{\text{phys,emb}} = PN^{\text{phys,latt}}P. \tag{2.105}$$

   This is due to the non-exactness of embedding, especially when DFT is used as the low-level theory. Currently, μ^{emb} is determined using the constrained HF.

   e) Collect $\mathcal{D}^{\text{emb}}$, transform it back to the original electron representation, and analyze the magnetic and pairing orders.

   f) Fit u^{corr} in the lattice problem by diagonalizing $\mathcal{F}+u^{\text{corr}}$ and least-square fitting. We only fit the Bogoliubov part of the density matrix subblocks (3-band and Cu-4s subblocks of $\mathcal{D}^{\alpha\beta}$).

   g) Extrapolate $\mathcal{D}$ and go back to (a) until the change $||\mathcal{D}_{i+1} - \mathcal{D}_i||$ is sufficiently small.

2.6 Ab initio many-body impurity solver

Full configuration interaction

The configuration interaction (CI) method is a linear variational approach with Slater determinant (or configuration state function, CSF) as its many-electron basis [115, 116]. Full CI (FCI) results (at a sufficiently large one-electron basis) have long been regarded as the exact solutions for small molecules. Not only for the benchmarking purpose, FCI is crucial in CASSCF calculation [117] or other quantum embedding methods [34]. Although conceptually simple, CI, especially FCI, has the drawback of exponential scaling towards the size of system, and requires large storage as well. To overcome the large memory requirement, *direct CI* [118] is developed to avoid the explicit storage of CI matrix. Furthermore, the use of Slater determinants as bases rather than CSFs leads to a highly efficient scheme for the evaluation of the matrix element in CI calculation [119].

In CI references [69, 116, 119], the many-electron Hamiltonian is often represented by replacement operators ($E_{pq} = a_p^\dagger a_q$),

$$\begin{aligned}\hat{H} &= \sum_{pq} h_{pq} E_{pq} + \frac{1}{2} \sum_{pqrs} g_{pqrs} (E_{pq} E_{rs} - \delta_{rq} E_{ps}) \\ &= \sum_{pq} k_{pq} E_{pq} + \frac{1}{2} \sum_{pqrs} g_{pqrs} E_{pq} E_{rs},\end{aligned} \tag{2.106}$$

where k is the effective 1-e integral in MO basis,

$$k_{pq} = h_{pq} - \frac{1}{2} \sum g_{prrq}. \tag{2.107}$$

In direct CI, one does not save the whole CI matrix H, but instead calculates the sigma vector,

$$\sigma = H \cdot C, \tag{2.108}$$

where C is the CI vector. Once we have a function to efficiently calculate the sigma vector, we can simply use the Davidson algorithm [120] to find the lowest energy and the corresponding CI vector.

The FCI method is also known as the exact diagonalization. The exponentially increasing configurations limit the FCI method to problems within about 16 electrons in 16 orbitals (if no further symmetry is utilized).

Density matrix renormalization group

The *ab initio* density matrix renormalization group (DMRG) [121–123] uses a matrix product state (MPS) defined on a 1-dimensional ordering of the orbitals,

$$|\Psi\rangle = \sum_{n_1,\cdots,n_L} \mathbf{A}^{n_1}\mathbf{A}^{n_2}\cdots\mathbf{A}^{n_L}\,|n_1 n_2\cdots n_L\rangle\,, \tag{2.109}$$

where L is the number of orbitals, n is the occupation number of an orbital and the $\mathbf{A}$'s are $M \times M$ matrices. The accuracy of DMRG is controlled by the so-called bond-dimension M and as $M \to \infty$, DMRG becomes exact. In the large bond dimension regime, the energy has a linear relation with respect to the DMRG discarded weight δ [124–126], which allows for stable extrapolation to the exact limit.

To carry out *ab initio* DMRG calculations using our embedding Hamiltonian, we follow the strategy described in Ref. [127]. We first define an orthogonal local basis as the orbitals in DMRG. In particular, we use split localized unrestricted Møller-Plesset second order perturbation (MP2) natural orbitals, where orbitals of occupied and virtual character are separately localized by the Edmiston-Ruedenberg (ER) method [85]. Using local natural orbitals improves the convergence of the DMRG with respect to bond dimension.

Coupled cluster theory

The main solver we use in our works is coupled cluster singles and doubles (CCSD) [128], which can be easily applied to *ab initio* Hamiltonians with hundreds of correlated orbitals. It is based on a wavefunction ansatz of the form

$$|\Psi\rangle = \mathrm{e}^{\hat{T}_1+\hat{T}_2}\,|\Phi\rangle\,, \tag{2.110}$$

where $|\Phi\rangle$ is a reference Slater determinant and the cluster excitation operators read,

$$\hat{T}_1 = \sum_{ia} t_i^a a_a^\dagger a_i, \tag{2.111}$$

$$\hat{T}_2 = \sum_{ijab} t_{ij}^{ab} a_a^\dagger a_b^\dagger a_j a_i. \tag{2.112}$$

CC approximations have a number of important properties. First, they are exact for all products of correlations involving a finite number of particles. For example, the CCSD approximation is exact for any product of two-particle correlations, which allows for the accurate description of correlated singlet-like physics. Second, they

are extensive, which means that the approximation does not deteriorate simply from increasing system size. Third, they are in principle systematically improvable, by increasing the excitation level (although the cost also increases exponentially with excitation level). Finally, they are especially accurate for gapped and ordered states. This describes the AFM parent state and magnetic configurations considered in this work. In ordered states, one chooses the reference $|\Phi\rangle$ to break the appropriate symmetry. Here, we break S^2 symmetry and choose an unrestricted (spin-polarized) Hartree-Fock determinant as our reference state, solving the unrestricted CC equations (UCCSD). Note that Hartree-Fock is truly a mean-field theory of the bare Coulomb interaction. Thus, all fluctuations observed in this work are due to the CC correlations.

The DMET energy expression requires the reduced density matrices. The CC density matrices are obtained from the CC Λ equations [129].

Because CCSD is an approximate method, it is always important to benchmark its accuracy for the phenomenon of interest. In molecular quantum chemistry, CCSD(T) (coupled cluster singles and doubles with perturbative triples) is often regarded as the "gold standard" because it achieves high accuracy for ordered or gapped reference states (so-called "single reference" states). In this work, we do not extensively use the triples correction because our implementation of the Λ equations is efficient only at the singles and doubles level. However, we can verify the accuracy of the unrestricted CCSD solver against unrestricted CCSD(T) in a smaller subset of examples. We also benchmark against the *ab initio* DMRG solver. Since DMRG works well away from ordered states (i.e., for multi-reference correlations), this test allows us to verify the basic assumption underlying the accuracy of CC approximations in these systems. We describe these benchmarks further below.

Since DMET involves a self-consistency loop and a search over the chemical potential, it is necessary to solve the quantum impurity problem many times. To do this efficiently, the solver can be approximately restarted from the previous solution by matching the embedding basis. Say C_1 and C_2 are the embedding bases in the first and the second cycles of a DMET calculation. The bases can be approximately matched using the orbital overlap matrix and an SVD,

$$C_1^\dagger S C_2 = U \Sigma V^\dagger, \tag{2.113}$$

where S is the overlap matrix in the computational basis (here this is the AO overlap

matrix), and

$$\tilde{C}_1 = C_1 R = C_1 U V^\dagger \tag{2.114}$$

defines the closest orbitals to C_2 in the Frobenius norm sense and $R = UV^\dagger$ is a unitary rotation matrix. The wavefunction from the first cycle can then be transformed with the rotation matrix, i.e., the one- and two-body amplitudes in the CCSD equations are rotated as,

$$\tilde{t}_k^c = \sum_{ia} R_{ca}^\dagger t_i^a R_{ik}, \tag{2.115}$$

$$\tilde{t}_{kl}^{cd} = \sum_{ijab} R_{ca}^\dagger R_{db}^\dagger t_{ij}^{ab} R_{ik} R_{jl}. \tag{2.116}$$

This restart scheme greatly reduces the total cost spent in the many-body solver. Typically, the CCSD amplitude equations converge in < 5 iterations after the second DMET iteration.

When the system is gapless, the gap of the embedding problem is also small. This creates difficulties for the impurity solver. Here, we discuss how CC solver may be tuned to solve metallic problem. The CCSD equation requires the projection [129],

$$r = \left\langle \Phi_{ij}^{ab} \middle| H \mathrm{e}^T \middle| \Phi \right\rangle = 0. \tag{2.117}$$

This is a non-linear root-finding problem and the standard way to solve it is by a Jacobian iteration with direct inversion of iterative space (DIIS) [130]. The Jacobian means the preconditioner is chosen as the diagonal of the matrix,

$$\mathcal{P} = \frac{1}{\epsilon_i - \epsilon_a} \propto \frac{1}{\mathrm{gap}}, \tag{2.118}$$

and thus does not work for metal.

The failure of preconditions, however, does not mean that CC cannot be applied to metals. From a numerical analysis perspective, it means the system is more ill-conditioned (so that the convergence is harder). Several ideas are possible to enhance the convergence, e.g., through a regularized preconditioner,

$$\mathcal{P} = \frac{1}{\epsilon_i - \epsilon_a + \delta} \quad \text{or} \quad \frac{1}{\epsilon_i - \epsilon_a}\left[1 - \mathrm{e}^{-\kappa(\epsilon_i - \epsilon_a)}\right]. \tag{2.119}$$

Recently, there is trial to solve the projection equation by Newton-Krylov method, which approximates the inverse of Jacobian J^{-1} in a subspace and solves the root by an inexact Newton way,

$$t^{k+1} = t^k - J^{-1} r\left[t^k\right]. \tag{2.120}$$

This is potentially more reliable for systems with orbital degeneracy than the traditional DIIS method [131, 132]. We implemented the GSO version of the Newton-Krylov CCSD in MPI4PySCF with efficient MPI parallelism [133].

2.7 Analysis methods

Charge and spin population analysis

Since we allow S^2 symmetry breaking in our calculations, charge and spin order can be analyzed using the spin-resolved one-particle reduced density matrix ($\sigma = \alpha, \beta$),

$$\gamma_{ij}^{\sigma} = \left\langle a_{j\sigma}^{\dagger} a_{i\sigma} \right\rangle. \tag{2.121}$$

In particular, the charge of orbital i reads,

$$n_i = \gamma_{ii}^{\alpha} + \gamma_{ii}^{\beta}, \tag{2.122}$$

and the local magnetic moment of orbital i reads,

$$m_i = \gamma_{ii}^{\alpha} - \gamma_{ii}^{\beta}. \tag{2.123}$$

In principle, the charge (spin) populations depend on the choice of atom-centered local orbitals $\{\phi_i\}$. This typically has a strong basis set dependence if the population analysis is carried out using the computational AO basis. However, the basis dependence can be largely removed by measuring the population in the IAO basis [95], which is what we do here.

Bonding analysis

To analyze bonding in the system in a straightforward way, we can use the atom-centered local orbitals, i.e., the IAOs + PAOs used in the population analysis above, and evaluate bond orders, which measure the off-diagonal density matrix element between two local orbitals. In this work, we use the 2-center Mayer bond order [134] which, for atoms A and B (or two subsets of orbitals) is defined as,

$$b_{AB} = \sum_{\sigma} b_{AB}^{\sigma} = 2 \sum_{\sigma} \sum_{i \in A} \sum_{j \in B} (\gamma^{\sigma} S)_{ji} (\gamma^{\sigma} S)_{ij}, \tag{2.124}$$

where γ^{σ} is the one-particle density matrix with spin σ and S is the overlap matrix of the local basis. Since we use IAOs + PAOs as our basis, S is the identity matrix. For non-polarized covalent bonds, the Mayer bond order typically agrees very well with chemical intuition (e.g., H_2 and N_2 roughly have bond orders 1 and 3 in calculations).

For strong polarized covalent bonds or even ionic bonds, the Mayer bond order is generally qualitatively reasonable.

As an alternative to the bond order, we also use the electron density $\rho(\mathbf{r})$ and electron localization function $\mathrm{ELF}^{\sigma}(\mathbf{r})$ [135, 136] as real space indicators of the bonding. ELF was originally proposed to measure the localization of electrons and helps reveal atomic shell structure, bonding, and lone electron pairs. ELF values lie in $[0, 1]$. When $\mathrm{ELF} = 1$, the electron is completely localized while $\mathrm{ELF} = \frac{1}{2}$ suggests that the electron behaves like it does in the electron gas of the given density at that position. Since ELF is defined in real space it is less sensitive to the choice of basis set. Typically, large ELF values indicate a core region, a lone pair of electrons, and covalent bonding. Thus, the ELF is a useful tool to distinguish between covalent and non-covalent (such as ionic) bonding.

A third way to understand the bonding is to examine the individual localized orbitals in the occupied and virtual spaces, which reveals the bonds and antibonds of the system. Here, we localized the occupied and virtual embedding orbitals via Pipek-Mezey (PM) localization [84], which maximizes the population charges on the atoms,

$$U = \underset{U}{\operatorname{argmax}}\, w(U) = \underset{U}{\operatorname{argmax}} \sum_{I}^{\text{atoms}} \sum_{i} |q_i^I|^2, \tag{2.125}$$

and q_i^I is the charge of the i^{th} orbital of atom I (IAOs + PAOs are used as the population method, in order to reduce the basis set dependence). The resulting unitary rotation U defines a set of localized orbitals,

$$\left|\phi_i^{\text{PM}}\right\rangle = \sum_{m} |\psi_m\rangle\, U_{mi}\,. \tag{2.126}$$

Note that PM localization preserves the separation between σ and π orbitals.

Spin-spin correlation function

The (S_z component) spin-spin correlation function $\langle S_z(0) S_z(r)\rangle$ reflects the spin-spin correlation between metal center (e.g., Cu) in the reference cell (0) and another metal atom at position (r). If the correlation function does not decay to 0 at large r, the system has long-range order.

Using the spin operator of local orbital i

$$\hat{S}_i^z = \frac{1}{2}\left(a_{i\alpha}^{\dagger} a_{i\alpha} - a_{i\beta}^{\dagger} a_{i\beta}\right), \tag{2.127}$$

we express the correlation function as a contraction of the reduced 1-particle γ^{σ}_{ij} and 2-particle $\Gamma^{\sigma\tau}_{ijkl} \equiv \left\langle a^{\dagger}_{i\sigma} a^{\dagger}_{k\tau} a_{l\tau} a_{j\sigma} \right\rangle$ density matrices,

$$\begin{aligned}\langle S_z(0) S_z(r) \rangle &= \sum_{i \in \mathrm{Cu}(0)} \sum_{j \in \mathrm{Cu}(r)} \left\langle \hat{S}^z_i \hat{S}^z_j \right\rangle \\ &= \frac{1}{4} \sum_{i \in \mathrm{Cu}(0)} \sum_{j \in \mathrm{Cu}(r)} \left(\gamma^{\alpha}_{ij} \delta_{ij} + \Gamma^{\alpha\alpha}_{iijj} - \Gamma^{\alpha\beta}_{iijj} - \Gamma^{\alpha\beta}_{jjii} + \gamma^{\beta}_{ij} \delta_{ij} + \Gamma^{\beta\beta}_{iijj} \right).\end{aligned} \tag{2.128}$$

where the summation is constrained to the local orbitals of Cu. Note that we do not consider the oxygen contribution to the correlation function.

Natural orbital analysis

Spin-traced natural orbitals can be obtained by diagonalizing the (spin-traced) density matrix γ,

$$\gamma^{\mathbf{k}}_{qp} C^{\mathbf{k}}_{pi} = C^{\mathbf{k}}_{qi} \Lambda^{\mathbf{k}}_{i}, \tag{2.129}$$

where Λ_p is a natural occupation number (between 0 to 2) and C_{pi} are the natural orbital coefficients. If the density matrix originates from a pure state with $S = 0$, then the further the natural occupation is away from 0 or 2 (a single Slater determinant), the more correlated an orbital is. We can define the *half-filling index* to summarize the contribution of local orbitals $\{p\}$, to half-filled natural orbitals,

$$f^{\mathrm{half}}_{p} = \frac{1}{N_{\mathbf{k}} N_p} \sum_{i\mathbf{k}} |C^{\mathbf{k}}_{pi}|^2 \min(\Lambda^{\mathbf{k}}_i, 2 - \Lambda^{\mathbf{k}}_i), \tag{2.130}$$

where N_p is the number of orbitals in an orbital group (e.g., Cu $3d_{x^2-y^2}$, O $2p$). The situation is a bit more subtle for a state with $S \neq 0$ or a symmetry-broken state. In a symmetry-broken state, the degree of half-filling measures both the fluctuations as well as the degree of spatial symmetry breaking. For example, in a symmetry-broken Slater determinant with overall low-spin ($S_z = 0$) (which has no fluctuations), $\Lambda_p \to 1$ means that there are spin-orbitals of opposite spin with no spatial overlap. Nonetheless, since it is important to include spin fluctuations between such spin orbitals, the half-filling index remains a useful indicator of the most important local orbitals to include in a minimal atomic model.

The spin-resolved natural orbitals can be obtained by diagonalizing the spin-resolved density matrix γ^{σ}. Now Λ_p ranges from 0 to 1. In a symmetry broken state, it is the deviation of the *spin-resolved* occupancies Λ_p from their extremal values that measures the importance of dynamical fluctuations. If all spin-resolved occupancies

are 0 or 1, then the state is exactly of mean-field character and all single-particle lifetimes are infinite (no dynamical effects). Deviation from this occupancy pattern indicates correlation, and very strong deviation indicates strong correlation [e.g., in a system far from a Fermi liquid where the quasiparticle picture breaks down such as a Luttinger liquid, the occupancy (or momentum distribution function) no longer shows a jump between values close to 0 and values close to 1]. In this work, we estimate if there are strong dynamical effects by examining if all the natural occupancies are close to 0 or 1.

Also, although DMET does not provide direct access to the single-particle energy spectrum, we can use the occupancies of the spin-resolved natural orbitals as proxies for proximity to the top edge of the valence band/bottom edge of the conduction band. In particular, the highest occupied natural orbital (occupancy $> 1/2$ but furthest from 1) is a pseudo-valence-band maximum; while the lowest occupied natural orbital (occupancy $< 1/2$ but furthest from 0) is a pseudo-conduction band minimum.

Pairing analysis

To characterize the doping dependence of the superconducting ground-state, we define the averaged SC order parameters.

For the three-band Hubbard models the SC order parameter here is evaluated as the average of the Cu-Cu and O-O d-wave pairing components,

$$\begin{aligned} m_{\mathrm{SC}} = &\sum_{\langle ii' \rangle} \frac{1}{\sqrt{2}} \eta^{\mathrm{SC}}_{ii'} \left(\left\langle d_{i\alpha} d_{i'\beta} \right\rangle + \left\langle d_{i'\alpha} d_{i\beta} \right\rangle \right) \\ &+ \sum_{\langle\langle jj' \rangle\rangle} \frac{1}{\sqrt{2}} \eta^{\mathrm{SC}}_{jj'} \left(\left\langle p_{j\alpha} p_{j'\beta} \right\rangle + \left\langle p_{j'\alpha} p_{j\beta} \right\rangle \right), \end{aligned} \tag{2.131}$$

where $\langle \cdots \rangle$ limits the summation such that only the pairing between nearest Cu-d orbitals is taken into account, and similarly $\langle\langle \cdots \rangle\rangle$ involves only the next-nearest coupling between O-p orbitals. The d-wave superconducting structure factor η^{SC} is defined as,

$$\eta^{\mathrm{SC}}_{ii'} = \begin{cases} +1, \text{ if } \mathbf{R}_i - \mathbf{R}_{i'} = \pm \mathbf{e}_x, \\ -1, \text{ if } \mathbf{R}_i - \mathbf{R}_{i'} = \pm \mathbf{e}_y. \end{cases} \tag{2.132}$$

For the s-wave pairing, one simply let $\eta = 1$ for all terms. For the one-band Hubbard model, the oxygen part should be omitted.

For *ab initio* materials. There more orbitals $\{\phi\}$ in each atom, one can define the total atomic pairing coupling,

$$m_{\mathrm{SC}} = \sum_{\langle ii' \rangle} \frac{1}{\sqrt{2}} \eta^{\mathrm{SC}}_{ii'} \left(\langle \phi_{i\alpha} \phi_{i'\beta} \rangle + \langle \phi_{i'\alpha} \phi_{i\beta} \rangle \right), \tag{2.133}$$

where i (i') loops all of the local orbitals of atom I (I') and phase factor η is the same as before.

As we do not perform real finite-temperature simulations, we use the above zero-temperature local pairing orders as a proxy for the T_{c} in the phase diagram. This is an approximation, but it has been shown in the BCS theory $\Delta \propto T_{\mathrm{c}}$ [12]. Therefore, we expect that the materials trend of T_{c} can be reflected in the pairing order parameter m, at least to the leading order.

Chapter 3

PROJECTED DENSITY MATRIX EMBEDDING THEORY AND ONE-BAND HUBBARD MODEL

Based on the work published in *J. Chem. Phys.* **151**, 064108 (2019). Copyright 2019, American Institute of Physics. [107]

3.1 Introduction

This chapter focuses on a possible way to improve numerical algorithms to achieve self-consistency in the context of DMET. In many systems, using the bath orbitals generated from the HF Slater determinant yields energies and physical observables from DMET that already significantly improve on those from HF theory alone. Such calculations will be referred to as "single-shot" DMET calculations [35]. On the other hand, as mentioned in Sec. 2.2, when the physical system undergoes a phase transition not predicted by mean-field theory, we expect that a mean-field theory will produce the wrong order parameter, and the resulting bath orbitals will be very poor. In such a scenario, it is necessary to perform DMET *self-consistently* to improve the bath orbitals. The self-consistency condition is usually defined such that the 1-RDMs obtained from the low-level and high-level theories match each other according to some criterion. Self-consistency can be achieved by optimizing a single-body potential, termed the correlation potential, in the low-level theory. Each optimization step requires diagonalizing a matrix, similar to in a SCF iteration step in the solution of the HF equations.

Nonetheless, there are two outstanding numerical issues associated with the optimization of the correlation potential. First, the optimization procedure may require a large number of iterations to converge. It is not uncommon for the number of iterations to be 100 - 1000 especially for systems that are not translationally invariant. Hence when the system size becomes moderately large (a few hundred sites), the cost of the correlation potential optimization may exceed the cost of the impurity solver for small impurities. Second, the bath construction procedure of DMET requires the 1-RDM to be an idempotent matrix, and the corresponding low-level Hamiltonian should have a finite HOMO-LUMO gap. However, even if the strongly correlated global system is gapped, it is often the case that the low-level Hamiltonian

associated with a given correlation potential in the optimization procedure becomes gapless. The derivative of the bath orbitals with respect to the correlation potential will then become infinite, and the optimization cannot properly proceed. This work aims at addressing the first problem, namely the cost associated with the correlation potential optimization. The second problem should be addressed by properly considering the zero temperature limit of a finite temperature generalization of DMET. We have applied the finite-temperature smearing in both lattice mean-field and the fitting procedure, see other chapters for details.

In this chapter, we will introduce an alternate procedure to self-consistently determine the bath orbitals, which completely avoids the need to optimize the correlation potential. In the standard DMET, the bath orbitals are uniquely determined by the corresponding idempotent 1-RDM obtained from a low-level theory, denoted D^{LL}. The goal of the self-consistent DMET can then be formulated, in an abstract way, as finding the solution of the following fixed point problem

$$D^{\mathrm{LL}} = \mathcal{F}\left[\mathcal{D}[D^{\mathrm{LL}}]\right]. \tag{3.1}$$

Here the mapping $\mathcal{D}[\cdot]$ takes the idempotent 1-RDM as input, generates the corresponding bath orbitals, and solves all impurity problems to obtain the 1-RDM evaluated from the high-level theory. The mapping $\mathcal{F}$ takes the high-level correlated 1-RDM, denoted by $D^{\mathrm{HL}} := \mathcal{D}[D^{\mathrm{LL}}]$ as input, and generates another idempotent 1-RDM. The correlation potential optimization can be viewed as *one* way of achieving self-consistency as required by Eq. (3.1). To see this, we only need to define the mapping $\mathcal{F}$ to be the minimization procedure in the standard DMET, which uses a correlation potential to minimize the discrepancy between D^{LL} and D^{HL} evaluated on the impurity problems.

The perspective from the fixed point equation Eq. (3.1) suggests that other forms of $\mathcal{F}$ are possible which map D^{HL} to D^{LL} more efficiently. We propose that D^{LL} can be obtained by directly *projecting* D^{HL} onto the set of idempotent matrices with a given rank. The modified method is therefore called the projected density matrix embedding theory (p-DMET). The solution of p-DMET will *not* be identical to that of DMET, since they are defined using different mappings $\mathcal{F}$. In particular, unlike DMET, which can be defined to only use information from D^{HL} on the fragments during self-consistency, p-DMET requires the construction of D^{HL} on the global domain in order to define the projection operation.

Using the two-dimensional one-band Hubbard model and restricting to magnetic

and non-magnetic self-consistent solutions, we demonstrate that the results of p-DMET and DMET at self-consistency are very similar within the AFM and the PM phases. The discrepancy between the two methods is largest near the phase boundary, and for larger on-site interactions. We show that p-DMET significantly lowers the computational cost to achieve self-consistency for large lattices without translational invariance. For example, even for a moderately sized lattice with 128 sites and using 4-site impurities (without translational invariance), the correlation potential fitting procedure in standard DMET requires about 20000 s of CPU time, which is reduced to about 1 s in the p-DMET approach.

The rest of the chapter is organized as follows. We then discuss p-DMET and the associated numerical issues in Sec. 3.2. We demonstrate the performance of p-DMET for the two-dimensional Hubbard model in Sec. 3.3, before deriving conclusions in Sec. 3.4.

3.2 Projected density matrix embedding theory

Motivated by the fixed point formulation of self-consistency Eq. (3.1), we propose the following procedure to obtain D^{LL}:

$$D^{\mathrm{LL}} = \mathcal{F}[D^{\mathrm{HL}}] := \arg \min_{\substack{D=D^\dagger, D^2=D, \\ \mathrm{tr}(D)=N_e}} \|(D - D^{\mathrm{HL}}) \odot W\|_F^2. \tag{3.2}$$

Compared to Eq. (2.16), the main simplification of Eq. (3.2) comes from the fact that the admissible set is now the set of idempotent density matrices with N_e electrons without further constraints. To further simplify the method we let each entry of W be 1, i.e. $W_{pq} \equiv 1$. In other words, we measure the discrepancy of all entries of the density matrix on the same footing, and solve

$$D^{\mathrm{LL}} = \arg \min_{\substack{D=D^\dagger, D^2=D, \\ \mathrm{tr}(D)=N_e}} \|D - D^{\mathrm{HL}}\|_F^2. \tag{3.3}$$

Eq. (3.3) has a simple analytic solution. Let Ψ^{LL} be the eigenvectors corresponding to the largest N_e eigenvalues of D^{HL}, i.e. Ψ^{LL} consists of the leading N_e natural orbitals. Then the solution to Eq. (3.3) is

$$D^{\mathrm{LL}} = \Psi^{\mathrm{LL}}(\Psi^{\mathrm{LL}})^\dagger. \tag{3.4}$$

If D^{HL} is fixed, this is the closest projection operator to D^{HL} measured by the Frobenius norm. Informally, Ψ^{LL} is the single determinant that best captures the information contained in all the density matrices of the fragments. Once D^{LL} is

obtained, we may compute the bath orbitals according to Eq. (2.10), and proceed to solve for the ground-state of the impurity problems as in the standard DMET procedure. Hence we refer to this method as projected density matrix embedding theory (p-DMET). Again to make this procedure well defined, we require that there is a positive gap between the N_e-th and $(N_e + 1)$-th eigenvalue of the correlated density matrix D^{HL}. p-DMET assumes the high-level 1-RDM D^{HL} of the global system has been computed. As mentioned above, such a global 1-RDM can be constructed from the high-level 1-RDM's in each impurity using the democratic partitioning Eq. (2.14).

Let C_x be the collection of fragment and bath orbitals of the impurity x. Then we define

$$\begin{bmatrix} D^{(x)} \\ * \end{bmatrix} = \widetilde{D}^{(x)} C_x^{\dagger}, \tag{3.5}$$

where $\widetilde{D}^{(x)}$ is the 1-RDM of the impurity problem with size $(2L_A)\times(2L_A)$. $\widetilde{D}^{(x)}C_x^{\dagger}$ is a matrix of size $(2L_A) \times L$. $D^{(x)}$ is obtained by extracting the first L_A rows of $\widetilde{D}^{(x)}C_x^{\dagger}$, which is a block row of the density matrix corresponding to the fragment part of the impurity x. Since the fragments collectively form a non-overlapping partitioning of the global system, the global 1-RDM can be formed as

$$D^{\mathrm{HL}} = \begin{bmatrix} D^{(1)} \\ D^{(2)} \\ \vdots \\ D^{(N_f)} \end{bmatrix}. \tag{3.6}$$

Fig. 3.1 illustrates the procedure of constructing D^{HL} for a one-dimensional model with 12 sites partitioned into 6 fragments.

Since each block row of D^{HL} is obtained from the corresponding impurity problem independently, in general D^{HL} is not a Hermitian matrix. Therefore, after Eq. (3.6), we symmetrize the 1-RDM as

$$D^{\mathrm{HL}} \leftarrow \frac{D^{\mathrm{HL}} + (D^{\mathrm{HL}})^{\dagger}}{2}. \tag{3.7}$$

This symmetrization procedure corresponds to the choice of "democratic partitioning" for constructing the 1-RDM (and its contribution to the total energy) in DMET [35]. In general, D^{HL} will not be an idempotent matrix. Hence there is a non-zero discrepancy between D^{HL} and D^{LL}.

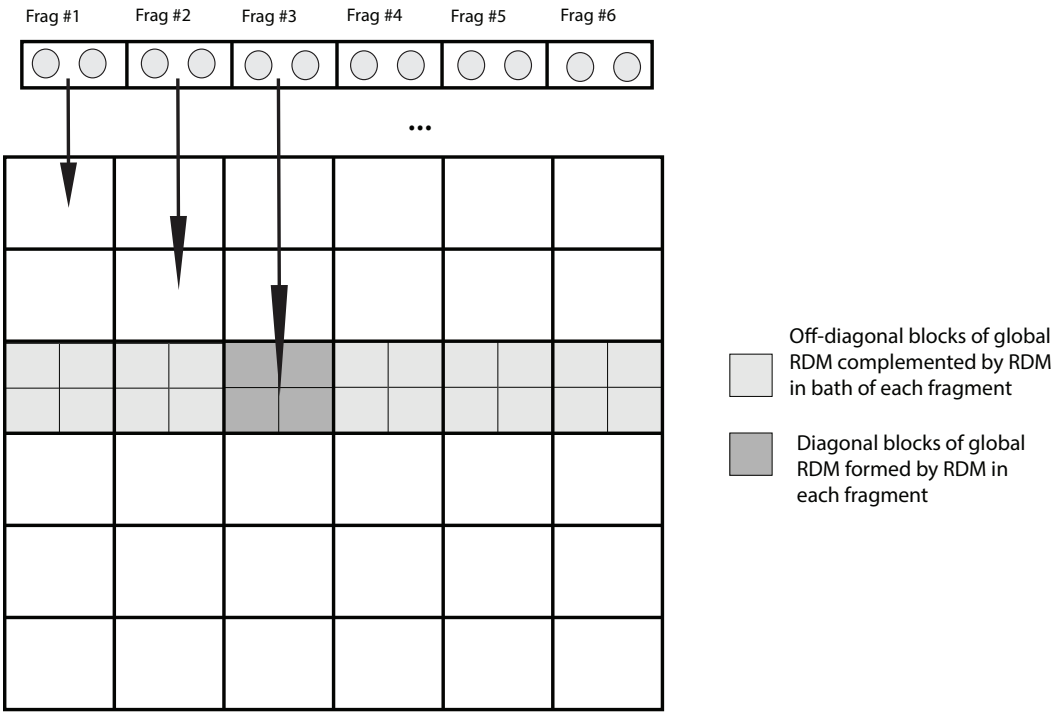

Figure 3.1: Construction of global density matrix. Each fragment contributes a rectangular block row of the global density matrix. Each block row has the same length as the global density matrix.

In order to solve the fixed point problem Eq. (3.1) in p-DMET, an extrapolation, or mixing scheme is usually beneficial to accelerate the convergence. In p-DMET we choose D^{HL} as the mixing variable. Let $D^{\mathrm{HL},(k)}$ be the correlated 1-RDM at the beginning of the k-th iteration. Then we first compute the low-level density matrix $\overline{D}^{\mathrm{LL}} = \mathcal{F}\left[D^{\mathrm{HL},(k)}\right]$ through the projection Eq. (3.4), construct the corresponding bath orbitals, and solve the impurity problem. From this we obtain an output correlated density matrix $\overline{D}^{\mathrm{HL}} := \mathcal{D}[\overline{D}^{\mathrm{LL}}]$. Define the residual as

$$R^{(k)} := D^{\mathrm{HL},(k)} - \overline{D}^{\mathrm{HL}}. \tag{3.8}$$

The simplest scheme to obtain $D^{\mathrm{HL},(k+1)}$ is the simple mixing

$$D^{\mathrm{HL},(k+1)} = D^{\mathrm{HL},(k)} - \alpha R^{(k)}. \tag{3.9}$$

Here $0 < \alpha \leqslant 1$ is a mixing parameter. The simple mixing method usually converges when α is set to be sufficiently small, but the convergence rate can be very slow. In order to accelerate the convergence, we can use the direct inversion in the iterative subspace (DIIS) method [130]. In DIIS, $D^{\mathrm{HL},(k+1)}$ is obtained by extrapolating the

1-RDM's from the previous $\ell + 1$ steps as

$$D^{\mathrm{HL},(k+1)} = \sum_{j=k-\ell}^{k} \alpha_j D^{\mathrm{HL},(j)}. \tag{3.10}$$

In order to obtain the mixing coefficient $\{\alpha_j\}_{j=k-\ell}^{k}$, we also record the residual $\{R^{(j)}\}_{j=k-\ell}^{k}$ as in Eq. (3.8), and solve the following minimization problem

$$\{\alpha_j\} = \underset{\{\alpha_j\}}{\arg\min} \left\| \sum_{j=k-\ell}^{k} \alpha_j R^{(j)} \right\|_F, \text{ s.t. } \sum_{j=k-\ell}^{k} \alpha_j = 1. \tag{3.11}$$

A pseudocode implementation for the p-DMET and DMET algorithm is provided in Algorithm 1.

Algorithm 1 A unified pseudocode for the projected density matrix embedding theory (p-DMET) and density matrix embedding theory (DMET).

Input: Initial guess of the correlated 1-RDM $D^{\mathrm{HL},(0)}$ and chemical potential $\mu^{(0)}$.
Output: Converged correlated 1-RDM D^{HL} and ground state energy E.

for $k = 0, \ldots,$ **do**
  for $\mu = \mu^{(k)}, \ldots,$ **do**
    for each impurity x **do**
      Compute fragment orbitals (C_f), and bath orbitals (C_b)
      Formulate the impurity Hamiltonian, $\hat{H}^{(x)}_{\mathrm{emb}}$ ▷ Eq. (2.12) and (2.13)
      Solve the impurity problem with μ ▷ via solvers such as FCI or DMRG
    end for
    Compute the total number of electrons, $\mathrm{tr}\left(D^{\mathrm{HL}}\right)$
    if convergence is not reached, update μ by Newton's iterations
  end for
  $\mu^{(k+1)} \leftarrow \mu$
  Construct the correlated 1-RDM $\overline{D}^{\mathrm{HL}}$ ▷ Eq. (3.6) followed by symmetrization
  Compute energy $E^{(k)}$ from $\overline{D}^{\mathrm{HL}}$ as well as the related 2-RDM ▷ Eq. (2.58)
  If convergence is reached, exit the loop
  if embedding method is p-DMET **then**
    Perform mixing scheme to obtain $D^{\mathrm{HL},(k+1)}$
    Compute low-level density matrix D^{LL} ▷ Eq. (3.4)
  else if embedding method is DMET **then**
    Solve the minimization problem ▷ Eq. (2.15)
    Perform mixing scheme to obtain a new correlation potential $u^{(k+1)}$
  end if
end for
Set $D^{\mathrm{HL}} \leftarrow D^{\mathrm{HL},(k)}$, $E \leftarrow E^{(k)}$

In principle, one could also choose the mean field density matrix D^{LL} as the mixing variable. However, there arises a practical question related to this choice, namely

that the linear combination of a few (or even two) idempotent matrices is generally not an idempotent matrix. Note that the same problem already arises in the context of HF calculations. Some of us have recently developed the projected commutator DIIS (PC-DIIS) method [137], which accelerates HF calculations within a large basis set (such as planewaves). The idea of PC-DIIS is to apply the idempotent density matrix D^{LL} to a gauge-fixing matrix Φ^{ref} as $\Phi = D^{\mathrm{LL}}\Phi^{\mathrm{ref}}$. It is clear that the information in D^{LL} and Φ is equivalent. In particular, D^{LL} can be reconstructed from Φ (Löwdin orthogonalization) as

$$D^{\mathrm{LL}} = \Phi(\Phi^\dagger\Phi)^{-1}\Phi^\dagger. \tag{3.12}$$

Thus PC-DIIS uses Φ as the mixing variable, and reconstructs the idempotent density matrix using Eq. (3.12).

Following the PC-DIIS method, we can then choose Φ as the mixing variable in the self-consistent p-DMET. The gauge-fixing matrix Φ^{ref} can be chosen to be, for instance, the HF occupied orbital coefficient matrix. We refer to this method as the projected density matrix embedding theory with a fixed gauge (p-DMET-f). Note that from the perspective of Eq. (3.1), p-DMET-f solves the same fixed point problem as p-DMET. The only difference is the choice of the mixing variable.

For translational invariant systems, note that D^{hl} constructed from democratic partitioning does not break the translational symmetry among fragments. Therefore, the D^{hl} can be represented in $\mathbf{k}$-space, denoted by $D^{\mathrm{hl}}(\mathbf{k})$. The corresponding $\Psi^{\mathrm{ll}}(\mathbf{k})$ is generated per $\mathbf{k}$ sector. The extrapolation over $D^{\mathrm{hl}}(\mathbf{k})$ also conserves the crystal momentum $\mathbf{k}$. Finally, we note that p-DMET-f can be formulated in a similar way by introducing a gauge-fixing matrix per $\mathbf{k}$ sector.

3.3 Numerical experiments

In this section, we investigate the performance of p-DMET and p-DMET-f for a 2D Hubbard model with periodic boundary conditions. The mean-field theory is chosen to be the unrestricted HF (UHF) theory, and the impurity Hamiltonian in DMET and p-DMET is defined within the interacting bath formulation. The impurity ground-states were computed using the FCI method implemented in the PySCF [138] package and the density matrix renormalization group (DMRG) method [121, 122], as implemented in the BLOCK program [125, 139–141], using a bond dimension of $M = 1000$, the split-localized orbital strategy described in [32], and the genetic algorithm for orbital ordering [127]. The fragments were chosen to be 2×2 clusters, treated without translational invariance, to allow a comparison between p-DMET

and DMET in a general setting, except in the case of the cluster size convergence tests, where fragments of up to 4×4 (16 sites) were used, and translational invariance was assumed. We used a convergence criterion on the energy difference between two consecutive iterations of less than 10^{-8} for the 2×2 clusters and 10^{-5} for the larger clusters. All energies are reported in units of hopping (t).

Accuracy

To investigate the accuracy of p-DMET, we plot the phase diagram of a 2D Hubbard model with 40×40 sites with periodic boundary conditions. This system has been studied in [32] using a translationally-invariant implementation of DMET. The initial 1-RDM is produced by a converged UHF calculation. Fig. 3.2 compares the phase diagrams generated by UHF, DMET, and p-DMET respectively, evaluated on a 21×21 grid with respect to the on-site interaction strength U, as well as the filling factor n.

The phase diagram is divided into two regions distinguished by their spin polarization, i.e. the anti-ferromagnetic (AFM) phase and the paramagnetic (PM) phase. The phase diagrams obtained from p-DMET and DMET are qualitatively similar. The two diagrams agree well with each other when $U \leqslant 4.0$, and larger discrepancies between p-DMET and DMET are observed in the region $U > 4.0$ and $0.6 \leqslant n \leqslant 0.8$. We also observe that the phase boundary obtained from p-DMET is slightly softer, i.e. the decay of the spin polarization from the AFM phase to the PM phase is slower than that in DMET.

A quantitative comparison of the total energy per site can be found in Table 3.1. Overall, the discrepancy between p-DMET and DMET is much smaller than that between UHF and DMET. The energies of p-DMET and DMET agree very well (the difference is less than 10^{-3}) inside the AFM / PM phases. The largest discrepancy occurs at $U = 6.0, n = 0.750$, again near the phase boundary, where the difference of the energy is 0.022. We remark that neither p-DMET nor DMET is variational, so we cannot determine from this single calculation which is better.

Convergence

We observe in Fig. 3.2 that the softer phase boundary in p-DMET coincides with the region where UHF and DMET predict different phases. Since the UHF solution only enters p-DMET as an initial guess, we may wonder whether the fixed-point of p-DMET depends on the initial guess. Below we demonstrate that the converged p-DMET/p-DMET-f solution can indeed depend on the initial guess, at least in certain

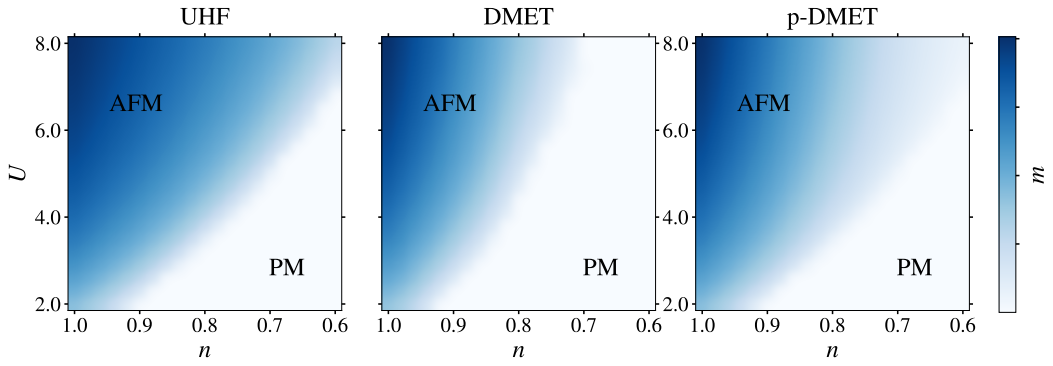

Figure 3.2: Phase diagrams of the 2D Hubbard model from UHF, DMET and p-DMET. The color represents the spin polarization ($m = \frac{1}{2}|n_\uparrow - n_\downarrow|$), where $n_\uparrow$ and $n_\downarrow$ are spin up and spin down densities respectively.

Table 3.1: Energy per site of the 2D Hubbard model by UHF, p-DMET and DMET as a function of U and doping (n). The self-consistent p-DMET and DMET calculations use the converged UHF solution as the initial guess.

	$n = 1.000$			$n = 0.875$			$n = 0.750$		
U	UHF	p-DMET	DMET	UHF	p-DMET	DMET	UHF	p-DMET	DMET
2.0	-1.13886	-1.17999	-1.17985	-1.22470	-1.27817	-1.27799	-1.27655	-1.32270	-1.32275
4.0	-0.79703	-0.86792	-0.86856	-0.88440	-1.03002	-1.03450	-0.99530	-1.16862	-1.16707
6.0	-0.59270	-0.66099	-0.66188	-0.66592	-0.87265	-0.87395	-0.75936	-1.04709	-1.06860
8.0	-0.46588	-0.52262	-0.52393	-0.52665	-0.77299	-0.77149	-0.60439	-0.97734	-0.98954

parts of the phase diagram. We consider a 2D Hubbard system with 6×6 sites with periodic boundary conditions. The onsite interaction U is set to 4.0, and we consider two fillings: $n = 1.0$ (half filling, $N_e = 36$), and $n = 0.722$ ($N_e = 26$). In both cases, the energy gap at the mean-field level is positive, and the self-consistent procedure for all methods are well defined without any finite temperature smearing.

In the first example ($n = 1.0$), DMET suggests that at convergence the system is in the AFM phase. Therefore, we start from the PM phase, and break the spin symmetry of the initial density by alternately adding/subtracting a small number (10^{-3}) on odd/even sites to create slightly polarized spin-up and spin-down densities. Starting from this initial density, UHF converges within 20 steps using DIIS. We input the initial 1-RDM for p-DMET/p-DMET-f after performing 1, 5, 10, 20 UHF iterations, respectively. For p-DMET-f, the gauge-fixing matrix is also obtained from the same 1-RDM. The convergence of the energies is reported in Fig. 3.3. We find that the convergence curves of p-DMET and p-DMET-f are very similar and almost coincide with each other in all cases. Both the converged energy and the spin polarization from p-DMET/p-DMET-f depend on the initial guess of the 1-RDM. Table 3.2 suggests that at convergence, UHF predicts an over-polarized spin configuration. However,

starting from a significantly under-polarized 1-RDM obtained from one iteration of UHF, the converged solution of p-DMET underestimates the spin polarization (by 0.022 relative to the converged DMET result). With initial guesses obtained from an increased number of UHF iterations, both the energy and spin polarization obtained from p-DMET approach the results from DMET. After 5-steps of UHF for the initial guess, p-DMET provides converged results in terms of energy and spin polarization. Remarkably, the solution of DMET is very robust with respect to the choice of the initial guess, even though neither DMET nor p-DMET/p-DMET-f guarantees a unique solution to the nonlinear fixed point problem *a priori*.

Table 3.2: Spin polarization for the 6×6 Hubbard model at $U = 4.0$, $n = 1.0$ obtained from converged UHF, DMET and p-DMET calculations. #UHF stands for the number of UHF steps to obtain the initial 1-RDM for the DMET calculation.

	initial	UHF	DMET (#UHF=1)	DMET (#UHF=5)	DMET (#UHF=20)
m	0.001	0.34876	0.30812	0.30812	0.30812
			p-DMET (#UHF=1)	p-DMET (#UHF=5)	p-DMET (#UHF=20)
m			0.28578	0.30851	0.31000

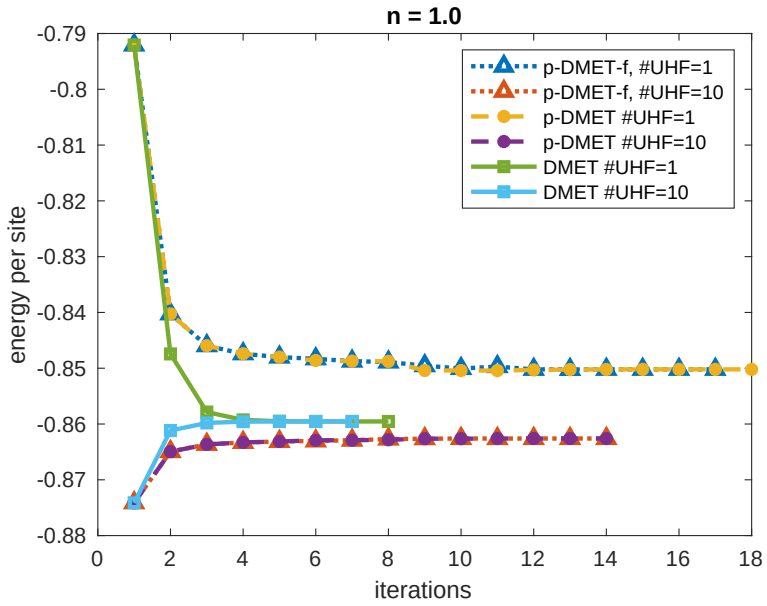

Figure 3.3: The convergence of the energy per site for p-DMET-f, p-DMET and DMET with different initial guesses. The system is a 6×6 Hubbard model at $U = 4.0, n = 1.0$.

In the second example, we set $n = 0.722$ ($N_e = 26$). We start from an initial

guess that exhibits AFM order, where the spin up component of the density is set to be 0.1444 and 0.5778 on alternate sites, and the spin down component is arranged alternately in the opposite way with the same values. The convergence of the energy (Fig. 3.4) is similar to that in the case of half-filling. For a spin-polarized initial 1-RDM obtained from one step of the UHF iteration, the converged solution of p-DMET remembers the initial guess and predicts an AFM phase with a small spin-polarization 0.04. Both the energy and spin polarization improve quickly as the number of UHF iterations used to define the initial guess increases. Eventually p-DMET also predicts a PM phase. Again, no initial guess dependence is observed in DMET.

Table 3.3: Spin polarization for the 6×6 Hubbard model at $U = 4.0$, $n = 0.278$ obtained from converged UHF, DMET and p-DMET calculations. #UHF stands for the number of UHF steps used to obtain the initial 1-RDM for the DMET and p-DMET calculations.

	initial	UHF	DMET (#UHF=1)	DMET (#UHF=5)	DMET (#UHF=20)
m	0.2167	2.166×10^{-11}	4.961×10^{-8}	1.365×10^{-7}	5.440×10^{-8}
			p-DMET (#UHF=1)	p-DMET (#UHF=5)	p-DMET (#UHF=20)
m			4.175×10^{-2}	2.719×10^{-2}	4.865×10^{-9}

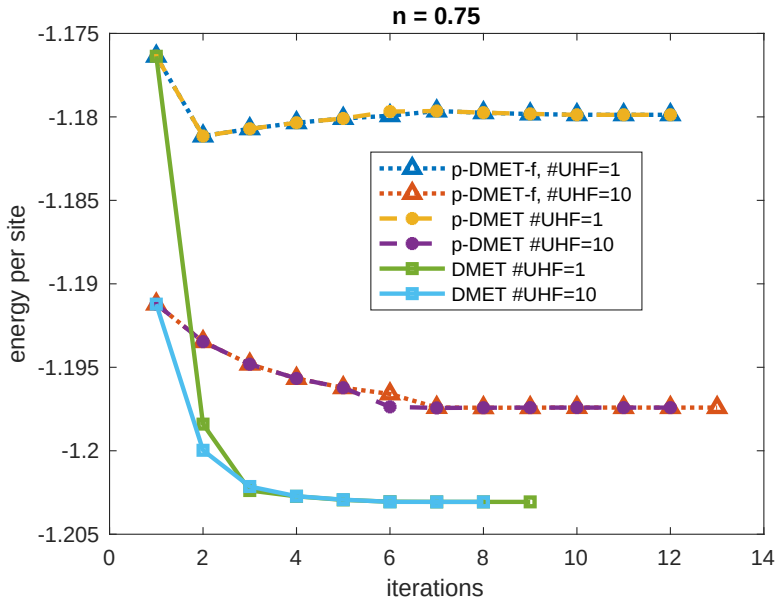

Figure 3.4: The convergence of the energy per site for p-DMET-f, p-DMET, and DMET with different initial guesses. 6×6 Hubbard model at $U = 4.0$, $n = 0.722$.

In both examples above, UHF and DMET predict the same phase of matter. We find that self-consistent p-DMET can significantly reduce the error of physical observables starting from converged or unconverged UHF solutions, but there is some initial guess dependence. Therefore, when UHF and DMET predict different phases, p-DMET can reduce but not eliminate the (presumed) error from UHF. Hence the phase diagram in Fig. 3.2 is similar to that of DMET, but softer near the boundary region.

Effect of fragment size

To understand the fragment size dependence of the physical observables in DMET and p-DMET, we carried out a number of 2D Hubbard model calculations (of 40×40 sites) at half-filling for different interaction strengths ($U = 2$, 4, 6 and 8) and with different fragment sizes (2×2, 2×4 and 4×4) using translational invariance. The same cluster sizes were previously considered in Ref. [32] where translationally invariant DMET is in the non-interacting bath (NIB) formulation only. We use the data from Ref. [32] as reference. DMET in the interacting bath formulation, as used everywhere else in this work, is here denoted DMET (IB). Given a set of 2D clusters with L_A sites, the DMET energy can be extrapolated to the thermodynamic limit (TDL) as a power series in $L_A^{-\frac{1}{2}}$ [33],

$$E(L) = E(\infty) + a_0 L_A^{-\frac{1}{2}} + b_0\left(L_A^{-\frac{1}{2}}\right)^2 + \ldots \tag{3.13}$$

We use the average of linear regression and a quadratic fit as the extrapolated result, and the error bar is defined to be the difference of the two fits.

Fig. 3.5 presents the calculated energy of three methods (p-DMET, DMET (IB), and DMET (NIB)) and the corresponding extrapolations. All three methods give reasonable extrapolated energy values, compared to the benchmark data (grey shaded region). For p-DMET, the largest error is about 5×10^{-3} at $U = 8$, while for DMET (IB), the largest error is about 3×10^{-3} at $U = 4$. The behavior of DMET and p-DMET as a function of $L_A^{-\frac{1}{2}}$ is relatively similar, while that of DMET (NIB) is quite different. This reflects the energy influence of the different choice of impurity Hamiltonian. In fact, extrapolations using DMET (NIB) have smaller error bars in general, and they are slightly more accurate than those of DMET (IB) and p-DMET. The results also indicate that after extrapolation, the performance of DMET and p-DMET is comparable reliable.

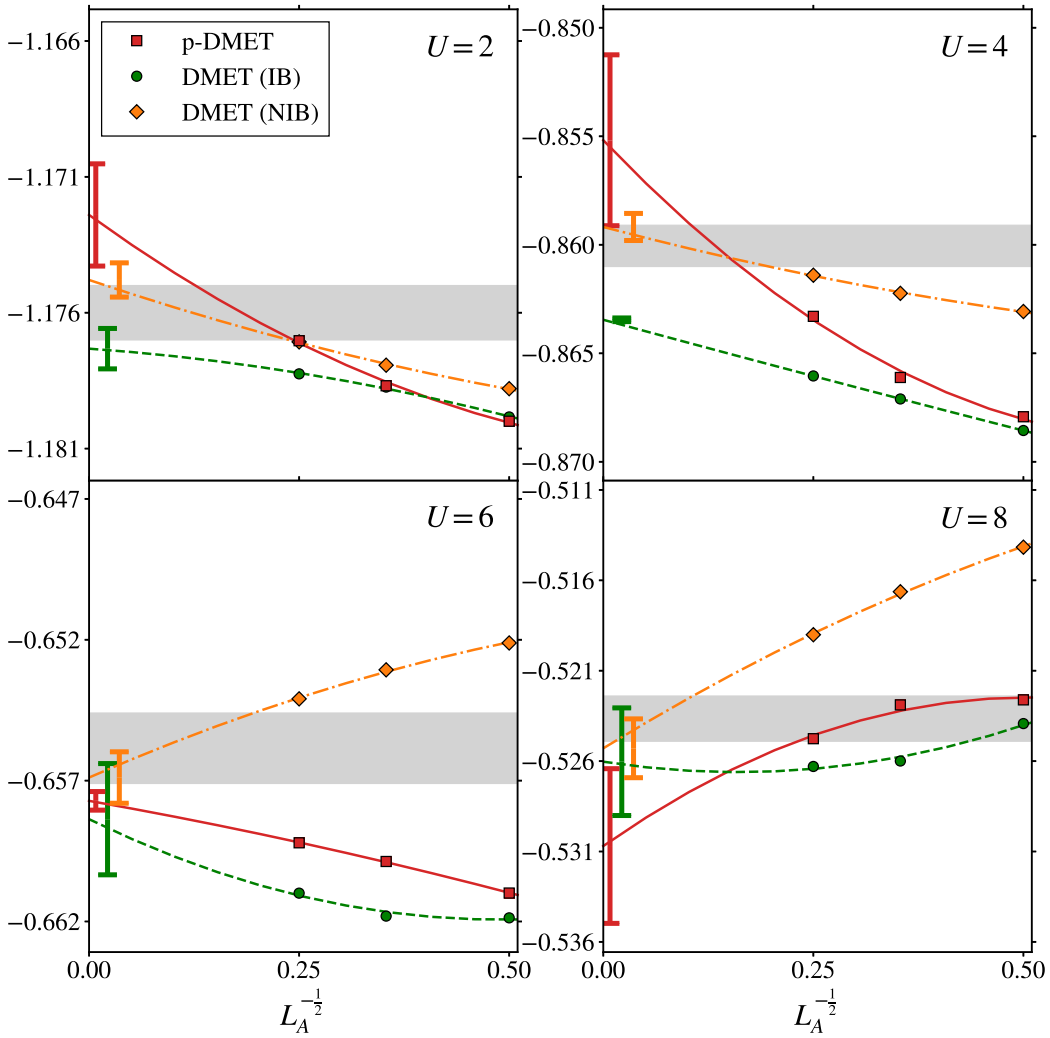

Figure 3.5: Energy extrapolation as a function of cluster size L_A for p-DMET, DMET(IB) and DMET(NIB), where IB and NIB denote the interacting- and non-interacting bath formulations respectively. The fitting curve is an average of linear regression and quadratic fitting. The error bar is chosen to be the difference between the linear and quadratic extrapolated values. The shaded area is generated from the AFQMC, DMRG, DMET and DCA-DMET benchmark numbers in Ref. [142] and Ref. [33].

Efficiency

To demonstrate the efficiency of p-DMET and p-DMET-f, we analyze two factors that affect the overall computational cost, i.e. the total number of iterations for self-consistent convergence and the (average) time cost per iteration.

We first consider the number of iterations required for convergence. We extracted the number of iterations from the calculations for the preceding phase diagram (Fig. 3.2) and plot the distribution of the number of iterations in Fig. 3.6. As shown in the figure, all three methods (p-DMET, p-DMET-f and DMET) a similar average convergence rate, with an average iteration number of 12 required to achieve an energy accuracy of 10^{-6}. In most cases, the iteration number is less than 20. We also remark that at least for systems studied in this work, the distribution in the case of p-DMET is slightly narrower with fewer outliers, and hence the self-consistent iteration is more stable.

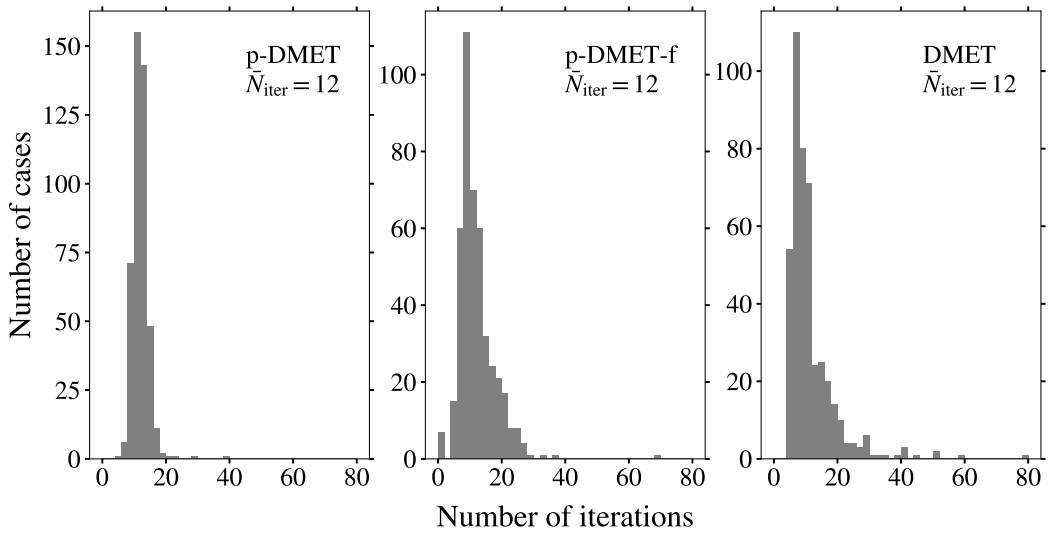

Figure 3.6: Distribution of the number of self-consistent iterations of p-DMET, p-DMET-f and DMET required to reach 10^{-6} in the energy across the phase diagram in Fig. 3.2. All calculations used DIIS.

Acquiring the similar average number of self-consistent iterations in p-DMET and DMET, we now discuss the total computational time. We performed a series of tests on lattices of size $2 \times N$ (N is the number of sites in the y direction ranging from 8 to 64). We set $U = 2.0$ and $n = 1.0$ (half filling). We chose this quasi one-dimensional structure to ensure that the mean-field problem always has a positive energy gap, which is not the case for arbitrary 2D lattices. All the tests are performed on 36 Intel Broadwell vCPUs of the Google Cloud Platform (GCP).

We measured the CPU time of DMET, p-DMET and p-DMET-f spent on single-particle type computations and to solve the impurity problems (many-body computations). When the fragment size is fixed, the cost to construct and solve the impurity problems (high-level computations) always scales linearly with respect to the global system size. In DMET, the single-particle type computations (low-level computations) include the diagonalization of the mean-field Hamiltonian, and optimization of the correlation potential; in p-DMET, the cost of the single-particle computations is mainly due to the diagonalization to obtain the projected 1-RDM.

In DMET, the single-particle computational cost significantly increases with N (Fig. 3.7). In each step of DMET, the correlation potential optimization typically requires more than 100 iterations to converge, and the number of iterations also grows with respect to the system size. When the system becomes moderately large (number of sites larger than 64), the cost at the mean-field level is much more expensive than solving the 2×2 impurity problems. When the number of sites is 128, the single particle computations in DMET take in total $\sim$ 20000 s. On the other hand, the main single-particle cost in p-DMET is only the eigenvalue decomposition to obtain D^{LL}. Similarly, p-DMET-f only needs to perform single-particle type matrix multiplications and inversions. For the system with 128 sites, the computational cost at the mean-field level of p-DMET is reduced to only $\sim$ 1 s. This demonstrates that p-DMET/p-DMET-f provide a significant reduction in computational cost relative to DMET for large, heterogeneous, systems.

3.4 Conclusions

An important computational bottleneck in DMET calculations for large systems is the correlation potential optimization required to achieve self-consistency. In this optimization, each evaluation of the cost function requires the diagonalization of a mean-field Hamiltonian, and each derivative evaluation amounts to a response calculation. Thus, for a moderately sized system, the correlation potential optimization procedure can be expensive. In this work, we viewed the self-consistent DMET as only one formulation of a more general fixed point problem to obtain the high-level global density matrix D^{HL}. From this general perspective, we proposed the projected density matrix embedding method (p-DMET) as a simpler and more efficient way to achieve self-consistency. We found that for the 2D Hubbard model, compared to the unrestricted HF (UHF) solution, p-DMET significantly improved the accuracy of the total energy and behaviour of the spin polarization across the entire parameter space. The phase diagrams predicted by p-DMET and DMET qual-

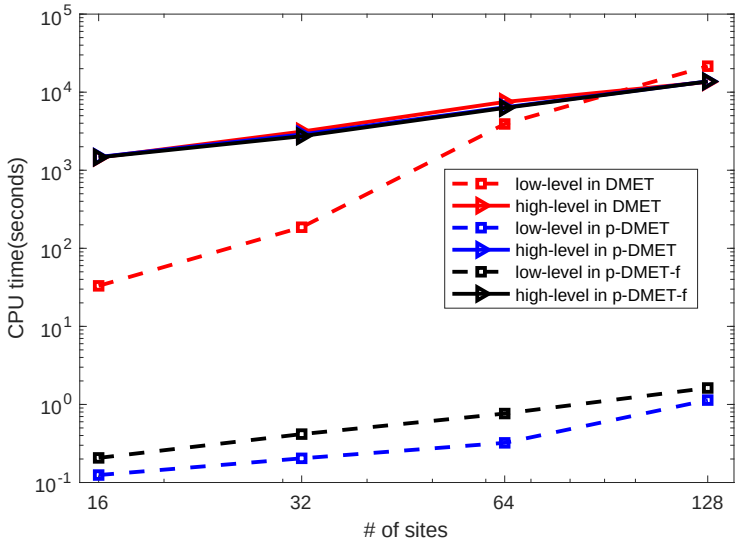

Figure 3.7: CPU time in DMET, p-DMET and p-DMET-f associated with (i) low-level density matrix computations (ii) high-level impurity problem computations.

itatively agreed with each other, but the phase boundary obtained from p-DMET was softer. Further investigation showed that this was because the self-consistent solution of p-DMET retained a weak dependence on the initial guess. On the other hand, the cost associated with achieving self-consistency in p-DMET was negligible compared to that needed to optimize the correlation potential in DMET.

There are a number of directions that should now be pursued. First, we would like to identify the root of the initial guess dependency of p-DMET. Second, we plan to generalize p-DMET to superconducting systems, where the low-level theory requires the solution of the Bogoliubov-de Gennes (BdG) equations. Third, a remaining numerical issue in DMET associated with self-consistency is the appearance of vanishing gaps in the DMET mean-field Hamiltonian during the optimization. This should then be treated using a zero temperature limit of a finite temperature formulation of DMET.

Chapter 4

PHASE DIAGRAM OF THREE-BAND HUBBARD MODEL FROM DENSITY MATRIX EMBEDDING THEORY

Based on the work published in *Phys. Rev. Research* **2**, 043259 (2020). Copyright 2020, American Physical Society. [99]

4.1 Introduction

The three-band Hubbard model, also known as the Emery model [21], is generally believed to contain the essential physics of the high-T_c cuprates that arises from the interplay between the copper $d_{x^2-y^2}$ and oxygen $p_{x(y)}$ orbitals in the CuO_2 layers. Given the complexity of the model, commonly, the three-band model is further simplified and several simpler low-energy Hamiltonians have been proposed, such as the one-band Hubbard model [22, 23], t-J model [23, 143], and two-band model [144]. The first two are effective one-band models and are equivalent in the strong-coupling limit. In particular, the two-dimensional (2D) one-band Hubbard model has been extensively investigated using various numerical approaches (see Refs. [24, 142] and the references therein). Much of the physics seen in high-T_c materials, e.g. d-wave pairing, density waves, the pseudogap phase and stripe order, has been observed in studies of the simpler one-band Hubbard model within certain ranges of parameters [24].

However, despite the progress in understanding the one-band Hubbard model and its variants, there are still important reasons to go beyond the one-band picture to study the original three-band model directly. For instance, (a) some important physics may be lost in the reduction to the one-band approximation (such as a role for the oxygen degrees of freedom in the pseudogap phase [7]), (b) near degeneracies of competing states seen in the one-band case [24] may in fact be resolved with the additional degrees of freedom of the three-band model, and (c) the three-band model retains the atomic structure of the CuO_2 layer and thus has a direct link to the structure of real materials as well as experimental measurements of orders at the atomic scale. Previously, the three-band Hubbard model has been investigated with several numerical methods, including direct simulations of finite lattices (by exact diagonalization (ED) [145–151], quantum Monte Carlo (QMC) [25, 151–158],

density matrix renormalization group (DMRG) [25, 159–161], and the random phase approximation [162–164]) and via Green's function based embedding theories (such as dynamical mean-field theory (DMFT) and its cluster extensions [165–170], and the variational cluster approximation (VCA) [171, 172]). However, due to the complexity of the model, unlike in the one-band case, a consensus on much of the physics has yet to be reached.

In earlier work, DMET successfully provided an accurate description of the ground-state orders of the one-band Hubbard model [32], including in the difficult underdoped region [24]. In this chapter, we therefore attempt to understand the more complicated three-band Hubbard model using DMET. As we shall see, we can use DMET to provide a detailed description of the ground-state phases and orders as a function of doping, including the doping asymmetry and atomic-scale orders that are new to the three-band case. Another complication of the three-band model is the much larger parameter space than the one-band case. We use both existing parametrizations that have been published in the literature, as well as explicitly model the influence of different individual parameters on the orders. Our findings provide insights into the detailed picture of magnetic and superconducting orders that is provided by three-band models.

4.2 Models and methods

Model parametrization

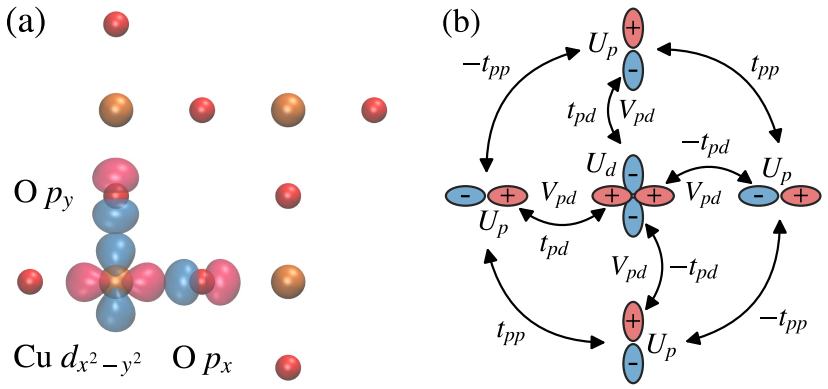

Figure 4.1: An illustration of the three-band Hubbard model: (a) the symmetric cluster used in the DMET calculations, where the orange and red atoms denote copper and oxygen respectively; (b) definition of the model parameters and the phase convention.

As a minimal atomic model of the CuO_2 layer in cuprates, the three-band model

describes the on-site and nearest-neighbor interactions among the Cu $d_{x^2-y^2}$ and O p_x, p_y orbitals [see Fig. 4.1(a)]. In the hole representation, the Hamiltonian reads,

$$\begin{aligned}\mathcal{H} = & t_{pd} \sum_{\langle ij\rangle\sigma} \left(d^\dagger_{i\sigma} p_{j\sigma} + \text{H.c.} \right) + t_{pp} \sum_{\langle jj'\rangle\sigma} \left(p^\dagger_{j\sigma} p_{j'\sigma} + \text{H.c.} \right) \\ & - \Delta_{pd} \sum_{i\sigma} n^d_{i\sigma} + U_d \sum_i n^d_{i\alpha} n^d_{i\beta} + U_p \sum_j n^p_{j\alpha} n^p_{j\beta} \\ & + V_{pd} \sum_{\langle ij\rangle\sigma\sigma'} n^d_{i\sigma} n^p_{j\sigma'},\end{aligned} \tag{4.1}$$

where $\langle \cdots \rangle$ denotes nearest neighbors, $d^{(\dagger)}_{i\sigma}$ and $p^{(\dagger)}_{j\sigma}$ destroy (create) a hole with spin σ ($\in \{\alpha, \beta\}$) on the Cu d and O p orbitals respectively, $n^d_{i\sigma}$ and $n^p_{j\sigma}$ are the corresponding hole particle-number operators, and the charge transfer gap Δ_{pd} is defined as the orbital energy difference, $\epsilon_p - \epsilon_d$. Similarly to in the one-band Hubbard model, the hopping term and on-site Coulomb repulsion will be denoted t and U, and the Coulomb interaction between nearest-neighbor p, d orbitals will be denoted V_{pd}. Note that the hopping term involves a phase factor (± 1) introduced by the choice of orbital orientation in the basis as shown in Fig. 4.1(b).

There has been much work to determine the parameters of the three-band model; however, a consensus set does not exist [167, 173–176]. There has been particular debate about the size of the charge transfer gap Δ_{pd} [167, 177].

Table 4.1: Parameters of the three-band Hubbard model used in this work, in units of eV. The parameters correspond to the hole representation.

Model	t_{pd}	Δ_{pd}	U_d	t_{pp}	U_p	V_{pd}
Hybertsen[a]	1.3	3.6	10.5			
Martin[b]	1.8	5.4	16.5			
Hanke[c]	1.5	4.5	12.0			
Hanke full[c]	1.5	4.5	12.0	0.75	5.25	0.75

[a] From Ref. [173]. [b] From Ref. [175]. [c] From Ref. [172].

In this work, we consider four sets of published model parameters, see Table 4.1, as well as the sensitivity of orders to changing these parameters. Note that all parameter sets are given in eV, thus all energies in this work are reported in units of eV unless otherwise specified. The first three sets include only the most essential terms, i.e., t_{pd}, U_d and Δ_{pd}, and thus we refer to them as *minimal* parametrizations. When normalized to units of t_{pd}, the other parameters vary within a range of 10%. The fourth set involves all terms in Eq. (4.1). We refer to this as a *full* parametrization. In

the hole representation, the minimal parametrization is equivalent to the full model with t_{pp}, U_p and V_{pd} set to zero.

Computational details

Framework

In this work, we are interested in both magnetic and superconducting phases. Consequently, the correlation potential takes the form

$$u = \sum_{ij\sigma} v_{ij}^{\sigma} a_{i\sigma}^{\dagger} a_{j\sigma} + \sum_{ij} \Delta_{ij}^{\alpha\beta} a_{i\alpha}^{\dagger} a_{j\beta}^{\dagger} + \text{H.c.}, \tag{4.2}$$

where optimizing over v^{σ} and $\Delta^{\alpha\beta}$ in the self-consistency procedure allows for formation of spin polarized and singlet superconducting pairing (between two spin channels α and β) order in the lattice and impurity problems. The non-interacting lattice Hamiltonian is then of Bogoliubov-de Gennes form [178]. The corresponding ground-state solution is a mean-field Bardeen-Cooper-Schrieffer (BCS) wavefunction, and a set of bath orbitals that describes the environment can be constructed from the corresponding generalized density matrix in Eq. (2.79). These routines have been implemented in LIBDMET [179, 180].

Impurity and lattice

We used a 2×2 impurity cluster of CuO_2 primitive cells [172] which retains the inversion and four-fold rotation symmetry of the lattice [see Fig 4.1(a)]. We embedded the cluster in a 20×20 unit-cell (40×40 site-length) lattice. We performed DMET calculations for dopings x ranging between -0.8 and 0.8 (negative denotes electron doping and positive denotes hole doping). Unless otherwise specified, we initialized u with an antiferromagnetic guess and a random pairing potential.

Impurity Hamiltonian and solver

The impurity model Hamiltonian was constructed using the non-interacting DMET bath formalism [30, 32], and the ground state was determined using a density matrix renormalization group (DMRG) solver [121, 122], allowing for particle number symmetry breaking and spin polarization [32]. During the DMET self-consistent cycle we used a maximum bond dimension $M = 800$. Subsequent bond dimension convergence checks were performed using (up to) $M = 2000$. To minimize entanglement and ensure a small bond dimension M in the ground state, we rotated the impurity Hamiltonian into a basis of split-localized molecular orbitals (MOs) obtained from the self-consistent Hartree-Fock-Bogoliubov (HFB) method,

where the occupied and virtual MOs were computed using the PySCF package [82, 138], and the occupied and virtual spaces were subsequently localized separately using the Edmiston-Ruedenberg procedure that maximizes the Coulomb energy of each orbital [85, 125]. The standard genetic algorithm implemented in the Block program [125, 139–141] was used to order the orbitals for the DMRG calculation. The tolerance of the DMRG sweep energy was set to 10^{-6}. Convergence checks on the accuracy of DMRG energies are described in Appendix E.1.

DMET self-consistency

We carried out DMET self-consistency using full impurity-bath fitting [32, 35], where the cost function measures the least-squares difference between the correlated one-particle density matrix γ^{corr} and the non-interacting lattice density matrix projected to the full impurity problem γ^{mf},

$$w(u) = \sum_{kl}^{\text{imp+bath}} \left[\gamma^{\text{mf}}_{kl}(u) - \gamma^{\text{corr}}_{kl}\right]^2. \tag{4.3}$$

We minimized w using a conjugate gradient (CG) minimizer with line search. Since the gap of the non-interacting lattice model is often small (in the case of doped systems), a finite inverse temperature $\beta = 1000\ t_{pd}$ was used to define the non-interacting density matrix to ensure smooth convergence (see Appendix D for further discussion and expressions for the analytic gradient of the cost function at finite temperature). We matched the particle number on the impurity sites and on the lattice exactly by separately fitting the chemical potential using quadratic interpolation [101]. Direct inversion in the iterative subspace (DIIS) [130, 181] was employed to accelerate the overall DMET convergence, using the difference of u between two adjacent iterations as the error vector. We chose the convergence threshold to be 10^{-4} in the correlation potential u (per site), which we observed to translate to an energy convergence per site of better than 10^{-4}. We further analyze the numerical convergence and error estimates for the DMET self-consistency in Appendix E.1.

4.3 The three-band phase diagram

Undoped state

Charge and magnetic moments

We present the order parameters for the undoped state from DMET and from reference calculations and experimental measurements in Table 4.2. As expected, the

Table 4.2: Charge, spin distribution (magnetic moments) and energy gap of the undoped three-band Hubbard model and reference data. Note that the experimental gaps reported are all optical gaps.

Model	ρ_{Cu}	ρ_{O}	m_{Cu}	m_{O}	E_{g} [eV]
Hybertsen	1.238	1.881	0.363	0.000	2.5
Martin	1.219	1.891	0.375	0.001	4.4
Hanke	1.220	1.890	0.373	0.000	3.9
Hanke full	1.358	1.821	0.279	0.002	2.2
Others	1.23[a]	1.89[a]	0.29[b], 0.31[c]		2.25[b],
Cuprate			0.3 ± 0.025[d]		1.5-2.0[e], 1.5-1.7[f]

[a] DMRG result from Ref. [161], using a similar model to Hanke full (with a different $U_p = 4.5$, $V_{pd} = 1.5$ and $V_{pp} = 1.125$).

[b] VCA result from Ref. [171], using basically the same model as Hanke full (with a different $U_p = 4.5$).

[c] VCA result from Ref. [172], using the same model as Hanke full.

[d] Experimental result for La_2CuO_4, from Ref. [182].

[e] Experimental result for La_2CuO_4, from Refs. [183–185].

[f] Experimental result for $YBa_2Cu_3O_6$, from Refs. [184, 186].

d orbitals are roughly half-filled and the p orbitals are roughly doubly occupied, with some charge transfer between the two due to hybridization. Comparing the full and minimal parametrizations, in the full parametrization, the Cu site is more strongly occupied by electrons, due to the t_{pp} term which smears out the oxygen charge and effectively transfers it to copper (while the effect of U_p is very small, see the discussion in Sec. 4.3). Unlike on the O site, the spin density on the Cu site is polarized, with a large local magnetic moment, which compares well to the experimental value 0.3 ± 0.025 μ_{B} (0.6 ± 0.05 μ_{B}) [182], as well as previously computed theoretical moments of 0.29 [171] and 0.31 [171] from VCA. In addition, the magnetic moment in the full parametrization is reduced relative to the minimal parametrizations, because the increased electron density on copper dilutes the polarized spin, while the additional holes on oxygen reduce the strength of the superexchange-based antiferromagnetic coupling. In fact, the local magnetic moments in the minimal models appear to be too large, while that of the full model is similar to experimental results. However, it is also known from one-band calculations, that the magnetic moments are overestimated in 2×2 DMET clusters relative to the thermodynamic limit (e.g., by about 25% at $U = 6$, see Fig. E.3 in Appendix E.2. Assuming similar finite size errors, then the minimal parametrization may provide

reasonable magnetic moments at half-filling in the thermodynamic limit (although this is not necessarily the case under doping, see below).

Band gap

As a simple estimate of the single-particle gap, we also computed the energy gap of the converged DMET non-interacting lattice Hamiltonian (DMET NI gap), i.e. $E_g = \varepsilon_{CBM} - \varepsilon_{VBM}$, where C(V)BM denotes conduction (valence) band minimum (maximum). Note that although the charge and spin densities in the different parametrizations are generally similar, the DMET NI gap varies more significantly, from 2.2 to 4.4 eV. The Hybertsen and Hanke parameter sets were derived from calculations on La_2CuO_4 (LCO), where the optical energy gap is variously reported as lying in the range 1.5 to 2.0 eV [183–185] (note that the optical gap is generally smaller than the fundamental gap). The estimated DMET NI gap of 2.5 and 2.2 eV for the Hybertsen and Hanke full parameter set respectively are thus in reasonable agreement with the experimental gap. However, the minimal Hanke parametrization seriously overestimates the gap. The Martin parameter set, obtained from calculations on finite-sized Cu-O clusters, are all systematically larger than in the other sets, and thus give the largest DMET NI gap. However, since the ratio of parameters in the Martin model remains similar to other parametrizations (and thus give rise to similar charge and spin distributions) this suggests that all energy parameters in the Martin model should simply be simultaneously rescaled downwards.

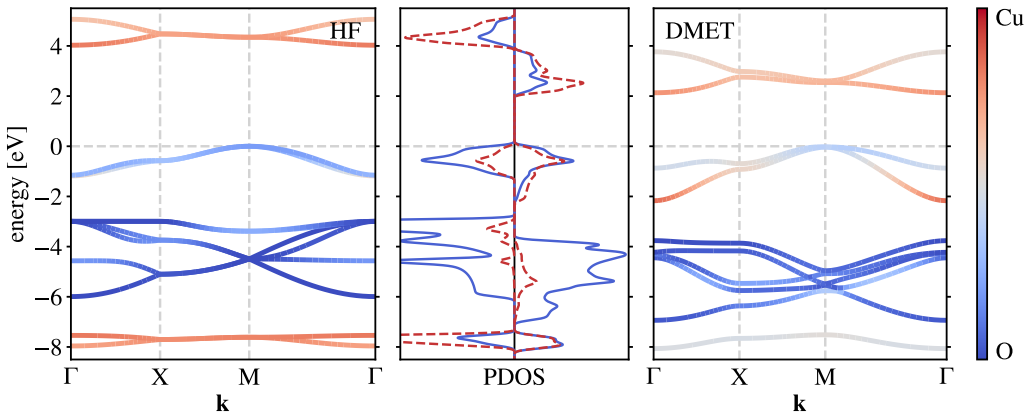

Figure 4.2: Orbital-projected electronic band structure and density of states (PDOS) of the undoped three-band Hubbard model with Hanke full parameters from HF (left) and DMET (right). The special **k** points [Γ: $(0,0)$, X: $(\pi,0)$, M: (π,π)] are in the first Brillouin zone of the 2×2 supercell lattice. The valence band maximum (VBM) is chosen as the energy zero.

Orbital resolved band structure

Unlike in the one-band Hubbard model, where the insulating gap arises between Hubbard bands, the gap in correlated insulators in the three-band model can arise from both Hubbard and charge-transfer mechanisms. In Fig. 4.2, we plot the projected electronic band structure and density of states from the DMET non-interacting lattice Hamiltonian, as converged for the fully parametrized Hanke model. The CBM is mainly of Cu d character (upper Hubbard band), while the VBM shows mixed character, dominated somewhat by O-p. The mixed orbital character of the valence bands around the Fermi level is consistent with the Zhang-Rice singlet (ZRS) hypothesis [143], in which hybridization between oxygen and copper orbitals induces superexchange that leads to singlets of O and Cu holes. Further support for the ZRS picture comes from the **k**-dependent orbital weights; that of Cu-d is greater at the Γ point, while that of O-p is larger at the M point, consistent with earlier model analysis of the ZRS state [187] and results from VCA [171]. In total, these observations indicate that the undoped three-band model ground state is a charge transfer insulator, with mainly a p-d type energy gap (see Ref. [5] for experimental evidence of the charge-transfer nature of the band gap). The strong **k**-dependent hybridization clearly poses challenges for numerical downfolding techniques to a one-band picture.

Comparing the DMET NI band structure to the Hartree-Fock mean-field description (also shown in Fig. 4.2), we find that the HF gap ($\approx$ 4 eV) is significantly overestimated, and the d-p hybridization is significantly weaker, resulting in a VBM with dominant oxygen p character and very narrow dispersion. Thus the reduced gap and d-p hybridization, both seen in experiment, are fluctuation driven phenomena, whose average effect is being captured by the DMET correlation potential u.

Doped states

Hole doped phases with standard parametrizations

More interesting ground states, including those with superconducting order, appear under doping. An important difference with the one-band case is the asymmetry of the three-band model under doping. We first focus on the orders that appear under hole-doping. Although our calculations are all at zero temperature, we can loosely identify the magnitude of the order parameters with transition temperatures in the phase diagram, thus allowing us to compare them to the experimental phase diagram. In Fig. 4.3, we plot the AFM and d-wave SC order parameters of the

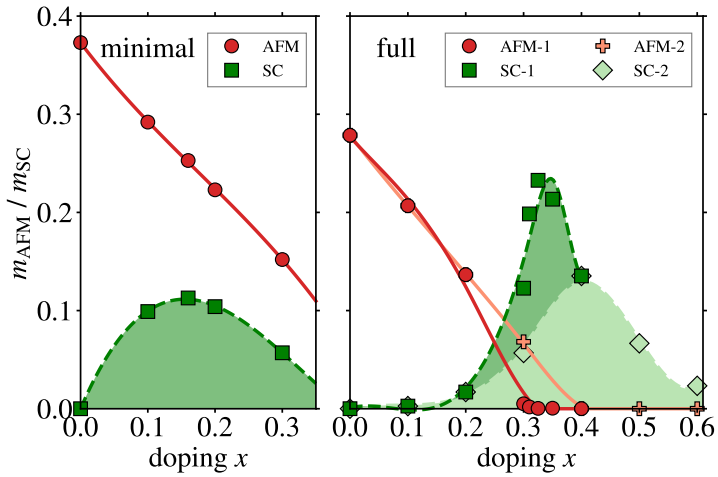

Figure 4.3: Antiferromagnetic and d-wave superconducting order parameters of the hole-doped three-band Hubbard model. The model settings are from the Hanke minimal (left) and Hanke full (right) parameter sets. Note that in the "Hanke full" case, we find two possible solutions between $x = 0.2$ and $x = 0.4$, marked as solution "1" (from a weakly polarized AFM guess) and "2" (from a strongly polarized AFM guess) in the figure. The curves are cubic-spline interpolated.

Hanke model as a function of hole doping (Hybertsen and Martin minimal model results are very similar to those of the Hanke minimal model, as shown in Fig. E.4. In the fully parametrized model, we find two different solutions of the DMET self-consistency, labelled solution 1 (obtained from a weakly spin polarized AFM guess) and solution 2 (obtained from a strongly polarized AFM guess).

For all parameter sets, we observe that the AFM order parameter decreases as doping increases, consistent with the general behavior of the cuprate phase diagram [5]. However, for the minimal models, the AFM order persists even up to large dopings (e.g. ≈ 0.15 at $x = 0.3$). In interpreting this discrepancy, one complication is that computation is measuring atomic scale local order, while experimental measurements are likely averages over various inhomogeneities (e.g. different orientations of stripes in different layers) which would typically lead to reduced moments. Leaving this aside, however, the overestimation of the computed moment could originate either from the remaining finite size error in the DMET calculation, or from the unphysical nature of the parametrization (e.g. the lack of doping dependence of the parameters). From our earlier work on the one-band Hubbard model [32], we know that DMET calculations using a 2×2 impurity (e.g. in the range $U/t = 6-8$) indeed overmagnetize not only at half-filling but also in the doped regime (see Fig. E.3). However, the one-band AFM order nonetheless vanishes at dopings larger than 0.25,

more rapidly than what we observe in the minimal parametrized three-band model. In addition, the full parametrization of the three-band model also predicts a more realistic trend for the AFM order at large doping. Taken together, this suggests that the observed persistent AFM order is likely due to the oversimplified minimal model parameters. Although the AFM order in the full model does decrease to zero in the observed doping range, it vanishes between $x = 0.2$ and 0.3 (more similar to the one-band model). This is beyond the experimental boundary for the pure AFM phase ($x < 0.1$), but close to the boundary of the pseudogap region [6, 43]. Like in the one-band model, we would expect longer wavelength orders (such as striped phases [24, 32]) to appear in this region with larger computational clusters.

From Fig. 4.3, we see that d-wave superconducting order (coexisting with antiferromagnetism) appears in the phase diagram of all parameter sets. (Discussion of additional pairing orders, as well as comparisons to the one-band model can be found further below). In the minimal models, the d-wave pairing reaches a maximum at around $x = 0.15 - 0.20$.

As a result of the overestimation of AFM order discussed above, the minimal models show coexistence of AFM + SC order for all the studied dopings. However, in the full parametrization, the two coexist in the range 0.1 to 0.4 (for solution 2), and 0.1 to 0.3 (for solution 1), with d-wave order reaching a maximum near $x \approx 0.30 - 0.35$, somewhat larger than seen in experiments ($\approx$ 0.15 - 0.2) [182]. Solutions 1 and 2 coincide for $x < 0.2$ and $x > 0.4$ but are distinct in between, reflecting the known competition between orders at intermediate doping [43]; solution 1 is slightly lower in energy and displays significantly stronger superconducting order. Note that it is also possible to converge a paramagnetic SC solution (by constraining the correlation potential in Eq. (4.2) so that $v^\alpha = v^\beta$ and $\Delta = \Delta^\dagger$). In this case, the SC order is already evident at $x = 0.1$, since the AFM order is artificially suppressed. However, the energy of this paramagnetic state is much higher than the AFM + SC states we have discussed, and is unstable if one releases the constraints on the potential. We thus believe the coexistence of AFM and SC order to be a true feature of the three-band model ground state, as has also been observed in VCA studies [171, 172].

Range of reasonable parameters

In view of the significant differences between the minimal and full parametrizations, we now examine more deeply how individual parameters influence the phase diagram. To do so, we change the individual parameters appearing in the Hanke min-

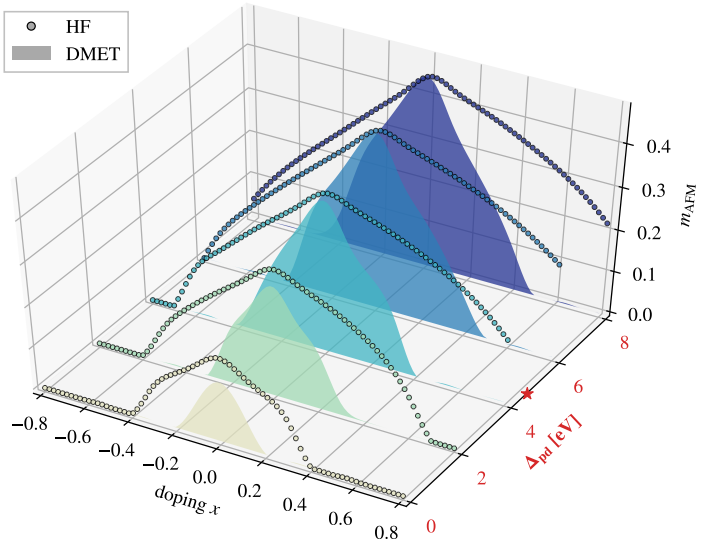

Figure 4.4: Effects of Δ_{pd} on the magnetic phase diagram of the three-band Hubbard model. Δ_{pd} ranges from 0.0 to 8.0 eV and the star marker labels the value used in the Hanke model (4.5 eV). Both Hartree-Fock (dotted line) and DMET (shaded area) results are shown.

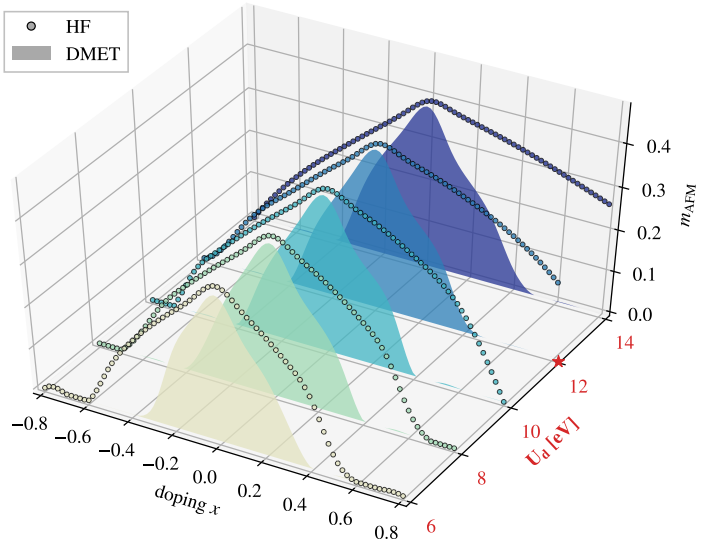

Figure 4.5: Effects of U_d on the magnetic phase diagram of the three-band Hubbard model. U_d ranges from 6.0 to 14.0 eV and the star marker labels the value used in the Hanke model (12.0 eV). Both Hartree-Fock (dotted line) and DMET (shaded area) results are shown.

imal model, and restrict ourselves to the magnetic order for simplicity. We compare the magnetic phase diagram computed using both Hartree-Fock and DMET. While the mean-field Hartree-Fock method overestimates the magnetic moments, and the

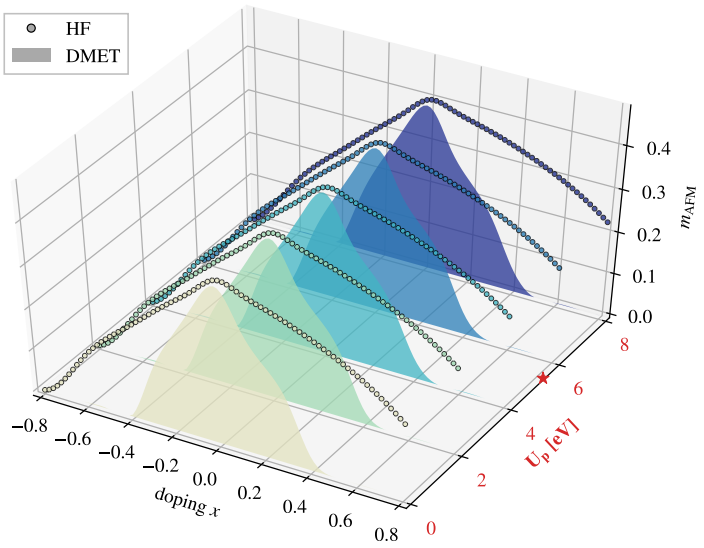

Figure 4.6: Effects of U_p on the magnetic phase diagram of the three-band Hubbard model. U_p ranges from 0.0 to 8.0 eV and the star marker labels the value used in the Hanke full model (5.25 eV). Both Hartree-Fock (dotted line) and DMET (shaded area) results are shown.

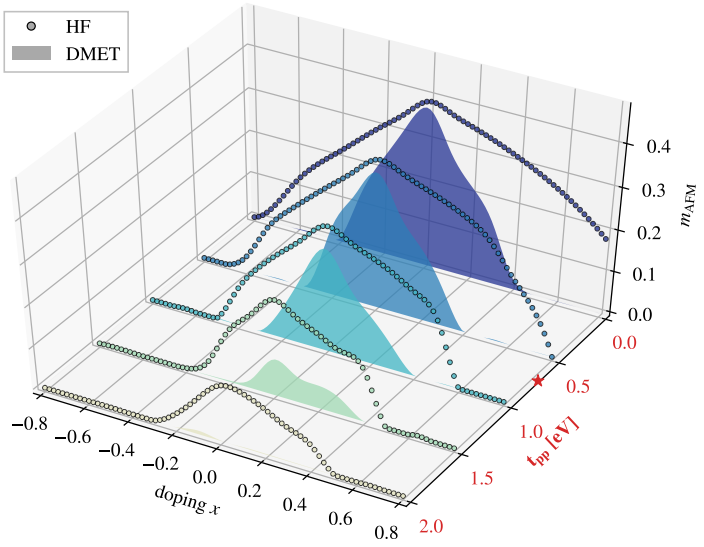

Figure 4.7: Effects of t_{pp} on the magnetic phase diagram of the three-band Hubbard model. t_{pp} ranges from 0.0 to 2.0 eV and the star marker labels the value used in the Hanke full model (0.75 eV). Both Hartree-Fock (dotted line) and DMET (shaded area) results are shown.

resulting AFM domes always lie above the DMET ones in the plots, it should be noted that parametrizations are often derived from mean-field calculations. Thus the difference in sensitivity between DMET and HF to the model parameters gives some

insight into the sizes of errors arising from mean-field parametrization schemes.

We first study the influence of Δ_{pd}, whose value is uncertain in the literature [167, 177]; the magnetic phase diagram computed using both Hartree-Fock and DMET is shown in Fig. 4.4. On the hole-doped side, when $\Delta_{pd} \gtrsim 4$ eV, the HF magnetic moment does not vanish even at a large doping of $x \approx 0.8$, while in contrast, DMET always predicts a finite AFM region with a sharp peak at $x = 0$. The DMET magnetic moment m_{AFM} increases monotonically from 0.14 to 0.44 as we increase Δ_{pd}, which can be understood from second-order perturbation theory: The effective d-d hopping $t_{dd} \propto \frac{t_{pd}^2}{\Delta_{pd}}$, thus a larger Δ_{pd} gives a smaller t_{dd} and thus enhances the magnetic moment. Along with the larger moments, the critical doping point where $m_{\mathrm{AFM}} \to 0$ shifts to larger doping as Δ_{pd} increases. Given that, even accounting for finite cluster errors (see above), the minimal model appears to overestimate the magnetic moment under doping and the critical doping concentration, these results suggest one should renormalize Δ_{pd} to smaller values, around 2-3 eV. Finally, we see that the asymmetry with respect to electron and hole doping becomes more pronounced when Δ_{pd} increases, and the magnetic moment is less sensitive to hole doping rather than electron doping. Thus, the appropriate value of Δ_{pd} should neither be too small (as the AFM order as well as doping asymmetry will both be too weak, see also Ref. [167] for a discussion of the unphysical behavior with small Δ_{pd}) nor too large (m_{AFM} order will be too strong to be suppressed by doping, especially on the hole doped side). Ref. [169] suggests a range (1.2 - 2.6 eV) of Δ_{pd} for cuprates, which overlaps the range of our estimates.

We next check the effect of on-site Coulomb repulsion terms. The moment versus U_d is shown in Fig. 4.5. Unlike Δ_{pd}, the influence of U_d on the shape of the curves is very small, e.g. the undoped DMET m_{AFM} only increases from 0.35 to 0.38 when U_d varies from 6 to 14 eV. The influence on the curve shape is more significant for HF than it is for DMET. In the one-band Hubbard model, however, the situation is very different, where m_{AFM} increases substantially as U is increased [32]. This observation supports viewing the three-band model as primarily a *charge transfer insulator* (and thus less sensitive to the change in the on-site Coulomb U_d), rather than a Mott insulator, whose magnetic moment is directly mediated by U. The situation for the on-site Coulomb repulsion U_p (see Fig. 4.6) is very similar to that for U_d: the undoped DMET m_{AFM} only increases from 0.37 to 0.38 as U_d varies from 0 to 8 eV, and the HF curves show a similarly weak sensitivity.

We finally study the effect of nearest neighbor oxygen hopping t_{pp} (see Fig. 4.7).

From the figure, we see that the AFM order is effectively frustrated by large t_{pp}, similar to the effect of t' in the one-band Hubbard model. It has been shown in Ref. [167] that t_{pp} can vary substantially for different cuprates (unlike t_{pd}, which is almost unchanged between materials). Our results here suggest that a reasonable range for this parameter is around 0.5 - 1.0 eV; too large a t_{pp} will suppress the AFM order.

Overall, we find that the magnetic phase diagram is sensitive to Δ_{pd} and t_{pp}, but not to U_d and U_p. The improved results of the full model are thus likely due to the introduction of t_{pp}, rather than U_p. In particular, if we wish to have a reasonable description of the three-band Hubbard model within a minimal set of parameters, Δ_{pd} should be renormalized to a smaller value to take the effect of t_{pp} into account. The Hanke parametrization of the full model yields more physical results, and thus we will only use this full model in the remainder of the discussion. However, we note that it is still not optimal with respect to choosing values of Δ_{pd} and t_{pp} that match experiment. This may in part be due to the mean-field derivation of some of the parameters.

Electron doped phases in the full model

We now turn to the electron doped orders, which as mentioned above, are different from the hole-doped orders, unlike in the one-band model [43, 161]. We show the AFM and SC order versus both hole and electron doping in Fig. 4.8 (the hole doped side corresponds to solution 1 in Fig. 4.3). As we dope with more electrons, the AFM order diminishes. The critical doping x_c that makes m_{AFM} vanish (0.15 - 0.20) is smaller than that on the hole doped side. This is quite different from what is seen in experiment: the commonly accepted cuprate phase diagram typically shows a sudden drop of AFM order on the hole doped side [5], with a larger region of coexistence on the electron doped side. This likely reflects the fact that a single parameter set does not describe the electron-doped and hole-doped materials equally well.

For the SC phase, the overall d-wave pairing magnitude is smaller in the electron doped region, similar to the lower T_cs seen in experiment. Also, the SC phase on the electron doped side has an interesting "M" shaped two-peak structure: The d-wave SC order increases first with respect to the doping, but decays to a small value around the AFM critical x_c, before growing to another peak after the AFM order vanishes. The first peak around $x = 0.05$ is very similar in shape to the peak in DMET calculations of the one-band Hubbard model, where the SC order

emerges immediately after doping (see the lower panel of Fig. 4.8). The second peak, occurring after the disappearance of the AFM order, is similar to the hole doped SC peak. The presence of two qualitatively different SC phases may be a hint of the types of competing orders that can arise on the electron-doped side, which to date have not been much investigated in numerical studies.

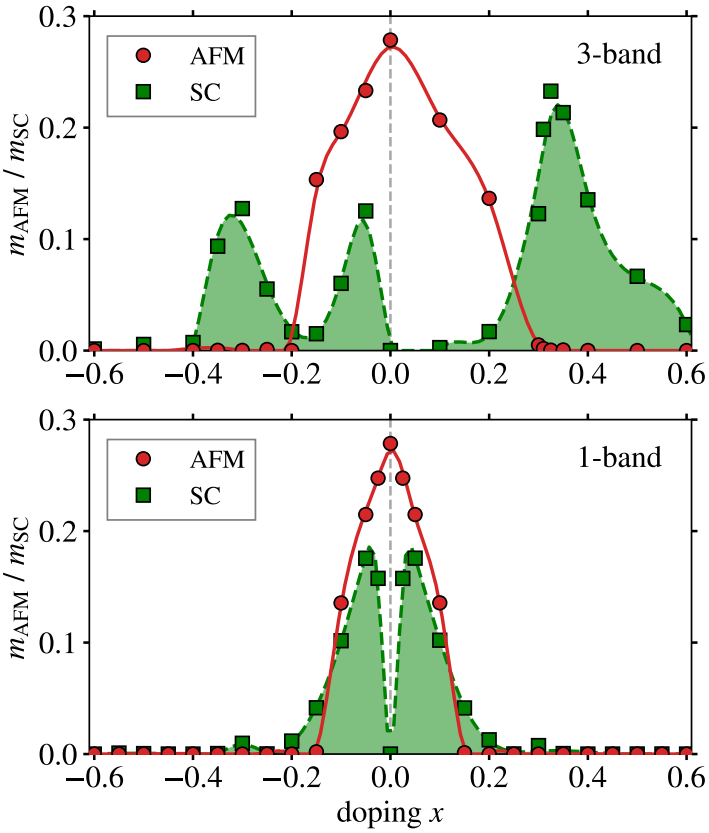

Figure 4.8: Comparison of electron doped ($x < 0$) and hole doped ($x > 0$) orders. Upper panel: AFM and SC order of the three-band Hubbard model (Hanke full parameter set). Lower panel: AFM and SC order of the one-band Hubbard model (2×2 DMET cluster), with U fitted such that at $x = 0$, m_{AFM} is the same as that of the three-band model.

Atomic scale orders in the full model

Beyond the bulk order parameters, the three-band model and the explicit inclusion of both copper and oxygen atoms into the DMET impurity cluster allows for the possibility of studying the magnetic and superconducting order at the atomic scale. The explicit charge, spin, and pairing orders are shown in Fig. 4.9. We only present representative results from the Hanke full model at $x = 0.0$, $x = 0.3$ (solution 1) and $x = -0.3$ doping, since the results from other parametrizations and dopings are

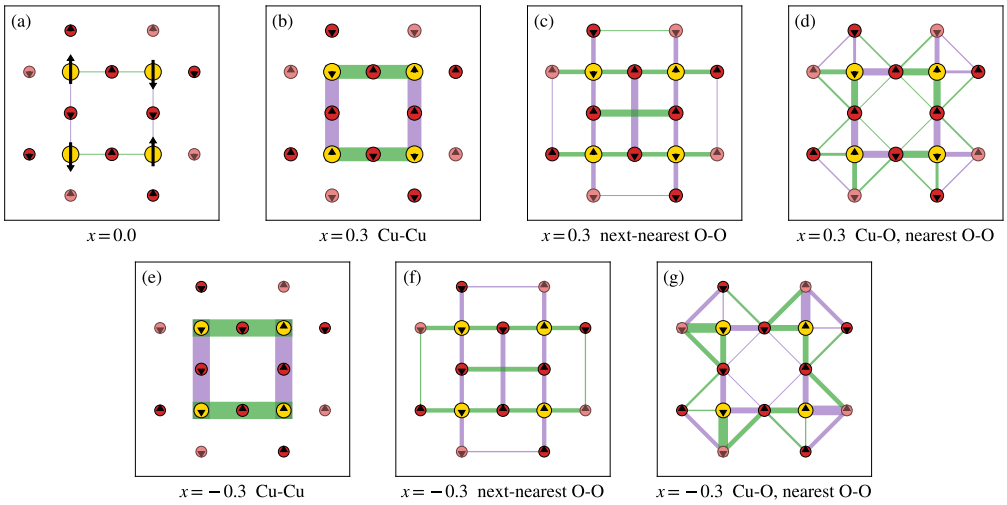

Figure 4.9: Charge, spin and pairing orders in the three-band Hubbard model. We use yellow and red circles for Cu and O respectively. The area of the circle reflects the corresponding local hole density, the length of the arrow denotes the magnitude of the local magnetic moment, the width of the lines is proportional to the pairing strength and different colors of the lines denote different coupling signs. The results are calculated based on the fully parametrized model at $x = 0.0$ [(a)], $x = 0.3$ doping [solution 1, (b) - (d)] and $x = -0.3$ doping [(e) - (g)]. (b) and (e) show the pairing strength between Cu and Cu; (c) and (f) show the pairing strength between the next nearest neighbor O; (d) and (g) illustrate the couplings of both the nearest Cu-O, and the nearest O-O.

qualitatively similar. (Further plots are presented in Figs. E.5 - E.10.) Comparing Figs. 4.9(a) and 4.9(b), we see that on doping the holes mainly occupy the oxygen sites and the hole density on copper only increases slightly. Combined with the fact that doped electrons mainly reside on Cu [see Fig. 4.9(e), the hole density on Cu is reduced], this reflects the particle-hole asymmetry of the three-band model [43, 161]. With respect to pairing order, we see $d_{x^2-y^2}$-wave symmetry clearly between neighboring Cu sites (i.e. it transforms according to the B-representation of the C_4 group and the sign of the pairing changes on rotating by 90°), see Figs. 4.9(b) and 4.9(e). The Cu-Cu pairing order is the largest pairing order between the atoms. From Figs. 4.9(c) and 4.9(f), we also see d-wave order between the *next-nearest* O p orbitals. Although the magnitude is slightly smaller than that of the Cu-Cu pairing, it still contributes almost $\approx 20\% - 40\%$ of the bulk d-wave order in Eq. (2.131). We note that the O-O pairing contribution is also asymmetric with respect to doping. In particular, its contribution can be as large as $\approx$ 40% in the hole doped side but only 20-30% in the electron doped region. Finally, we consider the pairing order between Cu-O and the nearest O-O atoms, see Figs. 4.9(d) and 4.9(g). We

see that the coupling between the nearest O-O atoms has s-wave symmetry but is quite weak, related to the incompatible orbital orientations. On the other hand, we find the pairing between Cu-O to be relatively strong (in all parameter sets). The local symmetry of Cu-O coupling has $p_{x(y)}$-wave [or $d_{xy(yz)}$-wave] symmetry (the pattern transforms according to the E-representation of the C_4 group), which to our knowledge has not previously been reported. We note that the superconducting phase pattern between Cu and O is similar to the orbital current-current correlation patterns in Ref. [149], although the current-current correlations were reported to be extremely weak. The pattern is also similar to the asymmetry reported as a hidden order in polarized elastic neutron diffraction experiments [7]. Further investigation of these and other intriguing connections to intracell orders is left to future work.

4.4 Conclusions

In summary, we have used density matrix embedding theory to characterize the ground-state phases of the three-band Hubbard model. We have calculated the charge, local magnetic moments, projected energy bands and density of states of the undoped three-band model, which support a charge-transfer insulating character at zero doping.

We also studied the doping dependence of the ground-state (phase diagram) of the model paying particular attention to the local AFM and SC orders. In a broad range of model parameters we find a decrease in AFM order upon doping and a SC dome. Unlike in the one-band picture, the models all predict a large region of coexistence of AFM + SC orders, with the AFM order decreasing quite slowly. Comparison to experimental data and earlier theoretical studies suggests that the minimal parametrized models overestimate the AFM order and lead to poorer energy gaps, relative to the full parametrizations, which also include oxygen and oxygen-copper Coulomb repulsion, and oxygen-oxygen hopping. The magnetic moment is particularly sensitive to the Δ_{pd} and t_{pp} parameters, and in the minimal model, the charge transfer gap Δ_{pd} should be renormalized downwards to better capture the experimental phase diagram. Within the full model, there are qualitative differences between the SC orders on the hole- and electron-doped side, with the electron-doped side supporting two different SC domes, one of which appears more similar to the one observed in the one-band model, and the other like the SC dome observed on the hole-doped side.

The three-band model further allowed us to study order at the atomic scale. In the

SC region, we observed strong d-wave pairing between Cu-Cu and the next-nearest O-O, weak extended s-wave coupling between the nearest O-O atoms, and p- (or d_{xz}, d_{yz})-like symmetry pairing between Cu-O. The intriguing symmetry of the latter order, similar to that seen in some experiments, illustrates the new physics that emerges at atomic length-scales in the three-band model. Exploring such physics in more detail will be the subject of future work.

Chapter 5

EFFICIENT IMPLEMENTATION OF AB INITIO QUANTUM EMBEDDING IN PERIODIC SYSTEMS

Based on the works published in *J. Chem. Theory Comput.* **16**, 119 (2020) and *J. Chem. Theory Comput.* **16**, 141 (2020). Copyright 2020, American Chemical Society. [98, 100]

5.1 Introduction

In this chapter, we will focus our attention on the *ab initio* implementation of DMET and DMFT in periodic solids. Our quantum embedding framework is featured by the impurities comprising the full unit cell or a supercell of atoms and for realistic quantum chemical basis sets, and is thus termed as *full-cell quantum embedding*. Their formulations have been summarized in Chap. 2.

In the DMET part, We apply DMET in the *ab initio* framework to a hexagonal boron nitride monolayer, crystalline silicon, and nickel monoxide in the antiferromagnetic phase, using large embedded clusters with up to 300 embedding orbitals. We demonstrate our formulation of *ab initio* DMET in the computation of ground-state properties such as the total energy, equation of state, magnetic moment and correlation functions.

In the DMFT part, we show that we are able to handle embedded impurity problems with several hundred orbitals. We apply our *ab initio* DMFT approach to study a hexagonal boron nitride monolayer, crystalline silicon, and nickel oxide in the antiferromagnetic phase, with up to 104 and 78 impurity orbitals in spin-restricted and unrestricted cluster DMFT calculations and over 100 bath orbitals. We show that our scheme produces accurate spectral functions compared to both benchmark periodic coupled-cluster computations and experimental spectra.

5.2 DMET computational details

We consider three prototypical solids: a 2D hexagonal boron nitride monolayer (h-BN), crystalline silicon (Si) and nickel monoxide (NiO). The lattice parameters were taken from experiment: $a = 2.50$Å for the BN monolayer[188] (with 20.0Å vacuum to eliminate fictitious interactions between mirrors); $a = 5.43053$Å for Si [189],

and $a = 4.17$Å for NiO [190]. To target the AFM-II state, the minimal unit cell of NiO was chosen as the rhombohedral cell that contains two formula units of NiO. We used 28 Intel E5-2680@2.40GHz cores in all the calculations. We summarize the computational parameters for DMET below. *Mean-field calculations.* All mean-field calculations were performed using the PySCF package [138] with Hartree-Fock or DFT [Perdew-Burke-Ernzerhof (PBE) functional [191]]. GTH pseudopotentials [192, 193] were used to replace the sharp core electron density, with corresponding GTH-DZVP ($2s2p3s3p3d$ AOs for B and N, and $3s3p3d4s4p$ AOs for Si) and GTH-DZVP-MOLOPT-SR ($3s3p3d4s4p4d4f5s$ AOs for Ni, and $2s2p3s3p3d$ AOs for O) basis sets [194] used to represent the valence electrons. Gaussian density fitting was used to compute the two-electron integrals [81]. We used an even-tempered Gaussian basis [195] as the density fitting auxiliary basis, i.e. $L_{nl}(r) \propto r^l \exp\left(\alpha\beta^n r^2\right)$, where we used the exponential factor $\beta = 2.3$ for NiO and $\beta = 2.0$ for all other systems. The number of fitting functions was chosen to ensure high accuracy, and thus the size of the auxiliary basis is about 10 times as large as the number of AOs. The GTH-SZV (h-BN and Si) and GTH-SZV-MOLOPT-SR (NiO) basis functions were used as the reference free-atom AOs to construct the IAOs. In the mean-field calculations used to derive the embedding Hamiltonian and in the DMET self-consistency, we sampled the Brillouin zone with a Γ centered mesh chosen so as to be able to fit unit multiples of the DMET impurity supercell. These included a $6 \times 6 \times 1$ mesh for BN, and a $4 \times 4 \times 4$ mesh for Si and NiO. Larger meshes were used in independent estimates of the mean-field TDL for BN (up to $12 \times 12 \times 1$) and Si (up to $8 \times 8 \times 8$). All mean-field calculations were converged to an accuracy of better than 10^{-10} a.u. per unit cell. In the case of Hartree-Fock energies, all energies included the leading-order exchange finite-size correction (probe-charge Ewald [196, 197], `exxdiv=ewald` in PySCF). Note that the above correction applies to all DMET energies as these use the Hartree-Fock expression for the mean-field energy even when density functional orbitals are used.

Impurity solver. We used coupled cluster singles and doubles (CCSD) [128] as an impurity solver, as implemented in PySCF [138], which is able to treat a large number of orbitals efficiently. In NiO where DMET self-consistency produced symmetry breaking, we used unrestricted CCSD (UCCSD). The CC density matrices were obtained from the CC Λ equations [129]. The CC energies were converged to 10^{-8} a.u..

DMET self-consistency. For BN and NiO, the correlation potential u was added to only the valence orbitals and for Si, u was added to all impurity orbitals as this gave smoother DMET convergence. We carried out CSC calculations for all three systems, and included additional non-CSC results of NiO for comparison. The convergence criterion on the DMET self-consistency was chosen such that the maximal change of an element in u was less than 5×10^{-5} a.u., which corresponded roughly to an energy accuracy of better than 1×10^{-5} a.u..

5.3 DMET results

2D boron nitride

We first study the behavior of DMET on a 2D boron nitride monolayer. In a GTH-DZVP basis, BN has a unit cell of 2 atoms, with $2s2p$ AOs on each atom giving 8 valence orbitals per cell, and $3s3p3d$ AOs on each atom providing 18 higher-energy virtual orbitals per cell. We illustrate the valence IAOs of boron in BN in Fig. 5.1a. As expected, the IAOs of boron are quite local, retaining their original AO character

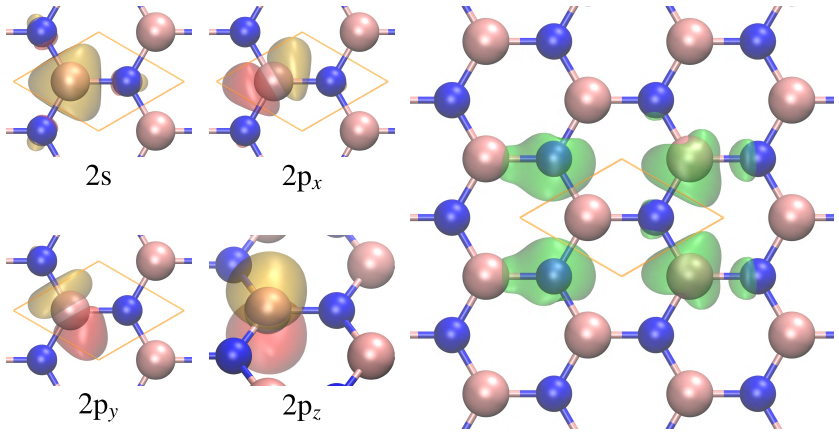

Figure 5.1: Impurity orbitals and bath density of BN used in the DMET calculations. The boron and nitrogen atoms are colored pink and blue respectively. (i) Impurity valence orbitals associated with one boron atom (IAOs from boron). (ii) Bath orbital density coupled to the first reference cell.

but with some slight polarization to reflect the mean-field solution in the crystal environment. The bath orbital density is plotted in Fig. 5.1b (we only show the total density summed over the bath orbitals here, since the embedded problem only depends on the linear span of the bath). It is clear that the bath orbitals are localized around the impurity cluster and give an effective representation of the remainder of the boron nitride crystal. In particular, the bath orbitals serve to terminate the

dangling bonds on the impurity boundary, thus turning the embedding problem into a closed-shell one at the mean-field level. The impurity valence orbitals and bath orbitals pictured here, together with the impurity virtual orbitals (not shown), constitute the embedding orbitals.

We computed total energies (per cell) from DMET for different cluster sizes, 1×1, 2×2 and 3×3. We compare these total energies to those from **k**-sampled periodic CCSD (**k**-CCSD) extrapolated to the TDL (see Fig. 5.2) which has recently been demonstrated to be a high accuracy method in a variety of different materials [80, 198, 199]. Note that, accounting fully for the **k**-point symmetry, **k**-CCSD has a computational scaling of $n_{\mathrm{AO}}^6 n_{\mathbf{k}}^4$. The reference TDL **k**-CCSD energy is the sum of the extrapolated HF energy using a large **k**-mesh (up to $12 \times 12 \times 1$, extrapolating with the form $n_{\mathbf{k}}^{-1}$ after using the Ewald exchange divergence correction [196, 200]) and the extrapolated **k**-CCSD correlation energy using a smaller **k**-mesh (up to $6 \times 6 \times 1$, extrapolating with the form $n_{\mathbf{k}}^{-1}$). Compared to the TDL reference energy, even using the smallest (1×1) cluster, DMET gives an accurate total energy that captures about 95% of the correlation energy. Extrapolating over the DMET cluster size (using the surface to volume form $N_{\mathrm{c}}^{-1/2}$, where N_{c} is the cluster size) further improves the accuracy by about 1-2% in the correlation energy. The one-shot DMET result (i.e. without DMET self-consistency) is less accurate than the self-consistent one by $\sim$ 8 mHartree (3% of the correlation energy), demonstrating the contribution of self-consistent matching between the high-level calculation and the low-level mean-field calculation. We note that self-consistency is generally not very important in non-magnetic weakly-correlated systems, as there are no symmetry broken phases to be generated by DMET, and only provides a modest quantitative correction to the observables.

Compared to small $N \times N \times 1$ **k**-mesh CCSD energies, the DMET total energies are more accurate for the 1×1 and 2×2 cluster sizes, but less accurate for the 3×3 case. The finite size error in the total energy, arising from the finite **k**-mesh or DMET cluster size, can be separated into two sources, (i) the finite size error in the mean-field energy and (ii) the finite size error in the many-body correlation energy. For embedding methods like DMET, the error from the first source is (largely) eliminated. Thus, as shown in Fig. 5.2, the DMET total energy is good even for a small cluster size. In the CCSD calculation, however, the error from (i) is large for small clusters, and therefore, a potentially better recipe for the total energy is to sum the HF energy from a larger cluster (or even extrapolated to the TDL) and the

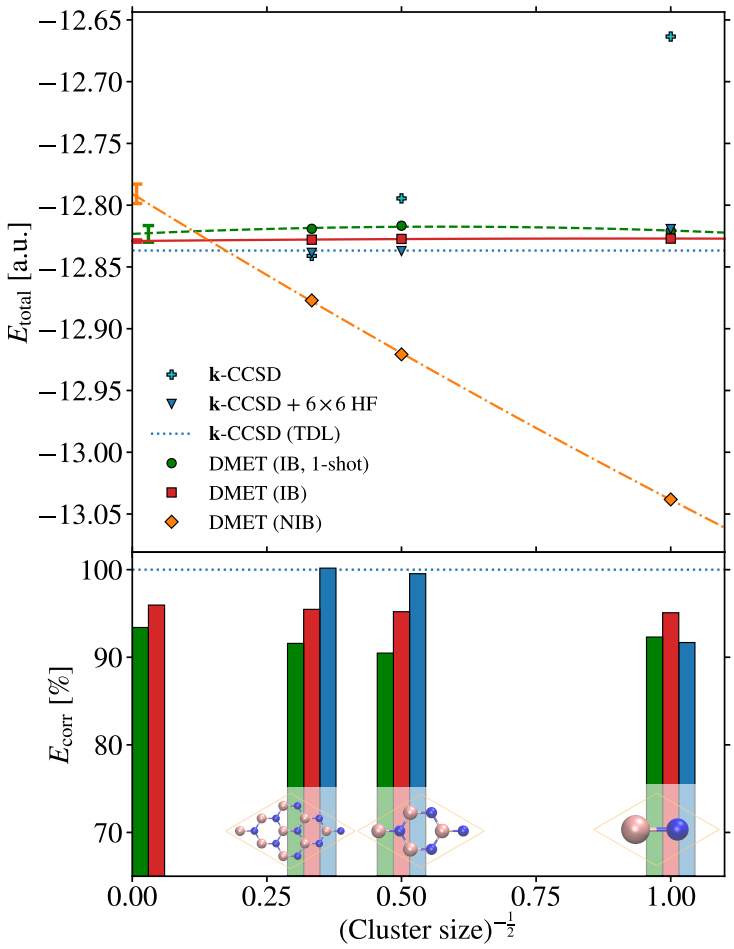

Figure 5.2: Upper panel: Total energy from DMET compared with **k**-sampled CCSD. In the case of DMET with the interacting bath (IB), both one-shot and self-consistent energies are reported. DMET with non-interacting bath (NIB) is also shown for comparison. The extrapolated values of DMET is from an average of linear regression and quadratic fitting. The error bar is the difference between the linear and quadratic fitted values. We plot the energy of **k**-CCSD with small **k**-mesh (one curve with HF energy at corresponding small **k**-mesh and the other with HF energy at 6×6 **k**-mesh) and the extrapolated TDL results as reference. Lower panel: Correlation energy ratio with respect to the extrapolated CCSD correlation energy.

correlation energy from the small cluster calculation. In the upper panel, we show the **k**-CCSD correlation energy added to the 6×6 HF energy (corresponding to the size of the DMET lattice), as well as to the extrapolated TDL HF energy. Together with the data in the lower panel of Fig. 5.2, we see that the correlation energy E_{corr} of CCSD, which relies on the above error cancellation, is already very accurate for the 2×2 cluster and is better than that of DMET for this cluster size. It is then

worth analyzing the source of errors in the small cluster DMET correlation energy. One source is the lack of embedding of the non-valence virtual orbitals, which are localized to the reference cell with the periodicity of the large DMET mean-field lattice, not the periodicity of the impurity (as in the **k**-CCSD calculation). The advantages of DMET in the current implementation thus manifest when the predominant correlation is within the valence space itself (which is fully embedded) as is typical of strong correlations, rather than primarily involving excitations to non-embedded, non-valence, virtual orbitals as in this system. One way to diminish the boundary effect on the DMET non-valence virtuals is to evaluate the energy from the central part of the supercell, for which the surrounding atoms effectively provide a bath for the virtuals. We find then that the energy evaluated using the central cell of the embedded cluster covers 103.8% of the correlation energy (using the preceding 3×3 cluster calculation) or 100.1% (if no chemical potential fitting is used), which is better than that obtained by direct energy evaluation using the entire embedded cluster. It may be possible to further reduce this boundary error using the dynamical cluster approximation formulation of DMET (DCA-DMET)[33] or bootstrap embedding[201–203].

We finally consider DMET results obtained using the non-interacting bath (NIB), as also shown in Fig. 5.2. We see that although the extrapolation is quite systematic, the accuracy is worse than that of the interacting bath for all three cluster sizes. This result is generally found in chemical systems with long-range Coulomb interactions, as the interacting bath carries some information about the inter-cluster interactions. However, the NIB formalism has the potential computational advantage that the construction of the NIB embedded Hamiltonian is cheaper than the IB one, since only the impurity part of the two-particle Hamiltonian is needed. In addition, the correlation potential can be used to mimic the effect of the long-range Coulomb contributions to the Fock matrix. This makes the NIB scheme an interesting possibility in large systems.

Bulk silicon

We next test the ability of DMET to describe the structural properties of bulk Si. We performed a series of calculations on different primitive cell volumes and fitted the relative total energy E as a function of the volume V using the Birch-Murnaghan (B-M) equation of state (EOS) [204, 205], from which the equilibrium volume and bulk modulus can then be determined. To obtain accurate results for the TDL, we considered three clusters of different shapes: a $1 \times 1 \times 1$ primitive cell (2 Si atoms),

a conventional diamond cubic cell (8 Si atoms) and a $2 \times 2 \times 2$ supercell (16 Si atoms). We performed the extrapolation with respect to cluster volume V_c using

$$E(V_c) = E(\infty) + a_0 V_c^{-1/3} + \cdots \tag{5.1}$$

The total energy includes the correction from HF at the TDL. The equilibrium volumes and bulk moduli are collected in Table 5.1.

Table 5.1: Equilibrium volume of the primitive cell V_0 and bulk modulus B_0 of silicon from different approaches. The extrapolated values are from the linear fit of $1 \times 1 \times 1$ and $2 \times 2 \times 2$ results. The CCSD results are taken from Ref. [80] , which uses the larger GTH-TZVP basis. The experimental V_0 is from Ref. [189] and B_0 is from Ref. [206] with a zero-point correction.

Methods		V_0 [Å^3]	B_0 [GPa]
HF	extrap.	40.30	107
DMET	$1 \times 1 \times 1$	42.83	87.9
	cubic cell	41.90	88.5
	$2 \times 2 \times 2$	41.26	91.1
	extrap.	39.69	99.0
CCSD	$3 \times 3 \times 3$	39.21	103
Expt.		40.04	101

From the table, we see that the equilibrium volume of DMET using the $1\times1\times1$ cluster deviates from the experimental value by 7%. The error from the smallest impurity cluster is thus larger for Si than for BN. This is because Si has a much smaller band gap and thus less local correlation involving the non-valence space. However, the results improve rapidly when increasing the size of cluster. To illustrate this, we show the EOS curves for different cluster sizes in Fig. 5.3. It is clear that the $1\times1\times1$ curve is shifted to larger volume compared to experiment or CCSD. Increasing the cluster size systematically shifts the curve back towards experiment and the **k**-CCSD benchmark, resulting in a very small relative error (w.r.t. experiment) of 0.9% for V_0 for the extrapolated curve. The extrapolated bulk modulus B_0 also agrees well with the experimental and **k**-CCSD benchmark values. Overall, the accuracy achieved by extrapolated DMET appears comparable to that of the **k**-CCSD benchmark in a full $3 \times 3 \times 3$ periodic calculation, although we note that a different basis was used.

Nickel monoxide

We now demonstrate the ability of DMET to treat a more strongly correlated problem by considering a typical transition metal compound, NiO. Below the Néel

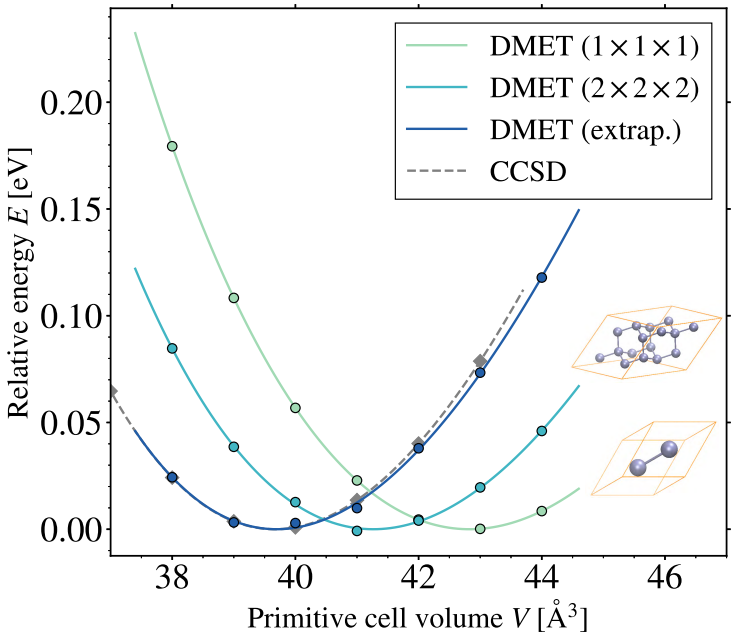

Figure 5.3: Equation of state curves of Si from DMET and CCSD. For DMET, we omit the cubic cell curve for clarity. CCSD data is taken from Ref. [80].

temperature, NiO displays an antiferromagnetic (AFM) phase with a staggered magnetization along the [111] direction (the so-called AFM-II phase). Although DFT (with PBE) and HF do predict spin-polarization, it is known that DFT often underpolarizes while HF often overpolarizes antiferromagnetic states. To avoid such biases in the DMET calculation, we embed the DMET calculation in an initial *unpolarized* mean-field state. We constructed the unpolarized mean-field state by using the orbitals obtained from the spin-averaged Fock matrix of an unrestricted Hartree-Fock or DFT calculation. We use the spin-averaged Fock matrix for convenience because without finite-temperature smearing, the restricted calculations either have difficulty converging due to the metallic nature (DFT) or exhibit an unphysical symmetry breaking of the density between the symmetry-equivalent nickel atoms (HF). The spin-averaged Fock matrix is similar to the restricted one with smearing but exactly preserves the symmetry between the two nickel atoms. We denote DMET calculations based on the spin-averaged mean-field orbitals by DMET@Φ^*_{RHF} (DMET@Φ^*_{RPBE}), where "$*$" means the restricted orbitals are actually from the spin-averaged unrestricted Fock matrix rather than a real restricted one.

The spectrum of such a spin-averaged Fock matrix is gapless. After adding an initial DMET correlation potential, e.g. taken from the local part of the UHF polarized

potential, the system becomes gapped and S^2 symmetry is broken. Without CSC, the final DMET mean-field gap is $\sim$ 3 eV and with CSC, the DMET mean-field gap is $\sim$ 10 eV, closer to the Hartree-Fock mean-field gap ($\sim$ 12 eV). (Note that the experimental band gap of AFM NiO is $\sim$ 4.3 eV [207]). It should be emphasized that although the band gap from the DMET lattice mean-field reflects the insulating nature of the system, its value does not correspond to the true fundamental gap of the system. Even if the density from the impurity solver were exact and the matching between density matrices were perfect, the mean-field gap is not exact due to the derivative discontinuity contribution[208], similar to the Kohn-Sham gap obtained from an optimized effective potential (OEP) calculation [209].

The ground state charges and local magnetic moments of NiO from DMET starting from different initial mean-fields (spin-averaged HF and PBE) are summarized in Table 5.2. Assignment of local observables to different atoms (population analysis) was performed using the IAOs + PAOs and the density matrix from the CC impurity solver. We also include unrestricted HF, PBE results for comparison.

Table 5.2: Local charge (in e) and magnetic moment (in μ_B) of NiO from different methods. The values on Ni (O) are averaged from the two Ni (O) sites in the primitive cell. We include the DMET results from different initial orbitals (Φ^*_{RHF} and Φ^*_{RPBE}), with / without charge self-consistency (CSC). The experimental data is taken from Refs. [190, 210, 211].

Methods	ρ_{Ni}	m_{Ni}	m_{O}
HF	1.42	1.86	0.000
PBE	1.02	1.42	0.000
DMET@Φ^*_{RHF} w/o CSC	1.32	1.77	0.018
DMET@Φ^*_{RPBE} w/o CSC	1.27	1.74	0.017
DMET@Φ^*_{RHF} w/ CSC	1.37	1.81	0.001
DMET@Φ^*_{RPBE} w/ CSC	1.35	1.78	0.000
Expt.		1.70-1.90	

First, we observe clear charge transfer from Ni to O in all methods. Among them, HF gives the largest ionic character while PBE smears out the charge and predicts the smallest charge transfer. The DMET results from different starting orbitals and CSC conditions are between these two limits and are relatively close to each other. The DMET results with CSC (starting from HF and PBE) are particularly close to each other as the inter-cluster part of density matrix is updated using information from the high-level embedded calculation. In fact, in the case of CSC, the only

effect of the initial choice of orbitals in DMET on the final result comes from the different definition of the local orbitals.

Compared to the experimental estimate of the magnetic moment, unrestricted Hartree-Fock gives a Ni magnetic moment at the higher-end of the experimental range, while PBE severely underestimates the magnetic moment. DMET yields results independent of the starting orbitals with a moment that agrees well with experiment. To illustrate the AFM distribution in NiO, we plot the spin density distribution in the (001) plane of NiO in Fig. 5.4. In the figure, the α- and β-

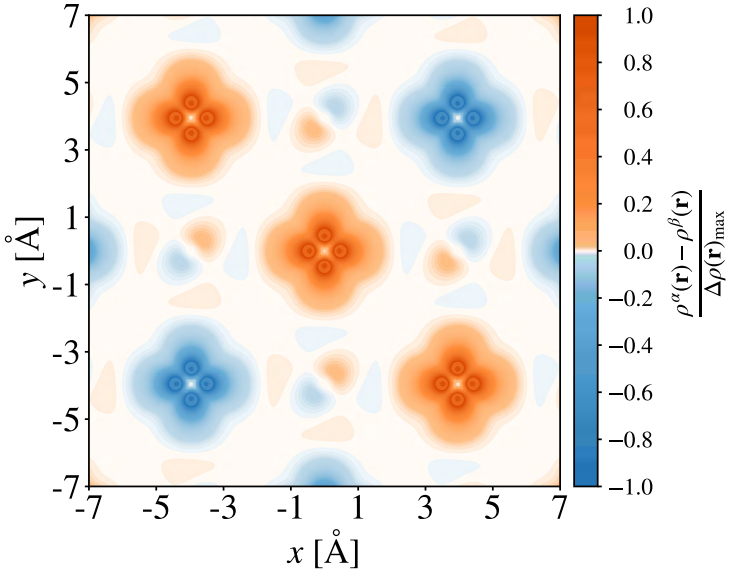

Figure 5.4: Spin density $\rho_\alpha - \rho_\beta$ on the (001) plane of NiO from DMET@Φ^*_{RHF} with charge self-consistency.

spin planes alternately appear along the diagonal direction, showing a clear AFM pattern. In particular, the spin density on Ni is in the shape of the $d_{x^2-y^2}$ orbital, indicating that its occupation is asymmetric with respect to the α and β electrons. In fact, the t_{2g} orbitals are almost fully occupied ($\sim 5.97\ e$ in our population analysis), and the e_g orbitals ($d_{x^2-y^2}$ and d_{z^2}) are occupied only in one spin sector ($\sim 1.99\ e$), and roughly empty in the other ($\sim 0.19\ e$). The local magnetic moment on Ni therefore mainly comes from the contribution of the e_g electron density, as expected from crystal field theory. The density on oxygen is in the shape of a p orbital and is polarized according to its orientation relative to Ni. The average polarization on oxygen should be close to zero due to symmetry. As shown in Table 5.2, the magnetic moments on oxygen from DMET (especially with CSC) are indeed close to zero.

We now take a closer look at the spin-spin correlation in NiO. To this end, we evaluate the spin-spin correlation function between the two nickels in the unit cell,

$$\sum_{i\in \mathrm{Ni}_1, j\in \mathrm{Ni}_2} \left\langle \mathbf{S}_i \cdot \mathbf{S}_j \right\rangle = \sum_{i\in \mathrm{Ni}_1, j\in \mathrm{Ni}_2} \sum_{a=x,y,z} \left\langle S_i^a S_j^a \right\rangle, \tag{5.2}$$

where i and j are the indices of LOs located on the first and second Ni respectively. In the DMET@Φ^*_{RHF} calculation with charge self-consistency, the expectation value is -0.8147, where the minus sign arises from the AFM correlation between the spins of two nickels. This value, however, is very close to the product $\langle S^z \rangle \langle S^z \rangle = -0.8149$. In addition, the spin non-collinear contributions ($\langle S^x S^x \rangle$ and $\langle S^y S^y \rangle$) are almost zero (note that the calculation spontaneously chooses a z magnetization axis due to the initial unrestricted Hartree-Fock reference or form of the correlation potential). All these features suggest that the ground-state of the AFM spin lattice in NiO is close to that of a classical Ising model, rather than a quantum one. Our results are consistent with experimental measurements on the critical behavior of the magnetic phase transition in NiO [212–214], where the critical exponents are found to be very close to those of the 3D Ising model.

In the above results, we found that the DMET order parameters are insensitive to the initial mean-field orbitals, due to the DMET self-consistency. As discussed in Sec. 2.4, this self-consistency contains two different contributions: self-consistency of the DMET correlation potential (expressed along the cluster blocks of the mean-field lattice Hamiltonian) and charge self-consistency of the mean-field Fock operator (for the off-diagonal blocks of the mean-field lattice Hamiltonian). To show the robustness of the self-consistency with respect to the correlation potential guess and the relative magnitude of these two contributions, we show the convergence of the local magnetic moment of Ni with respect to the number of iterations in Fig. 5.5 (for initial restricted orbitals from a spin-averaged Fock matrix Φ^*_{RHF}) with two different initial guesses for the correlation potential: the strongly polarized UHF potential, and a weakly polarized potential equal to the UHF potential scaled by a factor 0.1, both with and without charge self-consistency. From the figure, we see that starting from different initial guesses for the correlation potential, the magnetic moments from non-self-consistent (i.e. one-shot) DMET (the 0^{th} iteration in Fig. 5.5) can be very different. However, after only 1 step, the magnetic moments are significantly improved. Eventually, the magnetic moments from the two guesses converge to a very similar value, showing that the DMET self-consistency effectively removes the initial correlation potential guess dependence. The picture with and without charge

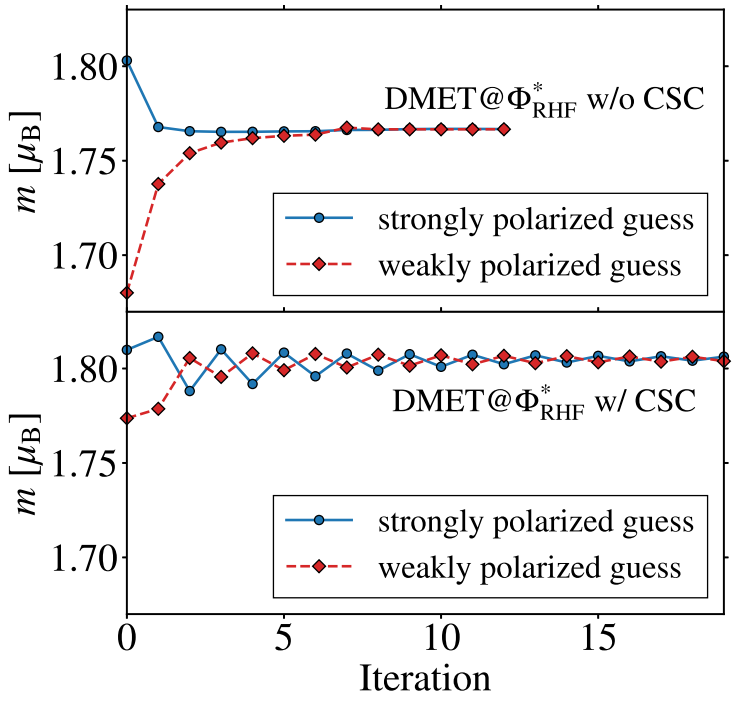

Figure 5.5: The convergence of the magnetic moment on Ni from different initial correlation potentials. Upper panel: DMET@Φ^*_{RHF} without CSC using different initial guesses: UHF potential (strongly polarized) or UHF potential scaled by 0.1 (weakly polarized). Lower panel: The same as the upper panel but with CSC.

self-consistency is very similar, showing that the DMET correlation potential is the main factor controlling the local order parameter. Note that in Fig. 5.5, the LOs are the same (based on Hartree-Fock) for all calculations and hence there is no initial LO dependence. Finally, as a rough indicator of cost, each DMET iteration takes about 1 hour (the computational setup is described in Sec. 5.2).

5.4 DMFT computational details

Coupled-cluster impurity solvers

In this work, we will use a coupled-cluster (CC) impurity solver to compute $G_{\text{imp}}(\omega)$ from the embedding Hamiltonian in Eq. (2.29). We recently studied the coupled-cluster Green's function (CCGF) approximation as an impurity solver in DMFT [215] (see also Ref. [216]) and showed that it performed well for small impurity clusters in Hubbard models. Here, we further explore its capabilities in the *ab initio* setting.

A detailed presentation of the CCGF formalism can be found in Refs. [215, 217–221]. Here, we will only comment on a few points related to DMFT. First, we use the

coupled-cluster singles and doubles Green's function approximation (CCSD-GF) as the impurity solver here. The cost of ground-state CCSD scales as $\mathcal{O}(N_{\text{emb}}^6)$ and CCSD-GF scales as $\mathcal{O}(N_\omega N_{\mathcal{C}} N_{\text{emb}}^5)$, where N_{emb} is the total number of orbitals (sites) in the embedding problem and $N_{\mathcal{C}}$ is the number of impurity orbitals. In practice, the CCSD-GF calculation can be parallelized over N_ω and $N_{\mathcal{C}}$. This low cost compared to ED allows us to treat around 200 embedding orbitals in DMFT. Second, the CCSD-GF is computed directly on the real frequency axis with a broadening factor η. We find that in *ab initio* calculations, when η is small (< 0.5 eV), causality issues may exist where the imaginary part of the CCSD self-energy is not always negative. We refer readers to Ref. [215] for a practical solution, where one computes the impurity plus bath self-energy and then uses the impurity block of the self-energy matrix, instead of directly computing the impurity self-energy matrix. This solution increases the CCSD-GF cost scaling slightly to $\mathcal{O}(N_\omega N_{\text{emb}} N_{\text{emb}}^5)$. We use this more expensive technique in the final calculation of spectra after DMFT convergence.

We applied the above DMFT scheme to study three realistic solids: weakly correlated 2D hexagonal boron nitride (h-BN) and crystalline silicon (Si), and a prototypical "strongly correlated" problem, nickel oxide (NiO) in the AFM-II phase. The experimental lattice constants were used for all calculations: 2.50Å for h-BN monolayer [188], 5.417Å for Si [189] and 4.17Å for NiO [190]. For h-BN, we used a vacuum spacing of 20Å along the z axis to avoid image interactions between neighboring sheets. In h-BN and Si we used (super)cells of the primitive cell as the impurity. In NiO, we used a supercell with two Ni and two O atoms along the [111] direction to allow for AFM spin symmetry breaking within the cell.

All mean-field calculations were performed and all integrals were generated using the PySCF quantum chemistry package [138]. Norm-conserving GTH-PADE pseudopotentials [192, 193] were employed to replace the core electrons. The GTH-DZVP basis set was used for h-BN and Si, while the GTH-DZVP-MOLOPT-SR basis set [194] was used for NiO. This corresponds to 26, 26 and 78 AOs in the impurity unit cells of h-BN, Si and NiO, and 104 AOs in our largest impurity supercell of Si. The minimal basis sets GTH-SZV (h-BN and Si) and GTH-SZV-MOLOPT-SR (NiO) were used as the pre-defined AOs to construct the IAOs, leading to 8, 8 and 28 valence orbitals in each unit cell respectively. Even-tempered auxiliary Gaussian basis sets were used to compute the GDF integrals. Uniform $6 \times 6 \times 1$ (h-BN), $4 \times 4 \times 4$ (Si) and $4 \times 4 \times 4$ (NiO) $\mathbf{k}$-point meshes were adopted for the mean-field and DMFT calculations. All meshes were Γ-centered.

Unless otherwise specified, we used HF as the initial lattice mean-field in the DMFT embedding. The CCSD-GF method was implemented based on the CCSD and EOM-CCSD routines from the PySCF package, and the DMFT algorithm was implemented in the Potato module. A spin-restricted CCSD-GF (RCCSD-GF) solver was used for h-BN and Si, while a spin-unrestricted CCSD-GF (UCCSD-GF) solver within the spin-unrestricted DMFT formalism was employed for NiO. A simplified and flexible variant of the GCROT method [GCROT(m,k)] [222] was used to solve the CCSD-GF linear response equations. Gauss-Legendre quadrature was used on frequency intervals of $[-1.0+\mu, 1.0+\mu]$ a.u. (h-BN), $[-0.6+\mu, 1.0+\mu]$ a.u. (Si) and $[-0.5+\mu, 0.5+\mu]$ a.u. (NiO) when discretizing the hybridization. We used a broadening factor of $\eta = 0.1$ a.u. during the DMFT self-consistent cycles and switched to a smaller η (depending on the required resolution) in the final production runs to compute $G(\mathbf{R} = \mathbf{0}, \omega)$. The DMFT self-consistency was converged to $||\Delta_{i+1}(\omega) - \Delta_i(\omega)|| < \theta = 10^{-4}$ a.u. between two DMFT iterations.

5.5 DMFT results

2D boron nitride

We first investigate the performance of our *ab initio* DMFT scheme for the 2D h-BN monolayer. We chose the impurity to be an h-BN unit cell, including the $2s2p3s3p3d$ orbitals for both boron and nitrogen atoms (26 impurity orbitals in total). The corresponding IAOs are projected $2s2p$ orbitals, giving 8 IAOs coupled to the bath. To study the convergence of DMFT with respect to the number of bath orbitals, we used a series of Gauss-Legendre quadratures to discretize the hybridization: $N_\omega = 4, 8, 12, 16$. This led to a total number of $N_b = 32, 64, 96, 128$ bath orbitals.

Table 5.3: Direct and indirect band gaps (in eV) of 2D h-BN.

Method	$\mathbf{K} \to \mathbf{K}$	$\mathbf{K} \to \Gamma$	$\Gamma \to \Gamma$
HF	11.31	10.70	13.14
PBE	4.61	5.90	7.37
DMFT(i26,b32)	5.69	6.85	10.10
DMFT(i26,b64)	7.23	7.76	9.63
DMFT(i26,b96)	7.61	8.00	9.75
DMFT(i26,b128)	7.73	8.08	9.76
EOM-CCSD ($3 \times 3 \times 1$)	9.50	9.36	11.44
EOM-CCSD ($6 \times 6 \times 1$)	**7.48**	**7.78**	**9.78**

The computed direct and indirect band gaps at special $\mathbf{k}$ points are presented in

Table 5.3. In this work, we use the notation "DMFT(iX,bY)" to mean that there are X impurity orbitals and Y bath orbitals to be treated by the CCSD-GF impurity solver. The DMFT band gaps are calculated from the valence and conduction peaks of **k**-resolved density of states (DOS). We compare our DMFT results to HF, DFT/PBE [191] and EOM-CCSD [223] gaps computed using PySCF, all with $6 \times 6 \times 1$ **k**-point meshes. EOM-CCSD with $3 \times 3 \times 1$ **k**-point sampling is also included for comparison. As shown in Table 5.3, $6 \times 6 \times 1$ EOM-CCSD with the GTH-DZVP basis predicts that 2D h-BN is a direct band-gap semiconductor, with a gap of 7.48 eV at the **K** point. The indirect band gap from **K** to Γ has a slightly larger value of 7.78 eV. These values are taken as the reference values. Compared to $6 \times 6 \times 1$ EOM-CCSD, HF overestimates the $\mathbf{K} \rightarrow \mathbf{K}$ gap by 3.8 eV, while PBE underestimates it by 2.9 eV. EOM-CCSD with a smaller $3 \times 3 \times 1$ **k** mesh also overestimates the band gaps by 1.6-2.0 eV, suggesting the importance of large **k**-point meshes to approach the thermodynamic limit.

Even with a small number (32) of bath orbitals, our DMFT(i26,b32) result shows significant improvement over mean-field methods, although the $\mathbf{K} \rightarrow \mathbf{K}$ gap is still underestimated by 1.8 eV. As we increase the number of bath orbitals N_b to 64, DMFT produces a better description of all three band gaps and the errors are all within 0.3 eV, indicating the necessity of using a sufficient number of bath orbitals to reduce the bath discretization error. Even with a $1 \times 1 \times 1$ unit cell as the impurity, the DMFT(i26,b64) result is superior to the EOM-CCSD ($3 \times 3 \times 1$) result due to the larger amount of **k**-point sampling. By further increasing N_b to 128, we also demonstrate that the DMFT band gaps are converged to around 0.1 eV at $N_b = 96$. Thus, we believe our DMFT results for 2D h-BN to be well converged with respect to the bath size. The DMFT(i26,b96) calculation takes 1.5 hours to converge on 2 nodes with 28 CPU cores per node. Further obtaining the Green's function and DOS at each frequency point takes about 4.5 minutes. This should be compared to the computational cost of a full EOM-CCSD calculation with the $6 \times 6 \times 1$ **k**-point mesh, which takes about 40 hours to obtain 4 IP and EA roots at all **k** points.

We next show the local density of states (DOS) in Fig. 5.6, where the DOS is computed from the spectral function: $\rho(\mathbf{R} = \mathbf{0}, \omega) = \mathrm{Tr}\mathbf{A}(\mathbf{R} = \mathbf{0}, \omega)$. Here we compare DMFT with HF and $6 \times 6 \times 1$ EOM-CCSD. Since we employ only a single **k**-point mesh to minimize cost, we only obtain a finite set of excitation energies from EOM-CCSD. Consequently, we have applied a Lorentzian broadening to the IP- and EA-EOM-CCSD roots to generate the corresponding DOS spectrum, as an

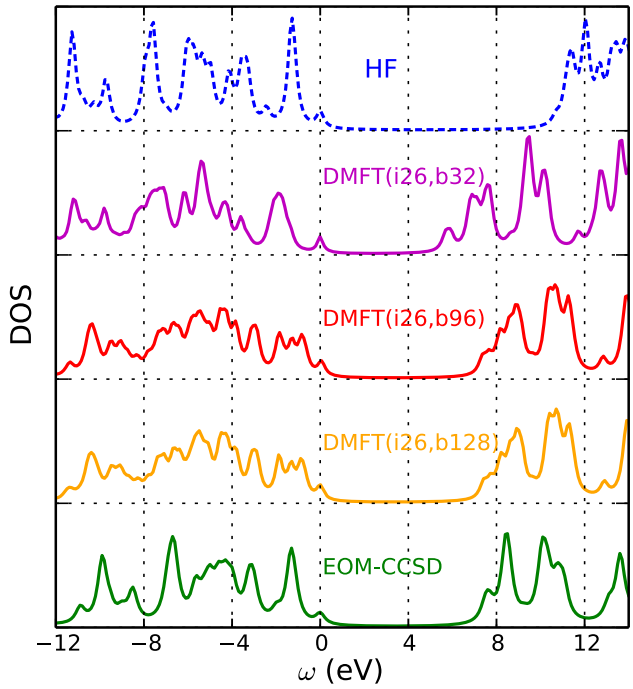

Figure 5.6: Local density of states of 2D h-BN monolayer. DMFT spectral functions are computed with a broadening factor $\eta = 0.2$ eV. EOM-CCSD ($6 \times 6 \times 1$) DOS is generated using a Lorentzian broadening.

approximation to the true CCSD-GF DOS in the TDL. As can be seen in Fig. 5.6, DMFT again significantly improves over HF. In addition to the much better band gaps, the DMFT DOS also has a better structure than the HF DOS. In particular, the DMFT conduction bands are almost identical to the EOM-CCSD ones, even for the high-energy bands. This is a result of including the high-energy virtual orbitals (PAOs) into the impurity problem. Comparing the DMFT(i26,b96) and DMFT(i26,b128) DOS plots, we find that the DMFT spectral functions are already well converged at $N_b = 96$.

On the other hand, the agreement between the DMFT DOS of the valence bands and that of EOM-CCSD is less perfect. Compared to EOM-CCSD, several valence peaks are broader in DMFT, such as the valence peak near the Fermi surface. To understand this behavior, we plotted the DMFT band structure of h-BN using the $N_b = 96$ data, as presented in Fig. 5.7. Compared to HF, we find that the point group symmetry at certain $\mathbf{k}$ points is broken in the DMFT band structure plot. For example, at the Γ point, there is a degeneracy in the highest valence band observed in both HF and EOM-CCSD, but this degeneracy is slightly broken in

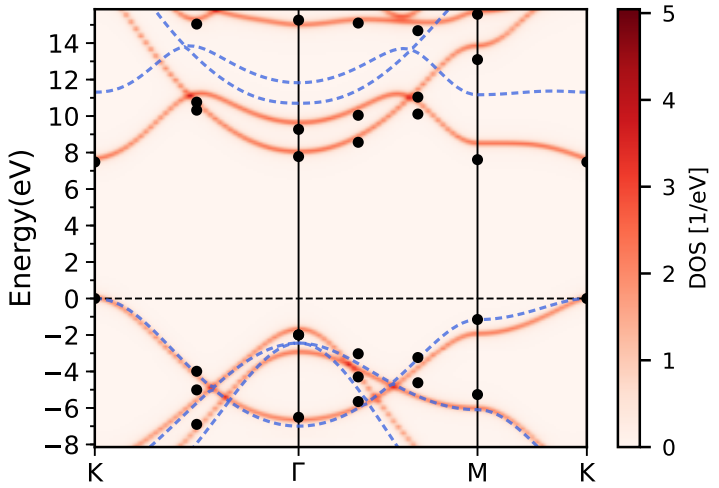

Figure 5.7: Band structure of 2D h-BN from DMFT(i26,b96) calculation with a broadening factor $\eta = 0.1$ eV (heat map). The blue dashed lines represent the HF band structure and the black circles are EOM-CCSD ($6 \times 6 \times 1$) charged excitation energies.

DMFT. This explains the broader DMFT valence bands in Fig. 5.6. We believe such behavior is due to a mismatch between the diagonal and off-diagonal parts of self-energy in DMFT: the diagonal part is computed from the impurity CCSD-GF, while the off-diagonal part is from the lattice **k**-point HF self-energy. Aside from the slight symmetry breaking, the DMFT band structure is in good agreement with the EOM-CCSD result.

Overall, however, the data demonstrates that our DMFT scheme works well in 2D h-BN. The DMFT procedure produces accurate band gaps and is also capable of modeling bands far away from the Fermi surface, even with a small number of bath orbitals ($N_b = 64$).

Bulk silicon

We next apply our DMFT implementation to the silicon crystal (Si). Silicon is a small band-gap semiconductor with delocalized valence electrons. Such a system presents a challenge to quantum embedding methods, including DMFT, as these methods all start from a local correlation approximation. Here, we assess the effect of impurity size on the description of spectral functions of bulk Si. Two different impurity sizes were considered: a $1 \times 1 \times 1$ unit cell and a $2 \times 2 \times 1$ supercell. The $2 \times 2 \times 1$ cell is the largest impurity size that can currently be handled using our

CCSD-GF solver. In the $1 \times 1 \times 1$ unit cell, there are 26 impurity orbitals, 8 of which are IAOs. Two Gauss-Legendre quadratures of $N_\omega = 4, 20$ ($N_b = 32, 160$) were used to show the effect of bath size on spectral functions. In the $2 \times 2 \times 1$ supercell impurity, there are 104 impurity orbitals. There we used a quadrature of $N_\omega = 4$ ($N_b = 128$). A $2 \times 2 \times 4$ **k**-mesh was employed for the larger impurity to generate a DMFT lattice $4 \times 4 \times 4$ **k**-mesh. We note that DMFT(i104,b128) should be directly compared to DMFT(i26,b32) to demonstrate the effect of impurity size, as these calculations share the same bath quadrature ($N_\omega = 4$) and similar bath discretization error.

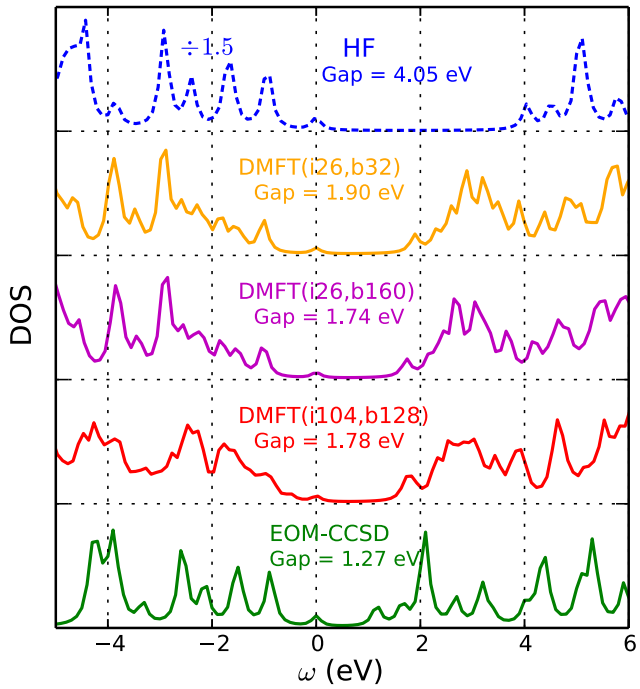

Figure 5.8: Local density of states of bulk Si. DMFT spectral functions are computed with a broadening factor $\eta = 0.1$ eV. The EOM-CCSD DOS is generated using $3 \times 3 \times 3$ **k**-point sampling and a Lorentzian broadening. The gap values correspond to the indirect band gap of $\Gamma \rightarrow \mathbf{X}$, and the EOM-CCSD gap is from a $4 \times 4 \times 4$ **k**-mesh calculation.

The computed local DOS of bulk Si are presented in Fig. 5.8. HF and EOM-CCSD results are included for comparison. A full $4 \times 4 \times 4$ **k**-point EOM-CCSD calculation for multiple IP/EA roots is very expensive, so we instead performed a $3 \times 3 \times 3$ **k**-mesh calculation. All **k** points in the $4 \times 4 \times 4$ **k**-mesh were sampled by shifting the $3 \times 3 \times 3$ **k**-mesh center. The final reference DOS was then generated by applying

a Lorentzian broadening. We also conducted a full $4 \times 4 \times 4$ **k**-mesh EOM-CCSD calculation to estimate the reference indirect $\Gamma \rightarrow \mathbf{X}$ band gap value, which we found to be 1.27 eV, as noted in Fig. 5.8.

DMFT(i26,b32) produces a better $\Gamma \rightarrow \mathbf{X}$ gap of 1.90 eV than HF, which overestimates the gap by 2.8 eV. Using a larger bath size of $N_b = 160$ further improves the DMFT gap to be 1.74 eV. However, the error of DMFT(i26,b160) is still around 0.5 eV, which is worse than the observed error of DMFT in 2D h-BN. In addition, the shape of the spectrum for DMFT(i26,b160) is not very accurate. These results support the observation that bulk Si is indeed a more difficult system for DMFT due to the stronger effects of the non-local interactions in such small band-gap systems. After increasing the impurity size, we find that DMFT gives better agreement with the reference EOM-CCSD spectrum. The DMFT(i104,b128) calculation finds the $\Gamma \rightarrow \mathbf{X}$ gap to be 1.78 eV, reducing the DMFT(i26,b32) error to 0.5 eV. This is also better than the $2 \times 2 \times 1$ **k**-point EOM-CCSD result, which estimates the $\Gamma \rightarrow \mathbf{X}$ gap to be 0.59 eV ($\sim$0.7 eV error). DMFT(i104,b128) does not produce a better band gap compared to DMFT(i26,b160) due to the insufficient bath size, suggesting that minimizing the bath discretization error is also important. Nevertheless, the DMFT(i104,b128) spectrum has an improved shape, especially in the valence region, where the bands have similar peak positions to the EOM-CCSD ones. Thus, bulk Si provides a good demonstration of the important role of impurity size in capturing the non-local self-energy in delocalized systems. However, even with the larger $2 \times 2 \times 1$ impurity, the DMFT results are still not completely accurate, indicating the need for both larger impurities and a better treatment of long-range interactions than the HF self-energy.

Nickel monoxide

We finally turn to discuss the prototypical strongly-correlated system, NiO. NiO has a type-II AFM phase below the Néel temperature (525 K), with ferromagnetic planes stacked in the [111] direction. Due to the partially filled d orbitals in Ni, spin-unpolarized DFT methods predict NiO to be a metal, and spin-polarized DFT (LSDA/GGA) significantly underestimates the band gap and magnetic moment. DFT+DMFT simulations with a single Ni $3d$ impurity have been shown to successfully reproduce features of the experimental spectral functions and band structure of NiO in the paramagnetic (PM) phase [224–230].

In this study, we use a unit cell of two Ni and two O atoms as the impurity in DMFT,

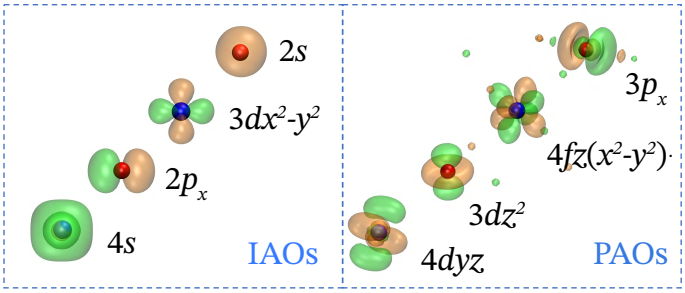

Figure 5.9: Representative IAOs and PAOs of NiO used in DMFT calculations within a unit cell. Ni and O atoms are marked in blue and red.

corresponding to 78 impurity orbitals. Compared to earlier single site studies, we can thus examine antiferromagnetic order within the cell, as well as the effect of all the interactions in the crystal bands. Some representative IAOs and PAOs in the cell are shown in Fig. 5.9. The IAOs include the projected $3s3p3d4s$ orbitals of Ni and $2s2p$ orbitals of O, and the PAOs include the remaining $4p4d4f5s$ orbitals of Ni and $3s3p3d$ orbitals of O. Since the $3s3p$ orbitals of Ni form very flat bands far below the Fermi surface, we do not couple bath orbitals to them, to reduce the computational cost. We also used the bath truncation technique described in Sec. 2.4 to remove very weakly coupled bath orbitals, setting the eigenvalue threshold to $\lambda = 0.005$ a.u. and $\lambda = 0.01$ a.u. for Gauss-Legendre quadratures of $N_\omega = 4$ and $N_\omega = 8$ respectively. This led to a significant reduction in the number of bath orbitals, e.g., from $N_b = 160$ to $N_b = 86$ in the DMFT(i78,b86)@Φ_{UHF} calculation.

To obtain an AFM solution in DMFT, we allowed spin symmetry to break by allowing different self-energies ($\Sigma^\sigma_{\text{imp}}(\omega)$) and hybridizations ($\Delta^\sigma(\omega)$) in different spin channels ($\sigma = \alpha, \beta$). The spin-unrestricted CCSD-GF (UCCSD-GF) impurity solver was employed to compute $\Sigma^\sigma_{\text{imp}}(\omega)$. We started from either spin-restricted or spin-unrestricted mean-field wavefunctions to construct the embedding problem. Spin-unrestricted HF (UHF) gives an AFM solution with a large band gap for NiO, as shown in Fig. 5.10. Starting from UHF, spin symmetry breaking happens already in the initial DMFT impurity Hamiltonian ($\mathbf{H}_{\text{imp}}$) and lattice HF self-energy. On the other hand, spin-restricted HF (RHF) with finite temperature smearing predicts NiO to be a metal (in PM phase), with no average local magnetic moment (Fig. 5.10). In this case, spin symmetry breaking is introduced *only* during DMFT self-consistency, which generates symmetry-broken $\Sigma^\sigma_{\text{imp}}(\omega)$ and $\Delta^\sigma(\omega)$.

In addition to starting from HF orbitals, we also explored the possibility of using

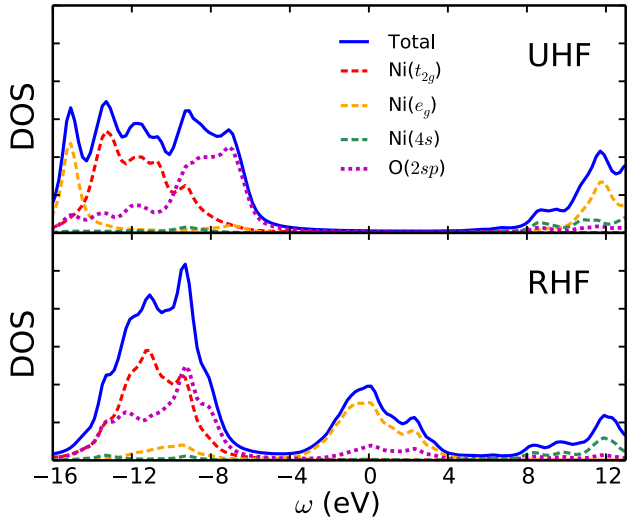

Figure 5.10: Local density of states of NiO from UHF and RHF. A broadening factor $\eta = 0.4$ eV is used.

DFT (LDA and PBE) orbitals to generate the DMFT impurity problem. We again emphasize that only the DFT orbitals were used here and no DFT Hamiltonians or self-energies enter into our DMFT calculations. That is to say, we still use the Fock matrix as the one-particle effective Hamiltonian, and the only difference is that the elements of the Fock matrix are evaluated using DFT orbitals. Since the local Fock self-energy can be exactly subtracted, there are no double counting errors in these DMFT calculations. One advantage of using DFT orbitals is that fully self-consistent HF calculations can be avoided, which is very expensive in large systems due to the quadratic scaling with respect to **k** points.

We present DMFT results on the band gap, magnetic moments and local charges of NiO in Table 5.4. The band gap is computed from the half maxima of the first valence and conduction bands of local DOS, as done in the XPS/BIS experiment [207]. Meanwhile, we also report the band gap values calculated from the valence and conduction peaks of the **k**-resolved DOS. The magnetic moments and local charges are calculated from the impurity UCCSD density matrix with atomic decomposition in the IAO+PAO basis. As can be seen, DMFT(i78,b86)@Φ_{UHF} improves the UHF band gap by 2.6 eV and produces an accurate magnetic moment. However, the band gap is still too large when compared to experiment (4.3 eV). This is likely because the off-diagonal (inter-cell) part of the self-energy from the inaccurate initial UHF solution has a large residual effect on the lattice Green's function. In

Table 5.4: Band gap (E_g), magnetic moment (m_{Ni}) and local charge (ρ_{Ni}) of NiO in the AFM phase. The first column of band gaps is computed from the half maxima of the first valence and conduction bands of the local DOS, as done in Ref. [207]. The second column of band gaps (in brackets) is computed from the valence and conduction peaks of the **k**-resolved DOS. The notation "@$\Phi_{\mathrm{HF/PBE/LDA}}$" indicates the underlying orbitals used to construct the Fock matrix in DMFT.

Method	E_g (eV)	m_{Ni} (μ_{B})	ρ_{Ni} (e)
UHF	- (11.6)	1.86	1.42
UPBE	- (1.3)	1.42	1.02
ULDA	- (0.6)	1.28	0.94
DMFT(i78,b50)@Φ_{UHF}	9.6 (9.4)	1.80	1.35
DMFT(i78,b86)@Φ_{UHF}	9.2 (9.0)	1.80	1.35
DMFT(i78,b52)@Φ_{UPBE}	7.4 (7.1)	1.65	1.12
DMFT(i78,b90)@Φ_{UPBE}	7.1 (6.5)	1.63	1.11
DMFT(i78,b52)@Φ_{ULDA}	6.5 (6.0)	1.63	1.10
DMFT(i78,b90)@Φ_{ULDA}	6.5 (5.8)	1.60	1.08
DMFT(i78,b56)@Φ_{RHF}	3.5 (3.3)	1.67	1.22
DMFT(i78,b98)@Φ_{RHF}	3.0 (3.1)	1.60	1.17
Exp	4.3 [207] (-)	1.77 [211],1.90 [190]	-

particular, this inaccurate off-diagonal self-energy leads to too large an amount of symmetry breaking in the initial impurity Hamiltonian, which cannot be completely corrected by the DMFT local self-energy. In contrast, when using UPBE orbitals, DMFT(i78,b90)@Φ_{UPBE} gives a better **k**-resolved band gap of 6.5 eV, suggesting that employing UPBE orbitals reduces the error in the off-diagonal HF self-energy. Using ULDA orbitals further improves the **k**-resolved band gap to 5.8 eV, although the error is still more than 1 eV. Overall, these results show that when starting from a spin-symmetry broken solution, our DMFT scheme is sensitive to the choice of underlying orbitals, which may lead to a variation of 3 eV in the predicted band gap of NiO. This sensitivity may be alleviated if charge self-consistency is further imposed outside of the DMFT loop [106, 231], which is absent in our current implementation. However, the systematic overestimation of the band gap suggests that besides charge self-consistency, non-local contributions to the self-energy need to be treated more accurately [232–235].

When we switch to a spin-restricted HF reference, the DMFT results are more accurate than the UHF-based DMFT results. DMFT(i78,b98)@Φ_{RHF} predicts a reasonable **k**-resolved band gap of 3.1 eV and magnetic moment of 1.60 μ_{B}. This superior performance can be attributed to the fact that the initial incorrect symmetry

breaking in the lattice HF self-energy and impurity Hamiltonian is avoided by using a spin-restricted reference. As a result, the spin symmetry breaking is solely determined by the accurate DMFT self-energy obtained from the UCCSD-GF impurity solver, leading to improved results, particularly for the spectral functions.

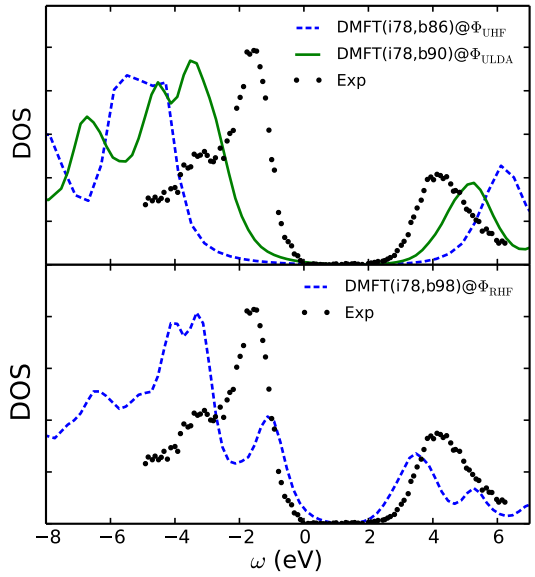

Figure 5.11: Local density of states of NiO in the AFM phase. The XPS/BIS experimental DOS is from Ref. [207]. The DMFT DOS is computed with a broadening factor $\eta = 0.4$ eV, and is shifted horizontally for an easier comparison to experiment.

We present the local DOS of NiO in Fig. 5.11. The upper panel shows that DMFT(i78,b86)@Φ_{ULDA} gives a similar spectral shape to experiment, although the band gap is larger and the first valence peak is broader. On the other hand, DMFT(i78,b90)@Φ_{UHF} spectrum has too wide a band gap. In the lower panel, the DMFT(i78,b98)@Φ_{RHF} result agrees well with experiment near the Fermi surface. However, the main valence peak is separated into two peaks, where the highest peak is around -3.5 eV and a shoulder peak appears around -1 eV. Such a two-peak structure is not observed in experiment.

To understand the deviations from experiment and to further study the character of the insulating gap, we plot the components of the NiO DOS in Fig. 5.12. From Panel 1 of Fig. 5.12a, DMFT(i78,b90)@Φ_{ULDA} predicts that the insulating gap is from a complicated charge transfer transition with mixed Mott character: the valence peak is of O $2sp$ and Ni t_{2g} and e_g characters, and the conduction peak is mainly of an e_g character with a small O $2sp$ contribution. On the other hand, it can be seen

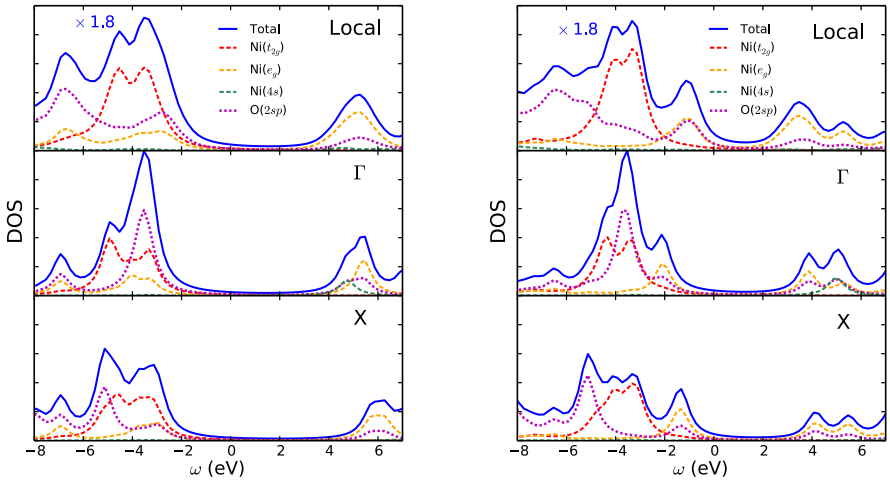

Figure 5.12: Components of NiO density of states from (a) DMFT(i78,b90)@Φ_{ULDA} and (b) DMFT(i78,b98)@Φ_{RHF} calculations. Panel 1 shows the local DOS, and Panels 2 and 3 show **k**-resolved DOS at Γ and **X** points.

in Fig. 5.10 that UHF predicts the insulating gap of NiO to be from a pure charge transfer transition from O $2p$ to Ni e_g. This comparison indicates that DMFT significantly corrects the positions of the Ni t_{2g} and e_g bands. Meanwhile, as shown in Fig. 5.12b, DMFT(i78,b98)@Φ_{RHF} also predicts mixed charge transfer and Mott character for the insulating gap, although the first valence peak has almost no Ni t_{2g} contribution. This indicates that the artificial shoulder valence peak near the Fermi surface arises because of a mismatch in the relative positions of the Ni t_{2g} and O $2sp$/Ni e_g bands. Once again, these results lead us to conclude that to obtain both the band gap and spectral shape accurately, we require either larger impurities or a more sophisticated treatment of the inter-cluster interactions. We also plot the **k**-resolved DOS in Panels 2 and 3 in Fig. 5.12. It can be seen that the O $2sp$ main valence peak is shifted by 2 eV at the **X** point compared to the Γ point. Interestingly, we find that the conduction band at the Γ point has a significant contribution from the Ni $4s$ and O $2sp$ orbitals. This has not been reported in previous DFT+DMFT studies but has also been found in quasiparticle self-consistent GW calculations [236].

5.6 Conclusions

In this chapter, we described *ab initio* quantum embedding schemes for density matrix embedding and dynamical mean-field calculations in solids, focusing on the practical implementation choices needed for an efficient computational scheme.

Our tests on the BN, Si, and NiO systems, that span a range of electronic structure, demonstrate that our implementation can handle both realistic unit cells and basis sets. The strengths of DMET and DMFT are most visible in the simulations of NiO, where the wide spread in magnetic behavior generated by different mean-field approximations is almost entirely removed in the subsequent DMET calculation. In more weakly correlated systems, more work is needed to improve the quantitative accuracy of DMET and DMFT arising from the treatment of excitations to non-valence orbitals and long-range screening effect, which are not fully embedded in our scheme. Overall, however, our results lead us to be optimistic that this computational framework provides a means to realize *ab initio* calculations on interesting correlated solids using quantum embedding.

Chapter 6

SYSTEMATIC ELECTRONIC STRUCTURE IN THE CUPRATE PARENT STATE FROM QUANTUM MANY-BODY SIMULATIONS

Based on the work published in *Science* **377**, 1192 (2022). Copyright 2022, American Association for the Advancement of Science. [114]

6.1 Introduction

Currently, we have a qualitative theoretical understanding of many electronic phases of matter. However, there remains a deficit in the quantitative understanding of correlated electron materials [70, 237]. This limits our ability to connect the atomic structure and composition to the electronic phenomena, as well to answer fundamental physical questions related to microscopic mechanisms. Here, we describe and apply a strategy to precisely simulate properties of a prototypical family of correlated electronic materials, the high-temperature superconducting cuprates, in their undoped, parent, electronic state. We directly approximate the solution of the *ab initio* many-electron Schrödinger equation instead of solving a low-energy effective model, within an approach that is numerically improvable without adjustable parameters. Using this strategy, we show that we can reveal the systematics of the cuprate parent state across a family of layered cuprate materials, connecting the observed low-energy physics to specific microscopic processes governed by the atomic and structural composition.

Among correlated quantum materials, the high temperature (T_c) superconductors remain a fertile source of new physics[17, 238–240]. We focus on the cuprates, where one finds the highest superconducting T_c in the mercury-barium cuprate family [4]. Although progress has been made in understanding the universal phase diagram through numerical calculations on lattice models, the understanding of properties of individual compounds remains largely empirical, with substantial difficulties in linking the observed trends to model parameters.

In principle, a quantitative understanding is simply a matter of many-electron quantum mechanics, but solving the Schrödinger equation beyond lattice models involves three challenges: the quantum many-body correlations, the thermodynamic limit

(TDL), and the high-energy degrees of freedom / long-range interactions of real materials. We here adopt a pragmatic computational framework where the challenges can be tackled simultaneously: *ab initio* solvers for the many-body problem beyond models [215, 241]; self-consistent quantum embedding to develop phases in the TDL [98, 100, 242]; and periodic quantum chemistry using local bases [81, 82] to efficiently treat long-range interactions and high-energy degrees of freedom. Each component has been individually tested in prior work, but the important feature of our combined strategy is that the solution process bypasses models with uncontrolled parameters; the only remaining parameters are the size of the computational cell, the basis size, and the level of the many-body solver. Thus, all aspects of the calculation can in principle be controlled towards exactness.

In this chapter, we describe the full application of this strategy to the *ab initio* simulation of a family of cuprates in their parent phase at zero temperature. Although the parent phase is qualitatively simple, and elements of our framework have been used to understand exotic physics in simplified models [24], obtaining quantitative material systematics and functional relationships even in the parent phase is a major challenge, which serves as a litmus test of the promise of our overall *ab initio* strategy. As we shall describe, our detailed simulations bring a new level of resolution to the electronic structure, with which we uncover direct links between the material specific physics and composition.

6.2 Cuprates and the parent state

Structure. The main structural feature of the cuprates is the two-dimensional CuO_2 (formally $[CuO_2]^{2-}$) square lattice plane [Fig. 6.1 (a)]. In different cuprates, the copper-oxygen plane is surrounded by other atoms and buffer layers in the vertical direction. We consider three specific compounds, in addition to layer-stacked idealized CuO_2 planes (geometries in Table F.1). The first is infinite layer $CaCuO_2$ (CCO) [Fig. 6.1 (d)], where calcium counterions intercalate between the CuO_2 planes in an infinitely repeating structure. CCO does not itself superconduct, due to difficulties in doping the material. However, high T_cs are observed in the related mercury-barium cuprates (the Hg-Ba-Ca-Cu-O family). Here, the CuO_2 plane is decorated by apical oxygens, which connect to buffers of Hg and Ba ions. Unlike in CCO, the buffer layers form large spacers between the copper-oxygen layers. Different mercury-barium cuprates can be synthesized with different numbers of CuO_2 planes between each buffer layer, leading to single-layer, double-layer, etc. cuprates. We consider two members in this family: $HgBa_2CuO_4$ (Hg-1201, single-

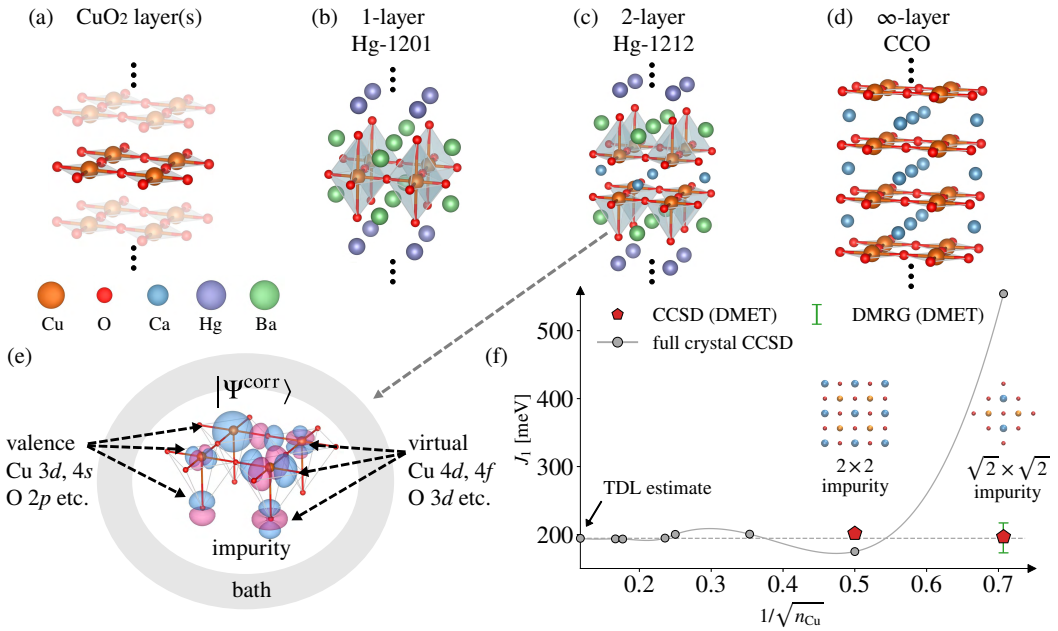

Figure 6.1: Structures and computational strategy. (a) $[CuO_2]^{2-}$ plane(s) in cuprates. (b) → (c) → (d): Relationship between single-layer Hg-1201 ($HgBa_2CuO_4$), double-layer Hg-1212 ($HgBa_2CaCu_2O_6$), infinite layer CCO ($CaCuO_2$); Ca layers replace the Hg-Ba-apical-O layers. (e) The *ab initio* density matrix embedding framework. The Hg-1212 lattice is divided into an impurity (e.g., the 2×2 cell) with the environment replaced by a bath; the atoms are represented by local valence and virtual orbitals, and the impurity problem is solved for the many-body wavefunction Ψ^{corr}. (f) Correlation and finite size effects in the nearest-neighbor Heisenberg exchange coupling J_1. We compare the exchange coupling (y axis) from a full crystal CCSD calculation as a function of CCO crystal size [plane side-length in units of Cu atoms, n_{Cu} (x axis)] in a small basis, to embedded calculations with two impurity sizes and two solvers DMRG, CCSD. The embedded 2×2 impurity is already close to the TDL, while the DMRG and CCSD impurity solvers agree well in the smallest impurity.

layer, $T_c = 97$ K) and $HgBa_2CaCu_2O_6$ (Hg-1212, double-layer, $T_c = 127$ K). Hg-1201 exhibits distorted octahedral Cu-O coordination [2 apical oxygens per Cu, Fig. 6.1 (b)], while each layer of Hg-1212 contains pyramidal Cu-O coordination [1 apical oxygen per Cu, Fig. 6.1 (c)]. Hg-1201, Hg-1212, and CCO are compositionally related by replacing Hg-Ba-apical O layers by Ca layers.

Parent state. Unlike conventional superconductors, the parent state of the cuprates is an antiferromagnetic (AFM) insulator with long-range order, due to the strong Cu d-d electron interaction. Typical Néel temperatures for the AFM state range from about 250 K (in Nd_2CuO_4) to 450 K (in $YBa_2Cu_3O_6$) [239], and only after doping does the ground-state enter the superconducting phase. It is generally thought

that the antiferromagnetism is to first order approximated by 2D nearest-neighbor (NN) Heisenberg-like physics. However, the 2D NN Heisenberg model does not reproduce the dispersion of the experimental spin-wave spectrum and questions remain as to the magnitude, sign, and material specific origin of corrections to the nearest-neighbor picture.

There have been many attempts to correlate properties of the cuprates in the superconducting phase (such as T_c) with structure, composition, and band structure [169, 243–247]. However, without a direct ability to simulate the material T_c with different parameters it is difficult to distinguish correlation from causation. Although there has been less focus on correlating properties of the parent state with physical features, many proposals relate the high Néel temperatures and strong exchange coupling in the parent state to the superconducting mechanism and other exotic physics under doping. Below, we establish causal, quantitative relationships between the magnetic features of the parent state and the atomic-scale structural and electronic features of the materials.

6.3 Theoretical techniques

Strategy. Previous numerical work on cuprate electronic structure [with a few exceptions e.g., [248, 249]] falls in two classes: (i) *ab initio* all electron simulations with a modest treatment of electron correlation [145, 250, 251], often used to derive low-energy effective models, and (ii) accurate many-body methods applied to low-energy effective models, to obtain phase diagrams and more exotic orders [161, 167, 252–256].

Our strategy is to use families of methods associated with the model studies of (ii), but technologically elevated to the fully *ab initio* Hamiltonians of (i). This bypasses the ambiguities of intermediate downfolded models, while allowing correlated physics to emerge. The three numerical components are the quantum embedding, the *ab initio* all-electron infrastructure, and the many-body solvers. Our technical setup uses density matrix embedding theory (DMET) to self-consistently embed a 2×2 supercell (impurity) of the cuprate material within an all-electron description, and we solve the resulting embedded impurity with an *ab initio* many-body approximation [coupled cluster (CC) theory]. To do so feasibly and reliably relies on recent advances and new techniques specific to this work, such as a sub-impurity formalism and improved DMET self-consistency algorithms for large impurities; improved *ab initio* matrix element generation; and careful solver bench-

marking against a massively parallel *ab initio* density matrix renormalization group (DMRG) implementation. Below we describe the quantum embedding and many body solvers; the *ab initio* infrastructure is discussed in Sec. 2.4.

Quantum embedding. This provides a framework for phases that emerge due to interactions [45], and includes dynamical mean-field theory and its relations [27, 28, 54], and the DMET [30, 35] used in this work. The material is separated into an impurity region and a bath that describes fluctuations out of the impurity, and their self-consistency yields emergent phases. The embedding becomes exact with increasing impurity size.

In previous work on the 1-band and 3-band Hubbard models, DMET has been extensively benchmarked against other methods, and for example, accurately resolves exotic order in the underdoped region [24, 33]. (The ability of DMET to capture exotic physics in doped lattices shines a light on the path from the *ab initio* studies of the parent state here to the physics of the doped materials). To move beyond models to the *ab initio* physics, we start from our recently introduced all-electron, full cell approach [98, 100, 242]. Here, the impurity is a supercell of the cuprate containing *all* atoms and orbitals, with all quartic interactions between the orbitals. In contrast to downfolded approaches with a handful of impurity orbitals and possibly simplified interactions [19, 28], our largest impurity (in Hg-1212) contains 48 atoms and close to 900 orbitals [Fig. 6.1(e)]. These orbitals include many "virtual" bands, which capture quantitative electron correlation effects and screening. Part of the reason why these large impurities are feasible is the DMET formulation itself, which bypasses expensive frequency dependent quantities. The other critical factors are the choice of solvers discussed below, and the periodic quantum chemistry infrastructure based on local atomic basis sets, which compactly discretize the virtual bands for electron correlation.

Ab initio many-body solvers. The quantum impurity problem in the full-cell approach is a many-body problem with hundreds of orbitals. This can be solved because many orbitals do not display strongly correlated physics. We use two impurity solvers in this work. The majority of the results are obtained using *ab initio* coupled cluster singles and doubles (CCSD) [128] solvers. Although approximate, they exactly treat clusters of (arbitrarily) strongly correlated particles, and have previously been shown to yield accurate results in various quantum impurity problems [98, 100, 215, 216, 242], particularly in ordered phases. To verify the accuracy of the CC approximation, we use a second solver, the quantum chemistry DMRG

[241, 257] to benchmark a subset of problems [see Sec. F.2].

Computational setup. The 2×2 supercell impurities are shown in Fig. 6.1 for the different mercury-barium cuprates. [In Sec. F.2, we also discuss a benchmark study of lanthanum copper oxide]. Every atom is represented in a valence double-ζ with polarization basis [def2-SVP [258]] e.g., each Cu is represented by $[5s3p2d1f]$ shells and each O by $[3s2p1d]$ shells, and the embedding lattice is chosen to be an $8\times8\times2$ lattice of the primitive cell. Large impurities (e.g., in Hg-1212) were further fragmented into smaller sub-impurities with up to 364 orbitals (280 impurity orbitals and 84 valence bath orbitals), and impurity solutions were obtained using CCSD or DMRG. (Unless otherwise indicated, data is from the CCSD solver; DMRG data is in Sec. F.2). The DMET equations were then solved with self-consistency and valence-shell lattice-impurity density matrix fitting.

Benchmarks. Within the above strategy, the only sources of error are from the finite size of the impurity (and embedding lattice), the approximate nature of the impurity solver, and the finite size of the local atomic basis. We have carried out extensive benchmarking to verify the specific approximations. In Fig. 6.1(f) we compare results from finite impurities to the TDL (which can be estimated from a full crystal calculation within a small local atomic basis) for the energy difference between the ferromagnetic (FM) and the AFM state ($\propto$ the NN exchange coupling J_1). We also show the deviation between this energy difference estimate from the *ab initio* DMRG and CCSD solvers in a small impurity where DMRG is tractable. Both sets of data illustrate that the TDL and many-body character of the physics is well-captured within the approximations in this work. Additional benchmarks (e.g. basis set convergence) can be found in Sec. F.2.

6.4 Results

Multi-orbital electronic structure

We start with general electronic trends across the series Hg-1201, Hg-1212, CCO, and $[CuO_2]^{2-}$ as a baseline to understand trends in the physics in later sections.

Order parameters and bonding. We first extract order parameters from the 2×2 computational supercell: charge, local moment, bond orders (from the off-diagonal elements of $\gamma_{ij} = \left\langle a_j^\dagger a_i \right\rangle$ where i, j label local atomic orbitals in the cell); and the spin correlation function $\langle S_z(0)S_z(r)\rangle$ measured across the full crystal [Figs. 6.2 (a) - (e)].

The key features are: (i) The ground-state is AFM with long-range order, with the

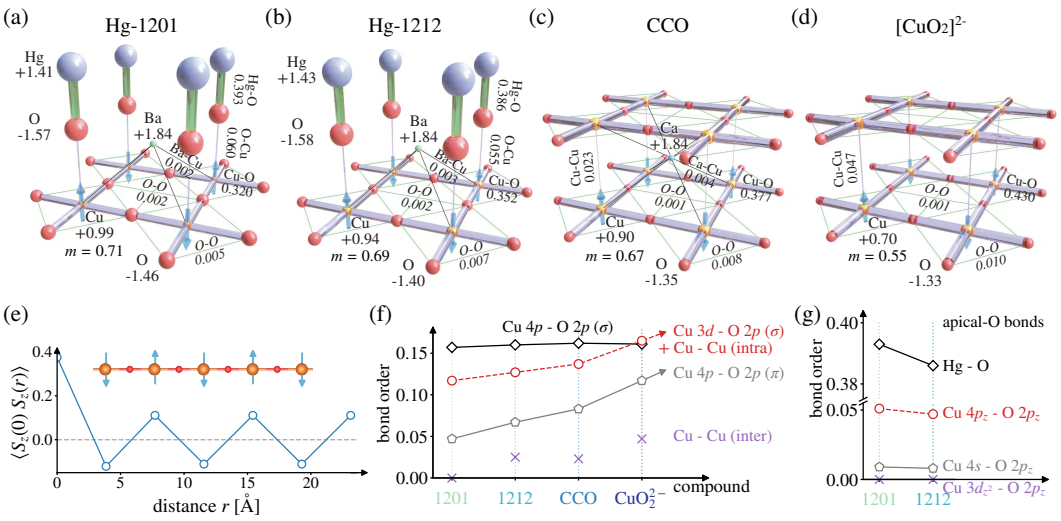

Figure 6.2: Charge, spin and bond orders. (a)-(d): Charge c, magnetic moment m and bond order b of different cuprates. Cu: yellow; O: red; Hg: violet; Ba: green; Ca: blue. Atomic sphere radius - number of electrons n (local charge $Z - n$ is labelled, Z: nuclear charge); arrow length - magnitude of local moment $m = n^{\uparrow} - n^{\downarrow}$; bond width - bond order b. (e) Spin-spin correlation function $\langle S_z(0)S_z(r)\rangle$ in CCO. (f) Cu orbital-resolved bond orders. (g) Apical O orbital-resolved bond orders. For more details, see Sec. F.3.

moment in the Cu half-filled $3d_{x^2-y^2}$ orbital. Cu $4s/4p$ occupancy reduces the total moment by about 10%. The unit cell moment ranges from 0.71 in Hg-1201 to 0.55 in $[CuO_2]^{2-}$. (ii) Charge is transferred from in-plane O orbitals to the other ions, with the degree of transfer increasing across the series. There is significant charge transfer to the Cu minority spin orbitals (as much as 0.3 electrons in $[CuO_2]^{2-}$). (iii) Ca and Ba buffer atoms in CCO, Hg-1201, and Hg-1212 are ionic, with Hg covalently bonded to the apical oxygen via the O $2p_z$-Hg $6s$, $5d_{z^2}$ bonds. Hg-1201 and Hg-1212 do not differ much with respect to the out-of-plane observables, but do differ for their observables in the CuO_2 plane. (iv) In-plane σ-bonding [Fig. 6.2(f)] is predominantly Cu $4p$-O $2p$ and does not differ much across the compounds. However, Cu $3d$-O $2p$ bonding and out-of-plane π bonding increase across the series, reflecting increasing in-plane $3d/4p$ hybridization. The change in bonding is not (solely) due to the structural changes (e.g., CCO and $[CuO_2]^{2-}$ have the same Cu-O bond-length but different bond orders) but instead reflects redistribution of charge from the buffer layers. (v) The apical oxygen bond order [Fig. 6.2(g)] decreases from Hg-1201 to Hg-1212, with the oxygen only weakly bound to Cu. Cu $4s$ and $4p_z$ contribute to apical bonding, with little $3d_{z^2}$ participation.

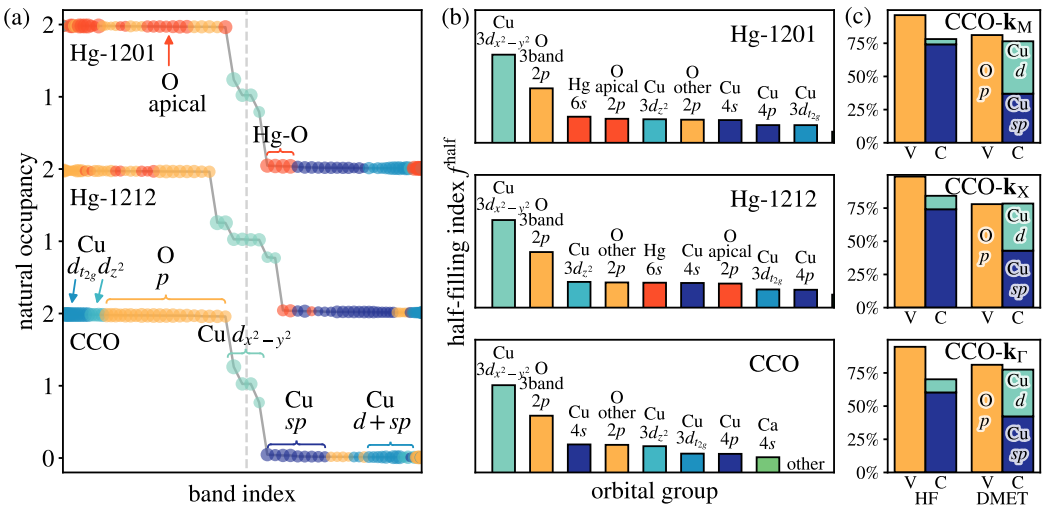

Figure 6.3: Natural occupancy distribution (eigenvalues of the single-particle density matrix) and quasiparticle character. (a) Occupancy of natural orbitals around the Fermi level (dashed line), from the spin-traced density matrix ($\gamma^{\alpha} + \gamma^{\beta}$) in Hg-1201, Hg-1212 and CCO. Orbital character denoted by colors and labels. (b) Half-filling index of the different local orbitals [Eq.(2.130)], measuring their importance in the most correlated orbitals of the calculation. (c) Orbital component analysis of the spin-resolved mean-field (HF) and correlated (DMET) top valence (V) and bottom conduction (C) bands of CCO at different $\mathbf{k}$ points (averaged from the 8 bands near the Fermi level), Γ: $(0,0)$; X: $(\frac{1}{2},0)$; M: $(\frac{1}{2},\frac{1}{2})$.

Natural occupancy distributions and effects of correlation. We obtain additional insight from the spin-resolved (γ^{σ}) and spin-traced ($\gamma = \sum_{\sigma}\gamma^{\sigma}$) single-particle density matrices (equal-time Green's functions) evaluated in the full crystal. These provide non-local and $\mathbf{k}$-space information on correlations. We first discuss the spin-traced single-particle density matrix. The eigenvalues (i.e., the natural occupancy distribution, sometimes called the momentum distribution function) and eigenvectors (natural orbitals) illustrate the degree of symmetry breaking and highlight the important degrees of freedom near the Fermi level. The spin-traced natural occupancy distribution together with the projected atomic character of the eigenvectors is shown in Figs. 6.3(a), (b). We see that the most important orbitals near the Fermi level are the classic 3-band orbitals - Cu $3d_{x^2-y^2}$ and O $2p_x$, $2p_y$. We also find no single next most important orbital: Cu $4s$, $4p$, $3d_{z^2}$, as well as the apical oxygen and Hg orbitals all contribute to a similar degree.

The spin-resolved natural occupancies and eigenvectors indirectly reflect the nature of the quasiparticles and the importance of dynamical effects. The eigenvectors with natural occupancies closest to the jump across the Fermi level can be viewed as

"pseudo"-valence band maximum (VBM)/conduction band minimum (CBM) states. Defined in this way, from Fig. 6.3(c), we see that the pseudo-VBM is dominated by O $2p_{x(y)}$, while the pseudo-CBM is dominated by Cu $3d_{x^2-y^2}$ (and the apical O and Hg bands in the Hg-Ba compounds). This classifies all the compounds as charge-transfer insulators.

We can further untangle the effect of interactions from pure single-particle physics by comparing the spin-resolved natural occupancies of the correlated calculation with that of a spin-polarized Hartree-Fock (HF) reference. The correlated spin-resolved natural occupancies are all quite close to 0 and 1 (Fig. F.14), i.e., the mean-field values, thus dynamical effects are small. However, the orbital components of the eigenvectors are very different between the mean-field and correlated distributions [Fig. 6.3(c)], indicating strong static effects. It appears in the AFM state, the effect of interactions on the quasiparticles is mainly static rather than dynamical, and can be largely captured via static screening of the interactions, correlation driven rehybridization of the orbitals, and renormalization of their energies.

Magnetic trends across the cuprates

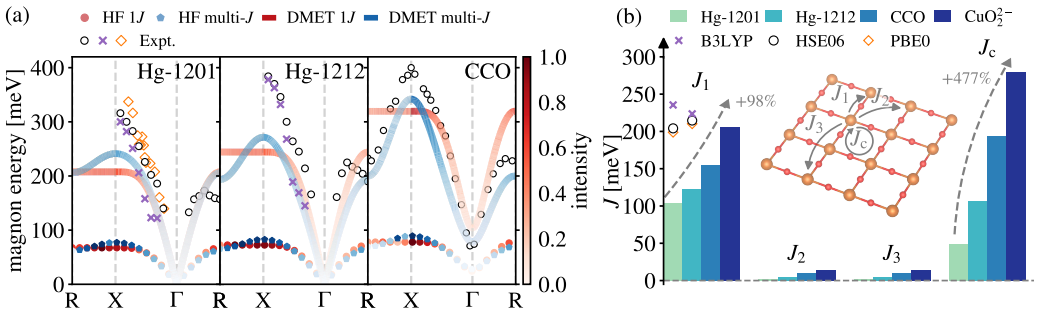

Figure 6.4: Spin wave dispersion of Hg-1201, Hg-1212 and CCO. (a) The 2D magnetic Brillouin zone is sampled along Γ: (0, 0), X: $(\frac{1}{2}, 0)$, R: $(\frac{1}{4}, \frac{1}{4})$, k_z is fixed at 0.46 to match the experimental conditions in CCO, and fixed at 0 for Hg-1201 and Hg-1212. NN Heisenberg ($1J$) and multi-J model curves are shown. The multi-J model includes a quantum renormalization factor of $Z_c = 1.219$ [259]. Experimental RIXS data is extracted from [260], [261] for Hg-1201 and Hg-1212; [262] for CCO. (b) Trends in the multi-J model parameters across the cuprate family. Hybrid density functional (PBE0, HSE06, B3LYP) results for the first two Hg compounds are also shown with symbols. For details, see Sec. F.4.

We next characterize the low-lying magnetic excitations across the series of cuprates. To do so compactly, we introduce a magnetic model (not to solve for the electronic structure, but for interpretation) and extract exchange couplings from our correlated

calculations of different spin-configurations: the AFM state, the FM state, and a spin-density wave state (Fig. F.2). From these we derive parameters for the NN Heisenberg model (J) and a multi-J Heisenberg model where the exchange couplings J_1, J_2, J_3 and J_c are related via the perturbation expansion of the 1-band Hubbard model (with only 3 free parameters). [A $3J^{\text{eff}}$ model where J_c is renormalized into the J_1, J_2, J_3 parameters can also be derived. In CCO, we also derive an interlayer $J_\perp$ using two AFM layer configurations. For a full discussion of all models and the spin-wave calculation see Sec. F.1]. The parameters are illustrated in Fig. 6.4(b) and tabulated in Tables F.14-F.17. We display the corresponding spin-wave spectrum from linear spin wave theory in Fig. 6.4 (a).

Spin-wave spectrum. In CCO the full experimental dispersion is available, while for Hg-1201 and Hg-1212 only part of the dispersion near the Γ point has been measured. As is well-known the NN Heisenberg model does not capture dispersion away from the Γ point, but the derived NN J agrees well with that derived from experiment by fitting near the Γ point; for example, in CCO, the NN J fit to DMET data yields $J = 155$ meV, compared to $J = 142, 158$ meV (the two numbers are from different experiments) [262, 263]. The multi-J model with *ab initio* parameters yields improved agreement across the experimental dispersion, illustrating the importance of long-range exchange. The discrepancies are largest near the X point $(\frac{1}{4}, \frac{1}{4})$, likely due to finite size effects in the embedding, although there are also confounding factors from the experimental setting in Hg-1201, Hg-1212 [Sec. F.4]. Compared to CCO, the Hg-Ba compounds display flatter dispersions, and we capture this in our derived spin-wave spectrum.

Magnetic parameters. Trends in the magnetic couplings of the multi-J Heisenberg model among the four compounds are shown in Fig. 6.4 (b). Across the series Hg-1201, Hg-1212, CCO, CuO_2^{2-}, all couplings J_1, J_2, J_3 and J_c increase significantly. J_1 roughly doubles and J_c increases by a factor of 5, illustrating (i) the importance of the buffer layers in the long-range exchange coupling and (ii) the increasing "delocalization" across the series of compounds. A recent resonant inelastic X-ray scattering (RIXS) experiment [260] suggests that J_1 increases significantly (by about 20 % - 30 %) from the single-layer Hg-1201 to the double-layer Hg-1212, similar to the increase in T_c. We find quantitative agreement with our correlated calculations, where Hg-1212 shows an increase in J_1 by about 18 %.

Effect of interactions. To understand the effect of interactions, we can compare to the mean-field HF results. These give almost flat dispersion curves, since the

J couplings are very small (e.g., $J_1 \sim 40$ meV), while the magnon energy at the Γ point is also lower than the experimental value. Thus, the observed magnetic energy scales require a careful treatment of electron correlation. As suggested in the last section, a large part of the effect of interactions can be captured by a renormalization of the low-energy band structure and interaction. Choosing a density functional treatment or Hubbard U parameter can mimic this, however, we do not find a single choice of functional or Hubbard U consistently or accurately reproduces the material trends. For example, moving from Hg-1201 to Hg-1212 should yield a significant increase in the exchange couplings, but from Fig. 6.4 (b) (symbol data), one finds J_1 decreases with the B3LYP functional, and increases only marginally with HSE06 (5%) and PBE0 (6%). In addition, J_1 is significantly overestimated by all the above functionals.

Untangling layer effects

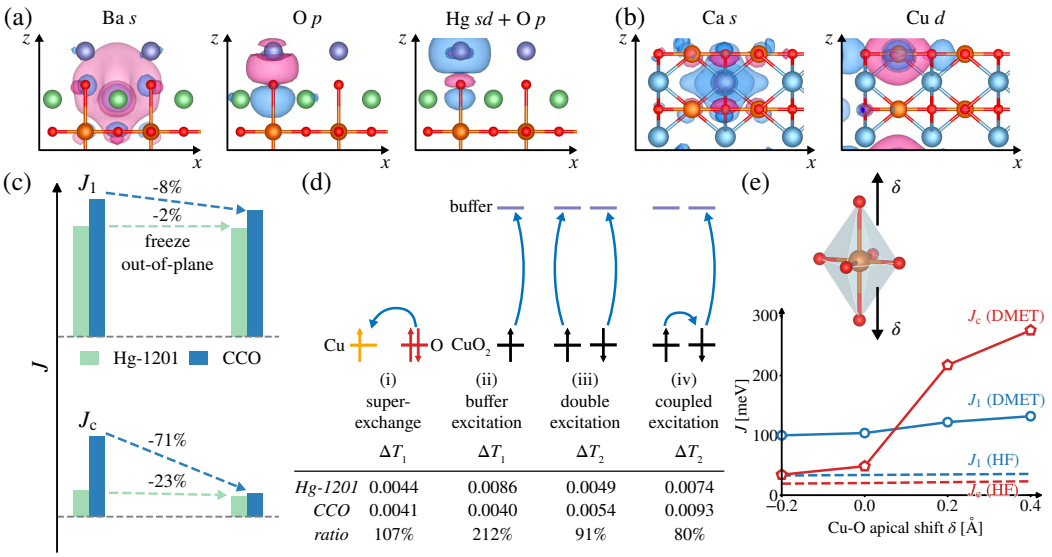

Figure 6.5: Effects of buffer layers. Representative out-of-plane orbitals (isosurfaces) in (a) Hg-1201 and in (b) CCO. (c) The effect of freezing fluctuations to out-of-plane orbitals on the NN magnetic coupling J_1 and cyclic exchange coupling J_c. (d) Excitations relevant to exchange pathways in cuprates: super-exchange is facilitated by excitations from in-plane oxygen orbitals to empty copper states (i); in Hg-1201, substantial excitations from the copper-oxygen plane to the buffer layer (ii) reduce super-exchange. The numbers (ΔT_1, ΔT_2) reflect the change in excitation weight upon unfreezing the buffer orbitals. (e) Influence of apical Cu-O distance on exchange coupling J_1 and J_c at the mean-field (HF) and correlated (DMET) level.

We now connect the microscopic correlated electronic structure with the trends in the magnetic physics observed above to derive mechanistic insights. As seen

above, changing the buffer layer leads to large changes in the exchange couplings (particularly for the non-local terms). However, this effect does not appear at the HF mean-field level. To verify that it originates due to fluctuations (electron correlation) with the buffer layers (and not simply via the effect of the electrostatic potential of the buffer layer on electron correlation within the cuprate plane), we first devise a procedure that allows us to switch electron correlation with the buffer layer orbitals on and off. To do so, we explicitly freeze excitations involving out-of-plane orbitals in the correlated impurity solver calculations [i.e. the impurity wavefunction excludes configurations with such excitations relative to the HF determinant, Sec. F.5]. Any changes from freezing and unfreezing these fluctuations therefore directly reflect the influence of electron correlation with the orbitals of the buffer plane.

Representative out-of-plane orbitals of Hg-1201 and CCO are shown in Fig. 6.5(a) and (b). The out-of-plane impurity orbitals consist of empty outer valence shells on Ca, Hg, and Ba, apical oxygen orbitals, and other orbitals that originate from the adjacent copper-oxygen plane. The Ca and Ba centered localized orbitals (4s and 6s) are similar in CCO and Hg-1201.

The changes in the J_1 and J_c from unfreezing the out-of-layer orbitals are shown in Fig. 6.5(c). In both compounds, the exchange couplings are decreased by freezing, but in CCO, the effect is stronger and J_c is especially strongly influenced by freezing, decreasing by as much as 71% in CCO. To understand this, we analyze the correlated impurity wavefunctions in CCO and Hg-1201. Shown in Fig. 6.5(d) are the changes in the weights of single-particle excitations ΔT_1 and connected two-particle excitations ΔT_2 upon unfreezing the buffer layer in the two compounds. Generally speaking, when the buffer layer is unfrozen, the increased excitation manifold increases screening and decreases the energetic penalty to excite from filled to empty states, such as the empty Cu and buffer layer states. In CCO and Hg-1201, we find that this increases the O $\rightarrow$ Cu excitation associated with superexchange [process (i) in Fig. 6.5(d)], increasing the exchange couplings. However, in Hg-1201, we see in addition a significant increase in excitations from in-plane Cu, O orbitals to the empty Hg, apical O states [process (ii)]. This change in the copper-plane to buffer excitation is more than twice as large in Hg-1201 than in CCO, and it depletes the ground configuration associated with in-plane exchange and reduces the effective non-local hopping by rehybridizing the Cu empty states [243], cancelling the enhancement of in-plane O $\rightarrow$ Cu excitations, and yielding an aggregate small change in exchange coupling upon unfreezing the buffer orbitals [Sec. F.5]. Note

that this also explains why the exchange couplings of Hg-1212 lie in between those of Hg-1201 and CCO, as the buffer suppression of in-plane super-exchange occurs via a single buffer layer in Hg-1212 versus two on either side in Hg-1201. The analysis also reveals (smaller) differences between the compounds in the connected two-particle fluctuations involving the buffer [processes (iii), (iv)]; these are material specific effects that cannot be folded into a static renormalization. Finally, in Fig. 6.5(e) we show the effect on the exchange coupling of increasing the apical oxygen distance in Hg-1201, both at the mean-field level and at the correlated level. Consistent with the above mechanism, we find that increasing apical oxygen distance removes the buffer suppression effect in the correlated calculation (increasing the exchange coupling), but makes little difference in the mean-field calculation, as fluctuations must first renormalize the energies of the empty states for them to be accessible.

6.5 Concluding remarks

We have demonstrated that through a numerical strategy combining quantum embedding, *ab initio* quantum solvers, and periodic quantum chemistry, we can determine at the many-body level, material specific correlated electron structure in the parent state of the cuprates. This reveals trends in the multi-orbital bonding, correlation effects in the Fermi distribution and quasiparticles, and gives a quantitative description of the low-energy magnetic excitations. Across a series of homologous mercury-barium and calcium cuprates, the systematic trends in the nature of the magnetic exchange can be explained through the analysis of the many-body state, which uncovers a competition between super-exchange and plane-to-buffer excitation processes.

A general observation is that while the interactions are strong, many of their effects in the parent state can be renormalized into a static low-energy theory. This supports the long-standing practice of interpreting physics in this region through simple band-structures and static interaction parameters. However, we also find that empirical approaches to determine this renormalization do not have the accuracy to capture the trends amongst the materials, unlike the controlled many-body approaches used here.

A strength of the many-body approach is that we can interrogate individual electronic processes, and our *ab initio* formulation allows us to trace these processes beyond models to the individual atomic orbital level. We use this capability to untangle the

links between layer composition and magnetic exchange. In prescient work, it was conjectured that the range of magnetic exchange is related to electronic processes involving an effective apical conduction band, and that this further correlates with the superconducting transition temperature [243]. We now have a direct picture of the first part of this conjecture, with rich atomic-scale and many-body resolution.

Components of the numerical strategy in this work have previously been used to describe exotic phases in models. The success of the current *ab initio* realization for cuprate parent states thus extrapolates to the exciting prospect that a similar approach may eventually yield a quantitative picture of more complex cuprate phases. If that is the case, we may be able to answer the second part of the above and similar conjectures about superconducting properties, through a direct *ab initio* simulation of the superconducting orders and the energy scales of the cuprates in their doped states.

Chapter 7

SUPERCONDUCTING STATES IN DOPED CUPRATES FROM AB INITIO QUANTUM EMBEDDING

This chapter presents work that has not been published before.

7.1 Introduction

We have shown that in both the one-band (Chap. 3) and the three-band model (Chap. 4), quantum embedding can provide reasonable phase diagrams in either magnetic or superconducting orders. In addition, we already see that the oxygen degrees of freedom are heavily involved in the d-wave superconducting orders. It is of great interest to see whether more degrees of freedom in the realistic crystal structures can participate in the phase diagram. In the meantime, we have provided an *ab initio* perspective on the magnetic trends in different cuprate parent states (Chap. 6). Following the roadmap in Sec. 1.2, we now have all components of the *ab initio* simulations of high-T_c superconductivity and attempt to predict the material-specific physics in the doped cuprates.

In conventional superconductors, the isotope effect provides decisive evidence for the electron-phonon coupling "glue" of the Cooper pair. In HTSCs, we also aim to search the clue of their superconducting mechanism. There are two important experimental observations that shed light on the possible superconducting mechanisms. One is the pressure effect, i.e., how T_c changes with respect to the external pressure the crystal. For most conventional superconductors, the pressure makes the T_c lower. This can be understood from Eq. (1.1). Although the lattice stiffness will increase and the density of states N_F remains essentially unchanged, the electron-phonon coupling g actually is weakened and therefore reduces the T_c. For HTSCs, how these factors influence the T_c is still not clear. Although there is anisotropy on three lattice vectors, most existing experiments suggest a positive $\mathrm{d}T_{c,\max}/\mathrm{d}p$ in the 2D-CuO_2 plane directions [239]. For example, the tri-layer $HgBa_2Ca_2Cu_3O_{8+\delta}$ (1223) compound also achieved a higher T_c of 164 K under 30 GPa pressure than under the ambient pressure (133 K) [264]. Therefore, we will explore this effect using the *ab initio* quantum embedding by changing the pressure.

The other important experimental fact is the layer effect. As we have shown in

Chap. 6, cuprates with different layers of CuO_2 and different buffer layers in a unit cell, have different T_c. For instance, the Hg-based cuprates have an interesting trend in T_c, from the single-layer compound Hg-1201 (97 K) to the double-layer Hg-1212 (127 K), to the tri-layer (133 K). However, the T_c will decrease if more than 4 layers of CuO_2 exist in a unit cell [244], possibly due to the imbalanced doping charges in different layers. One may also wonder whether we can predict the superconducting strength of the infinite-layer compound CCO and see if it can reach higher T_c.

Besides breaking the particle-number symmetry (see the GSO formalism in Sec. 2.5), one have to deal with the complexity of atomic modeling of the dopants since the parent state does not show any superconductivity. We will discuss the modeling of the doped cuprates in Sec. 7.2.

In this chapter, we focus on the application of the *ab initio* superconductivity formalism to the doped cuprates. As we shall describe, the superconducting states can spontaneously emerge not only in the model system but also in the realistic materials with doping. We showed that the d-wave superconducting magnitude increases with the pressure applied to crystals and the trend connects to the exchange coupling J. Furthermore, we also explore the buffer layer effect in the single-layer and infinite layer compounds.

7.2 Computational details

Atomic modeling of doping

The hole or electron doping of cuprates is generated by introducing substitution of buffer layer cations or additional anions. One famous example is the hole doping of La_2CuO_4 by replacing some of the La (III) ions using Sr (II), which effectively put a hole to the system. Another example is the hole doping of Hg-based cuprates, which introduces additional oxygen at the Hg-plane, such that some electrons of the CuO_2 plane is removed. The ideal way to simulate such doping is to use the supercell that explicitly includes the dopant atoms. Unfortunately, the supercell method is very expensive in practice and only high concentration of doping is possible, especially for methods beyond DFT.

To allow arbitrary doping concentration, the simplest way is the *rigid band approximation* (RBA) that directly dopes the hole or electrons in the system. This has the same spirit as doping in lattice models, since they both directly modify the number of electrons in the system. The tricky part in the *ab initio* system is the treatment of the Coulomb integral. Because of the additional charges, the electrically neu-

tral condition of the crystal is violated. One has to remove the divergent part of Eq. (2.35) by an additional neutralizing background charge.

Another method is the *virtual crystal approximation* (VCA) [265, 266], where the nuclear attractive potential is a simple mixing of different site compositions, e.g. if a lattice site has x probability being occupied by atom A, and $(1-x)$ probability by atom B, the VCA potential immediately follows,

$$\bar{H}_{\text{nuc}}^{\text{VCA}}(\mathbf{r}) = xV_{\text{nuc}}^{\text{A}}(\mathbf{r}) + (1-x)V_{\text{nuc}}^{\text{B}}(\mathbf{r}) \tag{7.1}$$

This approximation is still very crude as one can imagine the potential generated by a half-occupied oxygen ($Z = 8$) site is fundamentally different to the potential from a Be atom ($Z = 4$). A rigorous way to study the disordered system can be established by Green's functions G. One representative method is the coherent potential approximation (CPA) [267, 268], which introduces a single-site effective potential $\bar{\epsilon}$ that generates an effective medium Green's function $\bar{G}$. The replacement of the coherent potential $\bar{\epsilon}$ by a real site energy ϵ, on average, does not change the effective Green's function on a single site i,

$$\langle G_{ii} \rangle = \left\langle \left[\bar{\epsilon}_i - \epsilon_i + \bar{G}_{ii}^{-1} \right]^{-1} \right\rangle = \bar{G}_{ii} \tag{7.2}$$

For the current stage, we consider mainly the RBA and VCA in the chapter and leave supercell method and CPA to future development. The total lattice is neutral and the number of electrons is kept as an even integer (although the number of electrons per cell is typically a fractional number). We use a 2×2 supercell to allow superconducting orders. If we define the doping concentration as the number of additional charge per Cu, then this allows a minimal doping concentration of $1/(4n_{\mathbf{k}})$, where 4 is the number of Cu per cell. For VCA calculations of CCO, the VCA potential mixing happens at the Ca ion, whose nuclear charge is modified according to the doping.

Mean-field settings

The single particle mean-field (SCF) calculations (HF, DFT) were conducted in crystalline Gaussian bases using the PySCF package [82, 138], and were cross-checked with plane wave basis calculations using the VASP package [269–273].

For CCO and Hg-based cuprates, we used correlation consistent double-ζ basis GTH-cc-pVDZ (specially optimized for the solid-state calculations) and used the GTH pseudopotential for the core electrons [192, 193]. The basis then consists of

$3s3p2d1f$ shells for Cu, $2s2p1d$ for O, $3s3p2d$ for Ca, $3s3p3d1f$ for Hg and $4s3p2d$ for Ba. GDF was used to compute the two-electron integrals. We used a self-optimized Gaussian basis as the density fitting auxiliary basis of Cu, O and Ca; and used def2-TZVP-RI basis for the auxiliary basis of Hg and Ba ($n_{\text{aux}} \sim 5n_{\text{AO}}$).

For the plane wave basis calculations, a projector augmented wave (PAW) [273, 274] representation was used to treat the core electrons and we used a plane wave kinetic energy cutoff of 500 eV.

We sampled the Brillouin zone with a Γ-centered $\mathbf{k}$ mesh: $4 \times 4 \times 2$ for the 2×2 supercell of the single layer compounds CCO and Hg-1201.

All mean-field calculations used a Fermi-Dirac smearing of 0.2 eV. All mean-field calculations were converged to an accuracy of better than 10^{-8} a.u. per unit cell.

We used the PBE0 [275] hybrid functional for all doping RBA and VCA concentrations. The VCA is implemented by directly modifying the nuclear charges of Ca. All calculations are unrestricted so that the AFM order can be stabilized at the DFT level. HF calculations are also performed. However, due to the poor description of HF in the doped states, we use PBE0 as the DMET starting point.

DMET settings

All DMET routines, including the bath construction, integral transformation, solver interface and correlation potential fitting, are implemented in the LIBDMET package [98, 180]. To remove core orbitals, which make the bath construction unstable and increases computational cost, we froze the lowest mean-field bands ($3s3p$ bands for Cu and Ca, $2s$ bands for O, $5s$ bands for Ba); and we also froze the Cu $4f$ and O $3d$ virtuals to further reduce the cost.

We added the correlation potential u to the CuO_2 three-band orbitals and *only* fit the three-band orbital anomalous blocks of the density matrices, i.e., $\langle a_{i\alpha} a_{j\beta} \rangle$ where $ij \in$ 3band orbitals (and the self-consistency of the normal magnetic part is not considered in this work). We also enforce the C_{2h} symmetry of u since we do not consider inhomogeneous orders. The initial guess of u is chosen as a d-wave pattern on Cu $3d_{x^2-y^2}$ orbitals with a small amplitude 10^{-3}. The convergence criterion on the DMET self-consistency was chosen such that the maximal change of an element in u was less than 5×10^{-4} a.u..

In the DMET mean-field and correlation fitting, a small smearing of $\beta = 1/k_{\text{B}}T = 1000.0$ is added to the lattice.

Solver settings

We used the Newton-Krylov GCCSD methods implemented in MPI4PYSCF [133] as solvers. The CCSD T and Λ equations were converged to a residual smaller than 10^{-4} a.u.

The largest embedding problem we treated using the GCCSD solver was of size (376o, 188e), with multiple such size fragments solved in the multi-fragment embedding formalism.

Mean-field basis set completeness

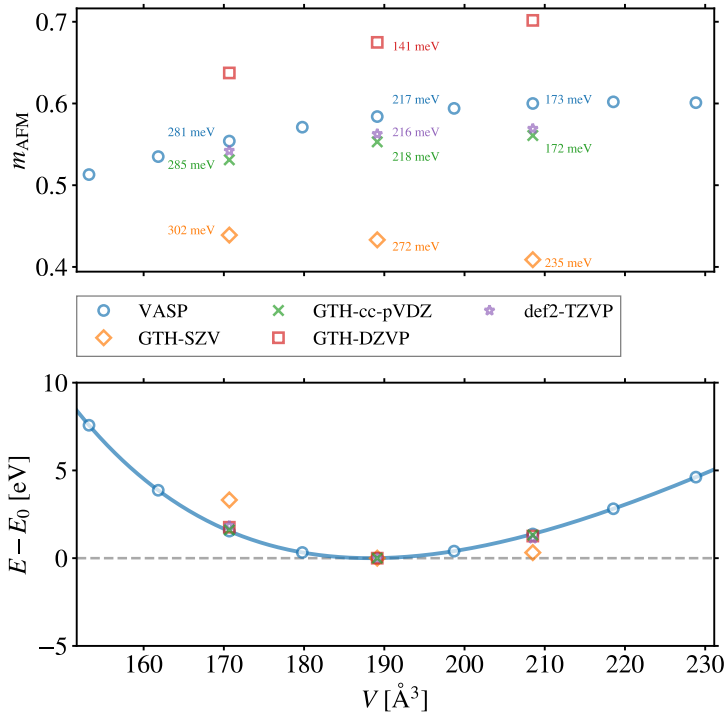

Figure 7.1: Mean-field basis check on the equation of state, magnetic moment m_{AFM} and magnetic exchange coupling J of CCO using unrestricted PBE0. J's are labeled as numbers.

We test different bases on CCO using unrestricted PBE0. From Fig. 7.1, it is clear that all basis beyond single-ζ level provide reasonable Birch-Murnaghan (B-M) equation of state (EOS) [204, 205]. The single-ζ basis (GTH-SZV), however, is too small to give the correct EOS.

In terms of magnetic properties, there is a decreasing trend in the magnetic moment when pressure increases (volume decreases); and there is a significant increasing trend of magnetic coupling J. The single-ζ basis trend is reversed, although the

J trend is qualitatively correct. The GTH-DZVP basis has a qualitatively correct trend but the absolute number of J (141 meV) is still far away from the plane-wave reference (217 meV). Optimized GTH-cc-pVDZ basis and all-electron triple-ζ-level def2-TZVP basis are both good agreement with the plane-wave reference (error in $\Delta J < 5$ meV). We therefore in the following use the double-ζ level GTH-cc-pVDZ basis as it best balances the accuracy and efficiency.

7.3 Results

Pressure effect

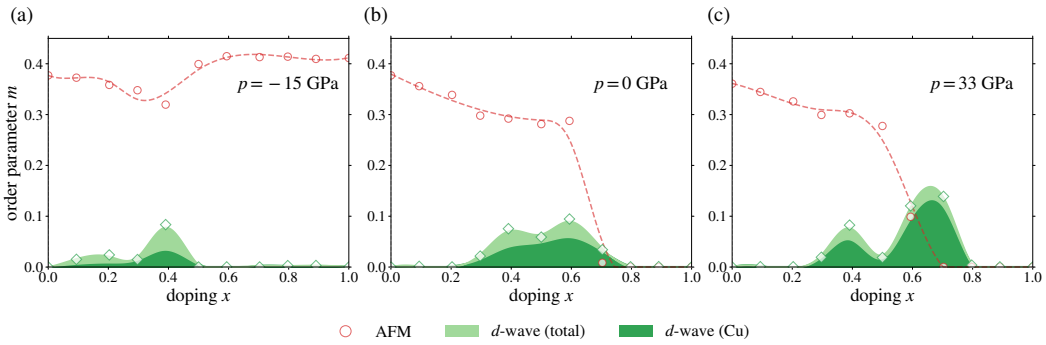

Figure 7.2: Pressure effect on hole-doped cuprates using DMET @ PBE0 + RBA. We consider three pressures, -15 GPa (left), 0 GPa (middle, the experimental structure) and 33 GPa (right). The pressure is applied to the horizontal ab plane.

We consider the pressure effect on CCO. The pressure is introduced by changing the lattice parameters in a and b axes uniformly. The hole doping is introduced through the RBA and VCA to the system. We show three pressure points in Fig. 7.2, corresponding to $p = -15$ GPa ($V = 209$ Å^3), $p = 0$ GPa ($V = 189$ Å^3) and $p = 33$ GPa ($V = 171$ Å^3). The negative pressure is hypothetical but in principle can be realized by chemical pressure or substrates with larger lattice constant. The magnetic and superconducting orders are plotted as a function of doping x (number of holes per Cu).

The AFM order decreases with respect to the doping concentration (for $p \gtrsim 0$), similar to what we have seen in the one-band and in the three-band models. However, the dropping of AFM order is generally slower than that in the experiments (and in the model calculations). There are several confounding factors in this slower decay. (i) It can be partly attributed to the distribution of the doped holes. In a realistic material, the doping charges will not completely fall into the CuO_2 plane, but will have substantial population on the buffer atoms. Of course, this is also related to the atomic models of the doped materials, where VCA and RBA are not as

accurate as the supercell approach. Nonetheless, the supercell approach is unlikely to have a faster decay of the AFM order, as the doped charges are even harder to move to the CuO_2 plane. (ii) The screening effect in realistic materials is not fully considered in the quantum embedding approach. The 2×2 supercell may not be large enough to take into account all long-range correlations. Also, we do not consider the self-consistency of the AFM order in this work. In the model systems, the screening effect is renormalized to the model parameters and thus has a faster decay. (iii) In experiments, the order parameters are measured in a long-range and thermo-averaged sense, meaning that the local orders may still exist. If we want to fully reproduce the experimental observations, it may require a larger supercell to consider the ensemble average of the inhomogeneous orders.

In general, the AFM order decay faster when pressure is applied (the extreme case is the negative pressure, where the AFM order does not vanish even with large doping $x > 0.5$). This is similar to the trend of the magnetic layer effect from Hg-1201 to CCO, where the stronger covalent bonding makes the J larger, but the magnetic moment smaller.

It is clear that there is SC dome(s) when doping happens. In some sense, we numerically verified that the theoretical prediction of the d-wave superconductivity in the lattice models is not an illusion, but is also valid in the *ab initio* settings. The d-wave order primarily consists of Cu-d characters (and in particular $3d_{x^2-y^2}$), the oxygen contribution is generally smaller and is more evident when pressure is low. One interesting feature is that we sometimes see a two-peak structure in the SC orders. It could be related to the different d-wave atomic characters, or the influence of AFM strength (i.e., one with a large AFM order, the other with a small AFM order).

It is interesting to see the SC order increases with respect to the pressure, in agreement with the experimental observations (T_c increases when pressure is applied to the CuO_2 plane). Here, we analyze the cause of the phenomenon. For the same compound, the doping charge distribution is largely similar, and therefore, the main change in the electronic parameter is the magnetic parameter (from Fig 7.1, we see that there is a significant change in J from 172 to 285 meV). A related fact is that the SC order always appears when the magnetic order starts to decay. Our result then supports the AFM fluctuation as the driving force of superconductivity (i.e. the ω_0 in T_c is related to the magnetic energy scale), and J is a good descriptor for the SC strength with pressure. The T_c-J relation has been proposed

recently by experiments [260] (see also the theoretical discussion in the three-band models [276]).

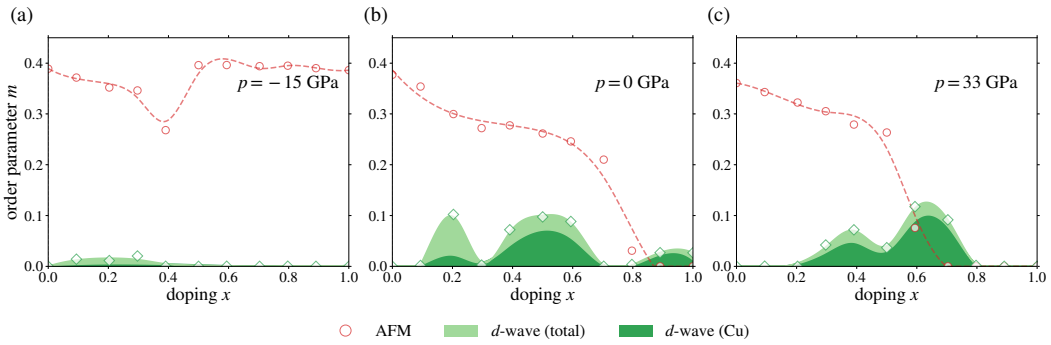

Figure 7.3: Pressure effect on hole-doped cuprates using DMET @ PBE0 + VCA. We consider three pressures, -15 GPa (left), 0 GPa (middle, the experimental structure) and 33 GPa (right). The pressure is applied to the horizontal ab plane.

In Fig. 7.3, we consider the VCA modeling of the doping holes. The general features, such as the decay of AFM orders, the emergence of SC dome(s), SC strength increases with pressure, are almost the same as the RBA. This indicates the robustness of our order parameter calculations. One interesting feature is that in the VCA, the SC order is very weak in the negative pressure case, possibly owing to the fact that fewer charges go the CuO_2 plane compared to the RBA.

Layer effect

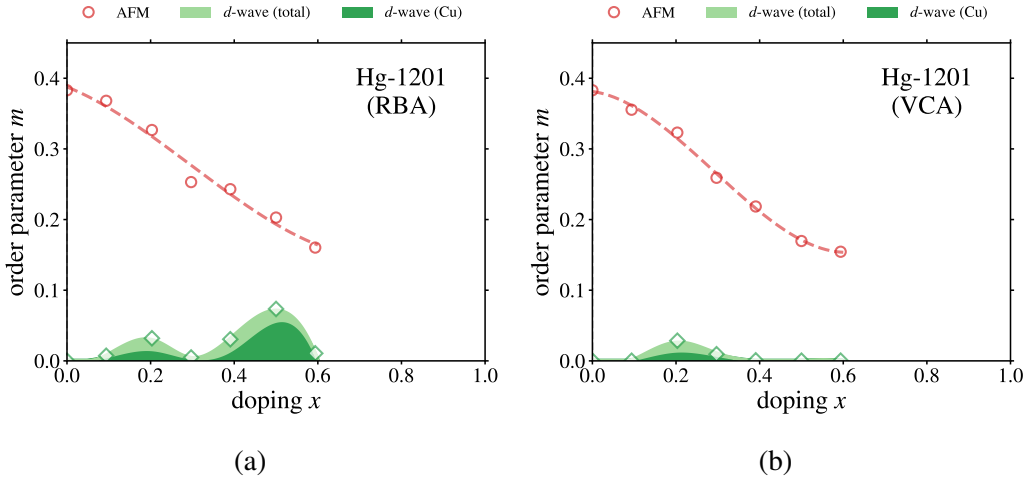

Figure 7.4: Layer effect on doped cuprates using DMET @ PBE0 with dopants simulated by (a) RBA and (b) VCA.

In Fig. 7.4 (a), we consider the Hg-1201 using RBA. It shows a slightly smaller SC

dome, seems to suggest the same trend of magnetic properties. However, we have not converged the points larger than $x > 0.6$. At the current stage, we can not draw decisive conclusions on the layer effect. There is more complexity, since the doping charge distribution is very different to that in CCO. We have shown that the RBA and VCA results of CCO are quite similar, but it is not the case for Hg-1201 (Fig. 7.4). In CCO, the buffer layer contains only Ca atoms and most of the doped charges enter into the CuO_2 layers, while in Hg-1201, the additional charges from the oxygen atoms have a greater effect on the buffer layer and make the phase diagram different. We see that in Fig. 7.4 (b), only a small SC region exists around $x = 0.2$. The results of Hg compounds then raise the necessity of careful assessment of different atomic modeling approaches for the doping phenomena.

Analysis on multi-orbital pairing orders

We first consider the orbital components of the d-wave parameter as a function of doping x (see Figs. 7.5 and 7.6). The largest component is the nearest $3d_{x^2-y^2}$-$3d_{x^2-y^2}$ coupling, which verifies the conclusion in the three-band Hubbard. The other important components are $3d_{x^2-y^2}$-$4s$, $4d_{x^2-y^2}$-$3d_{x^2-y^2}$ and $4s$-$4s$. For oxygen couplings, the important ones are $2p$-$2p$ and $2p$-$3p$. The results then suggests that for an accurate simulation, one should at least use a double-ζ-level basis. We also observed the change in the orbital characters during the doping. For example, the $3d$-$4s$ coupling is important at $x = 0.2$, whereas the $3d$-$4d$ and $4s$-$4s$ couplings become more important around $x = 0.5$. To some extent, this explains the different SC peak structures in Fig. 7.3 (b).

We then discuss the orbital components of the s-wave parameter (see Figs. 7.7 and 7.8). Overall, the s-wave order is much smaller than the d-wave one, especially for the Cu couplings. The s-wave, if can be observed in experiments, should more closely relate to the oxygen degrees of freedom.

7.4 Conclusions

The superconductivity in realistic materials is simulated for the first time without relying simplified models. The pressure effect and layer effects can be captured by the *ab initio* quantum embedding approach and supports the proposals of the relation between magnetic parameters and T_c. We also performed the orbital-character analysis on the d-wave and s-wave SC pairing order parameters, which highlights the orbital character evolution during the doping process. The work provides a promising route to study the material-specific physics of high-temperature

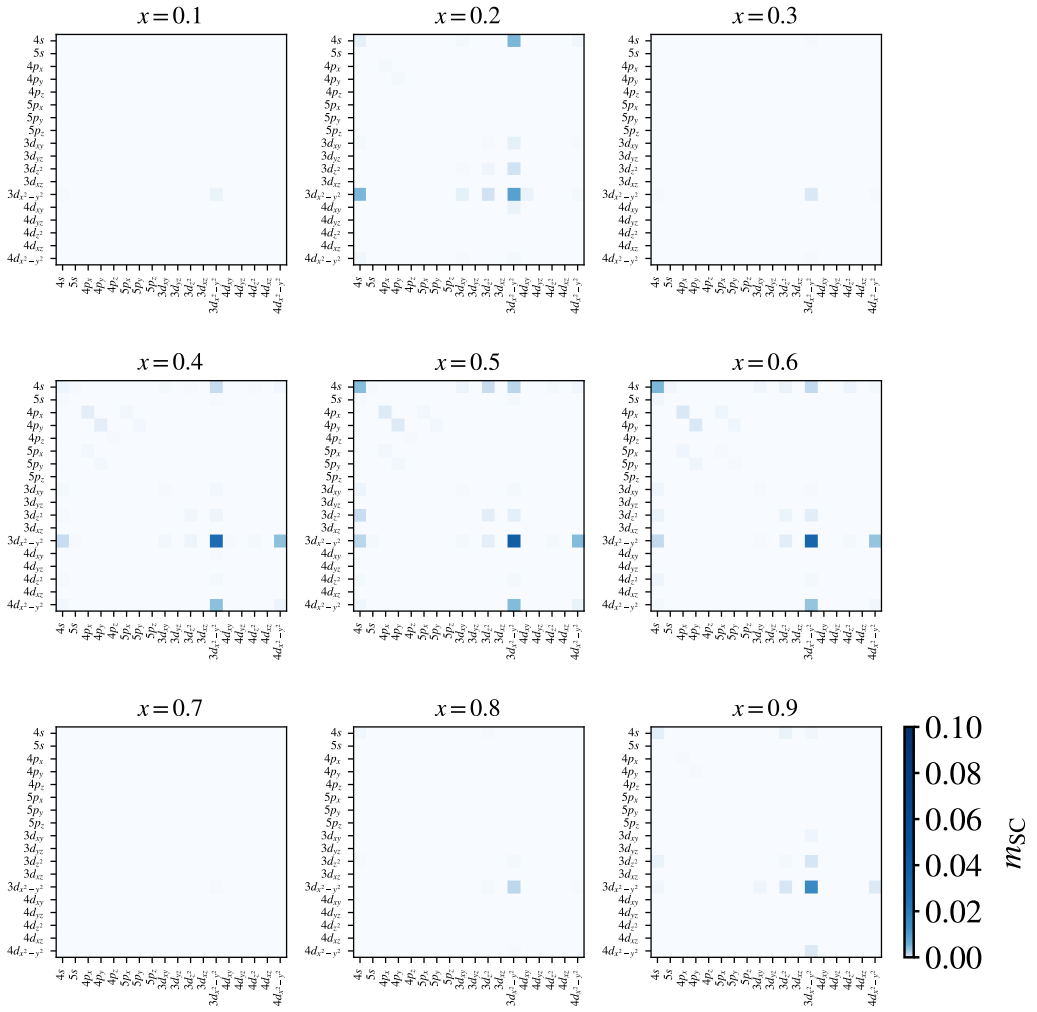

(a)

Figure 7.5: Copper orbital-resolved d-wave order parameter of CCO from DMET @ PBE0 using VCA ($4f$ orbitals are omitted for clarity).

superconductivity.

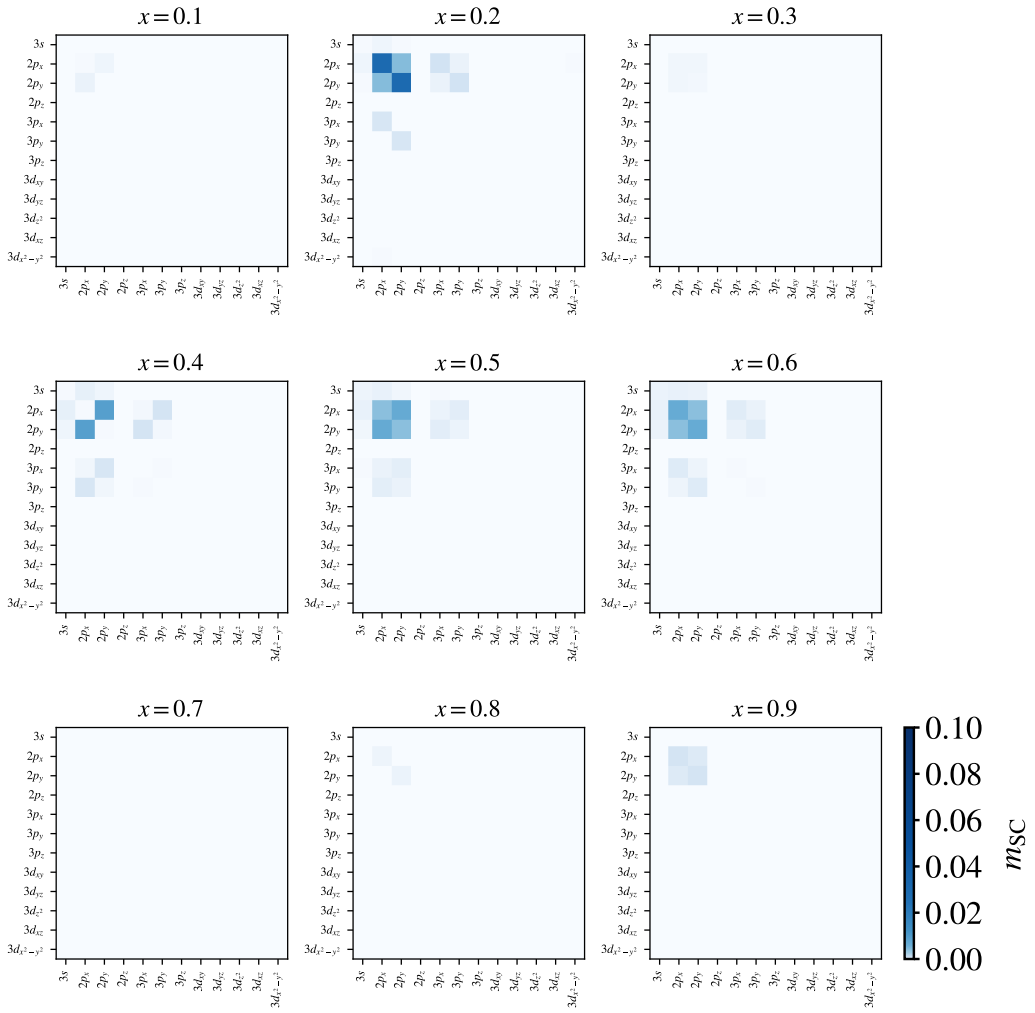

(a)

Figure 7.6: Oxygen orbital-resolved d-wave order parameter of CCO from DMET @ PBE0 using VCA.

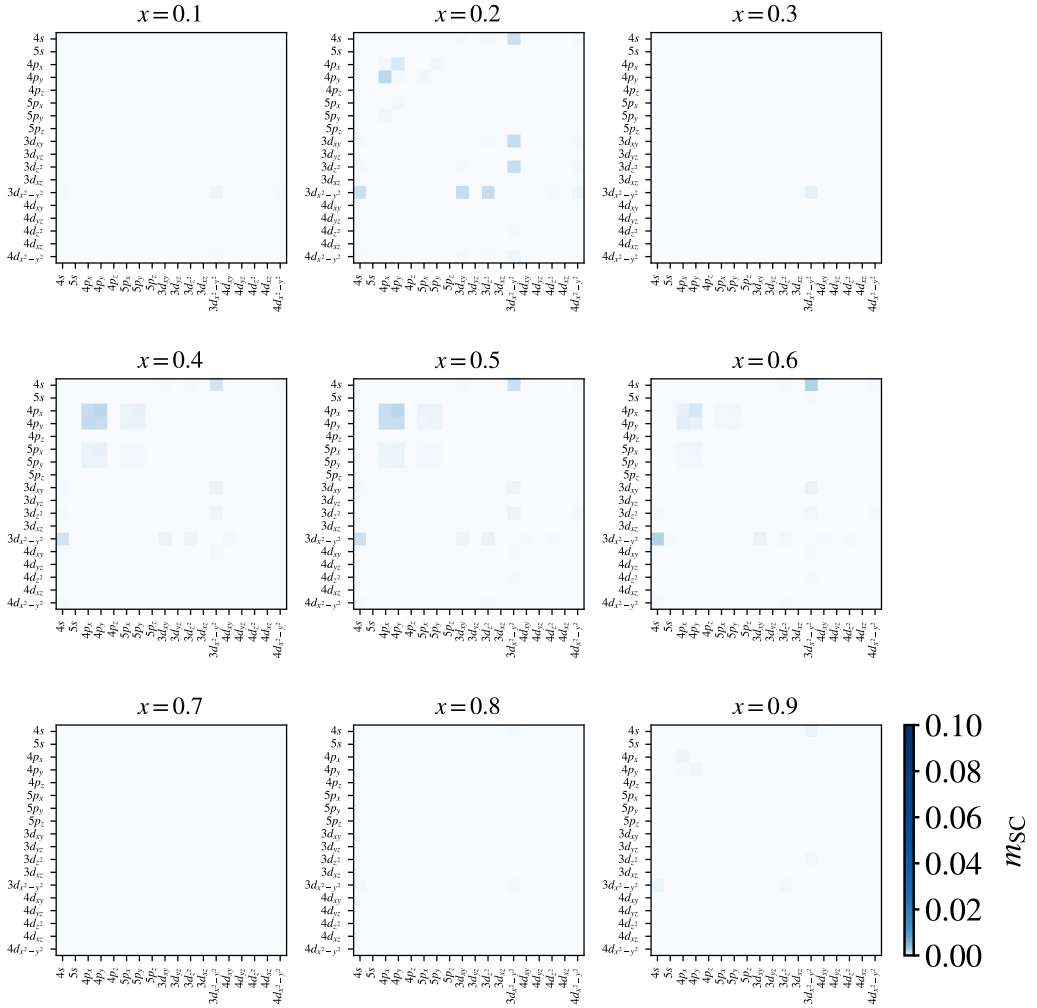

(a)

Figure 7.7: Copper orbital-resolved s-wave order parameter of CCO from DMET @ PBE0 using VCA ($4f$ orbitals are omitted for clarity).

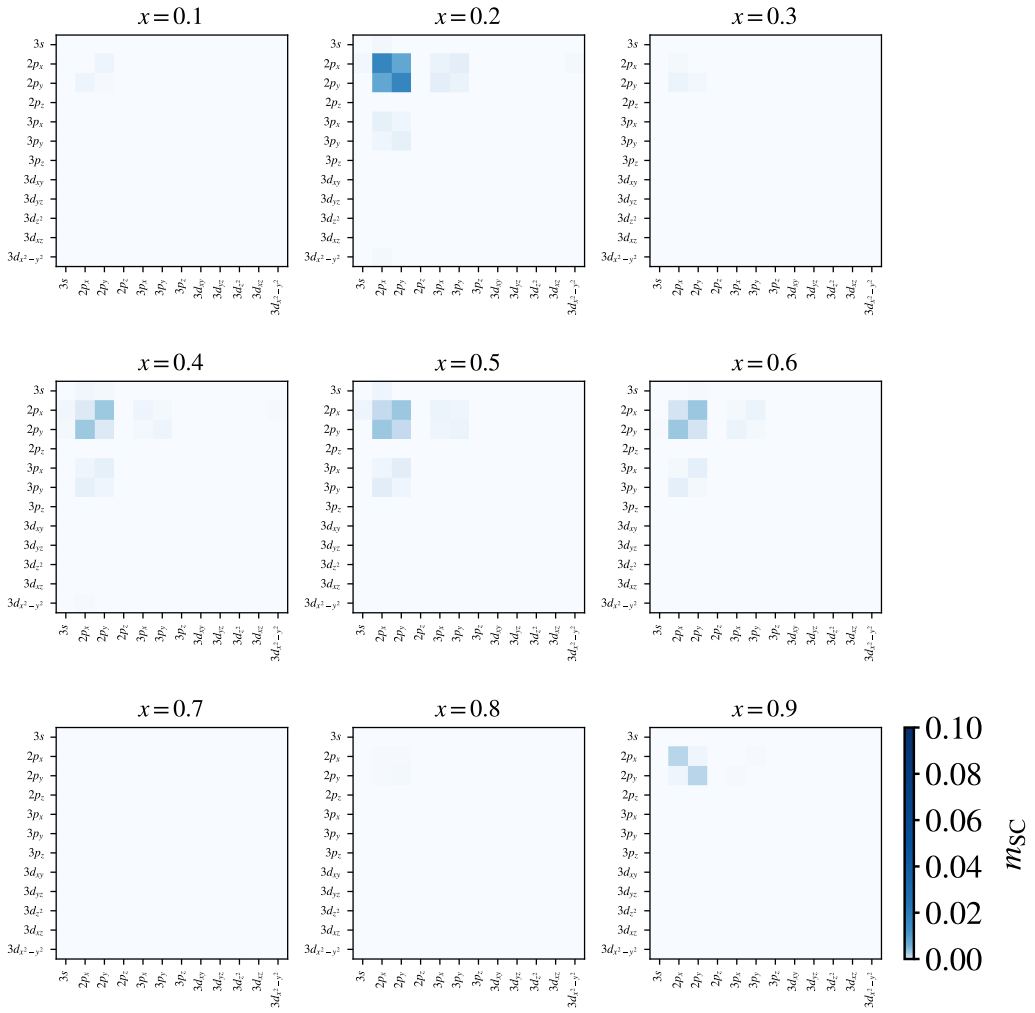

(a)

Figure 7.8: Oxygen orbital-resolved s-wave order parameter of CCO from DMET @ PBE0 using VCA.

Chapter 8

CONCLUDING REMARKS

To summarize, we presented our efforts in developing and applying quantum chemistry methods for faithful simulations of high-temperature superconductivity.

At the Hamiltonian level, we extended the original density matrix embedding theory and dynamical mean-field theory from the lattice models to the periodic *ab initio* materials. At the symmetry-breaking level, we developed a generalized spin-orbital formalism to simultaneously study the magnetic and superconducting phases. At the many-body solver level, we adapted the quantum chemistry solvers (coupled cluster, density matrix renormalization group etc.) to large-scale quantum embedding problems and made them suitable for symmetry-breaking Hamiltonians. At the technical level, we enhanced the robustness of the embedding self-consistency as well as the efficiency of the entire embedding and solver algorithms.

With these methodology advances, we studied the one-band and the three-band Hubbard model, which are minimal models for the high-T_c cuprates. Several interesting features are observed, such as the coexistence of AFM and SC orders occurs in all parameter sets, oxygen-participated d-wave SC orders, phase sensitivity to model parameters Δ_{pd} and t_{pp}. These all raise questions about whether real cuprates behave differently and how the structure determines the properties. With this in mind, we investigated a family of cuprate superconducting materials in their parent undoped states. We uncovered microscopic trends in the electron correlations and revealed the link between the material composition and magnetic energy scales via a many-body picture of excitation processes involving the buffer layers. We further applied our methods to the doped cuprates and studied the pressure and layer effect on the d-wave superconducting orders. The increased SC orders against pressure support the magnetic "glue" as the main driving force of the Cooper pair formation. The results also showed that even with a local quantum chemistry description, the material-specific trends of exotic phases can be reliably simulated without any artificial parameters. Our work illustrates a path towards a quantitative and reliable understanding of complex states of correlated materials at the *ab initio* many-body level.

Based on the existing works, there are several possible future directions to pursue.

(i) Searching for the descriptors of higher T_c. Although we can perform the quantum embedding on every possible material in the high-throughput screening, the embedding is still not a black-box tool and is very costly. It is useful to search for some simple descriptors and fit a function that could predict the T_c by a series of normal-state DFT calculations. (ii) Larger supercell for inhomogeneous orders. Similar to the study of the stripe order in the one-band Hubbard model [24], one could study the stripe order, density wave, and many other orders through an impurity beyond 2×2 supercell. This certainly makes the calculations more expensive. Nevertheless, it is still possible as we have demonstrated that the multi-fragment scheme allows for a further dividing of sub-impurities in the supercell. The bottleneck would then be the mean-field calculations and the correlation potential fitting. In these cases, a more mean-field implementation (potentially a linear scaling algorithm) would be preferred. (iii) Explicit doping atoms. The atomic model of doping in our work is still preliminary, i.e., using rigid band approximation or virtual crystal approximation. The optimal way is to enable a supercell calculation with explicit doping atoms. How different doping atoms / concentrations influence the magnetic and superconducting orders are of great interest to both computational modeling and experimental realizations. (iv) Long-range correlation. The local nature of the quantum embedding makes the description of inter-cell correlation is relatively inaccurate (we have seen this in the spin-wave spectrum in Chap. 6). There are several possible ways to improve it, e.g., a better set of baths that include more entanglement between the impurity and environment; more orbitals that follow the local correlation orbital selections; a better low-level theory beyond DFT (e.g., MP2 or GW). (v) Better multi-reference impurity solvers. The coupled cluster theory, although accurate enough for a moderately correlated system, could fail for extremely strong interactions. A quantum Monte Carlo solver can be a good candidate, but special treatment is needed to reduce the stochastic error in the density matrices or Green's functions. (vi) Excited states in the superconducting states. There exist many experiments like angle-resolved photoemission spectroscopy that measure the charge excitations in the cuprates. We can extend our scheme to the full-cell DMFT to study such phenomena. (vii) Finite temperature effect. As we have mentioned in Chap. 1, many phases emerge at finite temperatures, such as the pseudogap phase and strange metal phase. How to simulate the materials with realistic ensemble distribution is another important topic.

We hope that by combining the latest theoretical progresses and efficient algorithms, the *ab initio* prediction of properties of high-temperature superconductors is within

reach, and eventually the rational design of correlated materials can be routinely achieved *in silico*.

Appendix A

FOURIER TRANSFORM IN SOLIDS

A.1 Convention

The transformation between real $\mathbf{R}$ and reciprocal $\mathbf{k}$ spaces are ubiquitously used in the quantum embedding of solids and utilizing the $\mathbf{k}$-point symmetry is important for an efficient implementation. In the following, we will use $\mathbf{P}, \mathbf{Q}, \mathbf{R}, \mathbf{S}, \cdots$ for cell indices, and use $\mathbf{X}, \mathbf{Y}, \mathbf{Z}, \mathbf{W}, \cdots$ for $\mathbf{k}$-point indices.

We first define the convention of discretized Fourier transform of operators,

$$\begin{aligned} a_p^{\mathbf{X}\dagger} &= \frac{1}{\sqrt{N}} \sum_{\mathbf{P}} a_p^{\mathbf{P}\dagger} \mathrm{e}^{\mathrm{i}\mathbf{P}\cdot\mathbf{X}}, \\ a_p^{\mathbf{P}\dagger} &= \frac{1}{\sqrt{N}} \sum_{\mathbf{X}} a_p^{\mathbf{X}\dagger} \mathrm{e}^{-\mathrm{i}\mathbf{X}\cdot\mathbf{P}}, \end{aligned} \tag{A.1}$$

where N is the number of cells (or $\mathbf{k}$-points) in the lattice .

We can get the transformation rule of orbitals by acting Eq. (A.1) on the vacuum,

$$\left|\phi_p^{\mathbf{X}}\right\rangle = a_p^{\mathbf{X}\dagger} \left|\mathrm{vac}\right\rangle = \frac{1}{\sqrt{N}} \sum_{\mathbf{P}} a_p^{\mathbf{P}\dagger} \mathrm{e}^{\mathrm{i}\mathbf{P}\cdot\mathbf{X}} \left|\mathrm{vac}\right\rangle = \frac{1}{\sqrt{N}} \sum_{\mathbf{P}} \left|\phi_p^{\mathbf{P}}\right\rangle \mathrm{e}^{\mathrm{i}\mathbf{P}\cdot\mathbf{X}}. \tag{A.2}$$

By applying $\langle\mathbf{r}|$ to left, we have

$$\phi_p^{\mathbf{X}}(\mathbf{r}) = \frac{1}{\sqrt{N}} \sum_{\mathbf{P}} \phi_p^{\mathbf{P}}(\mathbf{r}) \mathrm{e}^{\mathrm{i}\mathbf{P}\cdot\mathbf{X}}, \tag{A.3}$$

which gives the definition of crystalline gaussian bases [Eq. (2.32)] (up to a normalization factor).

Similarly, for the inverse transform, we have

$$\phi_p^{\mathbf{P}}(\mathbf{r}) = \frac{1}{\sqrt{N}} \sum_{\mathbf{X}} \phi_p^{\mathbf{X}}(\mathbf{r}) \mathrm{e}^{-\mathrm{i}\mathbf{X}\cdot\mathbf{P}}. \tag{A.4}$$

There are several useful identities when working with discrete Fourier transforms,

$$\frac{1}{N} \sum_{\mathbf{k}} \mathrm{e}^{\mathrm{i}(\mathbf{R}-\mathbf{R}')\cdot\mathbf{k}} = \delta_{\mathbf{R},\mathbf{R}'}, \tag{A.5}$$

$$\frac{1}{N} \sum_{\mathbf{R}} \mathrm{e}^{-\mathrm{i}(\mathbf{k}-\mathbf{k}')\cdot\mathbf{R}} = \delta_{\mathbf{k},\mathbf{k}'}. \tag{A.6}$$

The continuous version of such identity is

$$\frac{1}{V} \int \mathrm{d}\mathbf{r}\, \mathrm{e}^{-\mathrm{i}(\mathbf{G}-\mathbf{G}')\cdot\mathbf{r}} = \delta_{\mathbf{G},\mathbf{G}'}. \tag{A.7}$$

A.2 Orbital coefficients

Given a set of MOs in **k**-space,

$$\psi_i^{\mathbf{k}}(\mathbf{r}) = \sum_{\mu} \phi_{\mu}^{\mathbf{k}}(\mathbf{r}) C_{\mu i}^{\mathbf{k}}, \tag{A.8}$$

and the corresponding representation in **R**-space (Wannier function),

$$\psi_i^{\mathbf{R}}(\mathbf{r}) = \sum_{\mathbf{T}\mu} \phi_{\mu}^{\mathbf{T}}(\mathbf{r}) C_{\mu i}^{\mathbf{TR}}. \tag{A.9}$$

We want to know the relation between $C_{\mu i}^{\mathbf{k}}$ and $C^{\mathbf{TR}}$. To do so, the l.h.s. of Eq. (A.9) can be expanded in **k**,

$$\psi_i^{\mathbf{R}}(\mathbf{r}) = \frac{1}{\sqrt{N}} \sum_{\mathbf{k}} \psi_i^{\mathbf{k}}(\mathbf{r}) \mathrm{e}^{-\mathrm{i}\mathbf{k}\cdot\mathbf{R}} = \frac{1}{\sqrt{N}} \sum_{\mathbf{k}\mu} \phi_{\mu}^{\mathbf{k}}(\mathbf{r}) C_{\mu i}^{\mathbf{k}} \mathrm{e}^{-\mathrm{i}\mathbf{k}\cdot\mathbf{R}}, \tag{A.10}$$

and the r.h.s. can be expressed as

$$\frac{1}{\sqrt{N}} \sum_{\mathbf{T}\mu} \sum_{\mathbf{k}} \phi_{\mu}^{\mathbf{k}}(\mathbf{r}) \mathrm{e}^{-\mathrm{i}\mathbf{k}\cdot\mathbf{T}} C_{\mu i}^{\mathbf{TR}}. \tag{A.11}$$

Equaling the two parts, we have

$$C_{\mu i}^{\mathbf{k}} = \sum_{\mathbf{T}-\mathbf{R}} \mathrm{e}^{-\mathrm{i}\mathbf{k}\cdot(\mathbf{T}-\mathbf{R})} C_{\mu i}^{\mathbf{TR}}. \tag{A.12}$$

Similarly, the inverse transformation can be derived by multiplying $\mathrm{e}^{\mathrm{i}\mathbf{R}'\cdot\mathbf{k}}$ on both sides and summing over **k**. The final expression is,

$$C_{\mu i}^{\mathbf{TR}} = \frac{1}{N} \sum_{\mathbf{k}} \mathrm{e}^{\mathrm{i}(\mathbf{T}-\mathbf{R})\cdot\mathbf{k}} C_{\mu i}^{\mathbf{k}}. \tag{A.13}$$

Note that the resulting supercell coefficients may have imaginary parts due to the phase discontinuity in **k**.

Sometimes it is useful to project back the supercell (SC) band structures to the unit cell (UC) Brillouin zone. This procedure is called Brillouin zone *unfolding*. To do so, we need

to evaluate the AO overlap matrix between different **k**-meshes,

$$
\begin{aligned}
&\left\langle \phi_p^{\mathbf{k}} \middle| \phi_Q^{\mathbf{K}} \right\rangle \\
=&\int \mathrm{d}\mathbf{r} \frac{1}{\sqrt{N_{\mathrm{UC}} N_{\mathrm{SC}}}} \sum_{\mathbf{T}'\mathbf{v}'\mathbf{T}} \phi_p^*[\mathbf{r} - (\mathbf{T}' + \mathbf{v}')] \mathrm{e}^{-\mathrm{i}\mathbf{k}\cdot(\mathbf{T}'+\mathbf{v}')} \phi_q[\mathbf{r} - (\mathbf{T} + \mathbf{v}_0)] \mathrm{e}^{\mathrm{i}\mathbf{K}\cdot\mathbf{T}} \\
=&\int \mathrm{d}\mathbf{r} \frac{1}{\sqrt{N_{\mathrm{UC}} N_{\mathrm{SC}}}} \sum_{\mathbf{T}'+\mathbf{v}'-\mathbf{T}-\mathbf{v}_0} \sum_{\mathbf{T}+\mathbf{v}_0} \phi_p^*[\mathbf{r} - (\mathbf{T}' + \mathbf{v}' - \mathbf{T} - \mathbf{v}_0)] \mathrm{e}^{-\mathrm{i}\mathbf{k}\cdot(\mathbf{T}'+\mathbf{v}'-\mathbf{T}-\mathbf{v}_0)} \\
&\times \phi_q(\mathbf{r}) \mathrm{e}^{-\mathrm{i}\mathbf{k}\cdot(\mathbf{T}+\mathbf{v}_0)} \mathrm{e}^{\mathrm{i}\mathbf{K}\cdot\mathbf{T}} \\
=&\frac{1}{\sqrt{N_{\mathrm{UC}} N_{\mathrm{SC}}}} \left[\sum_{\mathbf{T}'\in\mathrm{UC}} \int \mathrm{d}\mathbf{r} \phi_p^*(\mathbf{r} - \mathbf{T}') \mathrm{e}^{-\mathrm{i}\mathbf{k}\cdot\mathbf{T}'} \phi_q(\mathbf{r}) \right] \left[\mathrm{e}^{-\mathrm{i}\mathbf{k}\cdot\mathbf{v}_0} \sum_{\mathbf{T}\in\mathrm{SC}} \mathrm{e}^{\mathrm{i}(\mathbf{K}-\mathbf{k})\cdot\mathbf{T}} \right] \\
=&\frac{1}{\sqrt{N_{\mathrm{UC}} N_{\mathrm{SC}}}} S_{pq}^{\mathbf{k}} \left[\mathrm{e}^{-\mathrm{i}\mathbf{k}\cdot\mathbf{v}_0} \sum_{\mathbf{T}\in\mathrm{SC}} \mathrm{e}^{\mathrm{i}(\mathbf{K}-\mathbf{k})\cdot\mathbf{T}} \right] \\
=&\sqrt{\frac{N_{\mathrm{SC}}}{N_{\mathrm{UC}}}} S_{pq}^{\mathbf{k}} \mathrm{e}^{-\mathrm{i}\mathbf{k}\cdot\mathbf{v}_0} \delta_{\mathbf{k}-\mathbf{K},n\mathbf{b}} \\
=&S_{pq}^{\mathbf{k}} f_{\mathbf{k},\mathbf{K},\mathbf{v}0}
\end{aligned}
\tag{A.14}
$$

where $Q = \mathbf{v}_0 q$ with $\mathbf{v}_0$ is any lattice vector of the unit cell within the supercell; $n\mathbf{b}$ is integer multiples of reciprocal lattice vectors.

The projection of MO coefficients then reads,

$$
\begin{aligned}
C_{rm}^{\mathbf{k}} &= \sum_{pQ\mathbf{K}} S_{rp}^{\mathbf{k},-1} \left\langle \phi_p^{\mathbf{k}} \middle| \phi_Q^{\mathbf{K}} \right\rangle C_{Qm}^{\mathbf{K}} \\
&= \sum_{\mathbf{K}\mathbf{v}_0} f_{\mathbf{k},\mathbf{K},\mathbf{v}0} C_{\mathbf{v}_0 rm}^{\mathbf{K}}
\end{aligned}
\tag{A.15}
$$

We thus do not need to pre-compute the UC MOs and overlap matrices, only a structure factor f is needed. If the SC MOs have the same symmetry of UC (no symmetry breaking happens), the resulting UC MOs will have zero columns, i.e., at some **k**-points, there is no projection from a specific SC MO state (the number of bands is reduced). Otherwise, there will be multiple bands with non-integer spectral weights.

A.3 Overlap and one-body matrices

The orbital overlap matrix can be computed as the integral over the normalized **k**-adapted orbitals,

$$\begin{aligned} S_{pq}^{\mathbf{XY}} &= \int \mathrm{d}\mathbf{r}\, \phi_p^{\mathbf{X}*}(\mathbf{r})\phi_q^{\mathbf{Y}}(\mathbf{r}) \\ &= \int \mathrm{d}\mathbf{r}\, \frac{1}{N}\sum_{\mathbf{PQ}} \phi_p^{\mathbf{P}*}(\mathbf{r})\mathrm{e}^{-\mathrm{i}\mathbf{P}\cdot\mathbf{X}}\phi_q^{\mathbf{Q}}(\mathbf{r})\mathrm{e}^{\mathrm{i}\mathbf{Q}\cdot\mathbf{Y}} \\ &= \int \mathrm{d}\mathbf{r}\, \frac{1}{N}\sum_{\mathbf{P-Q},\mathbf{Q}} \phi_p^{\mathbf{P-Q}*}(\mathbf{r})\mathrm{e}^{-\mathrm{i}\mathbf{X}\cdot(\mathbf{P-Q})}\phi_q^{\mathbf{0}}(\mathbf{r})\mathrm{e}^{-\mathrm{i}(\mathbf{X-Y})\cdot\mathbf{Q}} \\ &= \int \mathrm{d}\mathbf{r} \sum_{\mathbf{P-Q}} \phi_p^{\mathbf{P-Q}*}(\mathbf{r})\mathrm{e}^{-\mathrm{i}\mathbf{X}\cdot(\mathbf{P-Q})}\phi_q^{\mathbf{0}}(\mathbf{r}) \left[\frac{1}{N}\sum_{\mathbf{Q}} \mathrm{e}^{-\mathrm{i}(\mathbf{X-Y})\cdot\mathbf{Q}}\right] \\ &= \delta_{\mathbf{X},\mathbf{Y}} \sum_{\mathbf{T}} \mathrm{e}^{-\mathrm{i}\mathbf{T}\cdot\mathbf{X}} \int \mathrm{d}\mathbf{r}\, \phi_p^{\mathbf{T}*}(\mathbf{r})\phi_q^{\mathbf{0}}(\mathbf{r}), \end{aligned} \tag{A.16}$$

where we have used $\sum_{\mathbf{PQ}} = \sum_{\mathbf{P-Q},\mathbf{Q}}$ by shifting the origin of $\mathbf{r}$ to $\mathbf{Q}$ and Eq. (A.6). The δ function makes the overlap matrix diagonal in the **k** space. This completes the derivation of Eq. (2.33).

In general, a translational invariant one-body quantity A (such as Hamiltonian matrix h or density matrix γ) can be compactly stored as a stripe (columns of the reference cell),

$$A^{\mathbf{P},\mathbf{Q}} = A^{\mathbf{P-Q},\mathbf{0}}. \tag{A.17}$$

We now consider how it can be related to the **k**-space quantity.

$$\begin{aligned} \hat{A} &= \sum_{\mathbf{PQ}}\sum_{pq} A_{pq}^{\mathbf{PQ}} a_p^{\mathbf{P}\dagger} a_q^{\mathbf{Q}} \\ &= \frac{1}{N}\sum_{\mathbf{XY}}\sum_{\mathbf{PQ}pq} A_{pq}^{\mathbf{PQ}} a_p^{\mathbf{X}\dagger}\mathrm{e}^{-\mathrm{i}\mathbf{X}\cdot\mathbf{P}} a_q^{\mathbf{Y}}\mathrm{e}^{\mathrm{i}\mathbf{Y}\cdot\mathbf{Q}} \\ &= \sum_{\mathbf{XY}pq}\sum_{\mathbf{P-Q}} A_{pq}^{\mathbf{P-Q},\mathbf{0}}\mathrm{e}^{-\mathrm{i}\mathbf{X}\cdot(\mathbf{P-Q})} a_p^{\mathbf{X}\dagger} a_q^{\mathbf{Y}} \left[\frac{1}{N}\sum_{\mathbf{Q}} \mathrm{e}^{-\mathrm{i}(\mathbf{X-Y})\cdot\mathbf{Q}}\right] \\ &= \sum_{\mathbf{X}pq}\sum_{\mathbf{P-Q}} t_{pq}^{\mathbf{P-Q},\mathbf{0}}\mathrm{e}^{-\mathrm{i}\mathbf{X}\cdot(\mathbf{P-Q})} a_p^{\mathbf{X}\dagger} a_q^{\mathbf{X}} \\ &= \sum_{\mathbf{X}pq} A_{pq}^{\mathbf{X}} a_p^{\mathbf{X}\dagger} a_q^{\mathbf{X}}, \end{aligned} \tag{A.18}$$

where

$$A_{pq}^{\mathbf{X}} = \sum_{\mathbf{P-Q}} A_{pq}^{\mathbf{P-Q},\mathbf{0}}\mathrm{e}^{-\mathrm{i}\mathbf{X}\cdot(\mathbf{P-Q})}, \tag{A.19}$$

which corresponds to the forward fast Fourier transform (FFT). This also verifies the Eq. (A.16).

For the inverse transformation, we have

$$\begin{aligned}\hat{A} &= \sum_{\mathbf{X}} \sum_{pq} A_{pq}^{\mathbf{X}} a_p^{\mathbf{X}\dagger} a_q^{\mathbf{X}} \\ &= \sum_{\mathbf{PQ}pq} a_p^{\mathbf{P}\dagger} a_p^{\mathbf{Q}} \frac{1}{N} \sum_{\mathbf{X}} \mathrm{e}^{\mathrm{i}(\mathbf{P}-\mathbf{Q})\cdot\mathbf{X}} A_{pq}^{\mathbf{X}} \\ &= \sum_{\mathbf{PQ}pq} a_p^{\mathbf{P}\dagger} a_p^{\mathbf{Q}} A_{pq}^{\mathbf{PQ}},\end{aligned} \tag{A.20}$$

where

$$A_{pq}^{\mathbf{PQ}} = A_{pq}^{\mathbf{P}-\mathbf{Q},\mathbf{0}} = \frac{1}{N} \sum_{\mathbf{X}} \mathrm{e}^{\mathrm{i}(\mathbf{P}-\mathbf{Q})\cdot\mathbf{X}} A_{pq}^{\mathbf{X}}, \tag{A.21}$$

which corresponds to the inverse FFT (iFFT). Note that there is a $1/N$ factor.

A.4 Two-body quantities

Following the same trick, we can obtain the relation of two-body quantities between **R** and **k** space.

$$\begin{aligned}\hat{V} &= \sum_{\mathbf{PQRS}} \sum_{pqrs} V_{pqrs}^{\mathbf{PQRS}} a_p^{\mathbf{P}\dagger} a_r^{\mathbf{R}\dagger} a_s^{\mathbf{S}} a_q^{\mathbf{Q}} \\ &= \frac{1}{N^2} \sum_{\mathbf{XYZW}} \sum_{\mathbf{PQRS}pqrs} V_{pqrs}^{\mathbf{PQRS}} \mathrm{e}^{-\mathrm{i}\mathbf{X}\cdot\mathbf{P}} \mathrm{e}^{\mathrm{i}\mathbf{Y}\cdot\mathbf{Q}} \mathrm{e}^{-\mathrm{i}\mathbf{Z}\cdot\mathbf{R}} \mathrm{e}^{\mathrm{i}\mathbf{W}\cdot\mathbf{S}} a_p^{\mathbf{X}\dagger} a_r^{\mathbf{Z}\dagger} a_s^{\mathbf{W}} a_q^{\mathbf{Y}} \\ &= \frac{1}{N^2} \sum_{\mathbf{XYZW}} \sum_{\mathbf{PQRS}pqrs} V_{pqrs}^{\mathbf{PQRS}} a_p^{\mathbf{X}\dagger} a_r^{\mathbf{Z}\dagger} a_s^{\mathbf{W}} a_q^{\mathbf{Y}} \mathrm{e}^{-\mathrm{i}\mathbf{X}\cdot(\mathbf{P}-\mathbf{S})} \mathrm{e}^{\mathrm{i}\mathbf{Y}\cdot(\mathbf{Q}-\mathbf{S})} \mathrm{e}^{-\mathrm{i}\mathbf{Z}\cdot(\mathbf{R}-\mathbf{S})} \mathrm{e}^{-\mathrm{i}(\mathbf{X}-\mathbf{Y}+\mathbf{Z}-\mathbf{W})\cdot\mathbf{S}} \\ &= \frac{1}{N} \sum_{\mathbf{XYZW}} \sum_{\mathbf{PQR}pqrs} V_{pqrs}^{\mathbf{PQRS}} a_p^{\mathbf{X}\dagger} a_r^{\mathbf{Z}\dagger} a_s^{\mathbf{W}} a_q^{\mathbf{Y}} \mathrm{e}^{-\mathrm{i}\mathbf{X}\cdot(\mathbf{P}-\mathbf{S})} \mathrm{e}^{\mathrm{i}\mathbf{Y}\cdot(\mathbf{Q}-\mathbf{S})} \mathrm{e}^{-\mathrm{i}\mathbf{Z}\cdot(\mathbf{R}-\mathbf{S})} \frac{1}{N} \sum_{\mathbf{S}} \mathrm{e}^{-\mathrm{i}(\mathbf{X}-\mathbf{Y}+\mathbf{Z}-\mathbf{W})\cdot\mathbf{S}} \\ &= \frac{1}{N} \sum_{\mathbf{XYZW}} \sum_{\mathbf{PQR}pqrs} V_{pqrs}^{\mathbf{PQRS}} a_p^{\mathbf{X}\dagger} a_r^{\mathbf{Z}\dagger} a_s^{\mathbf{W}} a_q^{\mathbf{Y}} \mathrm{e}^{-\mathrm{i}\mathbf{X}\cdot(\mathbf{P}-\mathbf{S})} \mathrm{e}^{\mathrm{i}\mathbf{Y}\cdot(\mathbf{Q}-\mathbf{S})} \mathrm{e}^{-\mathrm{i}\mathbf{Z}\cdot(\mathbf{R}-\mathbf{S})} \delta_{\mathbf{X}-\mathbf{Y}+\mathbf{Z},\mathbf{W}} \\ &= \frac{1}{N} \sum_{\mathbf{XYZ}pqrs} \sum_{\mathbf{P}-\mathbf{S},\mathbf{Q}-\mathbf{S},\mathbf{R}-\mathbf{S}} V_{pqrs}^{\mathbf{P}-\mathbf{S},\mathbf{Q}-\mathbf{S},\mathbf{R}-\mathbf{S},\mathbf{0}} a_p^{\mathbf{X}\dagger} a_r^{\mathbf{Z}\dagger} a_s^{\mathbf{X}-\mathbf{Y}+\mathbf{Z}} a_q^{\mathbf{Y}} \mathrm{e}^{-\mathrm{i}\mathbf{X}\cdot(\mathbf{P}-\mathbf{S})} \mathrm{e}^{\mathrm{i}\mathbf{Y}\cdot(\mathbf{Q}-\mathbf{S})} \mathrm{e}^{-\mathrm{i}\mathbf{Z}\cdot(\mathbf{R}-\mathbf{S})} \\ &= \sum_{\mathbf{XYZ}pqrs} V_{pqrs}^{\mathbf{XYZ}} a_p^{\mathbf{X}\dagger} a_r^{\mathbf{Z}\dagger} a_s^{\mathbf{X}-\mathbf{Y}+\mathbf{Z}} a_q^{\mathbf{Y}},\end{aligned} \tag{A.22}$$

where

$$V_{pqrs}^{\mathbf{XYZ}} = \frac{1}{N} \sum_{\mathbf{PQR}} V_{pqrs}^{\mathbf{PQR0}} \mathrm{e}^{-\mathrm{i}\mathbf{X}\cdot\mathbf{P}} \mathrm{e}^{\mathrm{i}\mathbf{Y}\cdot\mathbf{Q}} \mathrm{e}^{-\mathrm{i}\mathbf{Z}\cdot\mathbf{R}}. \tag{A.23}$$

Similarly, the inverse transformation reads,

$$V_{pqrs}^{\mathbf{PQR0}} = \frac{1}{N^2} \sum_{\mathbf{XYZ}} V_{pqrs}^{\mathbf{XYZ}} \mathrm{e}^{\mathrm{i}\mathbf{X}\cdot\mathbf{P}} \mathrm{e}^{-\mathrm{i}\mathbf{Y}\cdot\mathbf{Q}} \mathrm{e}^{\mathrm{i}\mathbf{Z}\cdot\mathbf{R}}. \tag{A.24}$$

Note that in PySCF's implementation of ERI, there is an additional N factor in Eq. (A.23) that cancels the $1/N$ factor.

Appendix B

SINGLE-PARTICLE METHODS

Here, we briefly review three kinds of single-particle approaches. The first two are HF and hybrid DFT, which form the low-level mean-field methods that are the starting points for the quantum embedding. The third is the DFT+U calculation. The primary drawback of DFT+U is the level of empiricism that enters in the choice of U and double-counting correction, which means that the errors are not simply improvable. We provide DFT+U results in this thesis purely for comparison.

B.1 Coulomb and exchange matrices

The 7-dimension (7D) ERIs can be constructed from the density fitting integrals,

$$V_{pqrs}^{\mathbf{k}_p\mathbf{k}_q\mathbf{k}_r} = \sum_L W_{Lpq}^{\mathbf{k}_p\mathbf{k}_q} W_{Lrs}^{\mathbf{k}_r(\mathbf{k}_s)}, \tag{B.1}$$

where $\mathbf{k}_s$ is not independent. Note that there is no need for explicit complex conjugation since

$$W_{Lpq}^{\mathbf{k}_p\mathbf{k}_q} \equiv \big(L\big|p\mathbf{k}_p q\mathbf{k}_q\big) = \big(L\big|q\mathbf{k}_q p\mathbf{k}_p\big)^* \equiv \big(p\mathbf{k}_p q\mathbf{k}_q\big|L\big). \tag{B.2}$$

Coulomb J and exchange K matrices can be obtained directly from the 7D ERI,

$$J_{rs}^{\mathbf{k}_r} = \frac{1}{N_{\mathbf{k}_p}} \sum_{\mathbf{k}_p rs} V_{pqrs}^{\mathbf{k}_p\mathbf{k}_q\mathbf{k}_r} \gamma_{qp}^{\mathbf{k}_p}, \tag{B.3}$$

$$K_{ps}^{\mathbf{k}_p} = \frac{1}{N_{\mathbf{k}_q}} \sum_{\mathbf{k}_q qr} V_{pqrs}^{\mathbf{k}_p\mathbf{k}_q\mathbf{k}_r} \gamma_{qr}^{\mathbf{k}_q}. \tag{B.4}$$

In the PySCF program, thanks to the local Gaussian basis set and the density fitting techniques, the HF exact exchange can be efficiently evaluated in the all-electron periodic calculations. We first compute the auxiliary density,

$$\rho_L = \frac{1}{N_{\mathbf{k}}} \sum_{\mathbf{k}pq} W_{Lpq}^{\mathbf{k}\mathbf{k}}, \tag{B.5}$$

and then J is evaluated as a contraction of 3-center integral and ρ_L,

$$J_{rs}^{\mathbf{k}} = \sum_L \rho_L W_{Lrs}^{\mathbf{k}\mathbf{k}}. \tag{B.6}$$

Note that J matrix only requires the diagonal part of the 3-center integral.

K matrix, however, requires the off-diagonal part of the integral (two $\mathbf{k}$ points are involved). The first step is a partial contraction between the integral and density matrix,

$$X^{\mathbf{k}_q\mathbf{k}_p}_{Lqs} = \sum_r \gamma^{\mathbf{k}_q}_{qr} W^{\mathbf{k}_q\mathbf{k}_p}_{Lrs}, \tag{B.7}$$

and the second contraction gives the final exchange matrix,

$$K^{\mathbf{k}_p}_{ps} = \frac{1}{N_{\mathbf{k}}} \sum_{\mathbf{k}_q Lq} W^{\mathbf{k}_q\mathbf{k}_p *}_{Lqp} X^{\mathbf{k}_q\mathbf{k}_p}_{Lqs}. \tag{B.8}$$

where we have used Eq. (2.43). By using the complex conjugation, there is no need to load different $\mathbf{k}$-point pairs at one time (for efficient implementation). Note that the MPI parallelism can be ideally performed over $\mathbf{k}$ for the J matrix and for $\mathbf{k}$-pairs for the K matrix, and only the final step requires communications (reduce or gather operations).

B.2 Model system

Here, we discuss how several model Hamiltonian can be written in the PBC quantum chemistry format.

One-band Hubbard model.

$$V^{\mathbf{PQR0}}_{pqrs} = U\delta_{\mathbf{P},\mathbf{0}}\delta_{\mathbf{Q},\mathbf{0}}\delta_{\mathbf{R},\mathbf{0}}\delta_{pq}\delta_{rs}\delta_{qr}. \tag{B.9}$$

In $\mathbf{k}$-space,

$$\begin{aligned} V^{\mathbf{XYZ}}_{pqrs} &= \frac{1}{N}\sum_{\mathbf{PQR}} U\delta_{\mathbf{P},\mathbf{0}}\delta_{\mathbf{Q},\mathbf{0}}\delta_{\mathbf{R},\mathbf{0}}\delta_{pq}\delta_{rs}\delta_{qr} \mathrm{e}^{-\mathrm{i}\mathbf{X}\cdot\mathbf{P}}\mathrm{e}^{\mathrm{i}\mathbf{Y}\cdot\mathbf{Q}}\mathrm{e}^{-\mathrm{i}\mathbf{Z}\cdot\mathbf{R}} \\ &= \frac{1}{N} U\delta_{pq}\delta_{rs}\delta_{qr}. \end{aligned} \tag{B.10}$$

Therefore,

$$\hat{V}^{\mathrm{Hub}} = \frac{1}{N} U \sum_{\mathbf{XYZ}p} a^{\mathbf{X}\dagger}_p a^{\mathbf{Z}\dagger}_p a^{\mathbf{X}-\mathbf{Y}+\mathbf{Z}}_p a^{\mathbf{Y}}_p. \tag{B.11}$$

The corresponding J and K matrices (useful for HF),

$$J^{\mathbf{k}'}_{rs} = \sum_{\mathbf{k}pq} V^{\mathbf{kkk}'}_{pqrs}\gamma^{\mathbf{k}}_{qp} = \frac{U}{N}\sum_{\mathbf{k}p}\gamma^{\mathbf{k}}_{pp}, \tag{B.12}$$

$$K^{\mathbf{k}'}_{ps} = \sum_{\mathbf{k}qr} V^{\mathbf{k}'\mathbf{kk}}_{pqrs}\gamma^{\mathbf{k}}_{qr} = \frac{U}{N}\sum_{\mathbf{k}q}\gamma^{\mathbf{k}}_{qq}. \tag{B.13}$$

Local Hamiltonian.

More generally, for models with local interaction (i.e., without inter-cell two-body Hamiltonian),

$$V_{pqrs}^{\mathbf{PQR0}} = V_{pqrs}^{\mathbf{0000}} \delta_{\mathbf{P},\mathbf{0}} \delta_{\mathbf{Q},\mathbf{0}} \delta_{\mathbf{R},\mathbf{0}}. \tag{B.14}$$

Therefore,

$$\begin{aligned} V_{pqrs}^{\mathbf{XYZ}} &= \frac{1}{N} \sum_{\mathbf{PQR}} V_{pqrs}^{\mathbf{0000}} \delta_{\mathbf{P},\mathbf{0}} \delta_{\mathbf{Q},\mathbf{0}} \delta_{\mathbf{R},\mathbf{0}} \mathrm{e}^{-\mathrm{i}\mathbf{X}\cdot\mathbf{P}} \mathrm{e}^{\mathrm{i}\mathbf{Y}\cdot\mathbf{Q}} \mathrm{e}^{-\mathrm{i}\mathbf{Z}\cdot\mathbf{R}} \\ &= \frac{1}{N} V_{pqrs}^{\mathbf{0000}}. \end{aligned} \tag{B.15}$$

Corresponding J and K,

$$J_{rs}^{\mathbf{k}'} = \sum_{\mathbf{k}pq} V_{pqrs}^{\mathbf{kkk}'} \gamma_{qp}^{\mathbf{k}} = \sum_{pq} V_{pqrs}^{\mathbf{0000}} \left[\frac{1}{N} \sum_{\mathbf{k}} \gamma_{qp}^{\mathbf{k}} \right], \tag{B.16}$$

$$K_{ps}^{\mathbf{k}'} = \sum_{\mathbf{k}qr} V_{pqrs}^{\mathbf{k}'\mathbf{kk}} \gamma_{qr}^{\mathbf{k}} = \sum_{qr} V_{pqrs}^{\mathbf{0000}} \left[\frac{1}{N} \sum_{\mathbf{k}} \gamma_{qr}^{\mathbf{k}} \right]. \tag{B.17}$$

From above, we see that the *local* Hamiltonian gives $\mathbf{k}$-independent ERI, J and K.

Extended Hubbard Model.

$$V_{pqrs}^{\mathbf{PQR0}} = V_{pqrs}^{\mathbf{P},\mathbf{P},\mathbf{0},\mathbf{0}} \delta_{\mathbf{P},\mathbf{Q}} \delta_{\mathbf{R},\mathbf{0}}. \tag{B.18}$$

Therefore,

$$\begin{aligned} V_{pqrs}^{\mathbf{XYZ}} &= \frac{1}{N} \sum_{\mathbf{PQR}} V_{pqrs}^{\mathbf{P},\mathbf{P},\mathbf{0},\mathbf{0}} \delta_{\mathbf{P},\mathbf{Q}} \delta_{\mathbf{R},\mathbf{0}} \mathrm{e}^{-\mathrm{i}\mathbf{X}\cdot\mathbf{P}} \mathrm{e}^{\mathrm{i}\mathbf{Y}\cdot\mathbf{Q}} \mathrm{e}^{-\mathrm{i}\mathbf{Z}\cdot\mathbf{R}} \\ &= \frac{1}{N} \sum_{\mathbf{P}} V_{pqrs}^{\mathbf{P},\mathbf{P},\mathbf{0},\mathbf{0}} \mathrm{e}^{-\mathrm{i}(\mathbf{X}-\mathbf{Y})\cdot\mathbf{P}}. \end{aligned} \tag{B.19}$$

where $\mathbf{Z}$ is a redundant label, i.e., for all $\mathbf{Z}$, the integrals are the same, and only $V_{pqrs}^{\mathbf{X}-\mathbf{Y}}$ is need to be stored.

The corresponding J and K matrices are

$$\begin{aligned} J_{rs}^{\mathbf{Z}} &= \sum_{\mathbf{X}pq} V_{pqrs}^{\mathbf{XXZ}} \gamma_{qp}^{\mathbf{X}} \\ &= \sum_{pq} \left[\sum_{P} V_{pqrs}^{\mathbf{P},\mathbf{P},\mathbf{0},\mathbf{0}} \right]_{pqrs} \left[\frac{1}{N} \sum_{\mathbf{X}} \gamma_{qp}^{\mathbf{X}} \right]_{qp} \\ &= \sum_{pq} \left[\sum_{P} V_{pqrs}^{\mathbf{P},\mathbf{P},\mathbf{0},\mathbf{0}} \right]_{pqrs} \gamma_{qp}^{\mathbf{0}}, \end{aligned} \tag{B.20}$$

$$
\begin{aligned}
K^{\mathbf{X}}_{ps} &= \sum_{\mathbf{Y}qr} V^{\mathbf{XYY}}_{pqrs}\gamma^{\mathbf{Y}}_{qr} \\
&= \sum_{qr}\sum_{\mathbf{P}} V^{\mathbf{P},\mathbf{P},\mathbf{0},\mathbf{0}}_{pqrs} \mathrm{e}^{-\mathrm{i}\mathbf{X}\cdot\mathbf{P}} \left[\frac{1}{N}\sum_{\mathbf{Y}} \mathrm{e}^{\mathrm{i}\mathbf{Y}\cdot\mathbf{P}}\gamma^{\mathbf{Y}}_{qr}\right] \\
&= \sum_{\mathbf{P}qr} V^{\mathbf{P},\mathbf{P},\mathbf{0},\mathbf{0}}_{pqrs}\gamma^{\mathbf{P},\mathbf{0}}_{qr}\mathrm{e}^{-\mathrm{i}\mathbf{X}\cdot\mathbf{P}} \\
&= \sum_{\mathbf{P}} K^{\mathbf{P}}_{ps}\mathrm{e}^{-\mathrm{i}\mathbf{X}\cdot\mathbf{P}}.
\end{aligned}
\tag{B.21}
$$

These formulations are used for the three-band Hubbard model with inter-cell U_{pd} interactions.

B.3 Hartree-Fock and hybrid functionals

Hybrid functional is an extension of pure density functional through introducing a certain fraction of Hartree-Fock exact exchange. For example, one typical form of hybrid functional,

$$
E^{\mathrm{hyb}}[\rho(\mathbf{r}),\gamma] = \alpha^{\mathrm{HF}}\left(E^{\mathrm{HF}}_{\mathrm{x}}[\gamma] - E^{\mathrm{DFT}}_{\mathrm{x}}[\rho(\mathbf{r})]\right) + E^{\mathrm{DFT}}_{\mathrm{xc}}[\rho(\mathbf{r})], \tag{B.22}
$$

incorporates a fractional substitution of DFT exchange energy, while the correlation part is still approximated by the original functional. The fraction of exact exchange can be rationalized by the adiabatic connection, which bridges the free particle and fully interacting limits [275]. A reasonable choice of α^{HF} was obtained by matching the atomization energies of Møller–Plesset perturbation theory (MP4). Using Perdew–Burke-Ernzerhof (PBE) functional as the normal DFT part, this gives the so called PBE0 functional, whose $\alpha^{\mathrm{HF}} = 1/4$.

During the past decades, hybrid functional has achieved remarkable success, initially in the field of quantum chemistry [275, 277–280], and later in the area of solid-state physics [200, 208, 281–285]. It partially remedies the deficiency of the local, semi-local approximate functionals, including the self-interaction error (SIE) and the underestimation of the fundamental band gap. Due to the less SIE, for localized electrons, hybrid functional often behaves better. DFT+U can also be understood as a local hybrid functional, in which the hybrid region is limited to the correlated d or f orbitals and the exchange integral value is semi-empirically chosen so as to take the screening effect into account.

Compared to the standard DFT, hybrid functional is computationally more expensive, especially in the periodic system, where the exact exchange scales as $\mathcal{O}\left(n^2_{\mathbf{k}}n^4_{\mathrm{bas}}\right)$ [cf. local DFT scaling $\mathcal{O}\left(n^2_{\mathbf{k}}n^3_{\mathrm{bas}}\right)$]. This issue is more severe if the plane wave basis is used [286].

The final expression of the hybrid Kohn-Sham Hamiltonian (restricted case) is thus,

$$
h^{\mathrm{hyb},\mathbf{k}}_{pq} = h^{\mathrm{core},\mathbf{k}}_{pq} + J^{\mathbf{k}}_{pq} - \frac{1}{2}\alpha^{\mathrm{HF}}K^{\mathbf{k}}_{pq} + \left(1-\alpha^{\mathrm{HF}}\right)v^{\mathrm{x},\mathbf{k}}_{pq} + v^{\mathrm{c},\mathbf{k}}_{pq}, \tag{B.23}
$$

where v^{x} (v^{c}) is the normal Kohn-Sham effective exchange (correlation) potential expanded in the crystalline Gaussian basis set.

HF is the extreme case where $a^{\mathrm{HF}} = 0$ and the correlation term v^{c} is omitted.

B.4 DFT + U

DFT + U can be viewed as a combination of the DFT and the HF of a Hubbard model (with a few correlated orbitals). In the PySCF program, we have implemented Dudarev's rotationally invariant DFT+U formulation [287] in a periodic Gaussian basis. Suppose we have a set of local orbitals $\{\phi\}$ expanded in a crystalline AO basis $\{\chi\}$,

$$\left|\phi_i^{\mathbf{k}}\right\rangle = \sum_p \left|\chi_p^{\mathbf{k}}\right\rangle C_{pi}^{\mathrm{LO},\mathbf{k}} \tag{B.24}$$

and a set of molecular orbitals,

$$\left|\psi_m^{\mathbf{k}\sigma}\right\rangle = \sum_p \left|\chi_p^{\mathbf{k}}\right\rangle C_{pm}^{\mathrm{MO},\mathbf{k}\sigma}. \tag{B.25}$$

The default localized orbitals are atomic orbitals in the Gaussian basis set, whose projector is defined as,

$$\begin{aligned} \gamma_{ij}^{\mathbf{k}\sigma} &= \sum_m \left\langle \phi_i^{\mathbf{k}} \middle| \psi_m^{\mathbf{k}\sigma} \right\rangle f_m^{\mathbf{k}\sigma} \left\langle \psi_m^{\mathbf{k}\sigma} \middle| \phi_j^{\mathbf{k}} \right\rangle \\ &= \sum_{pqrs} C_{ip}^{\mathrm{LO},\mathbf{k}\dagger} S_{pq}^{\mathbf{k}} \gamma_{qr}^{\mathbf{k}\sigma} S_{rs}^{\mathbf{k}} C_{rj}^{\mathrm{LO},\mathbf{k}}, \end{aligned} \tag{B.26}$$

where $S_{pq}^{\mathbf{k}}$ is the AO overlap matrix and $\gamma_{pq}^{\mathbf{k}\sigma} = \sum_m C_{pm}^{\mathrm{MO},\mathbf{k}\sigma} f_m^{\mathbf{k}\sigma} C_{mq}^{\mathrm{MO},\mathbf{k}\sigma\dagger}$ is the reduced one-particle density matrix in the AO basis where $f_m^{\mathbf{k}\sigma}$ denotes the occupancy of molecular orbital $\psi_m^{\mathbf{k}\sigma}(\mathbf{r})$. The DFT+$U$ Hamiltonian is then obtained from a partial derivative,

$$\begin{aligned} h_{pq}^{\mathrm{DFT}+U,\mathbf{k}\sigma} &= \frac{\partial E^{\mathrm{DFT}}}{\partial \gamma_{qp}^{\mathbf{k}\sigma}} + \frac{\partial \left(E^U - E^{\mathrm{dc}}\right)}{\partial \gamma_{qp}^{\mathbf{k}\sigma}} \\ &= h_{pq}^{\mathrm{DFT},\mathbf{k}\sigma} + \sum_I \frac{U^I - J^I}{2} \sum_{rs} S_{pr}^{\mathbf{k}} \sum_{ij} C_{ri}^{\mathrm{LO},I\mathbf{k}} \left(\delta_{ij}^I - 2\gamma_{ij}^{I\mathbf{k}\sigma}\right) C_{js}^{\mathrm{LO},I\mathbf{k}\dagger} S_{sq}^{\mathbf{k}}, \end{aligned} \tag{B.27}$$

where I labels the atom whose d or f orbitals are corrected by the $U - J$ term.

Although conceptually very simple, the detailed implementation of DFT+U can differ in different computer programs due to two factors: (1) several versions of DFT+U exist, including various choices of double counting corrections [288, 289]. (2) different choices of local orbital projectors. For example, in the PySCF program, we implement U in a standard Gaussian basis, while in plane-wave codes, the local orbital is often chosen to be a pseudopotential atomic orbital [290] or a localized Wannier orbital [291, 292].

Besides some ambiguity in the implementation, the computational results further depend on the values of U and J, and the choice of orbitals where U is added. U and J are usually treated as semi-empirical parameters, or estimated via a variety of methods such as constrained DFT [173, 293, 294], linear response theory [295, 296] or constrained random phase approximation [297–301].

Appendix C

LOCALIZED ORBITALS

C.1 Maximally localized Wannier functions

The Maximally localized Wannier function (MLWF) aims to minimize the spatial spread,

$$\Omega = \sum_n \left\langle w_n^{\mathbf{0}}(\mathbf{r}) \middle| r^2 \middle| w_n^{\mathbf{0}}(\mathbf{r}) \right\rangle - \left| \left\langle w_n^{\mathbf{0}}(\mathbf{r}) \middle| \mathbf{r} \middle| w_n^{\mathbf{0}}(\mathbf{r}) \right\rangle \right|^2, \tag{C.1}$$

where the position operator $\mathbf{r}$ and r^2 will involve the $\nabla_{\mathbf{k}}$ of orbitals, and the cost function can be expressed using the overlap matrix between orbitals with a finite momentum difference $\mathbf{b}$,

$$M_{mn}^{\mathbf{k},\mathbf{k}+\mathbf{b}} = \left\langle u_m^{\mathbf{k}} \middle| u_n^{\mathbf{k}+\mathbf{b}} \right\rangle, \tag{C.2}$$

where

$$u_n^{\mathbf{k}+\mathbf{b}}(\mathbf{r}) = \mathrm{e}^{-\mathrm{i}(\mathbf{k}+\mathbf{b})\cdot\mathbf{r}} \psi_n^{\mathbf{k}+\mathbf{b}}(\mathbf{r}) \tag{C.3}$$

is the periodic part of the MOs. C is the MO coefficients,

$$\psi^{\mathbf{k}+\mathbf{b}}(\mathbf{r}) = \phi_q^{\mathbf{k}+\mathbf{b}}(\mathbf{r}) C_{qn}^{\mathbf{k}+\mathbf{b}}. \tag{C.4}$$

Expanding Eq. (C.2), we have

$$\begin{aligned} M_{mn}^{\mathbf{k},\mathbf{k}+\mathbf{b}} &= \int \mathrm{d}\mathbf{r}\, u_m^{\mathbf{k}*}(\mathbf{r}) u_n^{\mathbf{k}+\mathbf{b}}(\mathbf{r}) \\ &= C_{mp}^{\mathbf{k}\dagger} \left\langle \phi_p^{\mathbf{k}} \middle| \mathrm{e}^{-\mathrm{i}\mathbf{b}\cdot\mathbf{r}} \middle| \phi_q^{\mathbf{k}+\mathbf{b}} \right\rangle C_{qn}^{\mathbf{k}+\mathbf{b}}. \end{aligned} \tag{C.5}$$

$$\begin{aligned} \left\langle \phi_p^{\mathbf{k}} \middle| \mathrm{e}^{-\mathrm{i}\mathbf{b}\cdot\mathbf{r}} \middle| \phi_q^{\mathbf{k}+\mathbf{b}} \right\rangle &= \int \mathrm{d}\mathbf{r}\, \mathrm{e}^{-\mathrm{i}\mathbf{b}\cdot\mathbf{r}} \phi_p^{\mathbf{k}*}(\mathbf{r})\, \phi_q^{\mathbf{k}+\mathbf{b}}(\mathbf{r}) \\ &= \frac{1}{N} \sum_{\mathbf{T}\mathbf{T}'} \mathrm{e}^{-\mathrm{i}\mathbf{k}\cdot\mathbf{T}} \mathrm{e}^{\mathrm{i}(\mathbf{k}+\mathbf{b})\cdot\mathbf{T}'} \int \mathrm{d}\mathbf{r}\, \mathrm{e}^{-\mathrm{i}\mathbf{b}\cdot\mathbf{r}} \phi_p^*(\mathbf{r}-\mathbf{T})\, \phi_q(\mathbf{r}-\mathbf{T}') \\ &= \frac{1}{N} \sum_{\mathbf{T}\mathbf{T}'} \mathrm{e}^{-\mathrm{i}\mathbf{k}\cdot\mathbf{T}} \mathrm{e}^{\mathrm{i}(\mathbf{k}+\mathbf{b})\cdot\mathbf{T}'} \int \mathrm{d}\mathbf{r}\, \mathrm{e}^{-\mathrm{i}\mathbf{b}\cdot(\mathbf{r}+\mathbf{T})} \phi_p^*(\mathbf{r})\, \phi_q(\mathbf{r}-(\mathbf{T}'-\mathbf{T})) \\ &= \sum_{\mathbf{T}} \mathrm{e}^{\mathrm{i}(\mathbf{k}+\mathbf{b})\cdot\mathbf{T}} \int \mathrm{d}\mathbf{r}\, \mathrm{e}^{-\mathrm{i}\mathbf{b}\cdot\mathbf{r}} \phi_p^*(\mathbf{r})\, \phi_q(\mathbf{r}-\mathbf{T}). \end{aligned} \tag{C.6}$$

This integrals can be evaluated by the `ft_ao_pair` function in PySCF,

$$f_{pq}(\mathbf{k}_j, \mathbf{G}, \mathbf{q}) = \sum_{\mathbf{T}} \mathrm{e}^{\mathrm{i}\mathbf{k}_j\cdot\mathbf{T}} \int \mathrm{d}\mathbf{r}\, \mathrm{e}^{-\mathrm{i}(\mathbf{G}+\mathbf{q})\cdot\mathbf{r}} \phi_p^*(\mathbf{r}) \phi_q(\mathbf{r}-\mathbf{T}), \tag{C.7}$$

by setting $\mathbf{k}_j = (\mathbf{k} + \mathbf{b})$, $\mathbf{G} = \mathbf{b}$ and $\mathbf{q} = \mathbf{0}$.

The M matrix is used as an input of WANNIER90. The other input quantity is the $A^{\mathbf{k}}_{mi}$ matrix ($C^{\mathrm{MO,LO}}$), which serves as the initial guess. This is typically constructed by projected Wannier functions, e.g., IAO orbitals that we will discuss in the following.

C.2 Intrinsic atomic orbitals

k-adapted IAO. The key ingredients for IAO construction [95] are the occupied MOs $\{|\psi_m\rangle\}$ and two sets of bases, B_1 and B_2. Concretely, B_1 is the normal AO basis used in the mean-field calculation (labeled by $\mu, \nu, \cdots$) and B_2 is the reference minimal basis set (labeled by $\rho, \sigma, \cdots$). B_1 usually contains the space of B_2 and the extra part reflects the polarization. The goal of IAO construction is to obtain a set of AO-like orbitals that contains the occupied space but has the size of the small basis set B_2. To achieve this, we first define the *depolarized* MOs $\{|\bar{\psi}_m\rangle\}$ by projecting the MOs to B_2, then back to B_1,

$$|\bar{\psi}_m\rangle = \mathrm{orth}\Big(P^{B_1} P^{B_2} |\psi_m\rangle\Big), \tag{C.8}$$

where P is the resolution of identity (or projector) of AOs, e.g.

$$P^{B_1}_{\mu\nu} = \sum_{\mu\nu} |\phi_\mu\rangle S^{B_1}_{\mu\nu} \langle\phi_\nu| . \tag{C.9}$$

Using the depolarized MO projector $\bar{O} \equiv \sum_m |\bar{\psi}_m\rangle\langle\bar{\psi}_m|$, we can split the B_2 set into occupied $\bar{O}|\phi_\rho\rangle$ and virtual spaces $(1-\bar{O})|\phi_\rho\rangle$. The IAOs $\{|w_i\rangle\}$ are obtained by further projecting these two subspace bases onto their polarized counterparts ($O \equiv \sum_m |\psi_m\rangle\langle\psi_m|$ and $1-O$) and applying Löwdin orthogonalization,

$$|w_i\rangle = \mathrm{orth}\big\{\big[O\bar{O} + (1-O)(1-\bar{O})\big]|\phi_\rho\rangle\big\}. \tag{C.10}$$

In periodic systems, the quantities in the above equations should be understood to carry $\mathbf{k}$ labels, e.g. $|\phi_\mu\rangle \to |\phi^{\mathbf{k}}_\mu\rangle$ is a crystal AO, and $S^{B_1} \to S^{\mathbf{k},B_1}$ is the corresponding overlap matrix. These quantities are already evaluated in the mean-field calculations. The only thing we need additionally is the overlap matrix S_{12} between basis B_1 and B_2, which can be evaluated directly,

$$S^{\mathbf{k},B_1,B_2}_{\mu\rho} = \sum_{\mathbf{T}} \int \mathrm{d}\mathbf{r} e^{i\mathbf{k}\cdot\mathbf{T}} \phi^*_\mu(\mathbf{r})\phi_\rho(\mathbf{r}-\mathbf{T}), \tag{C.11}$$

where the summation is over the periodic images $\mathbf{T}$. After the IAOs are constructed, the $\mathbf{k}$-adapted PAOs are obtained by projecting out the IAO components from the AOs at each $\mathbf{k}$-point.

IAO with frozen-core orbitals. When dealing with frozen-core orbitals, the construction of IAOs needs to be adjusted. The key idea is that B_1 basis now becomes a subset of MOs (i.e.,

only treat the non-core part of MOs), C_{pP} (we use capital letters $P, Q, \cdots$ for non-core indices). So that new occupied coefficients in the non-core basis,

$$C^{\text{occ}}_{pm} \to \sum_{pq} C^{\dagger}_{Pq} S_{qp} C^{\text{occ}}_{pm}. \tag{C.12}$$

The large basis overlap S_1 matrix changes as the following,

$$S_{pq} \to S_{PQ} = \sum_{pq} C^{\dagger}_{Pp} S_{pq} C_{qQ}. \tag{C.13}$$

Similarly, the inter-molecular overlap S_{12} reads,

$$S_{p\mu} \to S_{P\mu} = \sum_{p} C^{\dagger}_{Pp} S_{p\mu}. \tag{C.14}$$

The core and non-core IAOs are then constructed separately.

IAO with finite-temperature smearing. For large basis O, we can replace occupied projector by a finite-temperature projector

$$O = \sum_{m}^{\text{occ}} |\psi_m\rangle \langle\psi_m| \to \sum_{m} |\psi_m\rangle \, f_m \, \langle\psi_m| \,, \tag{C.15}$$

where

$$f_m = \frac{1}{\mathrm{e}^{\beta(\varepsilon_m - \mu)+1}}. \tag{C.16}$$

The depolarized MO projector $\bar{O}$ becomes,

$$\bar{O} = \sum_{m}^{\text{occ}} \left|\bar{\psi}_m\right\rangle \left\langle\bar{\psi}_m\right| \to \sum_{\varepsilon_m < \mu} \left|\bar{\psi}_m\right\rangle \left\langle\bar{\psi}_m\right| , \tag{C.17}$$

We can not use the same formula in Eq. (C.15) since $\{\bar{\psi}\}$ is not a orthogonal orbital set. These definition makes the IAOs still roughly span the "occupied space" of the smeared wavefunction. The deviation of electron number is of order $1/\beta$.

C.3 Projected atomic orbitals

Projected atomic orbitals can be constructed by projecting out the contribution of valence part (i.e. IAOs),

$$\begin{aligned}
&\left[1 - \sum_{i}^{\text{IAO}} |i\rangle \langle i|\right] |\mu\rangle \\
=&\left[1 - \sum_{i}^{\text{IAO}} \sum_{\nu\lambda} C_{\nu i} \, |\nu\rangle \langle\lambda| \, C^{*}_{\lambda i}\right] |\mu\rangle \\
=&|\mu\rangle - \sum_{\nu} |\nu\rangle \left(\sum_{i}^{\text{IAO}} \sum_{\lambda} C_{\nu i} C^{\dagger}_{i\lambda} S_{\lambda\mu}\right) \\
=&\sum_{\nu} |\nu\rangle \left[\delta_{\nu\mu} - \left(CC^{\dagger}S\right)_{\nu\mu}\right].
\end{aligned} \tag{C.18}$$

Appendix D

ANALYTIC GRADIENTS OF DENSITY MATRIX FITTING

D.1 Analytic gradients of cost function Eq. (2.57) at finite temperature

Once the gradients of Eq. (2.57) are obtained, we can utilize efficient gradient-based numerical methods, such as CG or the Broyden-Fletcher-Goldfarb-Shanno (BFGS) algorithm, to optimize the correlation potential. By differentiating Eq. (2.57) with respect to u_{ij} we have,

$$\frac{\partial w}{\partial u_{ij}} = 2\sum_{kl}\left(\gamma^{\mathrm{mf}} - \gamma^{\mathrm{corr}}\right)_{kl}\frac{\partial \gamma^{\mathrm{mf}}_{kl}}{\partial u_{ij}}, \tag{D.1}$$

and thus the key task in Eq. (D.1) is to evaluate the response of the mean-field density matrix with respect to a perturbation, $\partial\gamma^{\mathrm{mf}}_{kl}/\partial u_{ij}$. The response at zero temperature can be written in terms of orbital coefficients and energies (see e.g. Refs. [35, 101]) using first order perturbation theory,

$$\frac{\partial \gamma^{\mathrm{mf}}_{kl}}{\partial u_{ij}} = \sum_{p}^{\mathrm{occ}}\sum_{q}^{\mathrm{virt}}\frac{C_{kp}C^*_{lq}C_{iq}C^*_{jp} - C_{kq}C^*_{lp}C_{iq}C^*_{jp}}{\varepsilon_p - \varepsilon_q}, \tag{D.2}$$

where we have assumed the system is *gapped*. However, when the system becomes (nearly) gapless, this expression diverges. In such cases, the divergent gradient causes the optimization to fail, and this is a source of many convergence difficulties in DMET.

One way to ameliorate this issue is to introduce a finite temperature smearing, similar to what is used in mean-field calculations of metals. With an inverse temperature β and a perturbation δu, the Fermi-Dirac density matrix is defined as,

$$\gamma_{kl} = \left[1 + \mathrm{e}^{\beta(h-\mu+\delta u)}\right]^{-1}_{kl}, \tag{D.3}$$

where μ is the Fermi level for the (quasi-)particles. The response of γ with respect to the correlation potential u then involves two terms,

$$\frac{\mathrm{d}\gamma_{kl}[u,\mu(u)]}{\mathrm{d}u_{ij}} = \left.\frac{\partial\gamma_{kl}}{\partial u_{ij}}\right|_{\mu} + \frac{\partial\gamma_{kl}}{\partial\mu}\frac{\partial\mu}{\partial u_{ij}}, \tag{D.4}$$

where the first term is the direct response of the density at a fixed Fermi level, while the second term reflects the contribution of the implicit change in the Fermi level due to the change in potential. The final expression for the first term in Eq. (D.4) is,

$$\frac{\partial\gamma_{kl}}{\partial u_{ij}} = \sum_{pq} C_{kp}C^*_{ip}K_{pq}C_{jq}C^*_{lq}, \tag{D.5}$$

where

$$K_{pq} \equiv n_p\big(1-n_q\big)\frac{1-\mathrm{e}^{\beta(\varepsilon_p-\varepsilon_q)}}{\varepsilon_p-\varepsilon_q}. \tag{D.6}$$

It is easy to check that K_{pq} is always finite when $\varepsilon_p = \varepsilon_q$. One can also let β go to infinity and choose p / q to label occupied / virtual orbitals; the gradient then gives the correct zero temperature limit in Eq. (D.2) (up to a symmetrization).

The final expressions for the second term in Eq. (D.4) are,

$$\begin{aligned}
\frac{\partial\gamma_{kl}}{\partial\mu} &= \sum_p \beta C_{kp} n_p (1-n_p) C^*_{lp}, \\
\frac{\partial\mu}{\partial u_{ij}} &= \left[\sum_p n_p(1-n_p) C^*_{ip} C_{jp}\right] \Big/ \left[\sum_p n_p(1-n_p)\right].
\end{aligned} \tag{D.7}$$

Usually this contribution is very small at low temperatures, compared to the direct response in Eq. (D.5). However, this contribution will be important in a real finite temperature simulation, e.g. in Ref. [302].

Now we first evaluate the direct response [Eq. (D.5)]. One can expand the exponential using the interaction picture,

$$\mathrm{e}^{\beta(h-\mu+\delta u)} = \mathcal{T}_\tau \exp\left[\int_0^\beta \mathrm{d}\tau \delta u(\tau)\right] \mathrm{e}^{\beta(h-\mu)}, \tag{D.8}$$

where $u(\tau)$ is in the interaction picture,

$$\delta u(\tau) = \mathrm{e}^{\tau(h-\mu)} \delta u \mathrm{e}^{-\tau(h-\mu)}. \tag{D.9}$$

To first order, the exponential becomes,

$$\left[1 + \int_0^\beta \mathrm{d}\tau \delta u(\tau)\right] \mathrm{e}^{\beta(h-\mu)}. \tag{D.10}$$

The density matrix is then

$$\begin{aligned}
\gamma &= \left[1 + \mathrm{e}^{\beta(h-\mu)} + \int_0^\beta \mathrm{d}\tau \delta u(\tau)\, \mathrm{e}^{\beta(h-\mu)}\right]^{-1} \\
&= \left\{\left(1+\mathrm{e}^{\beta(h-\mu)}\right)\left[1 + \left(1+\mathrm{e}^{\beta(h-\mu)}\right)^{-1} \int_0^\beta \mathrm{d}\tau \delta u(\tau) \mathrm{e}^{\beta(h-\mu)}\right]\right\}^{-1} \\
&= \left[1 + \left(1+\mathrm{e}^{\beta(h-\mu)}\right)^{-1} \int_0^\beta \mathrm{d}\tau \delta u(\tau) \mathrm{e}^{\beta(h-\mu)}\right]^{-1} \left(1+\mathrm{e}^{\beta(h-\mu)}\right)^{-1} \\
&= \gamma^{(0)} - \gamma^{(0)} \int_0^\beta \mathrm{d}\tau \delta u(\tau) \gamma^{(0)} \mathrm{e}^{\beta(h-\mu)}.
\end{aligned} \tag{D.11}$$

We can expand the first order term in the eigenstates of h (MO basis),

$$-\sum_{pq}|p\rangle\frac{1}{1+\mathrm{e}^{\beta(\varepsilon_p-\mu)}}\int_0^\beta \mathrm{d}\tau \mathrm{e}^{\tau(\varepsilon_p-\varepsilon_q)}\langle p|\delta u|q\rangle\frac{\mathrm{e}^{\beta(\varepsilon_q-\mu)}}{1+\mathrm{e}^{\beta(\varepsilon_q-\mu)}}\langle q|\,. \tag{D.12}$$

Performing the integral yields

$$\sum_{pq}|p\rangle n_p\frac{1-\mathrm{e}^{\beta(\varepsilon_p-\varepsilon_q)}}{\varepsilon_p-\varepsilon_q}\langle p|\delta u|q\rangle(1-n_q)\langle q|\,, \tag{D.13}$$

where $n_p\equiv 1/\left[1+\mathrm{e}^{\beta(\varepsilon_p-\mu)}\right]$. This expression can be easily transformed to the site basis using $|p\rangle=\sum_k|k\rangle C_{kp}$,

$$\sum_{ijklpq}|k\rangle C_{kp}n_p\frac{1-\mathrm{e}^{\beta(\varepsilon_p-\varepsilon_q)}}{\varepsilon_p-\varepsilon_q}C^*_{ip}\delta u_{ij}C_{jq}(1-n_q)C^*_{lq}\langle l|\,, \tag{D.14}$$

and we finally get the derivative of the density matrix with respect to the correlation potential at a finite temperature:

$$\frac{\partial\gamma_{kl}}{\partial u_{ij}}=\sum_{pq}C_{kp}C^*_{ip}K_{pq}C_{jq}C^*_{lq}, \tag{D.15}$$

where

$$K_{pq}\equiv n_p\big(1-n_q\big)\frac{1-\mathrm{e}^{\beta(\varepsilon_p-\varepsilon_q)}}{\varepsilon_p-\varepsilon_q}. \tag{D.16}$$

We then consider Eq. (D.7), i.e. if the Fermi level is allowed to change, this is the contribution from the change in Fermi level. The density response with respect to μ, by definition, is $\frac{\partial\gamma_{kl}}{\partial\mu}=\sum_p\beta C_{kp}n_p(1-n_p)C^*_{lp}$. The response of μ with respect to u can be evaluated by taking the derivative with respect to u_{ij} on both sides of the equality,

$$\sum_p\frac{1}{1+\mathrm{e}^{\beta(\varepsilon_p-\mu)}}=N_{\text{quasi}} \tag{D.17}$$

leading to the following expression,

$$\frac{\partial\mu}{\partial u_{ij}}=\left[\sum_p n_p(1-n_p)\frac{\partial\varepsilon_p}{\partial u_{ij}}\right]/\left[\sum_p n_p(1-n_p)\right]. \tag{D.18}$$

By using the first order perturbation expression for the orbital energy, we reach the final expression for the μ contribution,

$$\frac{\partial\mu}{\partial u_{ij}}=\left[\sum_p n_p(1-n_p)C^*_{ip}C_{jp}\right]/\left[\sum_p n_p(1-n_p)\right]. \tag{D.19}$$

Appendix E

SUPPLEMENTARY MATERIALS FOR CHAPTER IV

E.1 Numerical convergence

Here we assess the accuracy and convergence of the DMET procedure in the three-band model calculations. The error in the DMET calculations arises from three possible sources: (a) DMET self-consistency error (from incomplete convergence), (b) DMRG solver error due to the finite bond dimension, and (c) error from the finite size of the impurity. The finite size error (c) can, in principle, be eliminated by increasing the cluster size and extrapolating to the thermodynamic limit (TDL), as performed in the one-band Hubbard model case [32]. In this work, we use a fixed 2×2 cluster size due to the increased computational cost of the three-band model, thus we cannot assess the finite-size error, except via some comparisons to the 2×2 cluster error in the one-band model. However, the error due to (a) and (b) can be directly estimated in our framework, which we now discuss.

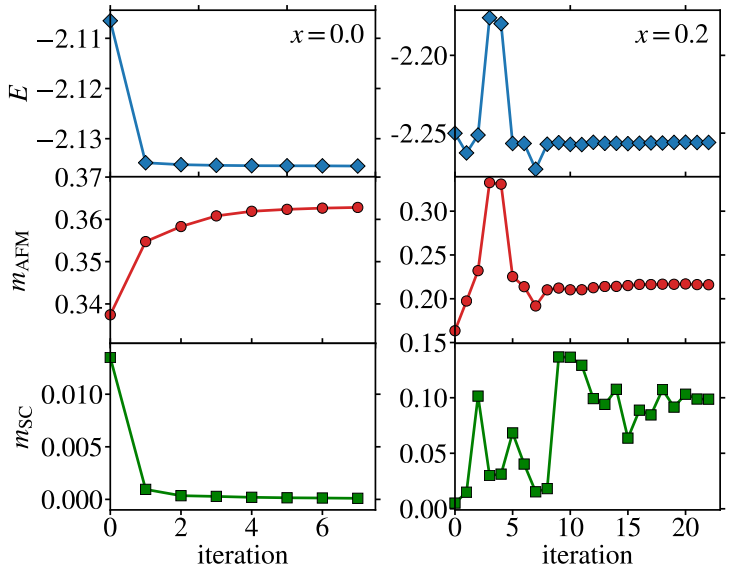

Figure E.1: DMET energy (in units of t_{pd}) and order parameters of the Hybertsen minimal parametrized three-band model, with respect to the number of iterations, at doping $x = 0.0$ (left) and $x = 0.2$ (right).

Fig. E.1 shows the overall convergence of DMET with respect to the number of DMET self-consistent iterations. We observe qualitatively different convergence in the normal and superconducting parts of the DMET phase diagram. To illustrate this, we plot the DMET energy, AFM, and (d-wave) SC order parameter for the Hybertsen model at different dopings

x. (These order parameters are defined precisely in Sec. 4.2). We first discuss the undoped system. Here we see that the DMET cycle converges smoothly within 7 iterations. For the DMET energy, a single DMET step is enough to converge to $\sim 10^{-4}$, demonstrating the utility of single-shot DMET calculations in normal (and especially non-magnetic) states. The order parameters (density matrices) are more strongly affected by self-consistency. We find that the AFM order increases during the iterations, while the SC order is suppressed, giving a pure antiferromagnetic state at convergence. We next consider $x = 0.2$ doping. Here, the self-consistency cycle converges more slowly, requiring about 20 DMET iterations to reach convergence. The total energy as well as AFM order converges at around the 10^{th} iteration, while the SC order oscillates until the 20^{th} iteration. This in part reflects the influence of the initial guess: the AFM guess [v^{σ} in Eq. (2.17)] is quite close to the converged potential, while the SC guess [$\Delta^{\alpha\beta}$ in Eq. (2.17)] is initialized randomly and thus needs more iterations to converge. If we were to restrict the DMET optimization to only pairing potentials with d-wave symmetry (as is commonly done in most cluster DMFT [53] or VCA calculations [172]), the convergence would be much faster. However, the more general form of the correlation potential in DMET allows for the possibility of other pairing channels and orders to emerge, as we will see in the discussion below. The remaining DMET self-consistency error can be estimated from the difference between the expectation values (e.g. DMET energy) of the last two iterations [32], e.g. $\delta E = \frac{1}{2}|E(n-1) - E(n)|$. Consistent with our chosen convergence criterion, the typical size of the DMET self-consistency error in the undoped region is less than 10^{-5} (for both the energy and order parameters), and less than 10^{-4} (for the energy) and $\sim 10^{-3}$ (for the order parameters) in the doped region.

The error from the DMRG solver can be estimated using standard techniques based on the discarded weight in the DMRG calculation [124–126] and can be further reduced by extrapolation. The error in the impurity observables (used to evaluate the DMET energy and order parameters) is linear in the (sufficiently small) discarded weight δ and hence can be extrapolated to the exact result ($\delta = 0$) [126]. The convergence with bond dimension M for fixed correlation potential u is shown in Fig. E.2. We find that the discarded weight in the normal state (undoped model) is extremely small and usually less than 10^{-8}, thus extrapolation is unnecessary. In fact, calculations can be carried out using a bond dimension as small as $M = 100$ without any significant error. On the other hand, when the system becomes superconducting, the discarded weight also increases, e.g. to 3×10^{-5} at $M = 800$, indicating that the system is more entangled. In such situations, extrapolation has a significant effect on the DMET expectation values. Compared to the extrapolated values, at $M = 800$ the error in the energy (per site) and order parameters is about 10^{-3}.

In summary, from the above analysis, we find that the DMET calculations can be smoothly converged, with minimal error from either the self-consistency or from the solver.

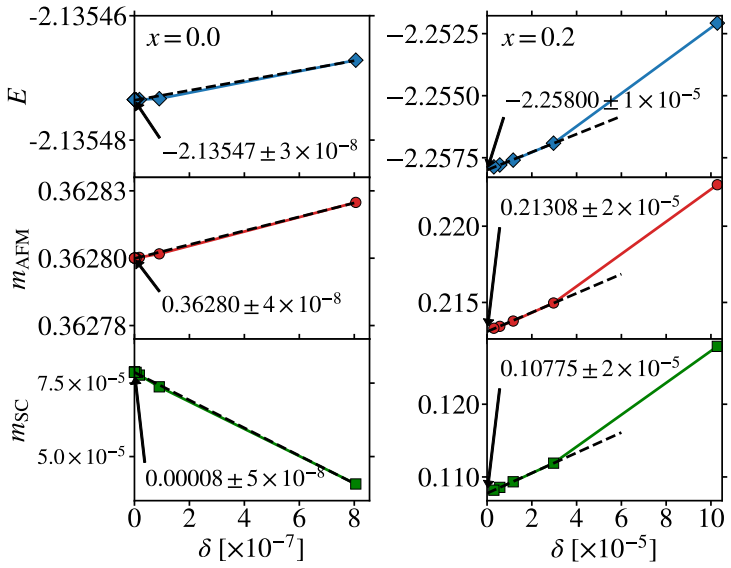

Figure E.2: DMET energy (in units of t_{pd}) and order parameters of the Hybertsen minimal parametrized three-band model, with respect to the discarded weight δ of the DMRG solver, at doping $x = 0.0$ (left) and $x = 0.2$ (right). The values are linearly extrapolated to the limit where $\delta = 0.0$ (dash line). The error shown is the standard deviation of linear regression.

E.2 Antiferromagnetic order of one-band Hubbard model

See Fig. E.3 for the AFM order of the one-band Hubbard model from DMET with different cluster sizes.

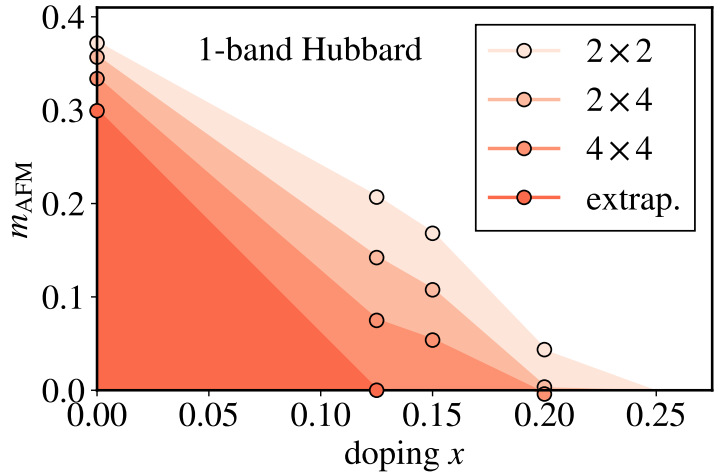

Figure E.3: AFM order parameter of the doped one-band Hubbard model ($U = 6$) from DMET with different cluster sizes (2×2, 2×4 and 4×4) and the corresponding extrapolated value. The data are taken from Ref. [32].

E.3 Phase diagram of Hybertsen and Martin models

See Fig. E.4 for the antiferromagnetic (AFM) and superconducting (SC) order of the three-band Hubbard model with Hybertsen and Martin minimal parametrizations from DMET.

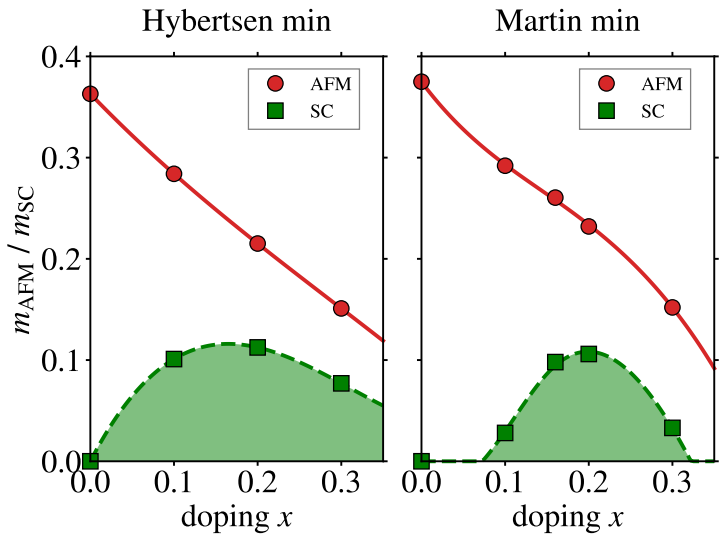

Figure E.4: AFM and SC order parameter of the hole-doped three-band Hubbard model (Hybertsen and Martin parameter sets) from DMET.

E.4 Charge, spin and pairing orders at different dopings and parametrizations

See Fig. E.5 - E.10 for charge, spin and pairing patterns at different dopings and parametrizations of the three-band Hubbard model.

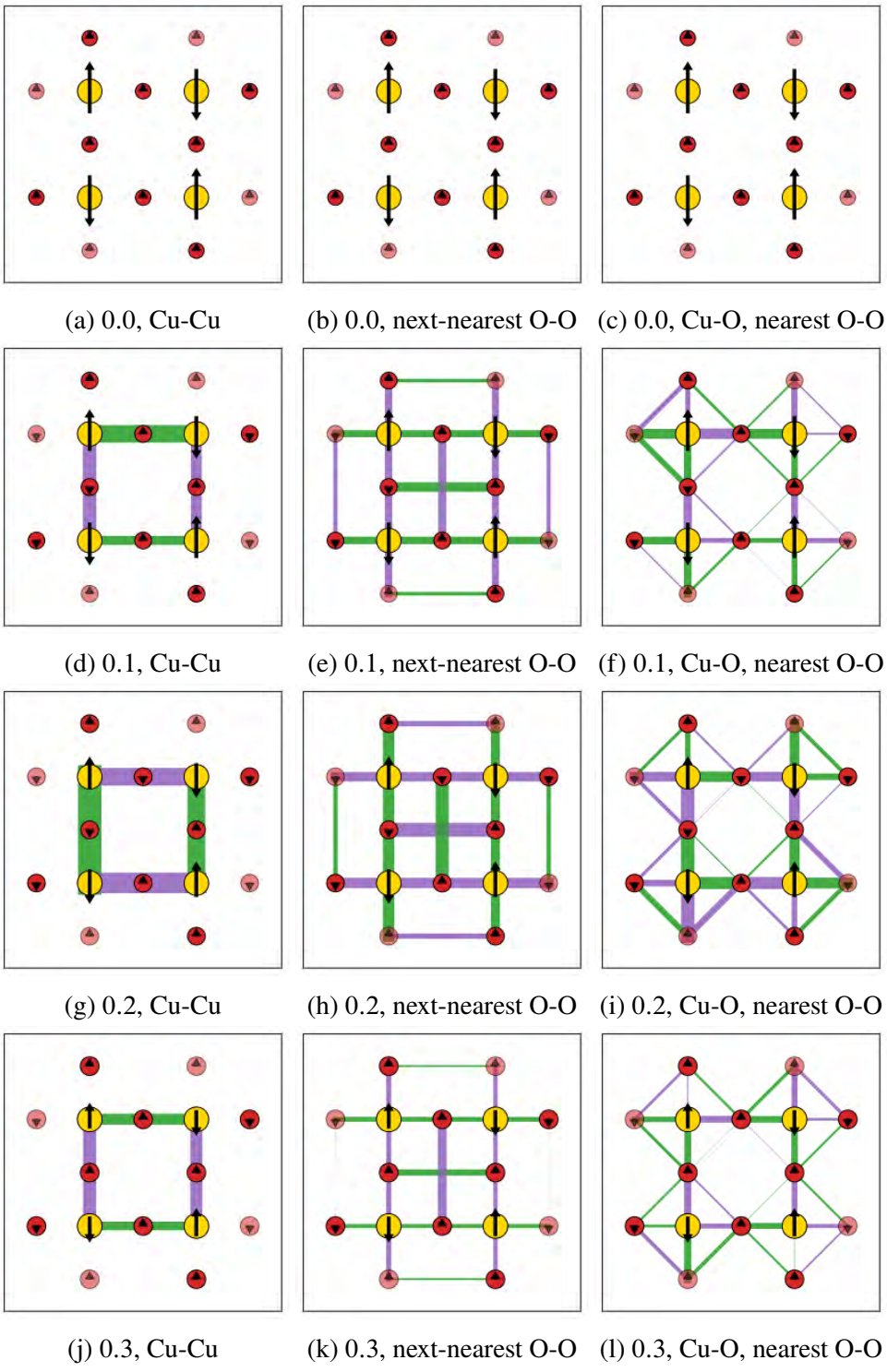

(a) 0.0, Cu-Cu (b) 0.0, next-nearest O-O (c) 0.0, Cu-O, nearest O-O

(d) 0.1, Cu-Cu (e) 0.1, next-nearest O-O (f) 0.1, Cu-O, nearest O-O

(g) 0.2, Cu-Cu (h) 0.2, next-nearest O-O (i) 0.2, Cu-O, nearest O-O

(j) 0.3, Cu-Cu (k) 0.3, next-nearest O-O (l) 0.3, Cu-O, nearest O-O

Figure E.5: Charge, spin and pairing patterns for the hole-doped Hybertsen model. See the caption of Fig. 4.9 in Chap. 4 for details.

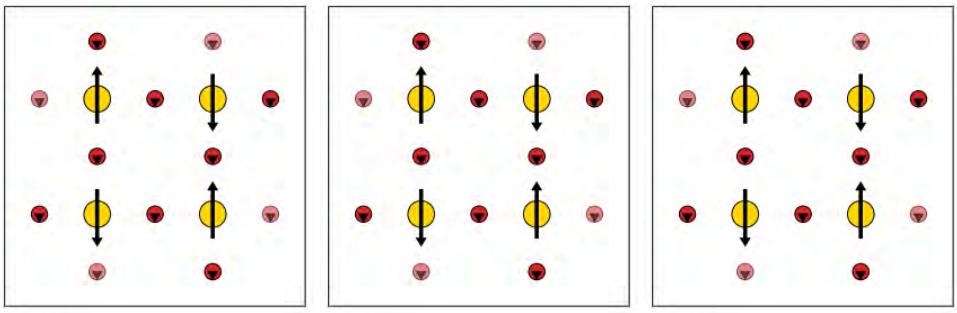

(a) 0.0, Cu-Cu (b) 0.0, next-nearest O-O (c) 0.0, Cu-O, nearest O-O

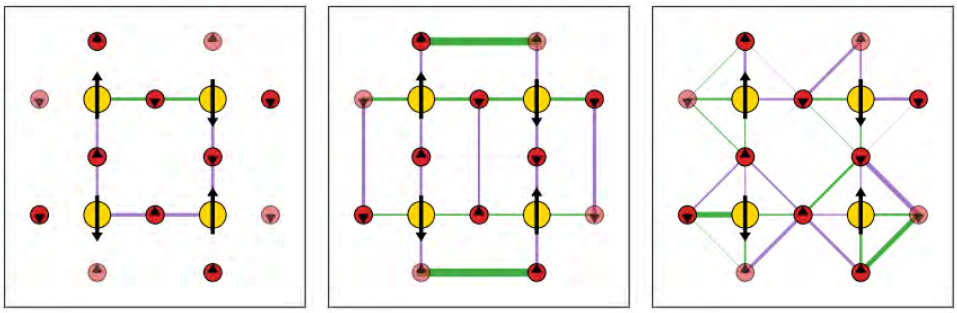

(d) 0.1, Cu-Cu (e) 0.1, next-nearest O-O (f) 0.1, Cu-O, nearest O-O

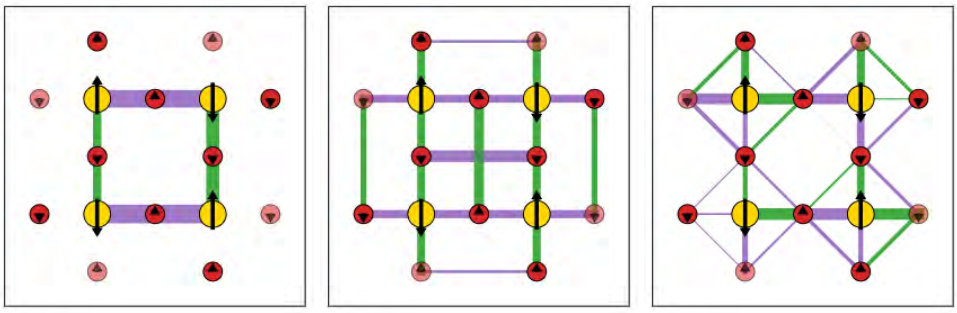

(g) 0.2, Cu-Cu (h) 0.2, next-nearest O-O (i) 0.2, Cu-O, nearest O-O

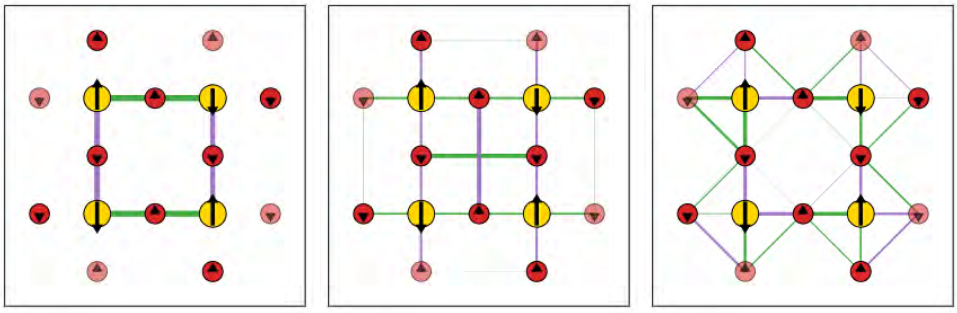

(j) 0.3, Cu-Cu (k) 0.3, next-nearest O-O (l) 0.3, Cu-O, nearest O-O

Figure E.6: Charge, spin and pairing distributions of the hole-doped Martin model. See the caption of Fig. 4.9 in Chap. 4 for details.

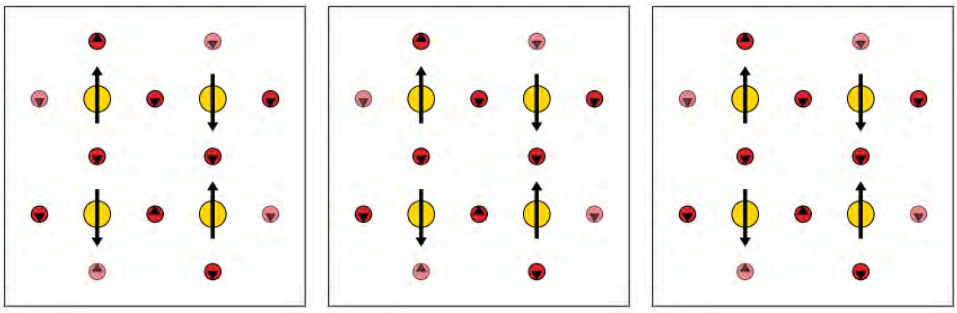

(a) 0.0, Cu-Cu (b) 0.0, next-nearest O-O (c) 0.0, Cu-O, nearest O-O

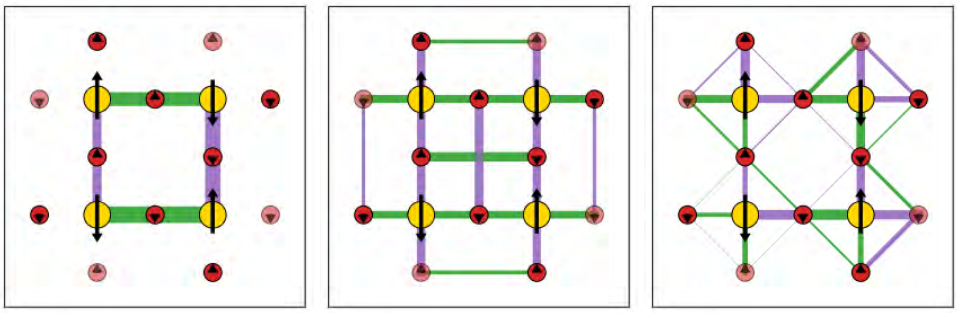

(d) 0.1, Cu-Cu (e) 0.1, next-nearest O-O (f) 0.1, Cu-O, nearest O-O

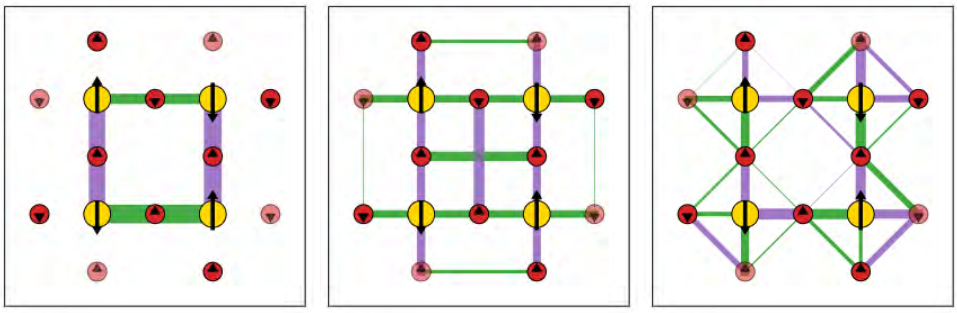

(g) 0.2, Cu-Cu (h) 0.2, next-nearest O-O (i) 0.2, Cu-O, nearest O-O

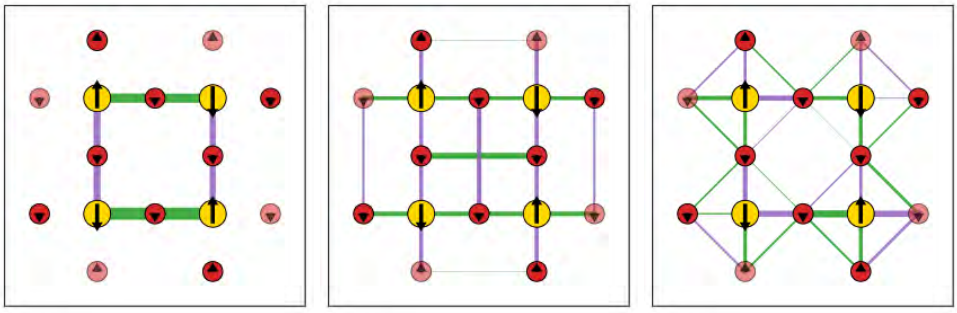

(j) 0.3, Cu-Cu (k) 0.3, next-nearest O-O (l) 0.3, Cu-O, nearest O-O

Figure E.7: Charge, spin and pairing distributions of the Hanke minimal model. See the caption of Fig. 4.9 in Chap. 4 for details.

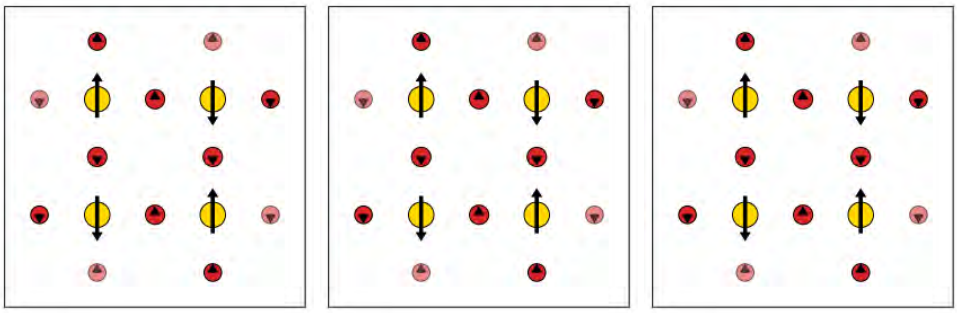

(a) 0.0, Cu-Cu (b) 0.0, next-nearest O-O (c) 0.0, Cu-O, nearest O-O

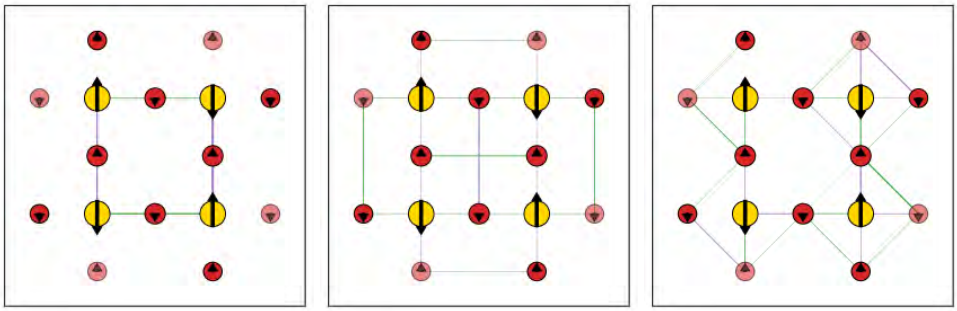

(d) 0.1, Cu-Cu (e) 0.1, next-nearest O-O (f) 0.1, Cu-O, nearest O-O

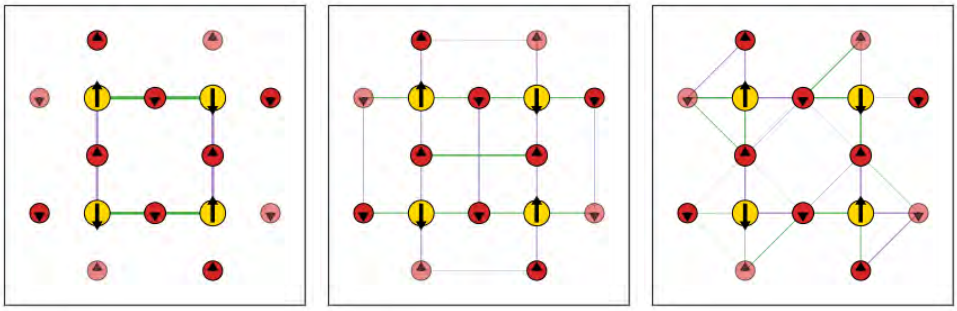

(g) 0.2, Cu-Cu (h) 0.2, next-nearest O-O (i) 0.2, Cu-O, nearest O-O

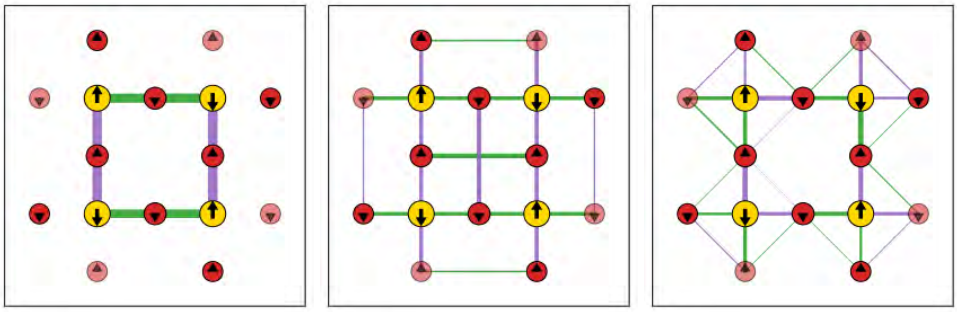

(j) 0.3, Cu-Cu (k) 0.3, next-nearest O-O (l) 0.3, Cu-O, nearest O-O

Figure E.8: Charge, spin and pairing distributions of the hole-doped Hanke full model (solution 2, from the strongly polarized guess). See the caption of Fig. 4.9 in Chap. 4 for details.

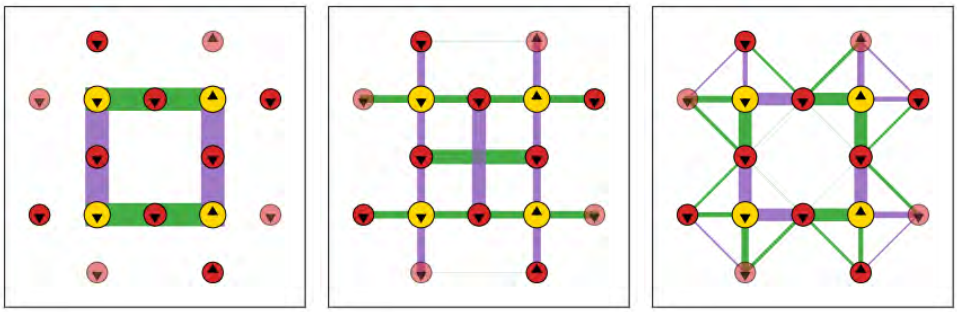

(m) 0.4, Cu-Cu (n) 0.4, next-nearest O-O (o) 0.4, Cu-O, nearest O-O

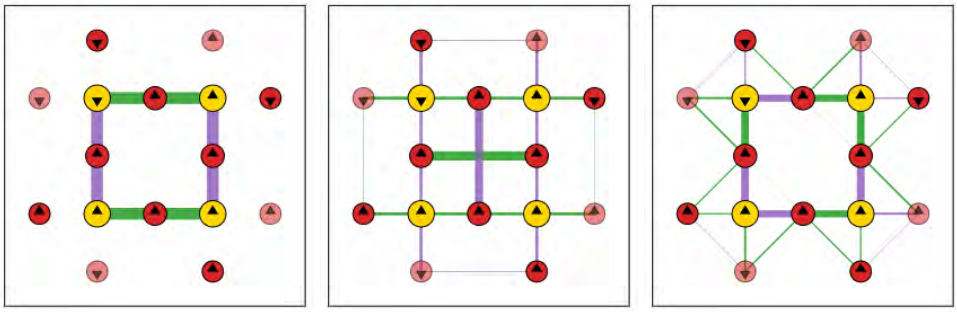

(p) 0.5, Cu-Cu (q) 0.5, next-nearest O-O (r) 0.5, Cu-O, nearest O-O

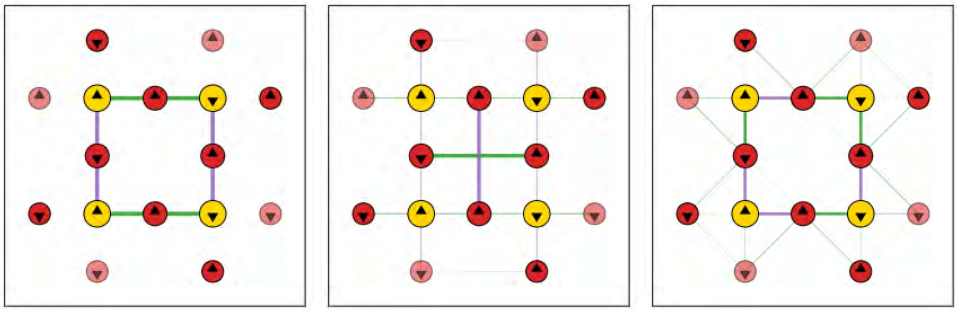

(s) 0.6, Cu-Cu (t) 0.6, next-nearest O-O (u) 0.6, Cu-O, nearest O-O

Figure E.8: Charge, spin and pairing distributions of the hole-doped Hanke full model (solution 2, from the strongly polarized guess). See Fig. 4.9 in Chap. 4 for details. (cont.).

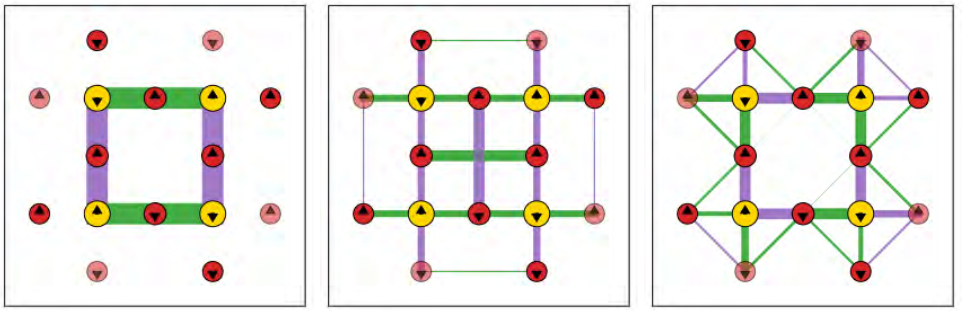

(a) 0.3, Cu-Cu (b) 0.3, next-nearest O-O (c) 0.3, Cu-O, nearest O-O

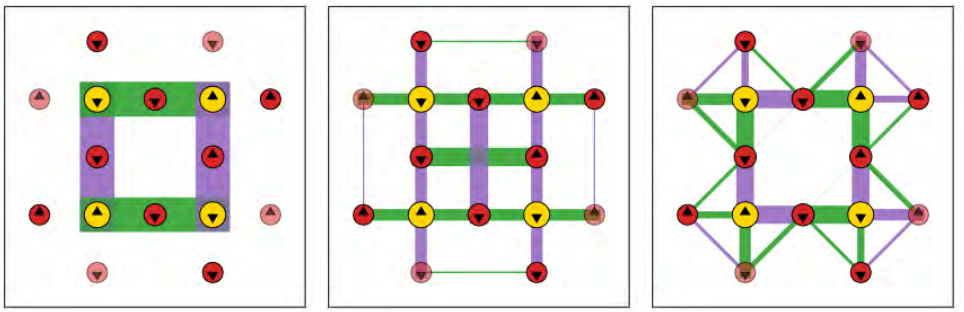

(d) 0.31, Cu-Cu (e) 0.31, next-nearest O-O (f) 0.31, Cu-O, nearest O-O

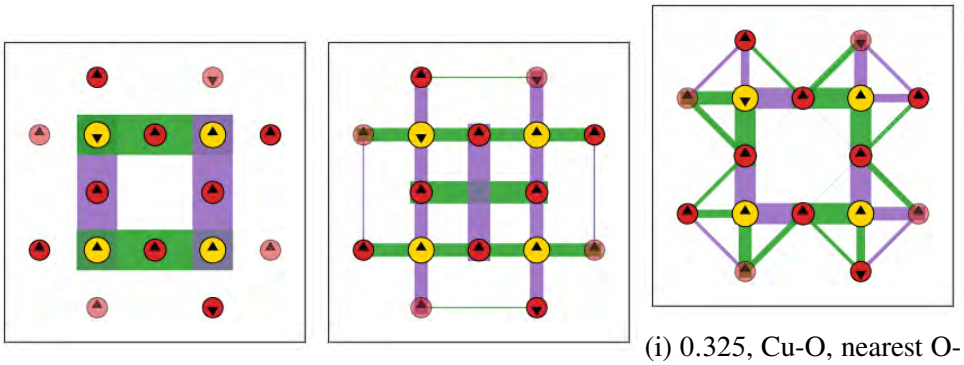

(g) 0.325, Cu-Cu (h) 0.325, next-nearest O-O (i) 0.325, Cu-O, nearest O-O

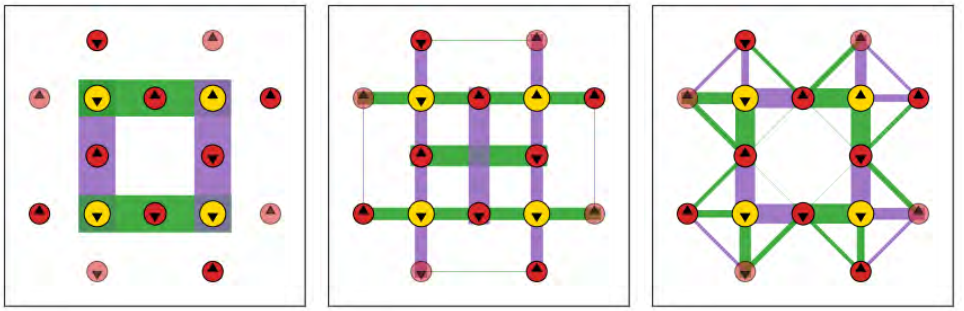

(j) 0.35, Cu-Cu (k) 0.35, next-nearest O-O (l) 0.35, Cu-O, nearest O-O

Figure E.9: Charge, spin and pairing distributions of the hole-doped Hanke full model (solution 1, from the weakly polarized guess). See the caption of Fig. 4.9 in Chap. 4 for details.

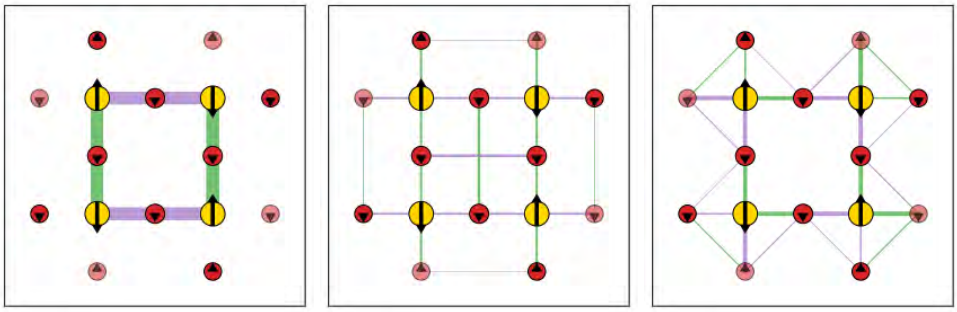

(a) −0.1, Cu-Cu (b) −0.1, next-nearest O-O (c) −0.1, Cu-O, nearest O-O

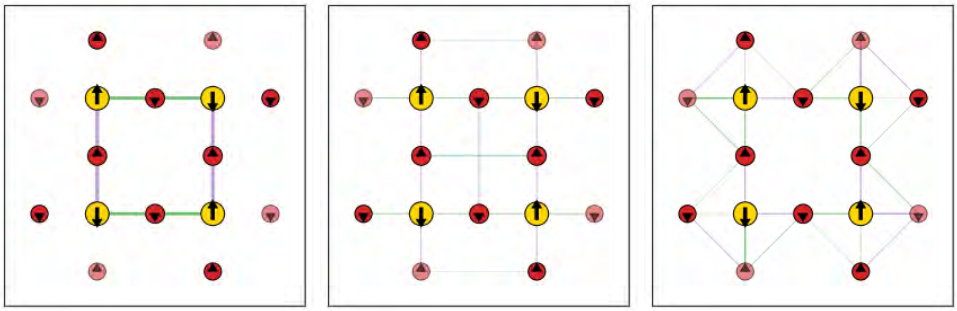

(d) −0.2, Cu-Cu (e) −0.2, next-nearest O-O (f) −0.2, Cu-O, nearest O-O

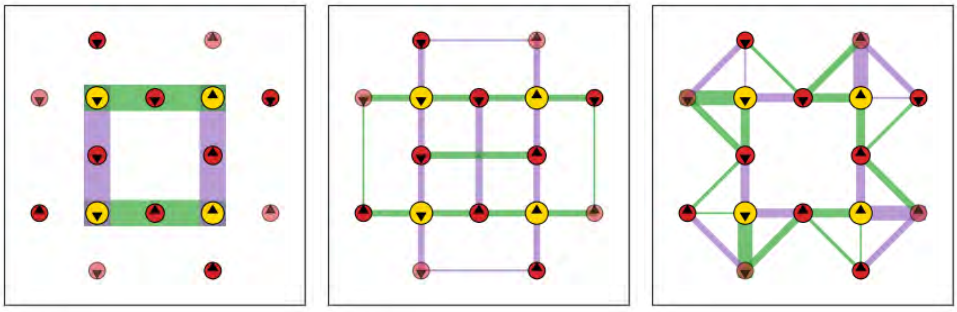

(g) −0.3, Cu-Cu (h) −0.3, next-nearest O-O (i) −0.3, Cu-O, nearest O-O

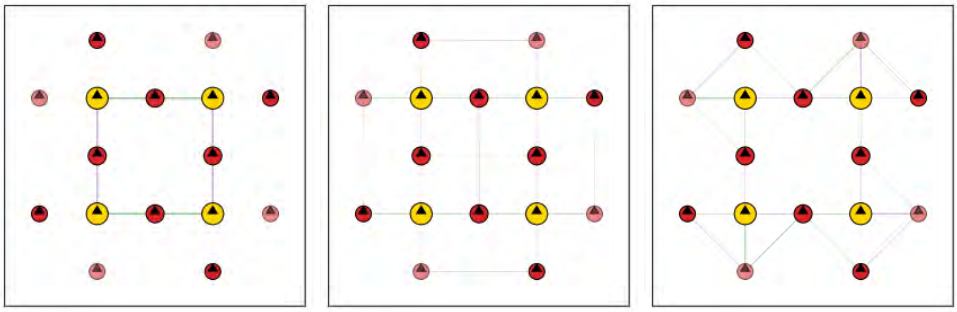

(j) −0.4, Cu-Cu (k) −0.4, next-nearest O-O (l) −0.4, Cu-O, nearest O-O

Figure E.10: Charge, spin and pairing distributions of the electron-doped Hanke full model. See the caption of Fig. 4.9 in Chap. 4 for details.

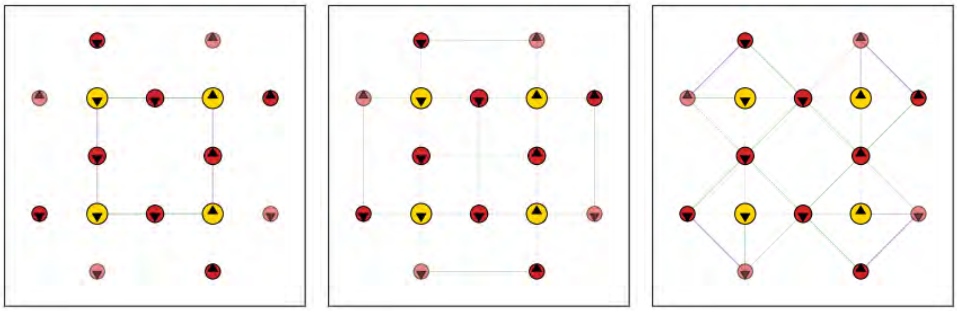

(m) -0.5, Cu-Cu (n) -0.5, next-nearest O-O (o) -0.5, Cu-O, nearest O-O

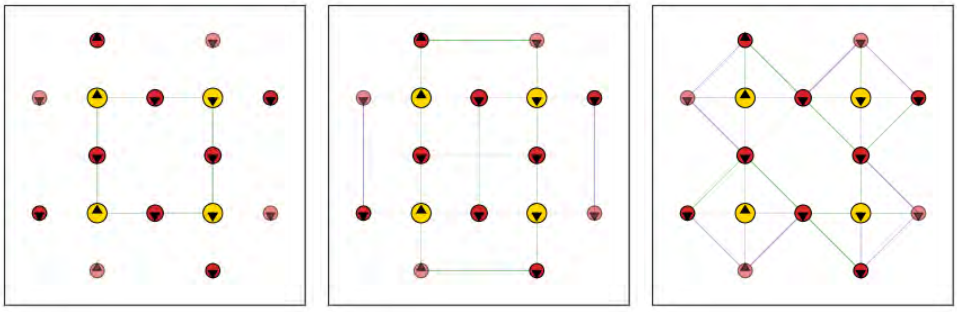

(p) -0.6, Cu-Cu (q) -0.6, next-nearest O-O (r) -0.6, Cu-O, nearest O-O

Figure E.10: Charge, spin and pairing distributions of the electron-doped Hanke full model. See the caption of Fig. 4.9 in Chap. 4 for details. (cont.).

Appendix F

SUPPLEMENTARY MATERIALS FOR CHAPTER VI

F.1 Computational details

System

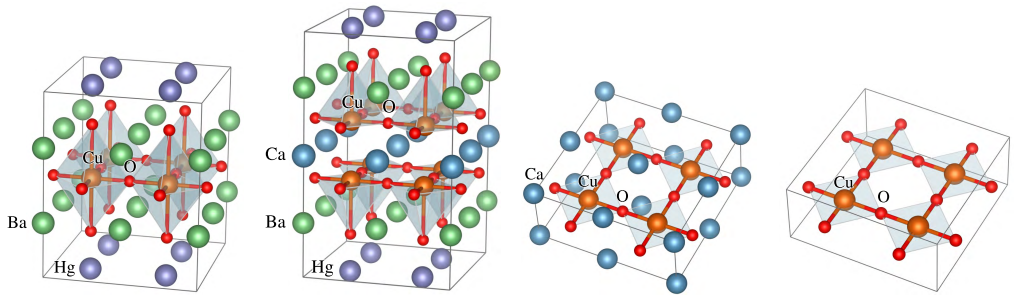

(a) Hg-1201 (b) Hg-1212 (c) CCO (d) CuO_2^{2-}

Figure F.1: Crystal structures of $HgBa_2CuO_4$ (Hg-1201), $HgBa_2CaCu_2O_6$ (Hg-1212), $CaCuO_2$ (CCO) and CuO_2^{2-}.

Table F.1: Crystal structures of $HgBa_2CuO_4$ (Hg-1201), $HgBa_2CaCu_2O_6$ (Hg-1212), $CaCuO_2$ (CCO) and CuO_2^{2-}.

Compound	a [Å]	c [Å]	∠ Cu-O-Cu [°]	apical $\delta^z_{\mathrm{Cu-O}}$ [Å]
Hg-1201 [a]	3.8714	9.5023	180.0	2.767
Hg-1212 [b]	3.8630	12.6978	179.5	2.822
CCO [c]	3.8556	3.1805	180.0	
CuO_2^{2-}	3.8556	3.1805	180.0	

[a] From Ref. [303]. [b] From Ref. [304]. [c] From Ref. [305].

We primarily consider 4 compounds in this work: (a) the single-layer compound $HgBa_2CuO_4$ (Hg-1201), (b) the double-layer compound $HgBa_2CaCu_2O_6$ (Hg-1212), (c) the infinite-layer compound $CaCuO_2$ (CCO), and (d) a hypothetical CuO_2^{2-} layer (repeated in the vertical direction) (see Fig. F.1). The lattice parameters are summarized in Table F.1.

We use two types ($\sqrt{2}\times\sqrt{2}$ and 2×2) of supercells in this work to accommodate different magnetic configurations (see Sec. F.1 for details). Their crystal structure files can be found at the GitHub repository `https://github.com/zhcui/cuprate_parent_state_data`.

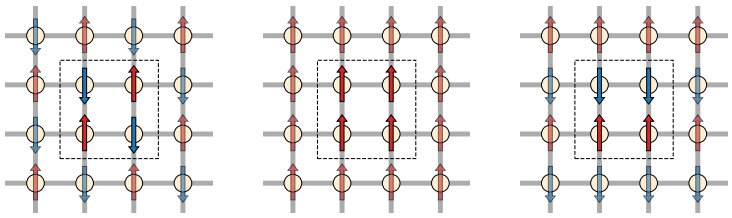

(a) AFM (b) FM (c) SDW

Figure F.2: Magnetic configurations considered in this work. Only Cu atoms are shown in the figure and the two flavors of spin are represented by up and down arrows respectively.

Magnetic configurations and model mapping

In this work, we consider 3 magnetic configurations for the in-plane exchange coupling in all cuprate calculations, namely AFM, FM, SDW states (see Fig. F.2). The spins in the AFM state [Fig. F.2(a)] are arranged in a checkerboard pattern while in the FM [Fig. F.2(b)] state the spins are all aligned in the same direction. In the SDW phase [Fig. F.2(c)], spins are aligned along the x direction, but are anti-parallel along the y direction.

Heisenberg model. In this work, we consider a nearest-neighbor (NN) Heisenberg spin Hamiltonian with the nearest (J_1) neighbor coupling parameter,

$$H = J_1 \sum_{\langle ij \rangle} \mathbf{S}_i \cdot \mathbf{S}_j, \tag{F.1}$$

where $\langle \cdots \rangle$ denotes the nearest neighbors. Within the Heisenberg model, the energies of the 3 magnetic states can be expressed as,

$$\begin{aligned} E^{\mathrm{AFM}} &= E_0 - J_1 N Z_1 S^2, \\ E^{\mathrm{FM}} &= E_0 + J_1 N Z_1 S^2, \\ E^{\mathrm{SDW}} &= E_0, \end{aligned} \tag{F.2}$$

where Z_n denotes the average number of n^{th} nearest neighbors (here $Z_1 = Z_2 = 2$), N is the number of Cu atoms per cell (here $N = 4$ for the 2×2 cell) and $S = 1/2$.

1-band Hubbard model. Using the fourth order perturbation theory of the one-band Hubbard model (with hopping t and onsite interaction U) around the $U = \infty$ limit, we obtain a spin Hamiltonian with 4 terms [306],

$$\begin{aligned} H =& J_1 \sum_{\langle ij \rangle} \mathbf{S}_i \cdot \mathbf{S}_j + J_2 \sum_{\langle\langle ij \rangle\rangle} \mathbf{S}_i \cdot \mathbf{S}_j + J_3 \sum_{\langle\langle\langle ij \rangle\rangle\rangle} \mathbf{S}_i \cdot \mathbf{S}_j \\ &+ J_{\mathrm{c}} \sum_{\langle ijkl \rangle} \big(\mathbf{S}_i \cdot \mathbf{S}_j\big)(\mathbf{S}_k \cdot \mathbf{S}_l) + (\mathbf{S}_i \cdot \mathbf{S}_l)\big(\mathbf{S}_k \cdot \mathbf{S}_j\big) - (\mathbf{S}_i \cdot \mathbf{S}_k)\big(\mathbf{S}_j \cdot \mathbf{S}_l\big), \end{aligned} \tag{F.3}$$

where

$$J_1 = 4\frac{t^2}{U} - 24\frac{t^4}{U^3}, \tag{F.4}$$

and

$$J_c = 80\frac{t^4}{U^3} \tag{F.5}$$

is the cyclic magnetic coupling parameter that measures the exchange pathway around the plaquette of the four Cu's.

$$J_2 = J_3 = \frac{J_c}{20} = 4\frac{t^4}{U^3}. \tag{F.6}$$

Within this expansion of the Hubbard model, the energies of the 3 magnetic states can be expressed as,

$$\begin{aligned} E^{\mathrm{AFM}} &= E_0 - J_1 N Z_1 S^2 + J_2 N Z_2 S^2 + J_3 N Z_3 S^2 + J_c N Z_c S^4, \\ E^{\mathrm{FM}} &= E_0 + J_1 N Z_1 S^2 + J_2 N Z_2 S^2 + J_3 N Z_3 S^2 + J_c N Z_c S^4, \\ E^{\mathrm{SDW}} &= E_0 - J_2 N Z_2 S^2 + J_3 N Z_3 S^2 + J_c N Z_c S^4, \end{aligned} \tag{F.7}$$

where $Z_1 = Z_2 = Z_3 = 2$, $Z_c = 1$. Equivalently, the energies can be expressed in terms of the two independent Hubbard parameters, t and U,

$$\begin{aligned} E^{\mathrm{AFM}} &= E_0 - 8\frac{t^2}{U} + 84\frac{t^4}{U^3}, \\ E^{\mathrm{FM}} &= E_0 + 8\frac{t^2}{U} - 12\frac{t^4}{U^3}, \\ E^{\mathrm{SDW}} &= E_0 + 20\frac{t^4}{U^3}. \end{aligned} \tag{F.8}$$

These parameters can be determined from the least-squares solution of the above equations.

Effective $3J$ *(multi-*J*) Heisenberg model.* The magnetic couplings from the 1-band Hubbard model can be renormalized into a multi-J Heisenberg model with couplings J_1, J_2 and J_3 [259, 262].

$$H = J_1^{\mathrm{eff}} \sum_{\langle ij \rangle} \mathbf{S}_i \cdot \mathbf{S}_j + J_2^{\mathrm{eff}} \sum_{\langle\langle ij \rangle\rangle} \mathbf{S}_i \cdot \mathbf{S}_j + J_3^{\mathrm{eff}} \sum_{\langle\langle\langle ij \rangle\rangle\rangle} \mathbf{S}_i \cdot \mathbf{S}_j. \tag{F.9}$$

The effective J's are related to the previous 1-band Hubbard J's,

$$\begin{aligned} J_1^{\mathrm{eff}} &= J_1 - 2J_c S^2, \\ J_2^{\mathrm{eff}} &= J_2 - J_c S^2, \\ J_3^{\mathrm{eff}} &= J_3. \end{aligned} \tag{F.10}$$

Inter-layer coupling $J_\perp$. We consider both inter-layer AFM and FM coupled configurations for CCO to evaluate the inter-layer coupling $J_\perp$,

$$J_\perp = \frac{E_{\mathrm{FM}} - E_{\mathrm{AFM}}}{2N_{\mathrm{Cu}} Z_\perp S^2}, \tag{F.11}$$

where the perpendicular coordination number $Z_\perp = 1$. (Note: the individual cuprate layers in CCO are AFM coupled; FM above refers only to the inter-layer, or layer-layer, coupling).

The inter-layer magnetic order of the double-layer compound Hg-1212 is fixed to be AFM coupled; we do not evaluate $J_\perp$ for this compound since it is not required for the spin-wave spectrum at $k_z = 0$, the setting for Hg-1212. The inter-layer couplings in the other compounds are very weak and are thus neglected.

Spin wave spectrum. Once the spin model parameters are determined from the *ab initio* calculation, the spin wave spectrum can be obtained from linear spin wave theory, which converts a spin problem to a quadratic bosonic problem [307, 308]. We use the SpinW program [308] to generate the spin wave dispersions of the three compounds and we compare them to data from resonant inelastic X-ray scattering (RIXS). We present spin-wave spectra for the NN Heisenberg and $3J^{\text{eff}}$ model. Following typical experimental conventions (which allows us to compare directly to the experimental couplings), we do not use a quantum renormalization factor for the NN Heisenberg spin-wave spectrum, but use a quantum renormalization factor of $Z_c = 1.219$ [259] for the multi-J model.

Single-particle method settings

The single particle mean-field (SCF) calculations (HF, DFT, DFT+U) were carried out in crystalline Gaussian bases using the PySCF package [82, 138], and were cross checked with plane wave basis calculations using the VASP package [269–273].

For CCO and CuO_2^{2-}, we used the minimal basis GTH-SVP-MOLOPT-SR for various benchmarks. This consists of $1s1p1d$ shells for Cu, $1s1p$ for O, $2s1p$ for Ca, and uses the GTH pseudopotential for the core electrons [192, 193]. GDF was used to compute the two-electron integrals. We used an even-tempered Gaussian basis as the density fitting auxiliary basis ($n_{\text{aux}} \sim 10 n_{\text{AO}}$).

For the more realistic calculations, we used an all-electron basis of polarized double-zeta (split-valence) quality, def2-SVP [258] for all elements (consisting of $5s3p2d1f$ shells for Cu, $3s2p1d$ for O, $4s2p1d$ for Ca, $5s2p2d1f$ for Hg, $3s2p1d$ for Ba, and $5s2p2d1f$ for La). The sufficiency of the basis was further checked with a larger polarized triple-zeta basis set def2-TZVP [258] as well as plane-wave basis calculations. For Hg, Ba and La, an effective core potential (ECP) was used to handle the core electrons and scalar relativistic effects [309, 310]. For the Hg, Ba, Ca and La bases, small exponent Gaussians (< 0.05) were dropped to remove linear dependencies and to ensure numerical stability. GDF was also used for the two-electron integrals. We used the density fitting auxiliary basis def2-SVP-RI [311, 312], which is specially optimized for correlated calculations with the def2-SVP basis ($n_{\text{aux}} \sim 5 n_{\text{AO}}$).

For the plane wave basis calculations, a projector augmented wave (PAW) [273, 274] representation was used to treat the core electrons and we used a plane wave kinetic energy cutoff of 500 eV.

We sampled the Brillouin zone with a Γ-centered **k** mesh: $6 \times 6 \times 2$ for the $\sqrt{2} \times \sqrt{2}$ cell of the single layer compounds CuO_2^{2-}, CCO and Hg-1201; $6 \times 6 \times 1$ for the $\sqrt{2} \times \sqrt{2}$ cell of the double layer compound Hg-1212; $4 \times 4 \times 2$ for the 2×2 supercell of the single layer compounds CuO_2, CCO and Hg-1201; $4 \times 4 \times 1$ for the 2×2 supercell of the double layer compound Hg-1212. All mean-field calculations were converged to an accuracy of better than 10^{-8} a.u. per unit cell.

We used the Perdew-Burke-Ernzerhof (PBE) functional [191] in the DFT+U calculations and also used the PBE0 [275] hybrid functional. PBE+U calculations were performed using Dudarev's approach with a U value of 7.5 eV for the Cu 3d AOs. We also refer to additional DFT data using other functionals from the literature (see below).

DMET settings

All DMET routines, including the bath construction, integral transformation, solver interface, chemical potential and correlation potential fitting, are implemented in the LIBDMET package [98, 180]. To remove core orbitals, which make the bath construction unstable and increases computational cost, we froze the lowest mean-field bands ($1s2s2p3s3p$ bands for Cu and Ca, $1s2s$ bands for O, $5s5p$ bands for Hg, Ba and La). We added the correlation potential u to all Cu and O orbitals and fit the three-band orbital blocks of the density matrices, which avoids any instabilities in the DMET self-consistency. The convergence criterion on the DMET self-consistency was chosen such that the maximal change of an element in u was less than 5×10^{-5} a.u., which corresponds roughly to an energy accuracy of better than 1×10^{-5} a.u.

Solver settings

We used the UCCSD and UCCSD(T) methods implemented in PYSCF as solvers. The CCSD energy and Λ equations were converged to an energy of better than 10^{-6} a.u.

The DMRG impurity solver used the BLOCK2 program [125, 139–141, 241]. We used the standard DMRG sweep settings and a genetic algorithm for orbital ordering. The tolerance of the DMRG sweep energy was set to 10^{-6} a.u., the largest bond dimension was chosen to be 5000 and extrapolation of the DMET energy was performed (see below).

The largest embedding problem we treated using the UCCSD solver was of size (364o, 168e), with multiple such size fragments solved in parallel in the multi-fragment embedding formalism. For the UCCSD(T) and DMRG solvers, the largest problems treated were of size (122o, 60e) and (60o, 60e) respectively.

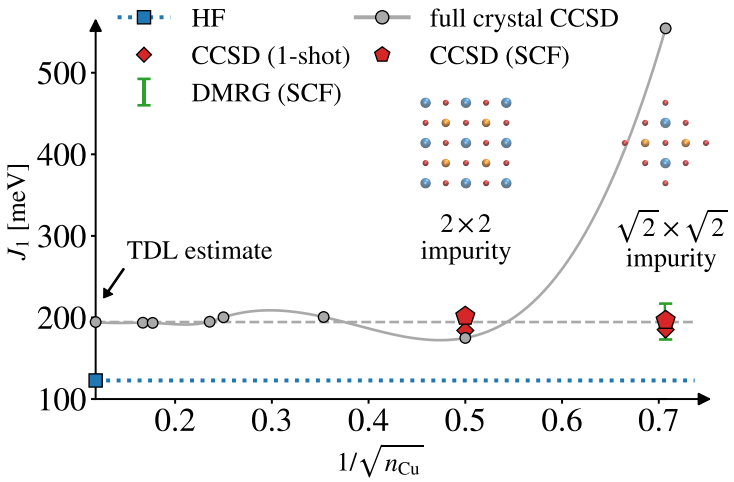

Figure F.3: Benchmark with **k**-CCSD. See the caption of Fig. 6.1(f). Here, we additionally show DMET 1-shot results and HF results.

F.2 Benchmarks

Finite size effects

We first benchmark the finite impurity size error of the DMET calculations. We extract the nearest-neighbor coupling J_1 in a large periodic lattice from a **k**-CCSD solver, and compare that to J_1 extracted from impurity calculations of different sizes, also with the CCSD solver. The difference between these results is the finite size error. The largest periodic lattice used for this purpose was a $6 \times 6 \times 1$ lattice of the AFM cell of CCO (72 primitive unit cells). In Fig. F.3, we show the convergence of the J_1 values from **k**-CCSD calculations and different **k** meshes (cluster sizes) (note that the mean-field finite size error is always corrected by the result from the largest mean-field calculation, so the data is showing the convergence with respect to correlation effects only).

For the impurity, we use two cluster shapes ($\sqrt{2} \times \sqrt{2}$ and 2×2 cells of CCO). Even in the very small $\sqrt{2} \times \sqrt{2}$ impurity (the smallest magnetic supercell), the embedding calculation gives a very accurate J_1. Importantly, the DMET calculations show significantly less finite size error compared to CCSD on periodic clusters of the same size, showing the effectiveness of the embedding. Another feature we observe is that the 1-shot DMET calculation (1^{st} iteration) gives similar results to the self-consistent one. This indicates that the initial mean-field, which breaks S^2 symmetry, is already close to the final one corrected by the correlation potential. This is, however, not true in the larger basis set calculations, where correlations produce larger corrections and self-consistency is important.

Table F.2: Local magnetic moment and nearest exchange coupling parameter of CCO with a minimal basis set.

Method	m_{AFM} [μ_{B}]	m_{FM} [μ_{B}]	J_1 [meV]
multi-frag ($\sqrt{2} \times \sqrt{2}$ cell, 1-shot)	0.62	0.76	178
multi-frag ($\sqrt{2} \times \sqrt{2}$ cell, SCF)	0.61	0.76	191
full-cell ($\sqrt{2} \times \sqrt{2}$ cell, 1-shot)	0.63	0.77	185
full-cell ($\sqrt{2} \times \sqrt{2}$ cell, SCF)	0.62	0.77	197
multi-frag (2×2 cell, 1-shot)	0.63	0.77	183
multi-frag (2×2 cell, SCF)	0.63	0.77	211
full-cell (2×2 cell, 1-shot)	0.63	0.78	184
full-cell (2×2 cell, SCF)	0.63	0.78	202
UCCSD (extrap.)			194

Multi-fragment scheme

We next test the accuracy of the multi-fragment scheme. From Table F.2, we see that the error in J_1 from the multi-fragment treatment is less than $\sim$ 10 meV and indeed energies in all the schemes are very close to the TDL **k**-CCSD value. The multi-fragment scheme also does not affect the local magnetic moments. Since the multi-fragment scheme does not introduce significant errors in the minimal basis but greatly reduces the computation cost, we use it in all following calculations.

Basis set completeness

We first check basis set convergence for the mean-field (single-particle) methods. Cross-checks between def2-SVP and a plane-wave basis are summarized in Tables F.3-F.6. The data clearly show that the relative energies in both the HF and DFT calculations are well converged. The error is 5 meV or less in HF, and 10 meV or less in PBE0. The deviation in PBE+U is larger, primarily due to the different choices of local projector, but not the basis set completeness. The basis convergence in HF is also shown in Table F.7, where the difference among def2-SVP (the main basis used in this work), def2-TZVP and plane wave is less than 1 meV.

Converging the correlation parts of the energy is in principle more challenging, requiring bases with more valence, polarization, and diffuse functions. We assess the basis set completeness in the small impurity ($\sqrt{2} \times \sqrt{2}$ cell) DMET calculations in Table F.7. Compared to a larger basis def2-TZVP, the magnetic moments from def2-SVP agree well, and the difference in the derived NN magnetic coupling J_1 is only 5 meV. This suggests that def2-SVP basis provides a satisfactory balance between accuracy and efficiency for this study, allowing for reasonably converged energy scales while enabling larger impurity sizes (2×2 supercell) in the following realistic calculations.

Table F.3: Comparison of the single-particle approach results for Hg-1201 from PySCF and VASP. Some long-range parameters are left blank since the SDW state in the plane wave basis converges to a paramagnetic state.

Method	software	Heisenberg	1-band Hubbard				$3J^{\text{eff}}$ Heisenberg		
		J_1	J_1	J_2, J_3	J_c	U/t	J_1^{eff}	J_2^{eff}	J_3^{eff}
PBE+U	PySCF	149.7	149.7	9.7	194.7	4.6	52.4	-38.9	9.7
	VASP	175.2	175.2	8.0	159.0	5.3	95.7	-31.8	8.0
PBE0	PySCF	198.8	198.8	11.3	225.4	4.9	86.1	-45.1	11.3
	VASP	206.0	206.0	13.9	278.2	4.6	66.9	-55.6	13.9
HF	PySCF	33.7	33.7	1.0	20.2	6.3	23.6	-4.0	1.0
	VASP	34.2							

Table F.4: Comparison of the single-particle approach results for Hg-1212 from PySCF and VASP.

Method	software	Heisenberg	1-band Hubbard				$3J^{\text{eff}}$ Heisenberg		
		J_1	J_1	J_2, J_3	J_c	U/t	J_1^{eff}	J_2^{eff}	J_3^{eff}
PBE+U	PySCF	159.6	159.6	11.0	220.9	4.5	49.1	-44.2	11.0
	VASP	181.5	181.5	7.5	149.5	5.5	106.8	-29.9	7.5
PBE0	PySCF	210.2	210.2	12.5	250.2	4.8	85.1	-50.0	12.5
	VASP	214.1	214.1	14.6	291.5	4.5	68.3	-58.3	14.6
HF	PySCF	36.3	36.3	1.2	23.4	6.1	24.6	-4.7	1.2
	VASP	36.1							

Table F.5: Comparison of the single-particle approach results for CCO from PySCF and VASP.

Method	software	Heisenberg	1-band Hubbard				$3J^{\text{eff}}$ Heisenberg		
		J_1	J_1	J_2, J_3	J_c	U/t	J_1^{eff}	J_2^{eff}	J_3^{eff}
PBE+U	PySCF	168.9	168.9	14.0	279.0	4.3	29.4	-55.8	14.0
	VASP	199.6	199.6	14.0	279.7	4.5	59.7	-55.9	14.0
PBE0	PySCF	213.9	213.9	13.4	267.2	4.7	80.3	-53.4	13.4
	VASP	217.2	217.2	16.0	319.0	4.4	57.6	-63.8	16.0
HF	PySCF	38.0	38.0	1.4	27.0	5.8	24.5	-5.4	1.4
	VASP	37.1	37.1	1.7	33.2	5.3	20.5	-6.6	1.7

Solver accuracy

We further check the accuracy of the solver (CCSD) against more accurate solvers [CCSD(T) and DMRG]. In Fig. F.4(a), we extrapolate the DMET energy from the DMRG solver to

Table F.6: Comparison of the single-particle approach results for CuO_2^{2-} from PySCF and VASP. Some long-range parameters are left blank since the SDW state in the plane wave basis converges to a paramagnetic state.

Method	software	Heisenberg	1-band Hubbard				$3J^{\text{eff}}$ Heisenberg		
		J_1	J_1	J_2, J_3	J_c	U/t	J_1^{eff}	J_2^{eff}	J_3^{eff}
PBE+U	PySCF	165.5	165.5	26.0	520.4	3.5	-94.7	-104.1	26.0
	VASP	194.8							
PBE0	PySCF	269.8	269.8	11.9	238.4	5.4	150.6	-47.7	11.9
	VASP	280.9							
HF	PySCF	55.5	55.5	2.1	41.9	5.7	34.6	-8.4	2.1
	VASP	50.9							

Table F.7: Basis set size convergence. Both mean-field (HF) and correlated (DMET with $\sqrt{2} \times \sqrt{2}$ impurity cell size) calculations of CCO are shown.

Basis set	method	m_{AFM} [μ_B]	m_{FM} [μ_B]	J_1 [meV]
def2-SVP				
	HF	0.81	0.87	38.0
	DMET (CCSD)	0.68	0.77	122
def2-TZVP				
	HF	0.81	0.86	37.5
	DMET (CCSD)	0.68	0.77	117
plane wave				
	HF			37.1

Table F.8: DMET solver benchmark. The results use the embedding Hamiltonian from the last DMET self-consistent iteration in CCO ($\sqrt{2} \times \sqrt{2}$ cell) with the minimal and def2-SVP basis sets.

Basis set	method	m_{AFM} [μ_B]	m_{FM} [μ_B]	J_1 [meV]
minimal basis				
	CCSD solver	0.61	0.76	191
	CCSD(T) solver	0.61	0.75	195
	DMRG solver ($M = 1000$)	0.61	0.76	231
	DMRG solver ($M = 5000$)	0.61	0.75	212
	DMRG solver (extrap.)	0.61	0.75	195 ± 22
def2-SVP				
	HF	0.81	0.87	38
	CCSD solver	0.68	0.77	122
	CCSD(T) solver	0.67	0.76	132

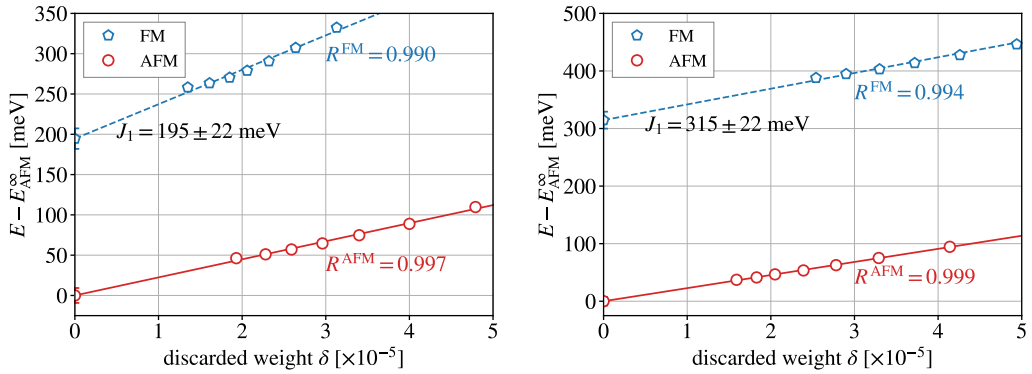

(a) CCO (b) CuO_2^{2-}

Figure F.4: Linear extrapolation of the DMET energy using a DMRG solver for (a) CCO and (b) CuO_2^{2-}. The energies are generated by reverse sweeps of the DMRG calculation from bond dimension $M = 5000$. We use $M = 1500, 2000, 2500, 3000, 3500, 4000, 4500$ to perform the linear energy extrapolation with respect to the discarded weight. The energy zero is taken as the extrapolated AFM energy (per Cu). The error bar is estimated as 1/5 of the extrapolation distance, i.e., $[E(M = 4500) - E(M = \infty)]/5$.

zero discarded weight $\delta \to 0$ [infinite bond dimension ($M \to \infty$)] for CCO. Both the AFM and FM states energies exhibit good linearity with respect to the discarded weight (the AFM state energy is slightly more linear). Despite the small size of the energy difference, the extrapolated J_1 agrees very well with the CCSD solver. This illustrates the accuracy of CCSD for the AFM ordered state starting from the symmetry broken mean-field reference. Similarly, the magnetic moments are also very close.

CCSD(T) includes more dynamical correlation than CCSD and this becomes important in larger basis sets. From Table F.8, one can see that for the minimal basis, CCSD(T) gives a very small correction of 4 meV in J_1. For the larger basis def2-SVP, as expected, it gives a slightly larger correction of 10 meV. The change in the magnetic moment is about 0.01 μ_{B}. We also show HF reference magnetic moments. The CC results are significantly different from the Hartree-Fock reference, showing the magnitude of magnetic fluctuations. In summary, for the parent state, CCSD yields good accuracy in the magnetic properties and its error mainly comes from the neglect of some dynamical correlation (about 10 meV in J), rather than any breakdown of the CC approximation due to multi-reference effects.

We also benchmarked the artificial CuO_2^{2-} material using the same strategy as above. The results are summarized in Fig. F.4(b) and Table F.9. The DMRG extrapolation shows a similar degree of linearity and energy uncertainty as in CCO, and the conclusions about the accuracy of CCSD in comparison to CCSD(T) and DMRG are unaltered.

Table F.9: Same as caption of Table F.8, but for CuO_2^{2-}.

Basis set	method	m_{AFM} [μ_{B}]	m_{FM} [μ_{B}]	J_1 [meV]
minimal basis				
	CCSD solver	0.50	0.69	294
	CCSD(T) solver	0.50	0.69	297
	DMRG solver ($M = 1000$)	0.50	0.70	395
	DMRG solver ($M = 5000$)	0.49	0.69	349
	DMRG solver (extrap.)	0.49	0.69	315 ± 22

Additional data for La_2CuO_4

As a more realistic benchmark example, we applied our methods to La_2CuO_4, which has been extensively studied both experimentally and theoretically. There are two commonly studied structural phases of La_2CuO_4, namely the high-temperature tetragonal (HTT) and low-temperature orthorhombic (LTO, stabilized below 520 K) phases. In the HTT phase, the CuO_6 octahedra are perfectly aligned along the z axis and all Cu's are equivalent while in the LTO phase, the octahedra are distorted and the Cu-O-Cu angle is no longer 180° (see Fig. F.5). We computed the exchange coupling parameters in the two phases in Table F.10 and plot their spin wave dispersions in Fig. F.5. When fitted to the NN Heisenberg model, the J_1 results of the two phases are similar and agree well with experimentally derived parameters, which reflects the fact that the local chemical environments of Cu are similar. However, the long-range parameters (J_2, J_3 and J_c) in the two phases are different and larger in the HTT phase. It is likely that the distortion among the CuO_6 octahedra is harmful for the long-range exchange process due to weaker overlap of orbitals. In general, the LTO phase spin-wave spectrum agrees better with the experimentally measured spectrum. Away from the Γ point and the Brillouin zone boundary, the error compared to the experimental spectrum is larger; this can be traced to the smaller value of J_1 compared to experiment.

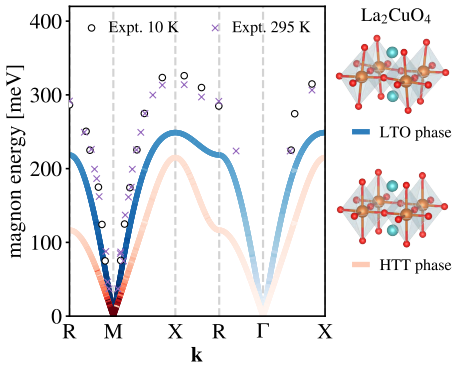

Figure F.5: Spin wave spectrum of La_2CuO_4. Experimental data is taken from Ref. [306]. Special points in Brillouin zone: R $(\frac{3}{4}, \frac{1}{4})$, M $(\frac{1}{2}, \frac{1}{2})$, X $(\frac{1}{2}, 0)$, Γ $(0, 0)$.

Table F.10: Magnetic exchange coupling parameters [in meV] of La_2CuO_4 fitted from *ab initio* DMET and experiments. [a] from Ref. [306], inelastic neutron scattering data fitted to the Heisenberg and 1-band Hubbard models.

Method	Heisenberg	Hubbard		
	J_1	J_1	J_2, J_3	J_c
HTT	102	102	7	135
LTO	106	106	2	42
Expt.[a]	112	138	2	39

F.3 Multi-orbital electronic structure

Population analysis

Table F.11: Population analysis. n: number of electron; m: magnetization.

Element	orbital	Hg-1201		Hg-1212		CCO		CuO_2^{2-}	
		n	m	n	m	n	m	n	m
Cu									
	$4s$	0.18	-0.02	0.21	-0.02	0.24	-0.02	0.27	-0.03
	$4p_x$	0.24	-0.02	0.25	-0.02	0.26	-0.02	0.28	-0.03
	$4p_y$	0.25	-0.02	0.26	-0.02	0.27	-0.02	0.28	-0.03
	$4p_z$	0.18	0.00	0.19	0.00	0.18	0.00	0.25	0.00
	$3d_{xy}$	1.99	0.00	1.99	0.00	1.99	0.00	1.99	0.00
	$3d_{yz}$	1.98	0.00	1.98	0.00	1.98	0.00	1.98	0.00
	$3d_{zx}$	1.98	0.00	1.98	0.00	1.98	0.00	1.98	0.00
	$3d_{z^2}$	1.95	0.00	1.93	0.01	1.91	0.00	1.90	0.00
	$3d_{x^2-y^2}$	1.20	0.76	1.21	0.74	1.22	0.72	1.29	0.63
	$5s$	0.00	0.00	0.00	0.00	0.00	0.00	0.00	0.00
	$4d_{xy}$	0.01	0.00	0.01	0.00	0.01	0.00	0.01	0.00
	$4d_{yz}$	0.01	0.00	0.01	0.00	0.01	0.00	0.01	0.00
	$4d_{z^2}$	0.01	0.00	0.01	0.00	0.01	0.00	0.01	0.00
	$4d_{xz}$	0.01	0.00	0.01	0.00	0.01	0.00	0.01	0.00
	$4d_{x^2-y^2}$	0.01	0.00	0.01	0.00	0.01	0.00	0.01	0.00
	$4f(\times 7)$	0.00	0.00	0.00	0.00	0.00	0.00	0.00	0.00
	total	**10.01**	**0.71**	**10.06**	**0.69**	**10.10**	**0.67**	**10.30**	**0.55**
O in-plane									
	$2p_x$	1.60	0.00	1.58	0.00	1.55	0.00	1.50	0.00
	$2p_y$	1.92	0.00	1.92	0.00	1.92	0.00	1.94	0.00
	$2p_z$	1.90	0.00	1.87	0.00	1.84	0.00	1.85	0.00
	$3s$	0.00	0.00	0.00	0.00	0.00	0.00	0.00	0.00
	$3p_x$	0.00	0.00	0.00	0.00	0.00	0.00	0.00	0.00
	$3p_y$	0.01	0.00	0.01	0.00	0.01	0.00	0.01	0.00
	$3p_z$	0.01	0.00	0.01	0.00	0.01	0.00	0.01	0.00
	$3d(\times 5)$	0.00	0.00	0.00	0.00	0.00	0.00	0.00	0.00
	total	**5.46**	**0.00**	**5.40**	**0.00**	**5.35**	**0.00**	**5.33**	**0.00**

Table F.11: Population analysis (cont.).

Element	orbital	Hg-1201		Hg-1212		CCO		CuO_2^{2-}	
		n	m	n	m	n	m	n	m
O apical									
	$2p_x$	1.95	0.00	1.95	0.00				
	$2p_y$	1.95	0.00	1.95	0.00				
	$2p_z$	1.63	0.00	1.65	0.00				
	$3s$	0.00	0.00	0.00	0.00				
	$3p_x$	0.01	0.00	0.01	0.00				
	$3p_y$	0.01	0.00	0.01	0.00				
	$3p_z$	0.00	0.00	0.00	0.00				
	$3d(\times 5)$	0.00	0.00	0.00	0.00				
	total	**5.57**	**0.00**	**5.58**	**0.00**				
Ca									
	$4s$			0.15	0.00	0.16	0.00		
	$3d(\times 5)$			0.00	0.00	0.00	0.00		
	total			**0.15**	**0.00**	**0.16**	**0.00**		
Ba									
	$6s$	0.16	0.00	0.16	0.00				
	$5d(\times 5)$	0.00	0.00	0.00	0.00				
	$6p(\times 3)$	0.00	0.00	0.00	0.00				
	$7s$	0.00	0.00	0.00	0.00				
	total	**0.16**	**0.00**	**0.16**	**0.00**				
Hg									
	$6s$	1.03	0.00	1.03	0.00				
	$5d_{xy}$	1.98	0.00	1.98	0.00				
	$5d_{yz}$	1.98	0.00	1.98	0.00				
	$5d_{zx}$	1.98	0.00	1.98	0.00				
	$5d_{z^2}$	1.55	0.00	1.52	0.00				
	$5d_{x^2-y^2}$	1.98	0.00	1.98	0.00				
	$6p_x$	0.01	0.00	0.01	0.00				
	$6p_y$	0.01	0.00	0.01	0.00				
	$6p_z$	0.00	0.00	0.00	0.00				
	$5f(\times 7)$	0.01	0.00	0.01	0.00				
	$6d(\times 5)$	0.00	0.00	0.00	0.00				
	$7s, 8s, 9s$	0.00	0.00	0.00	0.00				
	total	**10.59**	**0.00**	**10.57**	**0.00**				

Bonding analysis

Table F.12: Bonding analysis of different compounds. Both the total bond order b and orbital specific bond order are shown.

Bond type	Hg-1201		Hg-1212		CCO		CuO_2^{2-}	
	length	order	length	order	length	order	length	order
Cu-O (in plane)	1.936	0.320	1.932	0.352	1.928	0.377	1.928	0.430
Cu-O (apical)	2.767	0.060	2.824	0.055				
Cu-Cu (intra-layer)	3.871	0.044	3.863	0.052	3.856	0.060	3.856	0.073
Cu-Cu (inter-layer)	9.502	0.000	3.119	0.025	3.180	0.023	3.180	0.047
O-O (nearest)	2.737	0.005	2.732	0.007	2.726	0.008	2.726	0.010
O-O (next nearest)	3.871	0.002	3.863	0.002	3.856	0.001	3.856	0.001
Ca-Cu			3.145	0.004	3.156	0.004		
Ca-O			2.488	0.030	2.499	0.033		
Ba-Cu	3.340	0.002	3.351	0.003				
Ba-O	2.722	0.035	2.732	0.035				
Hg-O (apical)	1.984	0.393	1.966	0.386				
Orbital specific bond order								
Cu $3d_{x^2-y^2}$ - O $2p_x$		0.073		0.075		0.077		0.092
Cu $4s$ - O $2p_x$ (σ)		0.043		0.047		0.054		0.057
Cu $4p_x$ - O $2p_x$ (σ)		0.157		0.160		0.162		0.161
Cu $4p_y$ - O $2p_y$ (π)		0.009		0.012		0.015		0.024
Cu $4p_z$ - O $2p_z$ (π)		0.038		0.055		0.068		0.093
total		**0.320**		**0.349**		**0.376**		**0.427**
Cu $3d_{z^2}$ - O $2p_z$ (apical)		0.000		0.000				
Cu $4s$ - O $2p_z$ (apical)		0.009		0.008				
Cu $4p_z$ - O $2p_z$ (apical)		0.051		0.047				
total		**0.060**		**0.055**				

Comparison to DFT population

Table F.13: DFT charge, magnetic moment, bond order of CCO compared to DMET.

Method	n_{CuO_2}	m_{Cu}	b_{Cu-O}
PBE	15.58	0.00	0.442
PBE0	15.54	0.54	0.476
DMET	15.45	0.67	0.377
HF	15.37	0.81	0.356

We compare the population from different DFT functionals to DMET and HF in Table F.13. The semi-local PBE functional, as expected, completely fails in describing magnetism ($m_{Cu} = 0$). HF is in another limit, where the electrons are over-localized and the magnetic

moment is overestimated. PBE0, due to the mixing of 25% HF exchange in the functional, is between the two limits and predicts reasonable charge and magnetic moment similar to DMET. As described in the main text, hybrid functionals like PBE0, gives qualitatively correct results for a single compound. However, hybrid DFT or DFT+U may fail in predicting systematical trends among different compounds, especially for the subtle influence of the buffer layer.

Real space density and ELF analysis

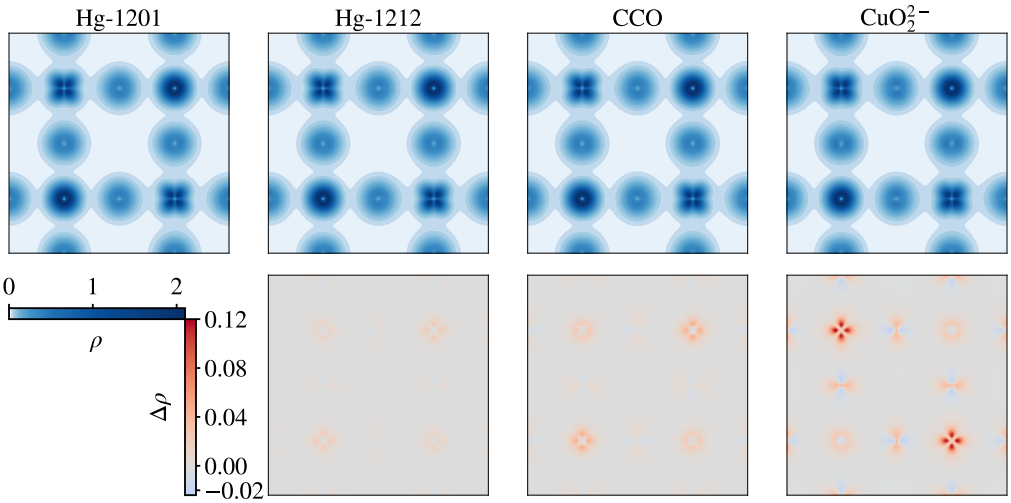

Figure F.6: Electron density contour in the CuO_2 plane of different compounds (From left to right: Hg-1201, Hg-1212, CCO, $CuO_2{}^{2-}$). Only the valence electron $\rho^{\alpha}(\mathbf{r})$ of the AFM state is shown. The second row shows the density difference between compounds X and the reference Hg-1201, i.e., $\Delta\rho = \rho(X) - \rho(\text{Hg-1201})$.

For a real space description of the charge and bonding in the xy plane, we have analyzed the electron density $\rho(\mathbf{r})$ in Fig. F.6 and the electron localization function (ELF) in Fig. F.7. In general, the three compounds have very similar plots of the density and ELF. From the density plot (Fig. F.6), the differential density shows that the Cu electron density increases from Hg-1201 to $CuO_2{}^{2-}$, consistent with the previous population analysis. In the ELF plots, we clearly see the lone electron pairs on the non-3-band oxygen $2p$'s. Between Cu and O, although there is a maximum in the ELF function, it does not show a very typical covalent bonding pattern. This suggests the bonding between Cu and O is more ionic than covalent. The differential ELF plots show that the electron is less likely to localize around the core region of oxygen moving from Hg-1201 to $CuO_2{}^{2-}$, i.e., the covalent bonding in the inter-atomic bonding region is increasing and the ionic character becomes weaker.

A similar analysis can be done for the xz plane, see Fig. F.8 and F.9. In the differential density plot, we see that the electron density around Cu increases in the xy plane, but decreases in the xz plane. This can be interpreted as a change in bond order. When the

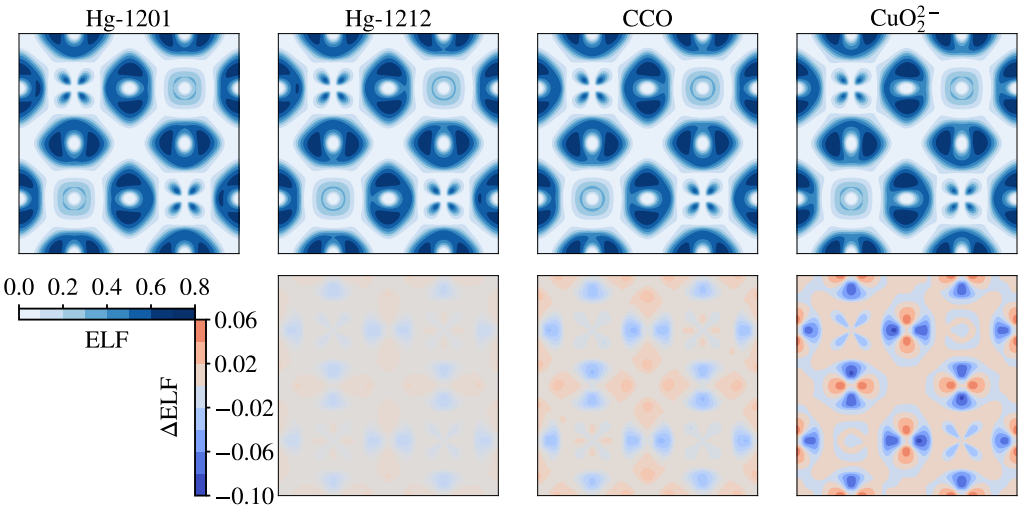

Figure F.7: Electron localization function (ELF) contour in the CuO_2 plane of different compounds (From left to right: Hg-1201, Hg-1212, CCO, $CuO_2{}^{2-}$). Only valence electrons $\mathrm{ELF}^{\alpha}(\mathbf{r})$ of the AFM state are shown. The second row shows the difference of ELF between compounds X and the reference Hg-1201, i.e., $\Delta\mathrm{ELF} = \mathrm{ELF}(X) - \mathrm{ELF}(\text{Hg-1201})$.

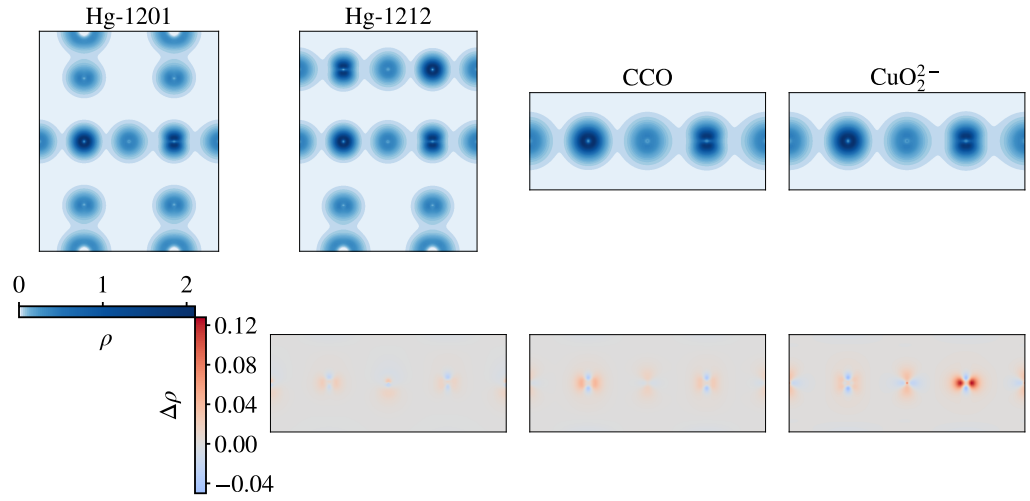

Figure F.8: Same caption as Fig. F.8, but on the xz plane.

system has apical oxygens, it has two effects: the first is to form bonds in the z direction with Cu. Since the total valence of Cu (the ability to form covalent bonds) is finite, Cu then has less ability to form covalent bonds in the CuO_2 plane. The other effect is to make Cu's change more positive and the whole system becomes more ionic and the overall covalent bond order is then decreased. In the language of electronic bands, the inclusion of apical oxygen enlarges the orbital energy gap between the Cu $3d$ and O $2p$ bands (c.f. $\Delta_{pd} = \epsilon_p - \epsilon_d$ is an important parameter in the 3-band model) and makes the hybridization weaker. Also, the density / ELF plots show covalency between Hg and the apical O, which

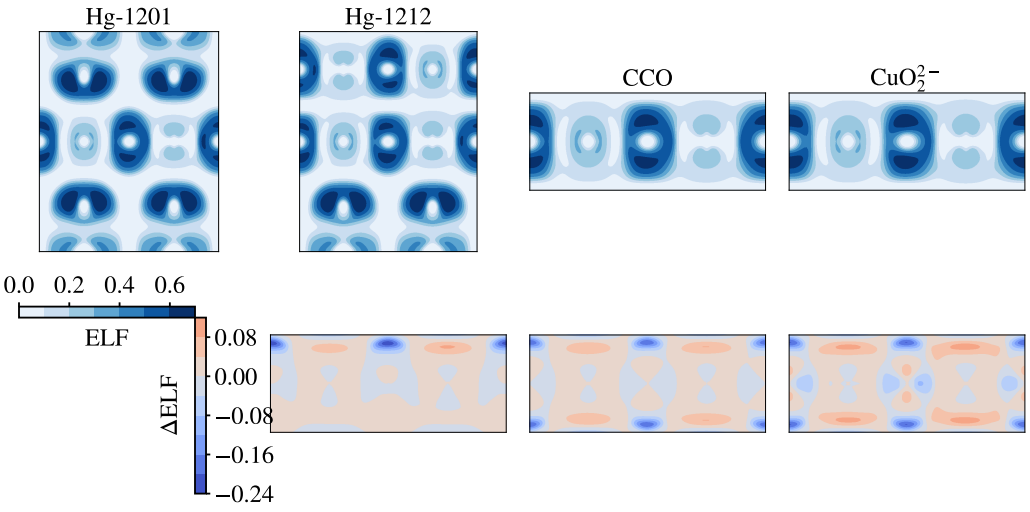

Figure F.9: Same caption as Fig. F.9, but in the xz plane.

has been discussed in the bond order analysis.

Spin-traced natural orbitals around Fermi level

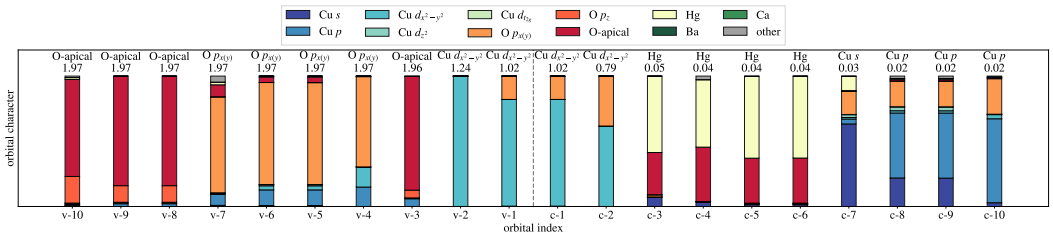

(a) $\Gamma(0,0,0)$

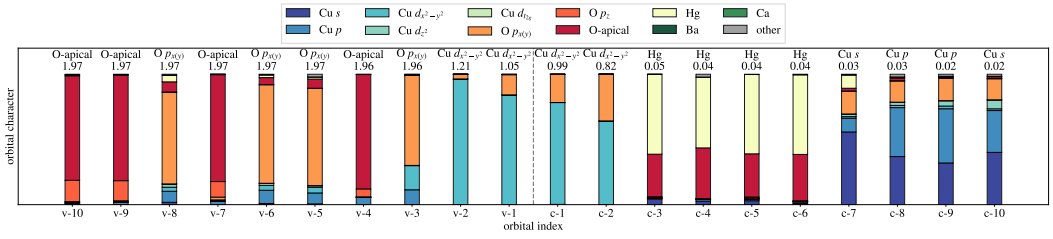

(b) $X(\frac{1}{2},0,0)$

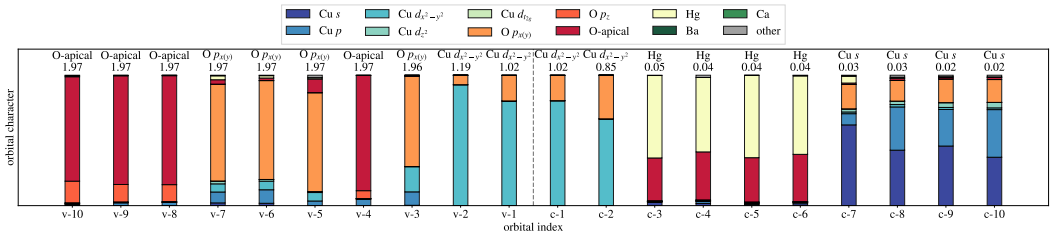

(c) $M(\frac{1}{2},\frac{1}{2},0)$

Figure F.10: Spin-traced natural orbitals of Hg-1201 from DMET around the Fermi level (dash line) at different **k** points. The main orbital character and the occupancy are labelled.

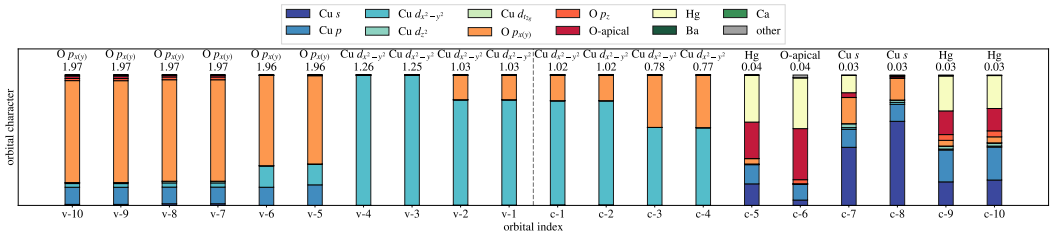

(a) $\Gamma(0,0,0)$

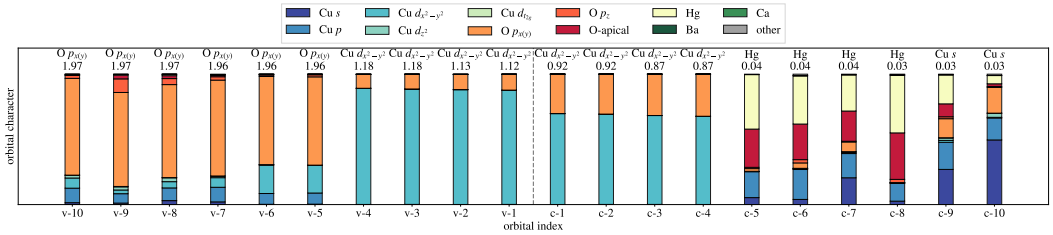

(b) $X(\frac{1}{2},0,0)$

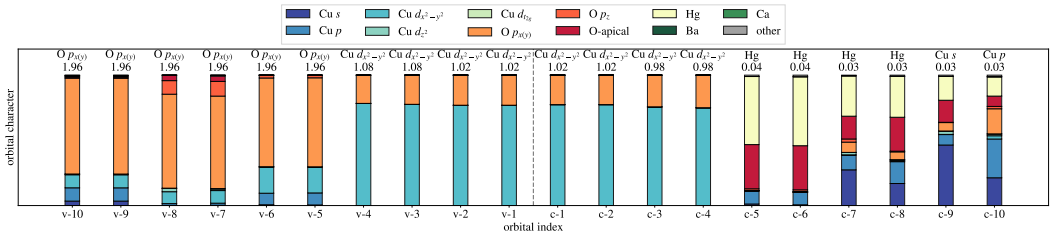

(c) $M(\frac{1}{2},\frac{1}{2},0)$

Figure F.11: Spin-traced natural orbitals of Hg-1212 from DMET around the Fermi level (dashed line) at different **k** points. The main orbital character and occupancy are labelled.

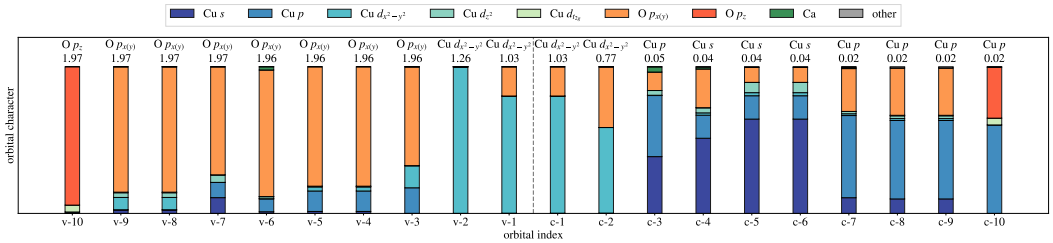

(a) $\Gamma(0,0,0)$

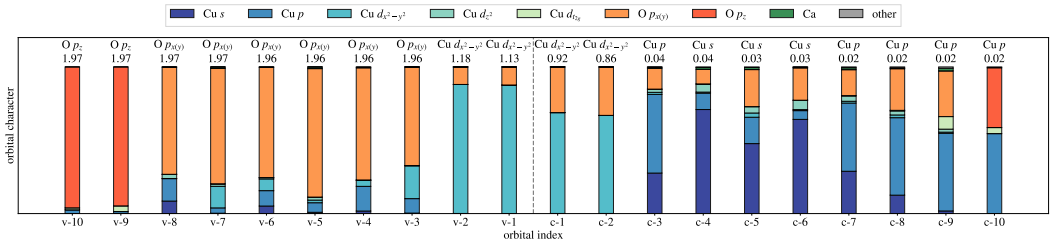

(b) $X(\frac{1}{2},0,0)$

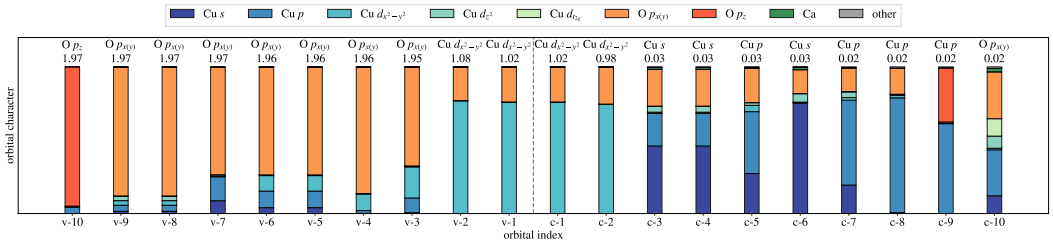

(c) $M(\frac{1}{2},\frac{1}{2},0)$

Figure F.12: Spin-traced natural orbitals of CCO from DMET around the Fermi level (dashed line) at different **k** points. The main orbital character and occupancy are labelled.

Although the correlated band structure is not currently available in our DMET calculations, one can analyze the orbitals around the Fermi level through the natural orbitals, see Figs. F.10, F.11 and F.12. Starting with the CCO natural orbitals, we can see that around the Fermi level, the valence bands mainly have O p character and the conduction bands have a mixture of Cu d and Cu s characters, which is typical for a charge transfer insulator. There is some dispersion along the different **k** points, but it does not change either the orbital character or natural occupancy significantly. The natural occupancies are not very far from 1 and 0, which means the system is not far from a symmetry-breaking single reference system (and this is why UCCSD gives a very accurate description).

Compared to the CCO natural orbitals, Hg-1212 has some Hg-apical O bands among the low-lying virtual bands (even more appear for Hg-1201). This feature has also been observed in the band structures using hybrid functionals [313], i.e., as the number of Hg-O layers increases, the system CBM is dominated by the Hg-O bands and the band gap approaches zero. This plays a role in the layer effects on the superexchange constants, as discussed in

the main text and further below.

Spin-resolved natural orbitals around Fermi level

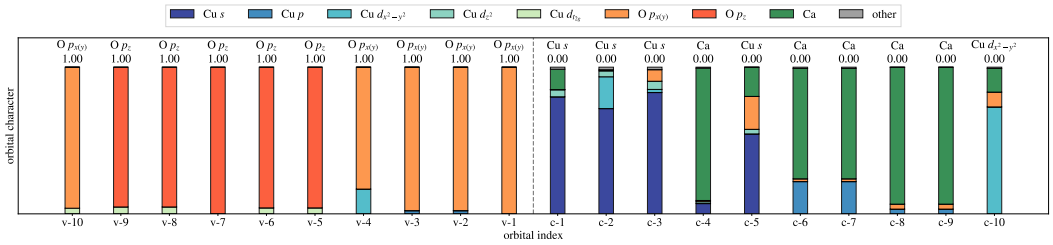

(a) $\Gamma(0,0,0)$

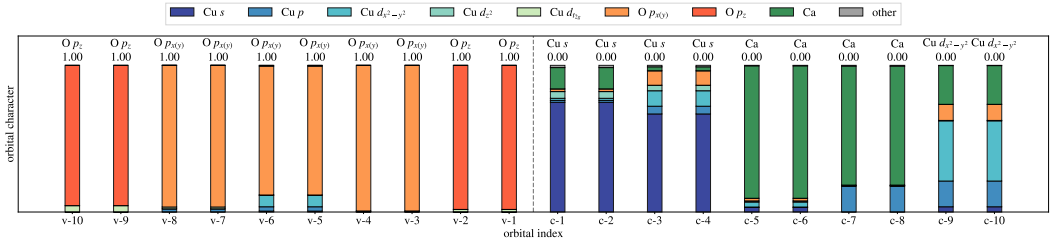

(b) $X(\frac{1}{2},0,0)$

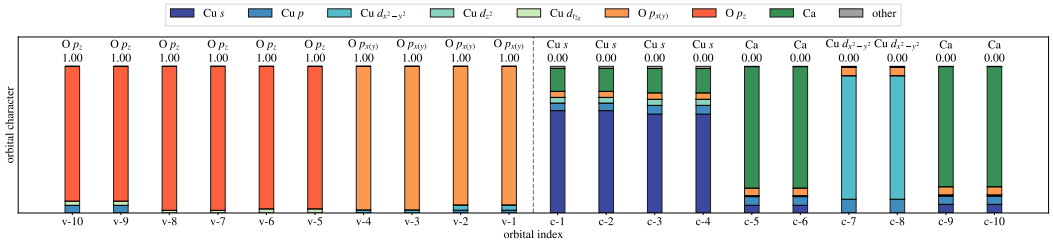

(c) $M(\frac{1}{2},\frac{1}{2},0)$

Figure F.13: Spin-resolved HF orbitals of CCO around Fermi level (dash line) at different **k** points. The main orbital character and the occupancy are labelled.

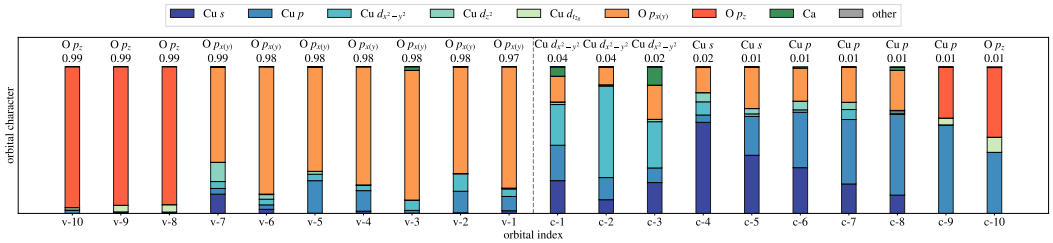

(a) $\Gamma(0,0,0)$

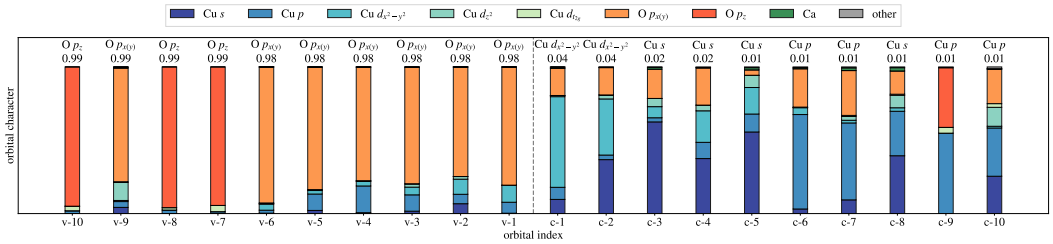

(b) $X(\frac{1}{2},0,0)$

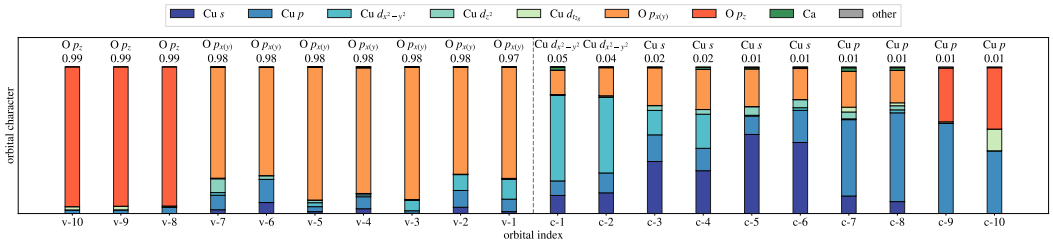

(c) $M(\frac{1}{2},\frac{1}{2},0)$

Figure F.14: Spin-resolved natural orbitals of CCO from DMET around the Fermi level (dash line) at different **k** points. The main orbital character and the occupancy are labelled.

F.4 Magnetic trends across the cuprates

We present additional data from the literature and mean-field methods on the magnetic exchange coupling parameters in this section. (Tables F.14, F.15, F.16, F.17).

Hg-1201

Table F.14: Magnetic exchange coupling parameters (in meV) of Hg-1201 calculated from different methods, fitted to different spin models.

Method	Heisenberg	1-band Hubbard				$3J^{\text{eff}}$ Heisenberg		
	J_1	J_1	J_2, J_3	J_c	U/t	J_1^{eff}	J_2^{eff}	J_3^{eff}
PBE+U	149.7	149.7	9.7	194.7	4.6	52.4	-38.9	9.7
PBE0	198.8	198.8	11.3	225.4	4.9	86.1	-45.1	11.3
HF	33.7	33.7	1.0	20.2	6.3	23.6	-4.0	1.0
DMET	103.8	103.8	2.4	48.4	7.0	79.6	-9.7	2.4
HSE06	204							
B3LYP	235							
DDCI	136.2 [a], 141 [b]							
CASPT2	123 [c]							
Expt.	123 [d], 135 [e]							

[a] From Ref. [250], difference dedicated configuration interaction (DDCI) (molecular model) calculation fitted to the Heisenberg model.

[b] From Ref. [314], difference dedicated configuration interaction (DDCI) (molecular model) calculation fitted to the Heisenberg model.

[c] From Ref. [314], complete active space second-order perturbation theory (CASPT2) (molecular model) calculation fitted to the Heisenberg model.

[d] From Ref. [261], resonant inelastic X-ray-scattering data fitted to the Heisenberg model.

[e] From Ref. [260], resonant inelastic X-ray-scattering data fitted to the Heisenberg model.

Hg-1212

Table F.15: Magnetic exchange coupling parameters (in meV) of Hg-1212 calculated from different methods, fitted to different spin models.

Method	Heisenberg	1-band Hubbard				$3J^{\text{eff}}$ Heisenberg		
	J_1	J_1	J_2, J_3	J_c	U/t	J_1^{eff}	J_2^{eff}	J_3^{eff}
PBE+U	159.6	159.6	11.0	220.9	4.5	49.1	-44.2	11.0
PBE0	210.2	210.2	12.5	250.2	4.8	85.1	-50.0	12.5
HF	36.3	36.3	1.2	23.4	6.1	24.6	-4.7	1.2
DMET	122.1	122.1	5.3	106.7	5.4	68.7	-21.3	5.3
HSE06	215							
B3LYP	224							
DDCI	153.8 [a]							
Expt.	176 [b]							

[a] From Ref. [250], DDCI (molecular model) calculation fitted to the Heisenberg model.

[b] From Ref. [260], resonant inelastic X-ray-scattering data fitted to the Heisenberg model.

CCO

Table F.16: Magnetic exchange coupling parameters (in meV) of CCO calculated from different methods, fitted to different spin models.

Method	Heisenberg	1-band Hubbard				$3J^{\text{eff}}$ Heisenberg			$J_\perp$
	J_1	J_1	J_2, J_3	J_c	U/t	J_1^{eff}	J_2^{eff}	J_3^{eff}	
PBE+U	168.9	168.9	14.0	279.0	4.3	29.4	-55.8	14.0	10.4
PBE0	213.9	213.9	13.4	267.2	4.7	80.3	-53.4	13.4	12.0
HF	38.0	38.0	1.4	27.0	5.8	24.5	-5.4	1.4	2.7
DMET	155.4	155.4	9.7	194.4	4.7	58.2	-38.9	9.7	8.9
QMC	142 [a]								
Expt.	142 [b], 158 [c]	182 [d]	10.3 [d]	205.6 [d]	4.9 [d]	79.5 [e]	-41.1 [e]	10.3 [e]	6.5 [e]

[a] From Ref. [248], fixed-node diffusion Monte Carlo (FN-DMC) (crystal) calculation fitted to the Heisenberg model.

[b] From Ref. [263], Raman spectrum data fitted to the Heisenberg model.

[c] From Ref. [262], RIXS data fitted to the Heisenberg model.

[d] From Ref. [262], RIXS data fitted to the 1-band Hubbard model.

[e] From Ref. [262], RIXS data fitted to the $3J^{\text{eff}}$ Heisenberg model.

CuO_2^{2-}

Table F.17: Magnetic exchange coupling parameters (in meV) of CuO_2^{2-} calculated from different methods, fitted to different spin models. $U = 7.5$ eV is added to the Cu $3d$ orbitals in the PBE+U method.

Method	Heisenberg	1-band Hubbard				$3J^{\text{eff}}$ Heisenberg		
	J_1	J_1	J_2, J_3	J_c	U/t	J_1^{eff}	J_2^{eff}	J_3^{eff}
PBE+U	165.5	165.5	26.0	520.4	3.5	-94.7	-104.1	26.0
PBE0	269.8	269.8	11.9	238.4	5.4	150.6	-47.7	11.9
HF	55.5	55.5	2.1	41.9	5.7	34.6	-8.4	2.1
DMET	205.5	205.5	14.0	279.6	4.6	65.8	-55.9	14.0
QMC	241 [a]							

[a] From Ref. [248], fixed-node diffusion Monte Carlo (FN-DMC) (crystal) calculation fitted to the Heisenberg model.

Remarks on sign and error of exchange coupling parameters

We note that the sign of the 2nd neighbor exchange coupling parameter J_2 is related to the specific spin model that is being fit. When fitting to a J_1-J_2 Heisenberg model, J_2 is positive, indicating an antiferromagnetic coupling. On the other hand, in the effective $3J$ model, after absorbing the cyclic exchange J_c , J_2 becomes negative, i.e., ferromagnetic coupling.

When comparing to the experimental spectra, there are several possible sources of error: (i) Finite-size effects: As the largest cluster size we used in the embedding calculation is a 2×2 supercell, it is more likely that the long-range parameters J_2, J_3, J_c have larger error. Errors in these parameters can typically be seen in the spin-wave dispersion away from the Γ point (e.g. the X point in Fig. 6.4 in the main text, where the curvature is dominated by J_c). Also because of the current mean-field Hartree-Fock treatment of long-range Coulomb interactions outside of the computational cell (and given that Hartree-Fock underestimates the Heisenberg exchange parameters in this system) we expect that if the cluster size is further enlarged, the derived J's will only increase, further improving agreement with with experiment. (ii) Model error: the current spin-wave spectrum is derived by fitting energies to spin models and then applying linear spin-wave theory. It is possible that the chosen spin models do not fully capture the high-energy part of the spin wave dispersion. Also, the mapping from the ab initio energies to the spin model assumes that the chosen electronic energies relate to Ising-like effective spins, but there is some ambiguity in this mapping. For instance, the current mapping assumes that $\langle S_z \rangle = \pm\frac{1}{2}$; however, due to the charge fluctuation of $3d_{x^2-y^2}$ orbitals, their $|\langle S_z \rangle| < \frac{1}{2}$ and fitting to such S_z will make the

J values larger. (iii) Experimental uncertainty: the mercury-barium cuprate samples are typically doped and the spin-wave dispersion can differ from that of the undoped parent state. The doping dependence of the spin-wave dispersion in La_2CuO_4 has been studied and the dispersion along Γ to R was found to be softened (to lower energy) compared to the parent state. On the other hand, the dispersion along Γ to X was insensitive to the doping [315].

F.5 Untangling layer effects

Freezing out-of-plane orbitals

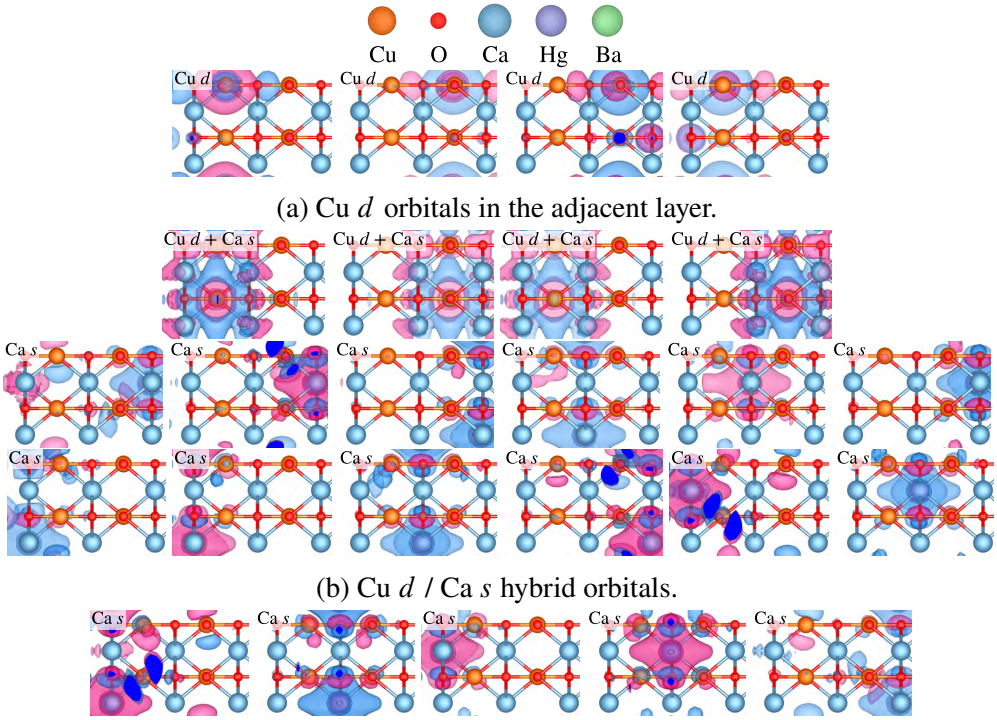

(a) Cu d orbitals in the adjacent layer.

(b) Cu d / Ca s hybrid orbitals.

(c) Ca s orbitals.

Figure F.15: Out-of-plane localized embedding orbitals (isosurfaces) of CCO (view along x axis). The main character of each orbital is labeled.

Table F.18: Effect of freezing orbitals on the magnetic exchange coupling parameters of CCO and Hg-1201 (in meV).

Compound	Heisenberg	1-band Hubbard				$3J^{\text{eff}}$ Heisenberg		
	J_1	J_1	J_2, J_3	J_c	U/t	J_1^{eff}	J_2^{eff}	J_3^{eff}
CCO (1-shot)	114.6	114.6	3.3	67.0	6.3	81.1	-13.4	3.3
CCO (frozen buffer)	105.7	105.7	1.0	19.7	10.6	95.8	-3.9	1.0
change	-8%			-71%	+68%			
Hg-1201 (1-shot)	92.3	92.3	1.1	22.0	9.5	81.3	-4.4	1.1
Hg-1201 (frozen buffer)	90.3	90.3	0.8	16.9	10.6	81.9	-3.4	0.8
change	-2%			-23%	+12%			

To understand the effects of the buffer layers (including the apical oxygens), we first localized the embedding orbitals using PM localization (see Fig. F.15 for CCO and F.16 for Hg-1201). We see that most of the out-of-plane orbitals are part of the virtual bands, except for some of the apical oxygen orbitals. The two compounds are similar w.r.t. Ca and Ba centered

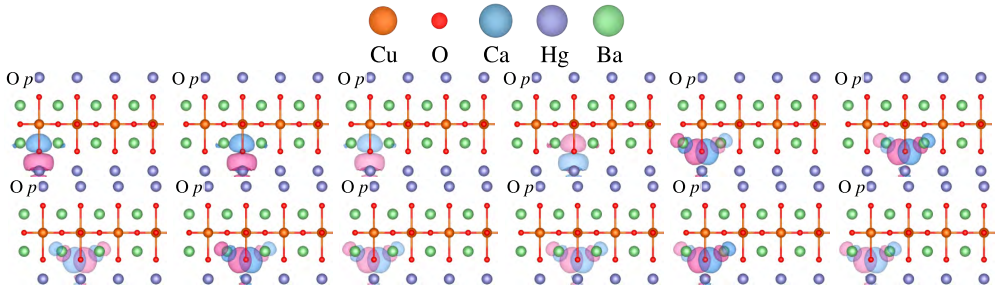

(b) apical O p orbitals.

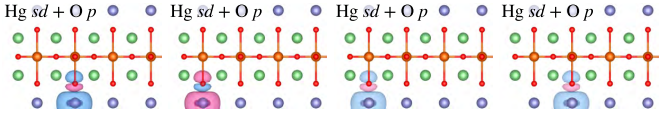

(c) Hg s and d orbitals hybridized with O p.

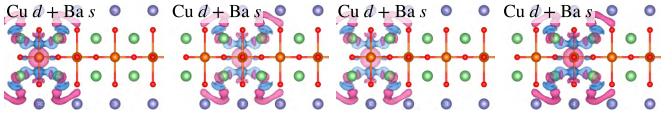

(d) Cu d / Ba s hybrid orbitals.

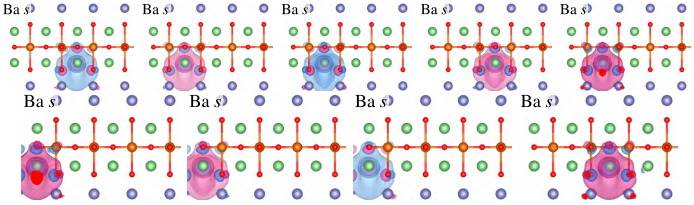

(e) Ba s orbitals.

Figure F.16: Out-of-plane localized embedding orbitals (isosurfaces) of Hg-1201 (view along x axis). The main character of each orbital is labeled. Only the bottom buffer layer orbitals are shown.

orbitals. The CCO bath also has some additional orbitals that come from the Cu d of the adjacent layers, while Hg-1201 has additional apical O and Hg orbitals.

We then freeze the out-of-plane orbitals in CCO and Hg-1201 and recompute the (1-shot) DMET impurity wavefunctions. Concretely, the buffer and its coupling to the CuO_2 layer are treated by HF in the impurity solver; then the freezing procedure forbids the excitation/de-excitation process (excitation = particle-hole excitations, including multiple particle-hole channels) from the CuO_2 layer to buffer layers. Thus the correlated impurity wavefunction, when formally expanded in singles, doubles, etc. excitations relative to the Hartree-Fock determinant, is missing those specific excited configurations. The resulting J values are shown in Table F.18. One sees that J_1 decreases by 8 %. J_c is very strongly influenced by the freezing of the buffer layer orbitals and decreases by 71%. This suggest that J_1 is a relatively local property and is less influenced by freezing exchange pathways that involve the buffer layers; J_c is a long-range property and its value is more strongly controlled by

excitations to / from buffer layers. In Hg-1201, J_1 is almost unchanged and the magnitude of the change in J_c is significantly smaller than in CCO. After freezing the buffer layer, the exchange couplings in CCO and Hg-1201 become very similar, highlighting the importance of explicit excitations involving the buffer in differentiating the physics.

Wavefunction excitation analysis

Additional insight into the type of excitations involving the buffer layer that affect the magnetic physics can be obtained by explicitly analyzing the CC wavefunction in the impurity solution. This is discussed below.

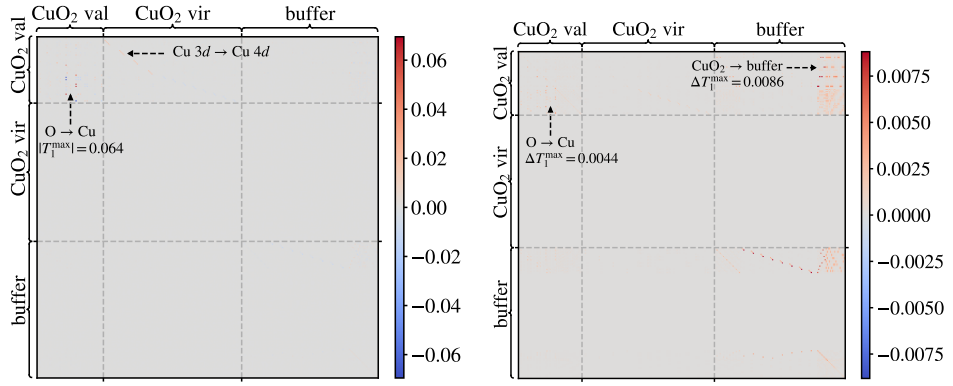

(a) T_1 (Hg-1201) (b) $\left|T_1^{\text{frozen}} - T_1\right|$ (Hg-1201)

(c) T_1 (CCO) (d) $\left|T_1^{\text{frozen}} - T_1\right|$ (CCO)

Figure F.17: Visualization of the coupled-cluster T_1 amplitude in a local orbital basis. The row indices are transformed from the occupied molecular orbitals and the column indices are transformed from the virtual orbitals. (a) T_1 amplitude of Hg-1201, where the important orbital hybridization excitations are labeled: O - Cu and Cu $3d$ - $4d$. (b) Difference between T_1 before and after freezing out-of-plane (buffer) orbitals of Hg-1201, where the primary changes are labeled: O - Cu and Cu - buffer. (c), (d): Same as (a), (b), but for CCO.

We first transform the CCSD T_1 amplitudes to the local orbital basis

$$T_p^q = \sum_{ij} C_{pi} t_i^a C_{qa}^\dagger, \tag{F.12}$$

and this quantity is plotted in Fig. F.17. The T_1 amplitude carries information on the single-particle excitations that correct the Hartree-Fock solution. It thus describes the change in orbital character (rehybridization) driven by fluctuations. Visualizing this quantity (a matrix) in the local orbital basis allows us to describe the rehybridization in terms of the atomic orbitals. The difference in the T_1 amplitude on freezing the orbitals thus identifies the change in fluctuation driven hybridization, where the fluctuations involve the buffer degrees of freedom.

The basic feature seen in the T_1 amplitude is a strong excitation from O $2p$ to Cu $3d$ and hybridization between Cu $3d$ and $4d$. The former is slightly stronger in CCO (0.070) than in Hg-1201 (0.065), reflecting the stronger super-exchange in CCO, which has a larger J_1 than Hg-1201. The latter has also been observed in some recent CASPT2 calculations [316].

We next focus on the amplitude change after freezing the buffer orbitals [see Fig. F.17 (b), (d)]. It is clear that freezing has three significant effects: (i) excitations within the buffer layer are prohibited (bottom right corner); (ii) excitations from the CuO_2 plane to the buffer layer are blocked (upper right corner); (iii) since screening effects from the buffer are also removed (which increases the charge-transfer gap), there is a change in the in-plane excitations, in particular the in-plane O $\rightarrow$ Cu excitation (upper left corner). (i) does not directly affect the in-plane magnetism, as it is limited to rehybridization of the buffer orbitals themselves. The change in (iii) is similar in the two compounds. However, the change in (ii) is almost two times larger in Hg-1201 than in CCO, due to much stronger CuO_2 $\rightarrow$ buffer (Hg and apical O) excitation.

The effect of these processes on the resulting super-exchange can be understood to come from several effects. First, the in-plane O$\rightarrow$Cu excitations directly lead to increased superexchange (as this is part of the superexchange mechanism). Second, longer range exchange (including ring-like exchange J_c) can be connected to non-local hopping between oxygen orbitals facilitated by a diffuse orbital on Cu. The strong excitation into the buffer layer changes the character of this orbital, reducing its effective mixing with the oxygen orbitals in the virtual hopping process. [This is similar to the mechanism envisioned in Ref. [243, 317]]. Third, excitations from the ground-configuration to other non-super-exchange configurations overall renormalizes all the exchange constants. The first and second effects are the likely the largest ones and they act in opposite directions in Hg-1201, leading to the overall insensitivity of the couplings to freezing/unfreezing the buffer orbitals.

The T_2 amplitudes contain information on the connected two-particle excitations (see Fig. F.18 for the largest 2000 elements in T_2 and ΔT_2). Again, the amplitudes are transformed to the local orbital basis and partitioned into 4 types: pure in-plane excitations; coupled and double excitation terms involving indices in both the buffer and the CuO_2 plane (double refers to two holes/two-particles in the buffer); pure buffer-buffer excitations. We

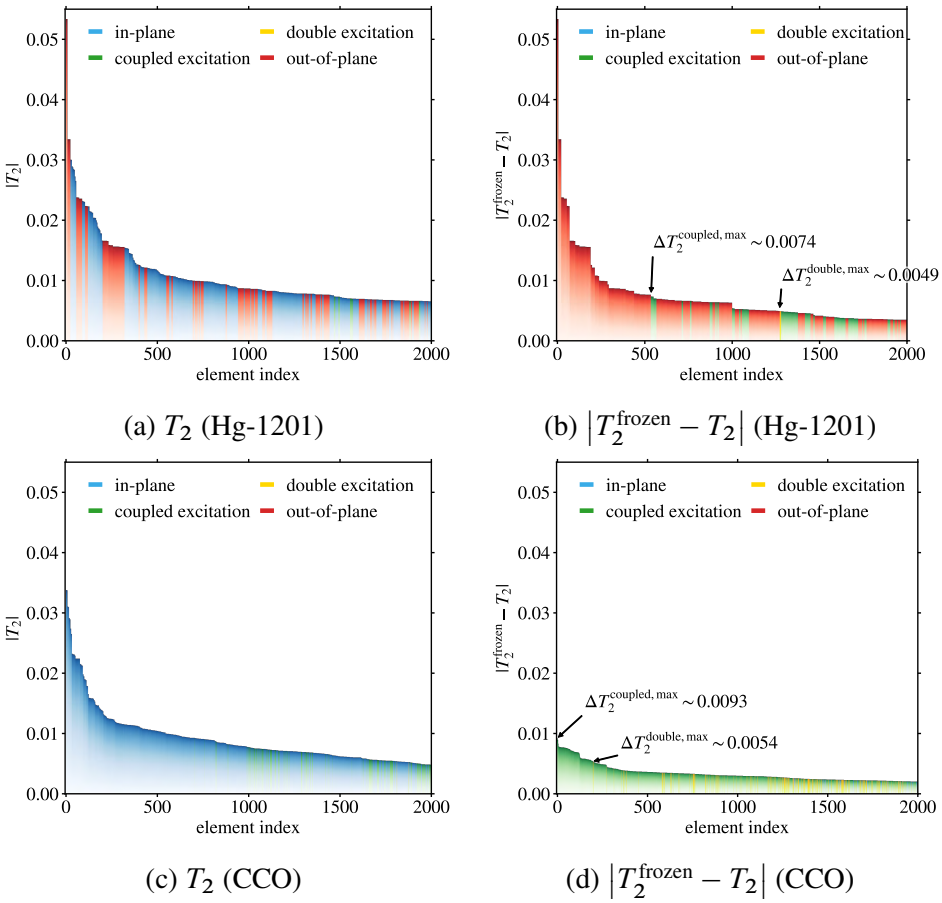

(a) T_2 (Hg-1201) (b) $\left|T_2^{\text{frozen}} - T_2\right|$ (Hg-1201)

(c) T_2 (CCO) (d) $\left|T_2^{\text{frozen}} - T_2\right|$ (CCO)

Figure F.18: Visualization of the coupled-cluster T_2 amplitude in a local orbital basis. The largest 2000 elements of $(T_2)_{pqrs}$ are labelled as in-plane (all 4 indices belong to the in-plane orbitals), coupled/double (some indices are in-plane and some are out-of-plane) and out-of-plane (all 4 indices are for out-of-plane orbitals). (a) T_2 of Hg-1201. (b) Difference between T_2 before and after freezing out-of-plane (buffer) orbitals of Hg-1201. (c), (d): Same as (a), (b), but for CCO.

find that CCO has a larger change in the coupling component of the two-particle excitations than Hg-1201. Note that this change in the connected two-particle excitation reflects a fluctuation that cannot be renormalized into an effective static picture, and is thus not contained in earlier arguments that rely on such a picture, e.g., Ref. [243, 317]. Although we have not carefully derived the influence on superexchange of this dynamical effect, it seems likely that the larger coupled layer-buffer excitation can couple into longer-range exchange processes in CCO, further increasing J_c relative to Hg-1201.

Effect of shifting apical oxygen

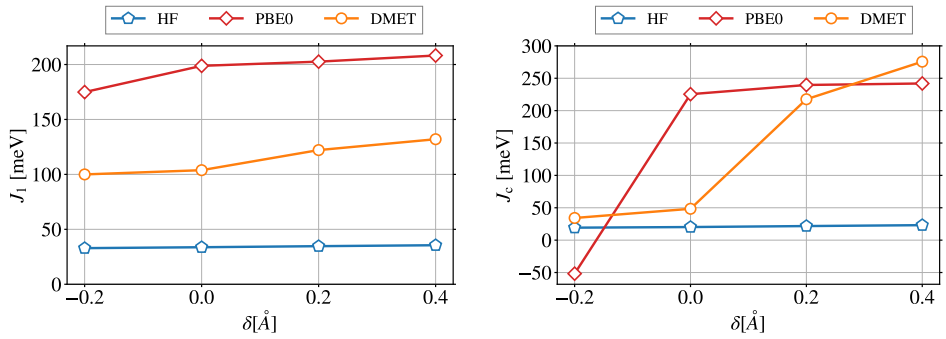

(a) (b)

Figure F.19: Effect of apical oxygen distance δ on (a) J_1 and (b) J_c of Hg-1201.

We studied the influence of apical oxygen in more detail by shifting the apical oxygen closer or further away from the CuO_2 plane of Hg-1201. Its influence on J_1 and J_c is shown in Fig. F.19.

BIBLIOGRAPHY

[1] J. G. Bednorz and K. A. Müller, Possible high T_c superconductivity in the Ba-La-Cu-O system, Z. Physik B - Cond. Matt. **64**, 189 (1986).

[2] J. R. Hull and M. Murakami, Applications of bulk high-temperature superconductors, Proc. IEEE **92**, 1705 (2004).

[3] D. Larbalestier, A. Gurevich, D. M. Feldmann, and A. Polyanskii, High-T_c superconducting materials for electric power applications, in *Materials for sustainable energy* (Co-Published with Macmillan Publishers Ltd, UK, 2010), pp. 311–320.

[4] A. Schilling, M. Cantoni, J. D. Guo, and H. R. Ott, Superconductivity above 130 K in the Hg–Ba–Ca–Cu–O system, Nature **363**, 56 (1993).

[5] A. Damascelli, Z. Hussain, and Z.-X. Shen, Angle-resolved photoemission studies of the cuprate superconductors, Rev. Mod. Phys. **75**, 473 (2003).

[6] T. Timusk and B. Statt, The pseudogap in high-temperature superconductors: an experimental survey, Rep. Prog. Phys. **62**, 61 (1999).

[7] B. Fauqué, Y. Sidis, V. Hinkov, S. Pailhès, C. T. Lin, X. Chaud, and P. Bourges, Magnetic order in the pseudogap phase of high T_c superconductors, Phys. Rev. Lett. **96**, 197001 (2006).

[8] T. Kondo, R. Khasanov, T. Takeuchi, J. Schmalian, and A. Kaminski, Competition between the pseudogap and superconductivity in the high-T_c copper oxides, Nature **457**, 296 (2009).

[9] L. D. Landau, The theory of a Fermi liquid, Sov. Phys. JETP **3**, 920 (1957).

[10] R. Daou, N. Doiron-Leyraud, D. LeBoeuf, S. Li, F. Laliberté, O. Cyr-Choiniere, Y. Jo, L. Balicas, J.-Q. Yan, J.-S. Zhou, et al., Linear temperature dependence of resistivity and change in the Fermi surface at the pseudogap critical point of a high-T_c superconductor, Nat. Phys. **5**, 31 (2009).

[11] Ø. Fischer, M. Kugler, I. Maggio-Aprile, C. Berthod, and C. Renner, Scanning tunneling spectroscopy of high-temperature superconductors, Rev. Mod. Phys. **79**, 353 (2007).

[12] J. Bardeen, L. N. Cooper, and J. R. Schrieffer, Microscopic theory of superconductivity, Phys. Rev. **106**, 162 (1957).

[13] J. Nagamatsu, N. Nakagawa, T. Muranaka, Y. Zenitani, and J. Akimitsu, Superconductivity at 39 K in magnesium diboride, Nature **410**, 63 (2001).

[14] J. Franck, Physical properties of high temperature superconductors IV, World Sci, Singapore, 189 (1994).

[15] R. M. Martin, *Electronic structure: basic theory and practical methods* (Cambridge University Press, Cambridge, UK, 2004).

[16] E. A. Carter, Challenges in modeling materials properties without experimental input, Science **321**, 800 (2008).

[17] E. Dagotto, Correlated electrons in high-temperature superconductors, Rev. Mod. Phys. **66**, 763 (1994).

[18] O. K. Andersen and T. Saha-Dasgupta, Muffin-tin orbitals of arbitrary order, Phys. Rev. B **62**, R16219 (2000).

[19] P. Werner and A. J. Millis, Dynamical screening in correlated electron materials, Phys. Rev. Lett. **104**, 146401 (2010).

[20] P. Werner and M. Casula, Dynamical screening in correlated electron systems - from lattice models to realistic materials, J. Phys. Condens. Matter **28**, 383001 (2016).

[21] V. J. Emery, Theory of high-T_c superconductivity in oxides, Phys. Rev. Lett. **58**, 2794 (1987).

[22] J. Hubbard, Electron correlations in narrow energy bands, Proc. R. Soc. London A **276**, 238 (1963).

[23] P. W. Anderson, The resonating valence bond state in La_2CuO_4 and superconductivity, Science **235**, 1196 (1987).

[24] B.-X. Zheng, C.-M. Chung, P. Corboz, G. Ehlers, M.-P. Qin, R. M. Noack, H. Shi, S. R. White, S. Zhang, and G. K.-L. Chan, Stripe order in the underdoped region of the two-dimensional Hubbard model, Science **358**, 1155 (2017).

[25] E. W. Huang, C. B. Mendl, S. Liu, S. Johnston, H.-C. Jiang, B. Moritz, and T. P. Devereaux, Numerical evidence of fluctuating stripes in the normal state of high-T_c cuprate superconductors, Science **358**, 1161 (2017).

[26] I. Peschel, Special review: entanglement in solvable many-particle models, Braz. J. Phys. **42**, 267 (2012).

[27] A. Georges, G. Kotliar, W. Krauth, and M. J. Rozenberg, Dynamical mean-field theory of strongly correlated fermion systems and the limit of infinite dimensions, Rev. Mod. Phys. **68**, 13 (1996).

[28] G. Kotliar, S. Y. Savrasov, K. Haule, V. S. Oudovenko, O. Parcollet, and C. A. Marianetti, Electronic structure calculations with dynamical mean-field theory, Rev. Mod. Phys. **78**, 865 (2006).

[29] P. W. Anderson, Local magnetic states in metals, Phys. Rev. **124**, 41 (1961).

[30] G. Knizia and G. K.-L. Chan, Density matrix embedding: a simple alternative to dynamical mean-field theory, Phys. Rev. Lett. **109**, 186404 (2012).

[31] I. W. Bulik, G. E. Scuseria, and J. Dukelsky, Density matrix embedding from broken symmetry lattice mean fields, Phys. Rev. B **89**, 035140 (2014).

[32] B.-X. Zheng and G. K.-L. Chan, Ground-state phase diagram of the square lattice Hubbard model from density matrix embedding theory, Phys. Rev. B **93**, 035126 (2016).

[33] B.-X. Zheng, J. S. Kretchmer, H. Shi, S. Zhang, and G. K.-L. Chan, Cluster size convergence of the density matrix embedding theory and its dynamical cluster formulation: A study with an auxiliary-field quantum Monte Carlo solver, Phys. Rev. B **95**, 045103 (2017).

[34] G. Knizia and G. K.-L. Chan, Density matrix embedding: a strong-coupling quantum embedding theory, J. Chem. Theory Comput. **9**, 1428 (2013).

[35] S. Wouters, C. A. Jiménez-Hoyos, Q. Sun, and G. K.-L. Chan, A practical guide to density matrix embedding theory in quantum chemistry, J. Chem. Theory Comput. **12**, 2706 (2016).

[36] H. Q. Pham, V. Bernales, and L. Gagliardi, Can density matrix embedding theory with the complete activate space self-consistent field solver describe single and double bond breaking in molecular systems?, J. Chem. Theory Comput. **14**, 1960 (2018).

[37] Z. Fan and Q.-l. Jie, Cluster density matrix embedding theory for quantum spin systems, Phys. Rev. B **91**, 195118 (2015).

[38] B. Sandhoefer and G. K.-L. Chan, Density matrix embedding theory for interacting electron-phonon systems, Phys. Rev. B **94**, 085115 (2016).

[39] G. H. Booth and G. K.-L. Chan, Spectral functions of strongly correlated extended systems via an exact quantum embedding, Phys. Rev. B **91**, 155107 (2015).

[40] J. S. Kretchmer and G. K.-L. Chan, A real-time extension of density matrix embedding theory for non-equilibrium electron dynamics, J. Chem. Phys. **148**, 054108 (2018).

[41] M. Imada, A. Fujimori, and Y. Tokura, Metal-insulator transitions, Rev. Mod. Phys. **70**, 1039 (1998).

[42] S. Sachdev, Colloquium: order and quantum phase transitions in the cuprate superconductors, Rev. Mod. Phys. **75**, 913 (2003).

[43] P. A. Lee, N. Nagaosa, and X.-G. Wen, Doping a mott insulator: physics of high-temperature superconductivity, Rev. Mod. Phys. **78**, 17 (2006).

[44] D. Zgid and G. K. Chan, Dynamical mean-field theory from a quantum chemical perspective, J. Chem. Phys. **134**, 094115 (2011).

[45] Q. Sun and G. K.-L. Chan, Quantum embedding theories, Acc. Chem. Res. **49**, 2705 (2016).

[46] M. S. Gordon, *Fragmentation: toward accurate calculations on complex molecular systems* (John Wiley & Sons, 2017).

[47] H. Ma, N. Sheng, M. Govoni, and G. Galli, Quantum embedding theory for strongly correlated states in materials, J. Chem. Theory Comput. **17**, 2116 (2021).

[48] M. Nusspickel and G. H. Booth, Systematic improvability in quantum embedding for real materials, Phys. Rev. X **12**, 011046 (2022).

[49] A. Georges and G. Kotliar, Hubbard model in infinite dimensions, Phys. Rev. B **45**, 6479 (1992).

[50] K. Held, Electronic structure calculations using dynamical mean field theory, Adv. in Phys. **56**, 829 (2007).

[51] T. Maier, M. Jarell, T. Pruschke, and M. H. Hettler, Quantum cluster theories, Rev. Mod. Phys. **77**, 1027 (2005).

[52] M. Potthoff, Self-energy-functional approach to systems of correlated electrons, Eur. Phys. J. B **32**, 429 (2003).

[53] D. Sénéchal, An introduction to quantum cluster methods, arXiv: 0806.2690 [cond-mat] (2008).

[54] A. A. Kananenka, E. Gull, and D. Zgid, Systematically improvable multiscale solver for correlated electron systems, Phys. Rev. B **91**, 121111 (2015).

[55] A. A. Rusakov, S. Iskakov, L. N. Tran, and D. Zgid, Self-energy embedding theory (seet) for periodic systems, J. Chem. Theory Comput. **15**, 229 (2019).

[56] S. Biermann, Dynamical screening effects in correlated electron materials-a progress report on combined many-body perturbation and dynamical mean field theory: GW+ DMFT, J. Phys. : Condens. Matter **26**, 173202 (2014).

[57] Q. Chen, G. H. Booth, S. Sharma, G. Knizia, and G. K.-L. Chan, Intermediate and spin-liquid phase of the half-filled honeycomb Hubbard model, Phys. Rev. B **89**, 165134 (2014).

[58] T. Wesolowski and A. Warshel, Frozen density functional approach for ab initio calculations of solvated molecules, J. Phys. Chem **97**, 8050 (1993).

[59] J. D. Goodpaster, N. Ananth, F. R. Manby, and T. F. Miller, Exact nonadditive kinetic potentials for embedded density functional theory, J. Chem. Phys. **133**, 084103 (2010).

[60] C. Huang, M. Pavone, and E. A. Carter, Quantum mechanical embedding theory based on a unique embedding potential, J. Chem. Phys. **134**, 154110 (2011).

[61] F. Libisch, C. Huang, and E. A. Carter, Embedded correlated wavefunction schemes: theory and applications, Acc. Chem. Res. **47**, 2768 (2014).

[62] C. R. Jacob and J. Neugebauer, Subsystem density-functional theory, WIREs Comput. Mol. Sci. **4**, 325 (2014).

[63] D. V. Chulhai and J. D. Goodpaster, Projection-based correlated wave function in density functional theory embedding for periodic systems, J. Chem. Theory Comput. **14**, 1928 (2018).

[64] S. J. R. Lee, M. Welborn, F. R. Manby, and T. F. Miller, Projection-based wavefunction-in-DFT embedding, Acc. Chem. Res. **52**, 1359 (2019).

[65] T. Zhu, P. de Silva, H. van Aggelen, and T. Van Voorhis, Many-electron expansion: a density functional hierarchy for strongly correlated systems, Phys. Rev. B **93**, 201108 (2016).

[66] T. Zhu, P. de Silva, and T. Van Voorhis, Implementation of the many-pair expansion for systematically improving density functional calculations of molecules, J. Chem. Theory Comput. **15**, 1089 (2019).

[67] A. Ekert and P. L. Knight, Entangled quantum systems and the Schmidt decomposition, Amer. J. Phys. **63**, 415 (1995).

[68] I. Klich, Lower entropy bounds and particle number fluctuations in a Fermi sea, J. Phys. A: Math. Gen. **39**, L85 (2006).

[69] T. Helgaker, P. Jorgensen, and J. Olsen, *Molecular electronic-structure theory* (John Wiley & Sons, 2000).

[70] R. M. Martin, L. Reining, and D. M. Ceperley, *Interacting electrons* (Cambridge University Press, 2016).

[71] Y. Lu, M. Höppner, O. Gunnarsson, and M. Haverkort, Efficient real-frequency solver for dynamical mean-field theory, Phys. Rev. B **90**, 085102 (2014).

[72] R. Bulla, T. A. Costi, and T. Pruschke, Numerical renormalization group method for quantum impurity systems, Rev. Mod. Phys. **80**, 395 (2008).

[73] R. Peters, Spectral functions for single- and multi-impurity models using density matrix renormalization group, Phys. Rev. B **84**, 075139 (2011).

[74] M. Ganahl, M. Aichhorn, H. G. Evertz, P. Thunström, K. Held, and F. Verstraete, Efficient DMFT impurity solver using real-time dynamics with matrix product states, Phys. Rev. B **92**, 155132 (2015).

[75] A. Liebsch and H. Ishida, Temperature and bath size in exact diagonalization dynamical mean field theory, J. Phys. Condens. Matter **24**, 053201 (2012).

[76] E. Koch, G. Sangiovanni, and O. Gunnarsson, Sum rules and bath parametrization for quantum cluster theories, Phys. Rev. B **78**, 115102 (2008).

[77] F. A. Wolf, A. Go, I. P. McCulloch, A. J. Millis, and U. Schollwöck, Imaginary-time matrix product state impurity solver for dynamical mean-field theory, Phys. Rev. X **5**, 041032 (2015).

[78] I. de Vega, U. Schollwöck, and F. A. Wolf, How to discretize a quantum bath for real-time evolution, Phys. Rev. B **92**, 155126 (2015).

[79] D. Marx and J. Hutter, Ab initio molecular dynamics: theory and implementation, Modern methods and algorithms of quantum chemistry **1**, 141 (2000).

[80] J. McClain, Q. Sun, G. K.-L. Chan, and T. C. Berkelbach, Gaussian-based coupled-cluster theory for the ground-state and band structure of solids, J. Chem. Theory Comput. **13**, 1209 (2017).

[81] Q. Sun, T. C. Berkelbach, J. D. McClain, and G. K.-L. Chan, Gaussian and plane-wave mixed density fitting for periodic systems, J. Chem. Phys. **147**, 164119 (2017).

[82] Q. Sun, X. Zhang, S. Banerjee, P. Bao, M. Barbry, N. S. Blunt, N. A. Bogdanov, G. H. Booth, J. Chen, Z.-H. Cui, J. J. Eriksen, Y. Gao, S. Guo, J. Hermann, M. R. Hermes, K. Koh, P. Koval, S. Lehtola, Z. Li, J. Liu, N. Mardirossian, J. D. McClain, M. Motta, B. Mussard, H. Q. Pham, A. Pulkin, W. Purwanto, P. J. Robinson, E. Ronca, E. Sayfutyarova, M. Scheurer, H. F. Schurkus, J. E. T. Smith, C. Sun, S.-N. Sun, S. Upadhyay, L. K. Wagner, X. Wang, A. White, J. D. Whitfield, M. J. Williamson, S. Wouters, J. Yang, J. M. Yu, T. Zhu, T. C. Berkelbach, S. Sharma, A. Sokolov, and G. K.-L. Chan, Recent developments in the PySCF program package, J. Chem. Phys. **153**, 024109 (2020),

[83] J. M. Foster and S. F. Boys, Canonical configurational interaction procedure, Rev. Mod. Phys. **32**, 300 (1960).

[84] J. Pipek and P. G. Mezey, A fast intrinsic localization procedure applicable for ab-initio and semiempirical linear combination of atomic orbital wave functions, J. Chem. Phys. **90**, 4916 (1998).

[85] C. Edmiston and K. Ruedenberg, Localized atomic and molecular orbitals, Rev. Mod. Phys. **35**, 457 (1963).

[86] N. Marzari and D. Vanderbilt, Maximally localized generalized Wannier functions for composite energy bands, Phys. Rev. B **56**, 12847 (1997).

[87] N. Marzari, A. A. Mostofi, Y. R. Yates, I. Souza, and D. Vanderbilt, Maximally localized wannier functions: theory and applications, Rev. Mod. Phys. **84**, 1419 (2012).

[88] E. Ö. Jónsson, S. Lehtola, M. Puska, and H. Jónsson, Theory and applications of generalized Pipek-Mezey Wannier functions, J. Chem. Theory Comput. **13**, 460 (2017).

[89] H. Q. Pham, M. R. Hermes, and L. Gagliardi, Periodic electronic structure calculations with the density matrix embedding theory, J. Chem. Theory Comput. **16**, 130 (2019).

[90] I. Souza, N. Marzari, and D. Vanderbilt, Maximally localized Wannier functions for entangled energy bands, Phys. Rev. B **65**, 035109 (2001).

[91] A. Damle and L. Lin, Disentanglement via entanglement: a unified method for wannier localization, Multiscale Model. Simul. **16**, 1392 (2018).

[92] P.-O. Löwdin, On the non-orthogonality problem connected with the use of atomic wave functions in the theory of molecules and crystals, J. Chem. Phys. **18**, 365 (1950).

[93] Q. Sun and G. K.-L. Chan, Exact and optimal quantum mechanics/molecular mechanics boundaries, J. Chem. Theory Comput. **10**, 3784 (2014).

[94] A. E. Reed, R. B. Weinstock, and F. Weinhold, Natural population analysis, J. Chem. Phys. **83**, 735 (1985).

[95] G. Knizia, Intrinsic atomic orbitals: an unbiased bridge between quantum theory and chemical concepts, J. Chem. Theory Comput. **9**, 4834 (2013).

[96] S. Saebø and P. Pulay, Local treatment of electron correlation, Annu. Rev. Phys. Chem. **44**, 213 (1993).

[97] M. Motta, D. M. Ceperley, G. K.-L. Chan, J. A. Gomez, E. Gull, S. Guo, C. A. Jiménez-Hoyos, T. N. Lan, J. Li, F. Ma, A. J. Millis, N. V. Prokof'ev, U. Ray, G. E. Scuseria, S. Sorella, E. M. Stoudenmire, Q. Sun, I. S. Tupitsyn, S. R. White, D. Zgid, and S. Zhang, Towards the solution of the many-electron problem in real materials: equation of state of the hydrogen chain with state-of-the-art many-body methods, Phys. Rev. X **7**, 031059 (2017).

[98] Z.-H. Cui, T. Zhu, and G. K.-L. Chan, Efficient implementation of ab initio quantum embedding in periodic systems: density matrix embedding theory, J. Chem. Theory Comput. **16**, 119 (2020),

[99] Z.-H. Cui, C. Sun, U. Ray, B.-X. Zheng, Q. Sun, and G. K.-L. Chan, Ground-state phase diagram of the three-band Hubbard model from density matrix embedding theory, Phys. Rev. Research **2**, 043259 (2020),

[100] T. Zhu, Z.-H. Cui, and G. K.-L. Chan, Efficient formulation of ab initio quantum embedding in periodic systems: dynamical mean-field theory, J. Chem. Theory Comput. **16**, 141 (2020),

[101] B.-X. Zheng, Density matrix embedding theory and strongly correlated lattice systems, arXiv: 1803.10259 [cond-mat] (2018).

[102] X. Wu, M. Lindsey, T. Zhou, Y. Tong, and L. Lin, Enhancing robustness and efficiency of density matrix embedding theory via semidefinite programming and local correlation potential fitting, Phys. Rev. B **102**, 085123 (2020).

[103] S. Y. Savrasov, G. Kotliar, and E. Abrahams, Correlated electrons in δ-plutonium within a dynamical mean-field picture, Nature **410**, 793 (2001).

[104] S. Y. Savrasov and G. Kotliar, Spectral density functionals for electronic structure calculations, Phys. Rev. B **65**, 245101 (2004).

[105] L. V. Pourovskii, B. Amadon, S. Biermann, and A. Georges, Self-consistency over the charge density in dynamical mean-field theory: A linear muffin-tin implementation and some physical implications, Phys. Rev. B **76**, 235101 (2007).

[106] H. Park, A. J. Millis, and C. A. Marianetti, Computing total energies in complex materials using charge self-consistent DFT+DMFT, Phys. Rev. B **90**, 235103 (2014).

[107] X. Wu, Z.-H. Cui, Y. Tong, M. Lindsey, G. K.-L. Chan, and L. Lin, Projected density matrix embedding theory with applications to the two-dimensional Hubbard model, J. Chem. Phys. **151**, 064108 (2019),

[108] N. Bogoliubov, V. V. Tolmachov, and D. Širkov, A new method in the theory of superconductivity, Fortschritte der physik **6**, 605 (1958).

[109] J.-P. Blaizot and G. Ripka, *Quantum theory of finite systems*, Vol. 3, 9 (MIT press Cambridge, MA, 1986).

[110] Y. Nambu, Quasi-particles and gauge invariance in the theory of superconductivity, Phys. Rev. **117**, 648 (1960).

[111] P. W. Anderson, Random-phase approximation in the theory of superconductivity, Phys. Rev. **112**, 1900 (1958).

[112] L. Lin and X. Wu, Numerical solution of large scale Hartree-Fock-Bogoliubov equations, ESAIM: Math. Model. Numer. Anal. **55**, 763 (2021).

[113] J.-X. Zhu, *Bogoliubov-de gennes method and its applications*, Vol. 924 (Springer, 2016).

[114] Z.-H. Cui, H. Zhai, X. Zhang, and G. K.-L. Chan, Systematic electronic structure in the cuprate parent state from quantum many-body simulations, Science **377**, 1192 (2022),

[115] A. Szabo and N. S. Ostlund, *Modern quantum chemistry* (McGraw-Hill, New York, 1989).

[116] C. D. Sherrill, An introduction to configuration interaction theory, (1995).

[117] P. E. M. Siegbahn, J. Almlöf, A. Heiberg, and B. O. Roos, The complete active space SCF (CASSCF) method in a Newton–Raphson formulation with application to the HNO molecule, J. Chem. Phys. **74**, 2384 (1981).

[118] P. E. M. Siegbahn, A new direct CI method for large CI expansions in a small orbital space, Chem. Phys. Lett. **109**, 417 (1984).

[119] P. J. Knowles and N. C. Handy, A new determinant-based full configuration interaction method, Chem. Phys. Lett. **111**, 315 (1984).

[120] E. R. Davidson, The iterative calculation of a few of the lowest eigenvalues and corresponding eigenvectors of large real-symmetric matrices, J. Comput. Phys. **17**, 87 (1975).

[121] S. R. White, Density matrix formulation for quantum renormalization groups, Phys. Rev. Lett. **69**, 2863 (1992).

[122] S. R. White, Density-matrix algorithms for quantum renormalization groups, Phys. Rev. B **48**, 10345 (1993).

[123] U. Schollwöck, The density-matrix renormalization group in the age of matrix product states, Ann. phys. **326**, 96 (2011).

[124] Ö. Legeza and G. Fáth, Accuracy of the density-matrix renormalization-group method, Phys. Rev. B **53**, 14349 (1996).

[125] G. K.-L. Chan and M. Head-Gordon, Highly correlated calculations with a polynomial cost algorithm: A study of the density matrix renormalization group, J. Chem. Phys. **116**, 4462 (2002).

[126] S. R. White and A. L. Chernyshev, Néel order in square and triangular lattice Heisenberg models, Phys. Rev. Lett. **99**, 127004 (2007).

[127] R. Olivares-Amaya, W. Hu, N. Nakatani, S. Sharma, J. Yang, and G. K.-L. Chan, The ab-initio density matrix renormalization group in practice, J. Chem. Phys. **142**, 034102 (2015).

[128] J. R. Bartlett and M. Musiał, Coupled-cluster theory in quantum chemistry, Rev. Mod. Phys. **79**, 291 (2007).

[129] I. Shavitt and R. J. Bartlett, *Many-body methods in chemistry and physics: mbpt and coupled cluster theory* (Cambridge University, 2009).

[130] P. Pulay, Convergence acceleration of iterative sequences. the case of SCF iteration, Chem. Phys. Lett. **73**, 393 (1980).

[131] C. Yang, J. Brabec, L. Veis, D. B. Williams-Young, and K. Kowalski, Solving coupled cluster equations by the Newton Krylov method, Front. Chem. **8**, 590184 (2020).

[132] D. A. Knoll and D. E. Keyes, Jacobian-free Newton-Krylov methods: a survey of approaches and applications, J. Comput. Phys. **193**, 357 (2004).

[133] MPI4PySCF, An MPI plugin for PySCF, `https://github.com/zhcui/mpi4pyscf` .

[134] I. Mayer, Charge, bond order and valence in the ab initio SCF theory, Chem. Phys. Lett. **97**, 270 (1983).

[135] A. D. Becke and K. E. Edgecombe, A simple measure of electron localization in atomic and molecular systems, J. Chem. Phys. **92**, 5397 (1990).

[136] B. Silvi and A. Savin, Classification of chemical bonds based on topological analysis of electron localization functions, Nature **371**, 683 (1994).

[137] W. Hu, L. Lin, and C. Yang, Projected commutator DIIS method for accelerating hybrid functional electronic structure calculations, J. Chem. Theory Comput. **13**, 5458 (2017).

[138] Q. Sun, T. C. Berkelbach, N. S. Blunt, G. H. Booth, S. Guo, Z. Li, J. Liu, J. D. McClain, E. R. Sayfutyarova, S. Sharma, S. Wouters, and G. K.-L. Chan, PySCF: the Python-based simulations of chemistry framework, WIREs Comput. Mol. Sci. **8**, e1340 (2018).

[139] G. K.-L. Chan, An algorithm for large scale density matrix renormalization group calculations, J. Chem. Phys. **120**, 3172 (2004).

[140] G. K.-L. Chan and S. Sharma, The density matrix renormalization group in quantum chemistry, Annu. Rev. Phys. Chem. **62**, 465 (2011).

[141] S. Sharma and G. K.-L. Chan, Spin-adapted density matrix renormalization group algorithms for quantum chemistry, J. Chem. Phys. **136**, 124121 (2012).

[142] J. P. F. LeBlanc, A. E. Antipov, F. Becca, I. W. Bulik, G. K.-L. Chan, C.-M. Chung, Y. Deng, M. Ferrero, T. M. Henderson, C. A. Jiménez-Hoyos, E. Kozik, X.-W. Liu, A. J. Millis, N. V. Prokof'ev, M. Qin, G. E. Scuseria, H. Shi, B. V. Svistunov, L. F. Tocchio, I. S. Tupitsyn, S. R. White, S. Zhang, B.-X. Zheng, Z. Zhu, and E. Gull, Solutions of the two-dimensional Hubbard model: benchmarks and results from a wide range of numerical algorithms, Phys. Rev. X **5**, 041041 (2015).

[143] F. C. Zhang and T. M. Rice, Effective Hamiltonian for the superconducting Cu oxides, Phys. Rev. B **37**, 3759 (1988).

[144] H. Sakakibara, H. Usui, K. Kuroki, R. Arita, and H. Aoki, Two-orbital model explains the higher transition temperature of the single-layer Hg-cuprate superconductor compared to that of the La-cuprate superconductor, Phys. Rev. Lett. **105**, 057003 (2010).

[145] M. S. Hybertsen, E. B. Stechel, M. Schluter, and D. R. Jennison, Renormalization from density-functional theory to strong-coupling models for electronic states in Cu-O materials, Phys. Rev. B **41**, 11068 (1990).

[146] R. T. Scalettar, D. J. Scalapino, R. L. Sugar, and S. R. White, Antiferromagnetic, charge-transfer, and pairing correlations in the three-band Hubbard model, Phys. Rev. B **44**, 770 (1991).

[147] M. Cini and A. Balzarotti, Cluster approach to the three-band Hubbard model of the Cu-O plane: Superconducting pairs, Phys. Rev. B **56**, 14711 (1997).

[148] M. Greiter and R. Thomale, No evidence for spontaneous orbital currents in numerical studies of three-band models for the cuo planes of high temperature superconductors, Phys. Rev. Lett. **99**, 027005 (2007).

[149] R. Thomale and M. Greiter, Numerical analysis of three-band models for cuo planes as candidates for a spontaneous t-violating orbital current phase, Phys. Rev. B **77**, 094511 (2008).

[150] T. Shirakawa, H. Watanabe, and S. Yunoki, Theoretical studies of a three-band Hubbard model with a strong spin-orbit coupling for 5d transition metal oxide Sr_2IrO_4, J. Phys.: Conf. Ser. **454**, 012068 (2013).

[151] Y. Kung, C.-C. Chen, B. Moritz, S. Johnston, R. Thomale, and T. Devereaux, Numerical exploration of spontaneous broken symmetries in multiorbital Hubbard models, Phys. Rev. B **90**, 224507 (2014).

[152] G. Dopf, A. Muramatsu, and W. Hanke, Three-band Hubbard model: A Monte Carlo study, Phys. Rev. B **41**, 9264 (1990).

[153] K. Kuroki and H. Aoki, Quantum Monte Carlo evidence for superconductivity in the three-band Hubbard model in two dimensions, Phys. Rev. Lett. **76**, 4400 (1996).

[154] M. Guerrero, J. E. Gubernatis, and S. Zhang, Quantum Monte Carlo study of hole binding and pairing correlations in the three-band Hubbard model, Phys. Rev. B **57**, 11980 (1998).

[155] T. Yanagisawa, S. Koike, and K. Yamaji, Ground state of the three-band Hubbard model, Phys. Rev. B **64**, 184509 (2001).

[156] C. Weber, T. Giamarchi, and C. Varma, Phase diagram of a three-orbital model for high-T_c cuprate superconductors, Phys. Rev. Lett. **112**, 117001 (2014).

[157] Y. F. Kung, C.-C. Chen, Y. Wang, E. W. Huang, E. A. Nowadnick, B. Moritz, R. T. Scalettar, S. Johnston, and T. P. Devereaux, Characterizing the three-orbital Hubbard model with determinant quantum Monte Carlo, Phys. Rev. B **93**, 155166 (2016).

[158] E. Vitali, H. Shi, A. Chiciak, and S. Zhang, Metal-insulator transition in the ground state of the three-band Hubbard model at half filling, Phys. Rev. B **99**, 165116 (2019).

[159] E. Jeckelmann, D. J. Scalapino, and S. R. White, Comparison of different ladder models, Phys. Rev. B **58**, 9492 (1998).

[160] S. Nishimoto, E. Jeckelmann, and D. J. Scalapino, Differences between hole and electron doping of a two-leg CuO ladder, Phys. Rev. B **66**, 245109 (2002).

[161] S. R. White and D. J. Scalapino, Doping asymmetry and striping in a three-orbital CuO_2 Hubbard model, Phys. Rev. B **92**, 205112 (2015).

[162] S. Bulut, W. A. Atkinson, and A. P. Kampf, Spatially modulated electronic nematicity in the three-band model of cuprate superconductors, Phys. Rev. B **88**, 155132 (2013).

[163] T. A. Maier and D. J. Scalapino, Pairing interaction near a nematic quantum critical point of a three-band CuO_2 model, Phys. Rev. B **90**, 174510 (2014).

[164] W. A. Atkinson, A. P. Kampf, and S. Bulut, Charge order in the pseudogap phase of cuprate superconductors, New J. Phys. **17**, 013025 (2015).

[165] T. Maier, M. Zölfl, T. Pruschke, and J. Keller, Magnetic properties of the three-band Hubbard model, Eur. Phys. J. B **7**, 377 (1999).

[166] M. Zölfl, T. Maier, T. Pruschke, and J. Keller, Electronic properties of CuO_2-planes: A DMFT study, Eur. Phys. J. B **13**, 47 (2000).

[167] P. R. C. Kent, T. Saha-Dasgupta, O. Jepsen, O. K. Andersen, A. Macridin, T. A. Maier, M. Jarrell, and T. C. Schulthess, Combined density functional and dynamical cluster quantum Monte Carlo calculations of the three-band Hubbard model for hole-doped cuprate superconductors, Phys. Rev. B **78**, 035132 (2008).

[168] L. de'Medici, X. Wang, M. Capone, and A. J. Millis, Correlation strength, gaps, and particle-hole asymmetry in high-T_c cuprates: A dynamical mean field study of the three-band copper-oxide model, Phys. Rev. B **80**, 054501 (2009).

[169] C. Weber, C. Yee, K. Haule, and G. Kotliar, Scaling of the transition temperature of hole-doped cuprate superconductors with the charge-transfer energy, EPL **100**, 37001 (2012).

[170] A. Go and A. J. Millis, Spatial correlations and the insulating phase of the high T_c cuprates: insights from a configuration-interaction-based solver for dynamical mean field theory, Phys. Rev. Lett. **114**, 016402 (2015).

[171] E. Arrigoni, M. Aichhorn, M. Daghofer, and W. Hanke, Phase diagram and single-particle spectrum of CuO_2 high-T_c layers: variational cluster approach to the three-band Hubbard model, New J. Phys. **11**, 055066 (2009).

[172] W. Hanke, M. Kiesel, M. Aichhorn, S. Brehm, and E. Arrigoni, The 3-band Hubbard-model versus the 1-band model for the high-T_c cuprates: Pairing dynamics, superconductivity and the ground-state phase diagram, Eur. Phys. J. Spec. Top. **188**, 15 (2010).

[173] M. S. Hybertsen, M. Schlüter, and N. E. Christensen, Calculation of coulomb-interaction parameters for La_2CuO_4 using a constrained-density functional approach, Phys. Rev. B **39**, 9028 (1989).

[174] A. K. McMahan, J. F. Annett, and R. M. Martin, Cuprate parameters from numerical Wannier functions, Phys. Rev. B **42**, 6268 (1990).

[175] R. L. Martin, Electronic localization in the cuprates, Phys. Rev. B **53**, 15501 (1996).

[176] M. Hirayama, Y. Yamaji, T. Misawa, and M. Imada, Ab initio effective Hamiltonians for cuprate superconductors, Phys. Rev. B **98**, 134501 (2018).

[177] A. Chiciak, E. Vitali, H. Shi, and S. Zhang, Magnetic orders in the hole-doped three-band Hubbard model: Spin spirals, nematicity, and ferromagnetic domain walls, Phys. Rev. B **97**, 235127 (2018).

[178] P.-G. de Gennes, *Superconductivity of metals and alloys* (Benjamin, New York, 1966).

[179] B.-X. Zheng, https://bitbucket.org/zhengbx/libdmet.

[180] libDMET: A library of density matrix embedding theory (DMET) for lattice models and realistic solids, `https://github.com/gkclab/libdmet_preview`.

[181] P. Pulay, Improved SCF convergence acceleration, J. Comput. Chem. **3**, 556 (1982).

[182] K. Yamada, E. Kudo, Y. Endoh, Y. Hidaka, M. Oda, M. Suzuki, and T. Murakami, The effect of the heat treatments on the antiferromagnetism in $La_2CuO_{4-\delta}$ single crystals, Solid State Commun. **64**, 753 (1987).

[183] Y. Tokura, S. Koshihara, T. Arima, H. Takagi, S. Ishibashi, T. Ido, and S. Uchida, Cu-O network dependence of optical charge-transfer gaps and spin-pair excitations in single-CuO_2-layer compounds, Phys. Rev. B **41**, 11657 (1990).

[184] S. L. Cooper, G. Thomas, A. Millis, P. Sulewski, J. Orenstein, D. Rapkine, S.-W. Cheong, and P. Trevor, Optical studies of gap, exchange, and hopping energies in the insulating cuprates, Phys. Rev. B **42**, 10785 (1990).

[185] S. Uchida, T. Ido, H. Takagi, T. Arima, Y. Tokura, and S. Tajima, Optical spectra of $La_{2-x}Sr_xCuO_4$: effect of carrier doping on the electronic structure of the CuO_2 plane, Phys. Rev. B **43**, 7942 (1991).

[186] H. Romberg, N. Nücker, J. Fink, T. Wolf, X. Xi, B. Koch, H. Geserich, M. Dürrler, W. Assmus, and B. Gegenheimer, Dielectric function of $YBa_2Cu_3O_7$ between 50 meV and 50 eV, Z. Phys., B, Condens. matter. **78**, 367 (1990).

[187] J. Jefferson, H. Eskes, and L. Feiner, Derivation of a single-band model for CuO_2 planes by a cell-perturbation method, Phys. Rev. B **45**, 7959 (1992).

[188] L. H. Li, Y. Chen, G. Behan, H. Zhang, M. Petravic, and A. M. Glushenkov, Large-scale mechanical peeling of boron nitride nanosheets by low-energy ball milling, J. Mater. Chem. **21**, 11862 (2011).

[189] D. Többens, N. Stüßer, K. Knorr, H. Mayer, and G. Lampert, E9: the new high-resolution neutron powder diffractometer at the berlin neutron scattering center, in European powder diffraction epdic 7, Vol. 378, Materials Science Forum (2001), pp. 288–293.

[190] A. K. Cheetham and D. A. O. Hope, Magnetic ordering and exchange effects in the antiferromagnetic solid solutions $Mn_xNi_{1-x}O$, Phys. Rev. B **27**, 6964 (1983).

[191] J. P. Perdew, K. Burke, and M. Ernzerhof, Generalized gradient approximation made simple, Phys. Rev. Lett. **77**, 3865 (1996).

[192] S. Goedecker, M. Teter, and J. Hutter, Separable dual-space gaussian pseudopotentials, Phys. Rev. B **54**, 1703 (1996).

[193] C. Hartwigsen, S. Goedecker, and J. Hutter, Relativistic separable dual-space Gaussian pseudopotentials from H to Rn, Phys. Rev. B **58**, 3641 (1998).

[194] J. VandeVondele and J. Hutter, Gaussian basis sets for accurate calculations on molecular systems in gas and condensed phases, J. Chem. Phys. **127**, 114105 (2007).

[195] G. L. Stoychev, A. A. Auer, and F. Neese, Automatic generation of auxiliary basis sets, J. Chem. Theory Comput. **13**, 554 (2017).

[196] J. Paier, R. Hirschl, M. Marsman, and G. Kresse, The perdew-burke-ernzerhof exchange-correlation functional applied to the G2-1 test set using a plane-wave basis set, J. Chem. Phys. **122**, 234102 (2005).

[197] R. Sundararaman and T. Arias, Regularization of the coulomb singularity in exact exchange by wigner-seitz truncated interactions: towards chemical accuracy in nontrivial systems, Phys. Rev. B **87**, 165122 (2013).

[198] Y. Gao, Q. Sun, M. Y. Jason, M. Motta, J. McClain, A. F. White, A. J. Minnich, and G. K.-L. Chan, Electronic structure of bulk manganese oxide and nickel oxide from coupled cluster theory, Phys. Rev. B **101**, 165138 (2020).

[199] I. Y. Zhang and A. Grüneis, Coupled cluster theory in materials science, Front. Mater. **6**, 123 (2019).

[200] F. Gygi and A. Baldereschi, Self-consistent Hartree-Fock and screened-exchange calculations in solids: applications to silicon, Phys. Rev. B **34**, 4405 (1986).

[201] M. Welborn, T. Tsuchimochi, and T. Van Voorhis, Bootstrap embedding: an internally consistent fragment-based method, J. Chem. Phys. **145**, 074102 (2016).

[202] N. Ricke, M. Welborn, H.-Z. Ye, and T. Van Voorhis, Performance of bootstrap embedding for long-range interactions and 2D systems, Mol. Phys. **115**, 2242 (2017).

[203] H.-Z. Ye, N. D. Ricke, H. K. Tran, and T. Van Voorhis, Bootstrap embedding for molecules, J. Chem. Theory Comput. **15**, 4497 (2019).

[204] F. D. Murnaghan, The compressibility of media under extreme pressures, Proc. Natl. Acad. Sci. U S A **30**, 244 (1944).

[205] F. Birch, Finite elastic strain of cubic crystals, Phys. Rev. **71**, 809 (1947).

[206] L. Schimka, J. Harl, and G. Kresse, Improved hybrid functional for solids: the hsesol functional, J. Chem. Phys. **134**, 024116 (2011).

[207] G. A. Sawatzky and J. W. Allen, Magnitude and origin of the band gap in NiO, Phys. Rev. Lett. **53**, 2339 (1984).

[208] J. P. Perdew, W. Yang, K. Burke, Z. Yang, E. K. U. Gross, M. Scheffler, G. E. Scuseria, T. M. Henderson, I. Y. Zhang, A. Ruzsinszky, H. Peng, J. Sun, E. Trushin, and A. Görling, Understanding band gaps of solids in generalized Kohn-Sham theory, Proc. Natl. Acad. Sci. USA **114**, 2801 (2017).

[209] S. Kümmel and L. Kronik, Orbital-dependent density functionals: theory and applications, Rev. Mod. Phys. **80**, 3 (2008).

[210] A. H. Alperin, J. Phys. Soc. Japan Suppl. B **17**, 12 (1962).

[211] B. E. F. Fender, A. J. Jacobson, and F. A. Wedgwood, Covalency parameters in mno, α-mns, and nio, J. Chem. Phys. **48**, 990 (1968).

[212] T. Chatterji, G. J. McIntyre, and P.-A. Lindgard, Antiferromagnetic phase transition and spin correlations in NiO, Phys. Rev. B **79**, 172403 (2009).

[213] K. H. Germann, K. Maier, and E. Strauß, Magnetic order induced birefringence and critical behaviour of the long range order parameter in nio, Solid State Commun. **14**, 1309 (1974).

[214] I. Negovetić and J. Konstantinović, The critical behaviour of spontaneous magnetization in the antiferromagnetic nio, Solid State Commun. **13**, 249 (1973).

[215] T. Zhu, C. A. Jiménez-Hoyos, J. McClain, T. C. Berkelbach, and G. K.-L. Chan, Coupled-cluster impurity solvers for dynamical mean-field theory, Phys. Rev. B **100**, 115154 (2019).

[216] A. Shee and D. Zgid, Coupled cluster as an impurity solver for Green's function embedding methods, J. Chem. Theory Comput. **15**, 6010 (2019).

[217] M. Nooijen and J. G. Snijders, Coupled cluster approach to the single-particle green's function, Int. J. Quantum Chem. **44**, 55 (1992).

[218] M. Nooijen and J. G. Snijders, Coupled cluster green's function method: working equations and applications, Int. J. Quantum Chem. **48**, 15 (1993).

[219] J. McClain, J. Lischner, T. Watson, D. A. Matthews, E. Ronca, S. G. Louie, T. C. Berkelbach, and G. K.-L. Chan, Spectral functions of the uniform electron gas via coupled-cluster theory and comparison to the GW and related approximations, Phys. Rev. B **93**, 235139 (2016).

[220] K. Bhaskaran-Nair, K. Kowalski, and W. A. Shelton, Coupled cluster green function: model involving single and double excitations, J. Chem. Phys. **144**, 144101 (2016).

[221] Y. Furukawa, T. Kosugi, H. Nishi, and Y.-i. Matsushita, Band structures in coupled-cluster singles-and-doubles green's function (GFCCSD), J. Chem. Phys. **148**, 204109 (2018).

[222] E. de Sturler, Truncation strategies for optimal Krylov subspace methods, SIAM J. Numer. Anal. **36**, 864 (1999).

[223] J. F. Stanton and R. J. Bartlett, The equation of motion coupled-cluster method. a systematic biorthogonal approach to molecular excitation energies, transition probabilities, and excited state properties, J. Chem. Phys. **98**, 7029 (1993).

[224] X. Ren, I. Leonov, G. Keller, M. Kollar, I. Nekrasov, and D. Vollhardt, LDA+DMFT computation of the electronic spectrum of NiO, Phys. Rev. B **74**, 195114 (2006).

[225] J. Kunes, V. I. Anisimov, S. L. Skornyakov, A. V. Lukoyanov, and D. Vollhardt, NiO: correlated band structure of a charge-transfer insulator, Phys. Rev. Lett. **99**, 156404 (2007).

[226] J. Kuneš, V. I. Anisimov, A. V. Lukoyanov, and D. Vollhardt, Local correlations and hole doping in NiO: a dynamical mean-field study, Phys. Rev. B **75**, 165115 (2007).

[227] Q. Yin, A. Gordienko, X. Wan, and S. Y. Savrasov, Calculated momentum dependence of Zhang-Rice states in transition metal oxides, Phys. Rev. Lett. **100**, 066406 (2008).

[228] M. Karolak, G. Ulm, T. Wehling, V. Mazurenko, A. Poteryaev, and A. Lichtenstein, Double counting in LDA + DMFT - the example of nio, J. Electron Spectros. Relat. Phenom. **181**, 11 (2010).

[229] P. Thunström, I. Di Marco, and O. Eriksson, Electronic entanglement in late transition metal oxides, Phys. Rev. Lett. **109**, 186401 (2012).

[230] I. Leonov, L. Pourovskii, A. Georges, and I. A. Abrikosov, Magnetic collapse and the behavior of transition metal oxides at high pressure, Phys. Rev. B **94**, 155135 (2016).

[231] O. Grånäs, I. Di Marco, P. Thunström, L. Nordström, O. Eriksson, T. Björkman, and J. Wills, Charge self-consistent dynamical mean-field theory based on the full-potential linear muffin-tin orbital method: methodology and applications, Comput. Mater. Sci. **55**, 295 (2012).

[232] Q. Si and J. L. Smith, Kosterlitz-thouless transition and short range spatial correlations in an extended Hubbard model, Phys. Rev. Lett. **77**, 3391 (1996).

[233] P. Sun and G. Kotliar, Extended dynamical mean-field theory and GW method, Phys. Rev. B **66**, 085120 (2002).

[234] S. Biermann, F. Aryasetiawan, and A. Georges, First-principles approach to the electronic structure of strongly correlated systems: combining the GW approximation and dynamical mean-field theory, Phys. Rev. Lett. **90**, 086402 (2003).

[235] P. Sun and G. Kotliar, Many-body approximation scheme beyond GW, Phys. Rev. Lett. **92**, 196402 (2004).

[236] S. Das, J. E. Coulter, and E. Manousakis, Convergence of quasiparticle self-consistent gw calculations of transition-metal monoxides, Phys. Rev. B **91**, 115105 (2015).

[237] E. Dagotto, Complexity in strongly correlated electronic systems, Science **309**, 257 (2005).

[238] J. Orenstein and A. Millis, Advances in the physics of high-temperature superconductivity, Science **288**, 468 (2000).

[239] N. Plakida, *High-temperature cuprate superconductors: experiment, theory, and applications*, Vol. 166 (Springer Science & Business Media, 2010).

[240] X. Zhou, W.-S. Lee, M. Imada, N. Trivedi, P. Phillips, H.-Y. Kee, P. Törmä, and M. Eremets, High-temperature superconductivity, Nat. Rev. Phys. **3**, 462 (2021).

[241] H. Zhai and G. K.-L. Chan, Low communication high performance ab initio density matrix renormalization group algorithms, J. Chem. Phys. **154**, 224116 (2021).

[242] T. Zhu and G. K.-L. Chan, Ab initio full cell GW + DMFT for correlated materials, Phys. Rev. X **11**, 021006 (2021).

[243] E. Pavarini, I. Dasgupta, T. Saha-Dasgupta, O. Jepsen, and O. Andersen, Band-structure trend in hole-doped cuprates and correlation with $T_{\mathrm{c\,max}}$, Phys. Rev. Lett. **87**, 047003 (2001).

[244] E. Antipov, A. Abakumov, and S. Putilin, Chemistry and structure of Hg-based superconducting Cu mixed oxides, Supercond. Sci. Tech. **15**, R31 (2002).

[245] K. Lokshin, D. A. Pavlov, S. Putilin, E. Antipov, D. Sheptyakov, and A. Balagurov, Enhancement of T_{c} in $HgBa_2Ca_2Cu_3O_{8+\delta}$ by fluorination, Phys. Rev. B **63**, 064511 (2001).

[246] H. Sakakibara, H. Usui, K. Kuroki, R. Arita, and H. Aoki, Two-orbital model explains the higher transition temperature of the single-layer Hg-cuprate superconductor compared to that of the La-cuprate superconductor, Phys. Rev. Lett. **105**, 057003 (2010).

[247] S. Kim, X. Chen, W. Fitzhugh, and X. Li, Apical charge flux-modulated in-plane transport properties of cuprate superconductors, Phys. Rev. Lett. **121**, 157001 (2018).

[248] L. K. Wagner and P. Abbamonte, Effect of electron correlation on the electronic structure and spin-lattice coupling of high-T_{c} cuprates: quantum Monte Carlo calculations, Phys. Rev. B **90**, 125129 (2014).

[249] K. Foyevtsova, J. T. Krogel, J. Kim, P. Kent, E. Dagotto, and F. A. Reboredo, Ab initio quantum Monte Carlo calculations of spin superexchange in cuprates: the benchmarking case of Ca_2CuO_3, Phys. Rev. X **4**, 031003 (2014).

[250] D. Muñoz, F. Illas, and I. de PR Moreira, Accurate prediction of large antiferromagnetic interactions in high-T_{c} $HgBa_2Ca_{n-1}Cu_nO_{2n+2+\delta}$ ($n = 2, 3$) superconductor parent compounds, Phys. Rev. Lett. **84**, 1579 (2000).

[251] C. Lane, J. W. Furness, I. G. Buda, Y. Zhang, R. S. Markiewicz, B. Barbiellini, J. Sun, and A. Bansil, Antiferromagnetic ground state of La_2CuO_4: a parameter-free ab initio description, Phys. Rev. B **98**, 125140 (2018).

[252] C. Weber, K. Haule, and G. Kotliar, Strength of correlations in electron-and hole-doped cuprates, Nat. Phys. **6**, 574 (2010).

[253] S. Choi, A. Kutepov, K. Haule, M. Van Schilfgaarde, and G. Kotliar, First-principles treatment of mott insulators: linearized QSGW+DMFT approach, Npj Quant. Mater. **1**, 1 (2016).

[254] M. Qin, C.-M. Chung, H. Shi, E. Vitali, C. Hubig, U. Schollwöck, S. R. White, S. Zhang, et al., Absence of superconductivity in the pure two-dimensional Hubbard model, Phys. Rev. X **10**, 031016 (2020).

[255] J. Karp, A. S. Botana, M. R. Norman, H. Park, M. Zingl, and A. Millis, Many-body electronic structure of $NdNiO_2$ and $CaCuO_2$, Phys. Rev. X **10**, 021061 (2020).

[256] P. Mai, G. Balduzzi, S. Johnston, and T. A. Maier, Orbital structure of the effective pairing interaction in the high-temperature superconducting cuprates, npj Quant. Mater. **6**, 1 (2021).

[257] S. R. White and R. L. Martin, Ab initio quantum chemistry using the density matrix renormalization group, J. Chem. Phys. **110**, 4127 (1999).

[258] F. Weigend and R. Ahlrichs, Balanced basis sets of split valence, triple zeta valence and quadruple zeta valence quality for H to Rn: design and assessment of accuracy, Phys. Chem. Chem. Phys. **7**, 3297 (2005).

[259] J.-Y. Delannoy, M. Gingras, P. Holdsworth, and A.-M. Tremblay, Low-energy theory of the t-t'-t''-U Hubbard model at half-filling: interaction strengths in cuprate superconductors and an effective spin-only description of La_2CuO_4, Phys. Rev. B **79**, 235130 (2009).

[260] L. Wang, G. He, Z. Yang, M. Garcia-Fernandez, A. Nag, K. Zhou, M. Minola, M. L. Tacon, B. Keimer, Y. Peng, et al., Paramagnons and high-temperature superconductivity in a model family of cuprates, Nat. Comm. **13**, 1 (2022).

[261] B. Yu, W. Tabis, I. Bialo, F. Yakhou, N. Brookes, Z. Anderson, Y. Tang, G. Yu, and M. Greven, Unusual dynamic charge correlations in simple-tetragonal $HgBa_2CuO_{4+\delta}$, Phys. Rev. X **10**, 021059 (2020).

[262] Y. Peng, G. Dellea, M. Minola, M. Conni, A. Amorese, D. Di Castro, G. De Luca, K. Kummer, M. Salluzzo, X. Sun, et al., Influence of apical oxygen on the extent of in-plane exchange interaction in cuprate superconductors, Nat. Phys. **13**, 1201 (2017).

[263] D. Kan, A. Yamanaka, T. Terashima, and M. Takano, Preparation and optical properties of single-crystalline $CaCuO_2$ thin films with infinite layer structure, Physica C: Supercond. **412**, 298 (2004).

[264] L. Gao, Y. Xue, F. Chen, Q. Xiong, R. Meng, D. Ramirez, C. Chu, J. Eggert, and H. Mao, Superconductivity up to 164 K in $HgBa_2Ca_{m-1}Cu_mO_{2m+2+\delta}$ ($m = 1$, 2, and 3) under quasihydrostatic pressures, Phys. Rev. B **50**, 4260 (1994).

[265] L. Nordheim, The electron theory of metals, Ann. Phys. **9**, 607 (1931).

[266] L. Bellaiche and D. Vanderbilt, Virtual crystal approximation revisited: application to dielectric and piezoelectric properties of perovskites, Phys. Rev. B **61**, 7877 (2000).

[267] P. Soven, Coherent-potential model of substitutional disordered alloys, Phys. Rev. **156**, 809 (1967).

[268] D. Taylor, Vibrational properties of imperfect crystals with large defect concentrations, Phys. Rev. **156**, 1017 (1967).

[269] G. Kresse and J. Hafner, Ab initio molecular dynamics for liquid metals, Phys. Rev. B **47**, 558 (1993).

[270] G. Kresse and J. Hafner, Ab initio molecular-dynamics simulation of the liquid-metal–amorphous-semiconductor transition in germanium, Phys. Rev. B **49**, 14251 (1994).

[271] G. Kresse and J. Furthmüller, Efficiency of ab-initio total energy calculations for metals and semiconductors using a plane-wave basis set, Comp. Mater. Sci. **6**, 15 (1996).

[272] G. Kresse and J. Furthmüller, Efficient iterative schemes for *ab initio* total-energy calculations using a plane-wave basis set, Phys. Rev. B **54**, 11169 (1996).

[273] G. Kresse and D. Joubert, From ultrasoft pseudopotentials to the projector augmented-wave method, Phys. Rev. B **59**, 1758 (1999).

[274] P. E. Blöchl, Projector augmented-wave method, Phys. Rev. B **50**, 17953 (1994).

[275] J. P. Perdew, M. Ernzerhof, and K. Burke, Rationale for mixing exact exchange with density functional approximations, J. Chem. Phys. **105**, 9982 (1996).

[276] N. Kowalski, S. S. Dash, P. Sémon, D. Sénéchal, and A.-M. Tremblay, Oxygen hole content, charge-transfer gap, covalency, and cuprate superconductivity, Proc. Natl. Acad. Sci. **118**, e2106476118 (2021).

[277] C. Lee, W. Yang, and R. G. Parr, Development of the Colle-Salvetti correlation-energy formula into a functional of the electron density, Phys. Rev. B **37**, 785 (1988).

[278] A. D. Becke, A new mixing of Hartree-Fock and local density-functional theories, J. Chem. Phys. **98**, 1372 (1993).

[279] A. D. Becke, Density-functional thermochemistry. III. the role of exact exchange, J. Chem. Phys. **98**, 5648 (1993).

[280] J. Heyd, G. E. Scuseria, and M. Ernzerhof, Hybrid functionals based on a screened coulomb potential, J. Chem. Phys. **118**, 8207 (2003).

[281] D. M. Bylander and L. Kleinman, Good semiconductor band gaps with a modified local-density approximation, Phys. Rev. B **41**, 7868 (1990).

[282] A. Seidl, A. Görling, P. Vogl, and J. A. Majewski, Generalized Kohn-Sham schemes and the band gap problem, Phys. Rev. B **53**, 3764 (1996).

[283] M. Marsman, J. Paier, A. Stroppa, and G. Kresse, Hybrid functionals applied to extended systems, J. Phys. : Condens. Matter **20**, 064201 (2008).

[284] H. Xiao, J. Tahir-Kheli, and W. A. Goddard III, Accurate band gaps for semiconductors from density functional theory, J. Phys. Chem. Lett. **2**, 212 (2011).

[285] M.-Y. Zhang, Z.-H. Cui, Y.-C. Wang, and H. Jiang, Hybrid functionals with system-dependent parameters: conceptual foundations and methodological developments, WIREs Comput. Mol. Sci. **10**, e1476 (2020).

[286] L. Lin, Adaptively compressed exchange operator, J. Chem. Theory Comput. **12**, 2242 (2016).

[287] S. L. Dudarev, G. A. Botton, S. Y. Savrasov, C. J. Humphreys, and A. P. Sutton, Electron-energy-loss spectra and the structural stability of nickel oxide: An LSDA+U study, Phys. Rev. B **57**, 1505 (1998).

[288] A. I. Liechtenstein, V. I. Anisimov, and J. Zaanen, Density-functional theory and strong interactions: orbital ordering in Mott-Hubbard insulators, Phys. Rev. B **52**, R5467 (1995).

[289] V. I. Anisimov, J. Zaanen, and O. K. Andersen, Band theory and Mott insulators: Hubbard U instead of Stoner I, Phys. Rev. B **44**, 943 (1991).

[290] A. Rohrbach, J. Hafner, and G. Kresse, Electronic correlation effects in transition-metal sulfides, J. Phys.: Cond. Matt. **15**, 979 (2003).

[291] V. Anisimov, A. Kozhevnikov, M. Korotin, A. Lukoyanov, and D. Khafizullin, Orbital density functional as a means to restore the discontinuities in the total-energy derivative and the exchange-correlation potential, J. Phys.: Cond. Matt. **19**, 106206 (2007).

[292] D. D. O'Regan, Subspace representations in ab initio methods for strongly correlated systems, in *Optimised projections for the ab initio simulation of large and strongly correlated systems* (Springer, 2012), pp. 89–123.

[293] P. H. Dederichs, S. Blügel, R. Zeller, and H. Akai, Ground states of constrained systems: application to Cerium impurities, Phys. Rev. Lett. **53**, 2512 (1984).

[294] A. K. McMahan, R. M. Martin, and S. Satpathy, Calculated effective hamiltonian for La_2CuO_4 and solution in the impurity Anderson approximation, Phys. Rev. B **38**, 6650 (1988).

[295] W. E. Pickett, S. C. Erwin, and E. C. Ethridge, Reformulation of the LDA + U method for a local-orbital basis, Phys. Rev. B **58**, 1201 (1998).

[296] M. Cococcioni and S. de Gironcoli, Linear response approach to the calculation of the effective interaction parameters in the LDA+U method, Phys. Rev. B **71**, 035105 (2005).

[297] F. Aryasetiawan, M. Imada, A. Georges, G. Kotliar, S. Biermann, and A. I. Lichtenstein, Frequency-dependent local interactions and low-energy effective models from electronic structure calculations, Phys. Rev. B **70**, 195104 (2004).

[298] F. Aryasetiawan, K. Karlsson, O. Jepsen, and U. Schönberger, Calculations of Hubbard U from first-principles, Phys. Rev. B **74**, 125106 (2006).

[299] T. Miyake and F. Aryasetiawan, Screened Coulomb interaction in the maximally localized Wannier basis, Phys. Rev. B **77**, 085122 (2008).

[300] N. J. Mosey, P. Liao, and E. A. Carter, Rotationally invariant ab initio evaluation of Coulomb and exchange parameters for DFT+U calculations, J. Chem. Phys. **129**, 014103 (2008).

[301] L. Vaugier, H. Jiang, and S. Biermann, Hubbard U and Hund exchange J in transition metal oxides: screening versus localization trends from constrained random phase approximation, Phys. Rev. B **86**, 165105 (2012).

[302] C. Sun, U. Ray, Z.-H. Cui, M. Stoudenmire, M. Ferrero, and G. K.-L. Chan, Finite-temperature density matrix embedding theory, Phys. Rev. B **101**, 075131 (2020),

[303] Q. Huang, J. Lynn, Q. Xiong, and C. Chu, Oxygen dependence of the crystal structure of $HgBa_2CuO_{4+\delta}$ and its relation to superconductivity, Phys. Rev. B **52**, 462 (1995).

[304] P. Radaelli, J. Wagner, B. Hunter, M. Beno, G. Knapp, J. Jorgensen, and D. Hinks, Structure, doping and superconductivity in $HgBa_2CaCu_2O_{6+\delta}$ ($T_c \leqslant 128$ K), Physica C: Supercond. **216**, 29 (1993).

[305] J. Karpinski, H. Schwer, I. Mangelschots, K. Conder, A. Morawski, T. Lada, and A. Paszewin, Single crystals of $Hg_{1-x}Pb_xBa_2Ca_{n-1}Cu_nO_{2n+2+\delta}$ and infinite-layer $CaCuO_2$. synthesis at gas pressure 10 kbar, properties and structure, Physica C: Supercond. **234**, 10 (1994).

[306] R. Coldea, S. Hayden, G. Aeppli, T. Perring, C. Frost, T. Mason, S.-W. Cheong, and Z. Fisk, Spin waves and electronic interactions in La_2CuO_4, Phys. Rev. Lett. **86**, 5377 (2001).

[307] S. Petit, Numerical simulations and magnetism, École thématique de la Société Française de la Neutronique **12**, 105 (2011).

[308] S. Toth and B. Lake, Linear spin wave theory for single-Q incommensurate magnetic structures, J. Phys.: Cond. Matt. **27**, 166002 (2015).

[309] D. Andrae, U. Haeussermann, M. Dolg, H. Stoll, and H. Preuss, Energy-adjusted ab initio pseudopotentials for the second and third row transition elements, Theoret. Chim. Acta **77**, 123 (1990).

[310] M. Kaupp, P. v. R. Schleyer, H. Stoll, and H. Preuss, Pseudopotential approaches to Ca, Sr, and Ba hydrides. why are some alkaline earth MX_2 compounds bent?, J. Chem. Phys. **94**, 1360 (1991).

[311] A. Hellweg, C. Hättig, S. Höfener, and W. Klopper, Optimized accurate auxiliary basis sets for RI-MP2 and RI-CC2 calculations for the atoms Rb to Rn, Theor. Chem. Acc. **117**, 587 (2007).

[312] F. Weigend, M. Häser, H. Patzelt, and R. Ahlrichs, RI-MP2: optimized auxiliary basis sets and demonstration of efficiency, Chem. Phys. Lett. **294**, 143 (1998).

[313] I. d. P. Moreira, P. Rivero, and F. Illas, Electronic structure of $HgBa_2Ca_{n-1}Cu_nO_{2n+2}$ (n = 1, 2, 3) superconductor parent compounds from periodic hybrid density functional theory, J. Chem. Phys. **134**, 074709 (2011).

[314] D. Muñoz, C. De Graaf, and F. Illas, Putting error bars on the ab initio theoretical estimates of the magnetic coupling constants: the parent compounds of superconducting cuprates as a case study, J. Comput. Chem. **25**, 1234 (2004).

[315] D. Meyers, H. Miao, A. Walters, V. Bisogni, R. Springell, M. d'Astuto, M. Dantz, J. Pelliciari, H. Huang, J. Okamoto, et al., Doping dependence of the magnetic excitations in $La_{2-x}Sr_xCuO_4$, Phys. Rev. B **95**, 075139 (2017).

[316] N. A. Bogdanov, G. Li Manni, S. Sharma, O. Gunnarsson, and A. Alavi, Enhancement of superexchange due to synergetic breathing and hopping in corner-sharing cuprates, Nat. Phys. **18**, 190 (2022).

[317] E. Pavarini, I. Dasgupta, T. Saha-Dasgupta, and O. Andersen, Comment on "apical charge flux-modulated in-plane transport properties of cuprate superconductors", Phys. Rev. Lett. **124**, 109701 (2020).